

NASA CONTRACTOR REPORT

NASA CR-1559



NASA CR-1559



TECH LIBRARY KAFB, NM

LOAN COPY: RETURN TO
AFWL (WL01)
KIRTLAND AFB, N MEEX

BASIC RESEARCH ON LIQUID-DROP-IMPACT EROSION

by O. G. Engel

Prepared by
GENERAL ELECTRIC COMPANY
Cincinnati, Ohio 45215
for Lewis Research Center



0060923

1. Report No. NASA CR-1559		2. Government Accession No.		3. Recipient's Catalog No.	
4. Title and Subtitle BASIC RESEARCH ON LIQUID-DROP-IMPACT EROSION		5. Report Date June 1970		6. Performing Organization Code	
		7. Author(s) by O. G. Engel		8. Performing Organization Report No. GESP-253	
9. Performing Organization Name and Address General Electric Company Missile and Space Division Cincinnati, Ohio 45215		10. Work Unit No.		11. Contract or Grant No. NAS W-1481	
		12. Sponsoring Agency Name and Address National Aeronautics and Space Administration Washington, D. C. 20546		13. Type of Report and Period Covered Contractor Report	
				14. Sponsoring Agency Code	
15. Supplementary Notes					
16. Abstract On the basis of additional cratering data that were collected, it has been found that the equation for crater depth which was reported earlier is applicable only to pure face-centered-cubic metals. The restricted applicability of the equation has been traced to differences in the yield behavior of the metals which result in different crater contours. To increase the applicability of the equation, a dimensionless quotient, which contains the yield stress and the elastic modulus both for the metal of the sphere, has been added to the equation. The revised equation has been found to be in acceptable agreement with available low-velocity cratering data for pure metals of all three lattice packing types and for alloys. Evidence of an elevated dynamic yield strength has been found in the cratering curves of metals of the body-centered-cubic and hexagonal close-packed lattice types and in the case of Udimet 700 alloy. No evidence of an elevated dynamic yield strength has been found in the cratering curves of pure face-centered-cubic metals.					
17. Key Words (Suggested by Author(s)) Crater formation in metals; Denting velocity; Dynamic yield strength; Erosion; Iron; Liquid impingement; Nickel; Tantalum; Udimet 700; and Zinc			18. Distribution Statement Unclassified - unlimited		
19. Security Classif. (of this report) Unclassified		20. Security Classif. (of this page) Unclassified		21. No. of Pages 247	22. Price* \$3.00

1. Corrosion
2. Metals -- effects of impact
3. Water Erosion



FOREWORD

The research described herein, which was conducted by the General Electric Missile and Space Division, was performed under NASA Contract NAS W-1481. The NASA Project Manager was Stanley G. Young, Materials and Structures Division, Lewis Research Center. The report was originally issued as General Electric report GESP-253.

Helpful conversations with Dr. Cecil Dunn of the General Electric Research Laboratory, Schenectady, New York, Dr. James F. Bell of the Johns Hopkins University, Baltimore, Maryland, and Dr. George Irwin of Lehigh University, Bethlehem, Pennsylvania, are gratefully acknowledged, without committing them to the conclusions that have been drawn or to the explanations that have been given in this report.



Table of Contents

Section	Page
1. Introduction	1
1.1 Stresses Produced by Drop Impact	1
1.2 Erosion Failure of Low-Strength Brittle Solids	2
1.3 Erosion Failure of Low-Strength Ductile Solids	2
1.4 Prediction of Relative Drop-Impact-Erosion Resistance	5
1.4.1 Moving-Plug Model of Crater Formation	5
1.4.2 Denting Velocity As a Criterion of Erosion Resistance	7
1.5 Areas of Uncertainty With Regard to the Cratering Equations	8
1.5.1 Effect of Inhibited Plastic Flow	8
1.5.2 Effect of Stress-Strain Behavior	10
1.5.3 Use of Dynamic or Quasi-Static Yield Strength	11
1.5.4 Effect of Plate Thickness	11
1.6 Program of Further Work on the Cratering Equations	12
2. Derivation of the Cratering Equations	14
2.1 Elastic Wave Theory Applied to the Impact of Rods	14
2.2 Derivation of Equation (1.1)	17
2.3 Derivation of Equation (1.3)	21
3. Preparation of Test Specimens and Measurement of Required Properties	25
3.1 Source and Chemical Composition Data for the Selected Metals	25
3.2 Preparation of Specimens	29
3.2.1 Machining	29
3.2.2 Heat Treatment	29
3.2.3 Polishing	33
3.3 Determination of Infinite Medium Sound Speed	35
3.4 Tensile Properties of the Metals	38
3.5 Steel Spheres for Use in the Firings	40
4. Test Firings and Measurement of Crater Dimensions	41
4.1 Guns and Velocity-Measuring System	42
4.2 Measurements of Crater Dimensions	42
4.3 First Set of Cratering Data	45
4.4 Diagnostic Tests	48
4.5 Check of the Velocity-Measuring System	55
5. Further Diagnostic Studies	66
5.1 Appearance of the Surface Metal at the Rim of the Crater	66
5.2 Studies of the Metal Around the Crater With Use of Cross-Sectional Cuts	69
5.2.1 Gross Surface Contour	69
5.2.2 Subsurface Microstructural Change	73
5.3 Information From Stress-Strain Behavior	88
5.4 Information on Work-Hardening Produced by the Impacts	91

Table of Contents, Continued

Section	Page
6. Statistical Analysis of the Experimental Data	118
6.1 Face-Centered-Cubic Metals and Alloys	120
6.1.1 Commercially Pure Aluminum.	121
6.1.2 Nickel 270.	135
6.1.3 Electrolytic Tough Pitch Copper	145
6.1.4 Solutioned Udimet 700 Alloy	151
6.1.5 Aged Udimet 700 Alloy	158
6.1.6 Aluminum Based Alloy 2024-0 Aluminum.	165
6.2 Hexagonal Close-Packed Metals	170
6.3 Body-Centered Cubic Metals.	177
6.3.1 Armco Iron.	177
6.3.2 Tantalum.	185
7. Objectives and Results.	192
7.1 Steel-Sphere Denting Velocities of the Selected Metals.	192
7.1.1 Steel-Sphere Denting Velocities by the Method of Davies	192
7.1.2 Steel-Sphere Denting Velocities from the Energy per Unit Volume Required for Flow	197
7.2 Denting Velocity at Elevated Temperatures	205
7.3 Dynamic Yield Strengths of the Selected Metals.	209
7.4 Test of the Cratering Equation.	213
7.5 Liquid-Drop Denting Velocities from Steel-Sphere Denting Velocities.	228
8. Summary of Conclusions and Suggested Further Research	231
REFERENCES.	234

List of Illustrations

Figure	Page
1.1 Stresses Produced During Impact Between a Solid Plate and a Liquid Drop or Solid Sphere	3
1.2 Stresses Produced at a Surface Elevation Along a Crack by the Radial Flow of Liquid from an Impacted Drop	3
1.3 Damage Mark on a White Sapphire Plate Produced by Impact of a 2-mm Mercury Drop at 3.58×10^4 cm/sec (1,175 ft/sec) . . .	4
1.4 Polygons of Cracks Formed in Poly(methyl methacrylate) As a Result of Impact Against Waterdrops	4
2.1 Schematic Representation of the Impact of Two Rods	15
2.2 Plane-Wave Idealization of the Impact Between a Steel Sphere and a Plate	18
4.1 View of the Benjamin Model 317 Air Rifle and Associated Electronic Equipment	43
4.2 Crater-Depth-Versus-Velocity Plots for Impacts of 0.175-inch Steel Spheres Against Plates of Nickel, Zinc, Iron, and Tantalum	47
4.3 Crater-Depth-Versus-Velocity Plot for Craters Formed in Nickel Plates Under a Variety of Conditions	51
4.4 Velocities Acquired by 0.175-inch Spheres at Arbitrary Gas Pressures	57
4.5 Comparison of Velocities Measured with Light Screens and Metal Screens	59
4.6 Plot of Chronograph Velocity Against Pendulum Velocity . . .	64
5.1 Surface View of Nickel Specimens Near the Rim of the Crater .	67
5.2 Surface Views of Selected Metals Near the Rim of the Crater .	68
5.3 Surface Contours Around the Impact Craters	70 & 71
5.4 Gross Surface Contour of the Craters	72
5.5 Subsurface Microstructural Change in Nickel at a Low Velocity	74
5.6 Subsurface Microstructural Change in Nickel at a High Velocity	75
5.7 Subsurface Microstructural Change in Zinc	76
5.8 Subsurface Microstructural Change in Udimet 700 Solutioned .	78
5.9 Subsurface Microstructural Change in Udimet 700 Aged	79
5.10 Subsurface Microstructural Change in Iron	81
5.11 Subsurface Microstructural Change in Tantalum	82
5.12 Microstructure of Nickel at the Bottom of the Crater	84
5.13 Change in the Microstructure of Zinc	85

List of Illustrations, Continued

Figure	Page
5.14 Microstructure of Udimet 700 at the Bottom of the Crater . .	86
5.15 Microstructure of Tantalum and Iron at the Bottom of the Crater	87
5.16 Stress-Strain Curves for Nickel, Zinc, and Aluminum	92
5.17 Stress-Strain Curves for Udimet 700 in Two Heat-Treatment States	93
5.18 Stress-Strain Curves for Tantalum and Iron	94
5.19 Stress-Strain Curve for Electrolytic Tough Pitch Copper . .	95
5.20 (a) Hardness Numbers Below a Crater Produced in Nickel . . .	96
5.20 (b) Hardness Numbers Around a Crater Produced in Nickel . .	97
5.21 (a) Hardness Numbers Below a Crater Produced in Nickel . . .	98
5.21 (b) Hardness Numbers Around a Crater Produced in Nickel . .	99
5.22 (a) Hardness Numbers Below a Crater Produced in Aged Udimet 700	100
5.22 (b) Hardness Numbers Around a Crater Produced in Aged Udimet 700	101
5.23 (a) Hardness Numbers Below a Crater Produced in Solutioned Udimet 700	102
5.23 (b) Hardness Numbers Around a Crater Produced in Solutioned Udimet 700	103
5.24 (a) Hardness Numbers Below a Crater Produced in Zinc	104
5.24 (b) Hardness Numbers Around a Crater Produced in Zinc . . .	105
5.25 (a) Hardness Numbers Below a Crater Produced in Iron	106
5.25 (b) Hardness Numbers Around a Crater Produced in Iron . . .	107
5.26 (a) Hardness Numbers Below a Crater Produced in Tantalum . .	108
5.26 (b) Hardness Numbers Around a Crater Produced in Tantalum .	109
5.27 (a) Hardness Numbers Below a Crater Produced in Aluminum . .	110
5.27 (b) Hardness Numbers Around a Crater Produced in Aluminum .	111
6.1 Theoretical Curves and Experimental Data for Impacts of Steel Spheres Against 1100-0 Aluminum	128
6.2 Theoretical Curves and Experimental Data for Impacts of Steel Spheres Against Nickel 270	144
6.3 Theoretical Curves and Experimental Data for Impacts of Steel Spheres Against Electrolytic Tough Pitch Copper. . . .	149
6.4 Theoretical Curves and Experimental Data for Impacts of Steel Spheres Against Solutioned Udimet 700 Alloy.	156
6.5 Theoretical Curves and Experimental Data for Impacts of Steel Spheres Against Aged Udimet 700 Alloy.	160

List of Illustrations, Continued

Figure	Page
6.6 Theoretical Curves and Experimental Data for Impacts of Steel Spheres Against 2024-0 Aluminum Alloy.	166
6.7 Theoretical Curves and Experimental Data for Impacts of Steel Spheres Against High-Purity Zinc	172
6.8 Theoretical Curves and Experimental Data for Impacts of Steel Spheres Against Armco Iron	183
6.9 Theoretical Curves and Experimental Data for Impacts of Steel Spheres Against Tantalum	189
7.1 Views of Dents at Specified Fall Heights for the Metals Considered	194
7.2 Plot of the Energy per Unit Volume Up to the 0.2 Percent Offset Yield Strength Against the 0.2 Percent Offset Yield Strength	201
7.3 Yield Strength of Udimet 700 With Increase in Temperature. .	208
7.4 Plot of the Constant k Against the Ratio of Yield Strength to Young's Modulus	223
7.5 Plot of Function R Against the Numerical Constant k.	224

List of Tables

Table	Page
1.1 Nominal Properties of the Selected Metals	13
2.1 Values of the Factor $(z_c/z'c')^{\frac{1}{2}}$ for Three Types of Projectile	23
3.1 Measured Speed of Sound in the Metals Used for the Firings	37
3.2 Tensile Data for the Metals Used in the Firings	39
4.1 Initial Set of Cratering Data for the Four Pure Metals	46
4.2 Cratering Data for Diagnostic Firings	50
5.1 Stress-Strain Behavior of the Selected Metals	89
5.2 Values of Crater Depth and Diameter	113
5.3 Data Obtained from the Solution of Equation (5.2)	116
6.1 Cratering Data for Annealed Commercially Pure Aluminum	122
6.2 Results of Statistical Analysis of the Cratering Data Obtained for Commercially Pure Aluminum	123
6.3 Results of Second Analysis of the Cratering Data Obtained for Commercially Pure Aluminum	129
6.4 Results of Statistical Analysis of the Data Obtained for Impacts of 0.175-inch Spheres Against 1100-0 Aluminum	132
6.5 Results of Analysis of Mercury-Drop Cratering Data for 1100-0 Aluminum	134
6.6 Cratering Data for Nickel 270	136
6.7 Results of Statistical Analysis of Cratering Data for Nickel 270 Using 0.175-inch Spheres	140
6.8 Results of Statistical Analysis of Cratering Data Obtained for Nickel 270 Using 0.0938-inch Spheres	141
6.9 Results of Statistical Analysis of Steel-Sphere Cratering Data Obtained for Electrolytic Tough Pitch Copper	146
6.10 Results of Analysis of Liquid-Drop Cratering Data for Electrolytic Tough Pitch Copper	150
6.11 Cratering Data for Solutioned Udimet 700	152
6.12 Results of Statistical Analysis of Data Obtained for Steel- Sphere Impacts Against Udimet 700 Solutioned	155
6.13 Cratering Data for Aged Udimet 700	159
6.14 Results of Statistical Analysis of Data Obtained for Steel- Sphere Impacts Against Udimet 700 Aged	162
6.15 Results of Statistical Analysis of the Cratering Data Obtained for 2024-0 Aluminum Alloy	167
6.16 Cratering Data for High-Purity Zinc.	171

List of Tables, Continued

Table	Page
6.17 Results of Statistical Analysis of Cratering Data Obtained for Pure Zinc Using 0.175-inch Spheres	173
6.18 Results of Statistical Analysis of Cratering Data Obtained for Pure Zinc Using 0.0938-inch Spheres.	174
6.19 Cratering Data for Armco Iron.	178
6.20 Results of Statistical Analysis of Cratering Data for Armco Iron Using 0.175-inch Spheres.	180
6.21 Results of Statistical Analysis of Cratering Data for Armco Iron Using 0.0938-inch Spheres	181
6.22 Cratering Data for Tantalum.	186
6.23 Results of Statistical Analysis of Cratering Data for Arc Cast Tantalum Using 0.175-inch Spheres	187
6.24 Results of Analysis of Cratering Data for Arc Cast Tantalum Using 0.0938-inch Spheres.	188
7.1 Steel-Sphere Denting Velocities of the Selected Metals . . .	196
7.2 Energy Per Unit Volume to Three Points on the Stress-Strain Curves	199
7.3 Sound Speed, Density, and Acoustic Impedance of the Metals Considered	203
7.4 Calculated Values of Denting Velocity for the Selected Metals	204
7.5 Elevated-Temperature Data for Udimet 700 and Calculated Values of Elevated-Temperature Denting Velocity of This Alloy.	206
7.6 Characteristics of the Low-Velocity and High-Velocity Branches of the Crater-Depth-Versus-Velocity Plots	210
7.7 Dynamic Denting Velocity, Dynamic Energy Per Unit Volume Required for Flow, and Dynamic Yield Strength.	213
7.8 Values of the Constants k^* and k	215
7.9 Comparison of the Variation in the Constant k With Variation in the Density and Sound Speed of the Test Metal	218
7.10 Yield Strength, Poisson's Ratio, and Young's Modulus from the Measured Stress-Strain Curves and Measured Sound Speeds of the Selected Metals	220
7.11 Values of the Ratio of Yield Stress to Young's Modulus for the Selected Metals and the Ratio of These Ratios to the Same Ratio for Steel	222
7.12 Theoretical and Experimental Values of the Slope of the Crater-Depth-Versus-Velocity Plots	226

BASIC RESEARCH ON LIQUID-DROP-IMPACT EROSION

1. INTRODUCTION

The work described in this report is a continuation of studies of crater formation in metals at velocities up to about 3×10^4 cm/sec (about 1,000 ft/sec) and of the denting velocity of metals. The velocity range selected is of interest for application to many engineering problems involving drop-impact erosion. In particular, the work described is a continuation of studies that were initiated at the National Bureau of Standards [1,2,3,4,5,6,7]⁽¹⁾. The purpose of these studies was to work toward an understanding of the mechanism of drop-impact erosion on materials of different kinds, to develop criteria for evaluating the drop-impact-erosion resistance of structural materials, and to assess the properties of a drop-impact-erosion-resistant material. Some of the major results of these studies are summarized below.

1.1 Stresses Produced by Drop Impact

An impinging drop has two characteristic damage-producing attributes. These are: (a) the impact pressure that the drop exerts, and (b) the high-speed sheet jet produced by the radial flow of the liquid contents of the drop as a result of the impact pressure [1,2,3]. Drop-impact erosion is uniquely the result of stresses that develop as a consequence of these damage-producing attributes. The localized impact pressure produces radial stresses⁽²⁾ in tension and shear around the compressed area of contact between a drop and a solid plate, shear stresses through the

(1) Numbers in brackets refer to literature references at the end of this report.

(2) The tensile and compressive stresses indicated in Figure 1.1 were studied with use of a foam rubber pad, a steel-sphere indenter, and a glass-sphere indenter flattened on one side.

plate, and tensile stresses on the rear face of the plate [2,3]. See Figure 1.1. The damage that results from the presence of these stresses in brittle and ductile solids is discussed below.

1.2 Erosion Failure of Low-Strength Brittle Solids

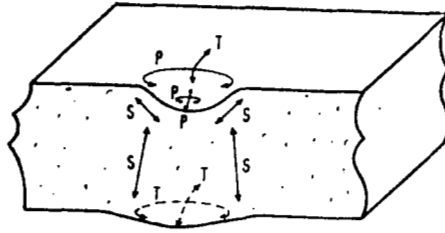
The erosion failure of low-strength brittle solids results directly from the two damage-producing attributes of an impinging drop. If the radial tensile stresses formed around the contact area as a result of the impact pressure are in excess of the tensile strength of the brittle solid, circumferential cracks will form (maximum stress theory of failure). In isotropic brittle solids, the circumferential cracks are circular; in anisotropic brittle solids, which have preferred cleavage planes, the circumferential cracks are polygonal [2,4].

Because the area of contact between the drop and the solid is subjected to pressure during the impact, the solid material on the sides of the cracks away from the center of impact is raised with respect to the solid material on the sides of the cracks that are adjacent to the center of impact. This circumstance makes the cracked surface of the brittle solid vulnerable to the outward radial flow of the drop liquid.

The outward radial flow of the drop liquid around the central point of impact exerts forces against the raised edges of the cracks (see Figure 1.2) and breaks the protruding material away [2,4]. The result of this action can be seen in Figure 1.3 which shows the surface damage mark produced by the impact of a 2-mm-diameter mercury drop against a 1/8-in.-thick plate of single crystal white sapphire at 3.58×10^4 cm/sec (1,175 ft/sec). It can be seen in Figure 1.3 that material is broken out of the white sapphire plate along the polygonal cracks and on the sides of the cracks that are away from the center of the impact. Figure 1.4 shows initial single-impact damage marks that are similar to that of Figure 1.3. The damage marks of Figure 1.4 accumulated on a specimen of poly (methyl methacrylate) during a 25-sec exposure to multiple-drop impact on a rotating arm device.

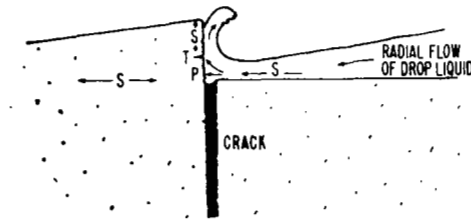
1.3 Erosion Failure of Low-Strength Ductile Solids

If the radial shear stresses that form around the contact area as a result of the impact pressure are in excess of the yield strength of



P = pressure T = tension S = shear

Figure 1.1. Stresses Produced During Impact Between a Solid Plate and a Liquid Drop or Solid Sphere.



P = pressure T = tension S = shear

Figure 1.2. Stresses Produced at a Surface Elevation Along a Crack by the Radial Flow of Liquid from an Impacted Drop.



Figure 1.3. Damage Mark on a White Sapphire Plate Produced by Impact of a 2-mm Mercury Drop at 3.58×10^4 cm/sec (1,175 ft/sec).

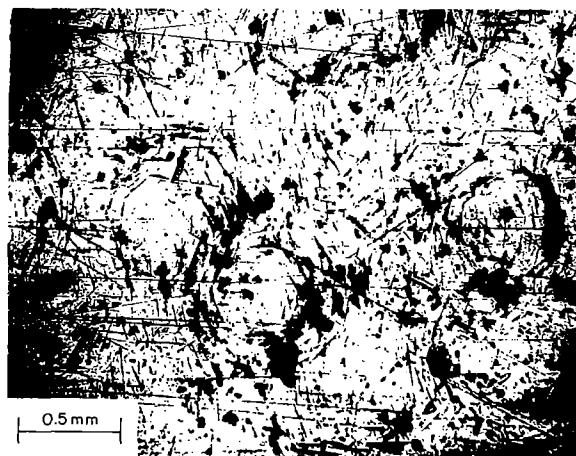


Figure 1.4. Polygons of Cracks Formed in Poly(methyl methacrylate) as a Result of Impact Against Waterdrops.

a ductile solid, plastic flow will take place and a crater will be produced in the solid [2,4]. The formation of a crater in a ductile solid does not produce erosion in itself because erosion involves a loss of mass and the formation of a crater does not necessarily involve a loss of mass. However, if drop impact is a continuing process, the surface of a solid will eventually become covered with craters and new craters will be superposed over old craters. If the solid is a metal that work-hardens, the metal will work-harden to the point of embrittlement. When this state is reached, cracks will form in the brittle metal and eventually pieces of the metal will break away between intersecting cracks [5].

1.4 Prediction of Relative Drop-Impact-Erosion Resistance

If the relative impact velocity between a liquid drop and a metal is too low to dent the metal, then the erosion-producing sequence of work-hardening, embrittlement, and eventual crack formation should not occur. On this reasoning, the minimum impact velocity that is required to dent a metal may provide a basis for evaluation of relative drop-impact-erosion resistance. This possibility makes it of interest to determine the denting velocity of metals.

When the depths of craters produced by the impact of liquid drops or of steel spheres against metal plates were plotted against the velocities at which the drops or spheres impinged, it was found that the points lie along straight lines that have intercepts on the velocity axis [6,7]. The physical interpretation of the intercept velocity has been that this is the minimum velocity required to dent the metal of which the target plate is composed. It is of interest, as far as the prediction of relative drop-impact-erosion resistance is concerned, to know what specific properties of a metal determine the slope and the velocity intercept of its straight-line crater-depth-versus-velocity plot. To obtain this knowledge, it is necessary to develop the mathematical equation of the straight-line relation between crater depth and impact velocity.

1.4.1 Moving-Plug Model of Crater Formation

When a liquid drop or steel sphere impinges against a metal target, a pressure pulse, which has an initial frontal area equal to the impact area, moves away from the area of contact into the target metal. The

target metal that is traversed by this pressure pulse has a particle velocity in the impact direction. Consequently, the target metal that is traversed by the pressure pulse moves in the impact direction with respect to the remaining metal of the target plate; it becomes a moving plug.

Taking the movement of this plug of target metal under the area of impact as a cratering model, an equation was developed for the depth, δ' , of a crater produced in a metal plate by the impact of a liquid drop [6]. This equation is

$$\delta' = 7.2 d z (V - V_i) / c (z + z') \quad (1.1)$$

where

$$z (= c\rho) \quad (1.2)$$

in acoustic impedance, c is speed of sound in infinite medium, ρ is density, d is drop diameter, V is relative impact velocity, and V_i is the intercept velocity. Primed quantities refer to the metal of the target plate and unprimed quantities refer to the liquid of the drop. The numerical coefficient was assessed with use of experimental data.

With recourse to dimensional analysis, the intercept velocity was found [6] to be given by

$$\begin{aligned} V_i &= 19 E' (z + z') / (\rho c' z'^3)^{1/2} \\ &= 19 (z c / z' c')^{1/2} \cdot E' (z + z') / z z' \end{aligned} \quad (1.3)$$

where E' is the energy per unit volume that the target metal can absorb without fracture or plastic flow. The numerical constant was obtained with recourse to plots of experimental crater depth against experimental impact velocity; the speed of sound in infinite medium was used for c' and the dynamic compressive yield strength was used for E' .

By trial, it was found that eqs (1.1) and (1.3) also apply to craters produced in metal plates by impacts of metal spheres [6,7]. For the case that the impinging metal sphere is a hardened steel sphere, the numerical coefficient in eq (1.1) was found to be 17.5 and the numerical coefficient in eq (1.3) was found to be unity.

1.4.2 Denting Velocity As a Criterion of Erosion Resistance

The form of eq (1.3) is of interest as far as predicting relative drop-impact-erosion resistance is concerned. According to Garcia, Hammitt, and Nystrom [8], there is no single material mechanical property that can be used to correlate cavitation damage even if coupling parameters are used to account for fluid property changes. They report that, in general, the best correlations include one or more energy-type mechanical properties, one or more strength-type properties, and one or more fluid-coupling parameters. Because drop-impact damage is closely related to cavitation damage, similar considerations can be expected to apply to it.

Equation (1.3) for denting velocity contains strength parameters in the ratio $(z c / z' c')^{\frac{1}{2}}$, a fluid-coupling parameter in the ratio $(z + z') / z z'$, and an energy parameter in E' . In addition, the infinite medium sound speed must be used for c and c' . Because

$$c = [Y (1 - \nu) / \rho (1 - 2\nu)(1 + \nu)]^{\frac{1}{2}} \quad (1.4)$$

it follows that

$$z c = c^2 \rho = Y (1 - \nu) / (1 + \nu)(1 - 2\nu) \quad (1.5)$$

where Y is Young's modulus of elasticity and ν is Poisson's ratio; c' is given by a similar equation. Equation (1.5) must be used for the impact of a solid sphere against a solid plate; a liquid has only one speed of sound. Use of eq (1.5) for solid-solid impacts brings Poisson's ratio for the projectile and target into play.

The above considerations add weight to the possibility that a comparison of denting velocities for a series of metals may provide insight into their relative drop-impact-erosion resistance. It is noteworthy that, although no dent is produced in a metal plate by the impact of a liquid drop or rigid sphere at a velocity lower than the denting velocity of the plate metal, microscopic subsurface damage (translational slip and twinning) may be produced in the metal. Consequently, it is possible that drop-impact erosion will be initiated in a metal plate that is subjected to multiple-drop impact over a prolonged period of time at velocities lower than the denting velocity. This, however, does not affect the usefulness of the denting velocity in assessing the relative erosion resistance of a series of metals.

1.5 Areas of Uncertainty with Regard to the Cratering Equations

Equations (1.1) and (1.3) were tested [6,7] with use of experimental crater-depth-versus-velocity plots. The experimental data collected were for: impacts of waterdrops against annealed electrolytic tough pitch copper, 2024-0 aluminum, and lead; impacts of mercury drops against plates of annealed electrolytic tough pitch copper, 2024-0 aluminum, 1100-0 aluminum, lead, and steel; impacts of hardened steel spheres against plates of annealed electrolytic tough pitch copper, 2024-0 aluminum, and 1100-0 aluminum. It is unfortunate that, with the exception of one set of data for impacts of mercury drops against steel, all of the metals for which cratering data were collected are face-centered cubics.

In general, acceptable qualitative agreement was found between the cratering equations and the experimental cratering data for the pure metals that were used as targets. In the case of steel-sphere impacts against 2024-0 aluminum, the slopes of the theoretical curves for the three sizes of steel spheres that were used were consistently steeper than those of the experimentally determined points. The lack of agreement between eq (1.1) and the experimental cratering data for 2024-0 aluminum was tentatively explained in terms of the work-hardening properties of this alloy [7]; in retrospect, it appears likely that the observed lack of agreement in the case of 2024-0 aluminum is the result of the alloying ingredients as well as of work-hardening. In the use of the moving-plug model of cratering, the effect of inhibited plastic flow is an area of uncertainty that needs further consideration.

1.5.1 Effect of Inhibited Plastic Flow

In terms of the moving-plug model of cratering, the average velocity that the moving plug acquires with respect to the remaining metal of the target plate determines the slope of the line that is given by eq (1.1). The moving plug is not a free rod; it remains attached to the remainder of the metal of the target plate. Consequently, the average velocity that the moving plug acquires must be affected by the susceptibility to plastic flow of the target metal that surrounds it.

Effect of Alloying

Foreign atoms, which may exist as individuals or as precipitated phases in various states of dispersion, interact with dislocations to

inhibit plastic flow [9]. The importance of this interaction is shown by the fact that a structural alloy in general displays a degree of susceptibility to plastic flow which is less than that of its major component in the pure state. With reference to the moving-plug model of cratering, the average velocity acquired by the plug as a result of the impact will be lower for an alloy than for a pure metal because an alloy has less susceptibility to plastic flow. The effect of this will be that the slope of the straight-line crater-depth-versus-velocity curve should be found to be lower for alloys than for pure metals.

Effect of Work-hardening

It has been pointed out [9] that a dislocation that reaches the boundary of its own grain in a polycrystal cannot continue its glide motion into another grain if the plane and direction of slip change from one grain to another. If a dislocation is stopped at a grain boundary, it obstructs the other dislocations following it in the slip plane. In work-hardened metals there is evidence which suggests that the main obstacles hindering the motion of dislocations are other dislocations moving on intersecting slip planes [9]. With reference to the moving-plug model of cratering, the average velocity acquired by the plug as a result of the impact will be reduced if work-hardening occurs in the target metal around the plug and adds a further restriction to its motion. The effect of this will be that the slope of the straight-line crater-depth-versus-velocity curve should be found to be lower after work-hardening of the target metal around the plug has occurred.

Effect of Lattice Packing Type

Lattice packing type also exerts an effect on the susceptibility of a metal to plastic flow. The number of available slip systems in the lattice packing types varies in the order: hexagonal close-packed < body-centered cubic < face-centered cubic. With reference to the moving-plug model of cratering, the average velocity acquired by the plug as a result of the impact will be lower for a body-centered-cubic metal than for a face-centered-cubic metal. The effect of this will be that the slope of the straight-line crater-depth-versus-velocity curve should be found to be lower for body-centered-cubic metals than for face-centered-cubic metals.

1.5.2 Effect of Stress-Strain Behavior

It has been pointed out [9] that in the dilatation field around a dislocation some atoms are squeezed into holes that are too small for them and some are stretched to fit large holes. The energy of the dislocation would be reduced if the sizes of the atoms coincided with the spaces available for them around the dislocation. In a solid solution containing atoms of different sizes, solute atoms migrate to dislocations; the solute atoms that are oversized, as far as the lattice spacing of the major constituent of the solid solution is concerned, collect on the expanded side of the slip plane and vice versa.

The motion of the dislocation is restricted by the presence of these foreign atoms. A large force is needed to break the bond between the dislocation and the foreign atoms that have become associated with it. After this bond is broken, the dislocation can move easily under forces that are lower than that which was required to break the bond. When many bound dislocations in a metal are supplied with a force that is sufficiently large to free them from their foreign atoms, the metal becomes softer. This is the Cottrell theory of the sharp yield point [9].

This type of stress-strain behavior will affect the applicability of the moving-plug model of cratering. When a liquid drop or steel sphere impinges against a metal target, a pressure pulse moves into the target metal. If the target metal is characterized by a stress-strain curve that rises continuously after the elastic limit has been passed, the target metal that has been traversed by the pressure pulse will move in the impact direction as a unit; it will become a moving plug. However, if the target metal that has just been traversed by the pressure pulse suddenly drops to a lower yield strength, this metal will be unable to sustain the pressure under which it exists. The result will be that the metal traversed by the pressure pulse may flow out radially instead of moving in the impact direction as a rigid body.

To the extent that metal flows out radially rather than in the single impact direction, the depth of the crater that is produced will be a function of the second rather than of the first power of the impact velocity; the crater-depth-versus-velocity plot will exhibit curvature.

For the case that the stress-strain curve rises again after a sharp yield, it can be expected that the cratering mechanism will still involve the moving-plug concept to a substantial degree. For this case, although curvature will exist, the crater-depth-versus-velocity plot will still be close to a straight line.

1.5.3 Use of Dynamic or Quasi-Static Yield Strength

Prior to publication of the papers describing the test of eqs (1.1) and (1.3), consideration was given to whether the quasi-static yield strengths or the elevated (dynamic) yield strengths of the target metals should be used for the quantity E' in eq (1.3). It was decided that, because the cratering process occurs with extreme rapidity, elevated yield strengths should be used; the elevated yield strengths that were used in calculating the theoretical curves were dynamic compressive yield strengths determined by Whiffin [10]. However, Bell [11] has found that thoroughly annealed pure metals are strain rate independent at a substantial distance from the end of a rod that is struck by another rod. On the basis of the results obtained by Bell, the question as to whether quasi-static or elevated (dynamic) strengths should be used for the quantity E' must be re-opened. In the case of crater formation to depths that are less than one sphere diameter below the surface of the target plate, it is still possible that some elevation of the quasi-static yield strength may occur [12]. If it proves to be true that the denting velocity can be used to rate metals for relative drop-impact-erosion resistance, it will be important to clarify this area of uncertainty.

1.5.4 Effect of Plate Thickness

Another area of uncertainty with regard to eqs (1.1) and (1.3) is the permissible thickness of the target plate. At the time these equations were first published [6], it was suggested that plates thinner than 1.5 to 2.0 drop (or sphere) diameters or thicker than 4 to 5 drop (or sphere) diameters should not be used. Since that time, further consideration has suggested that although the limit on plate thinness is critical, there may be no limit on plate thickness. If it is found that the denting velocity can serve as a practical criterion of drop-impact-erosion resistance, this is an area of uncertainty that should be explored further.

1.6 Program of Further Work on the Cratering Equations

Equation (1.1) was derived on the basis of a simple model (moving-plug concept) but eq (1.3) evolved from dimensional analysis. As part of a program of further work on these equations, it was considered advisable to re-examine the derivation of eq (1.1), to attempt to derive eq (1.3) from theoretical considerations, to consider the effect of a change in temperature of the target metal, and to explore as far as possible all areas of uncertainty.

It was proposed to make steel-sphere firings against target plates of iron, tantalum, nickel, zinc, and Udimet 700 alloy. The metals selected for use as target plates in the new firings impose a more stringent test on the equations than the metals used earlier [6,7]. When considered two at a time they either have similar sound speeds and different densities or similar densities and different sound speeds. See Table 1.1. With the sound speed essentially constant for the pairs tantalum-zinc, iron-nickel, and Udimet 700-aluminum, the effect of a change in density can be checked; with density essentially constant in the pairs zinc-iron, nickel-copper, and Udimet 700-iron, the effect of a change in sound speed can be checked.

Of the metals selected for use as target plates in the new firings, iron and tantalum have body-centered-cubic packing, zinc is hexagonal close-packed, and nickel (both in the pure state and in the nickel-based alloy Udimet 700) has a face-centered-cubic packing. The inclusion of metals of each of the three lattice packing types should be informative with regard to the area of uncertainty regarding the degree of susceptibility to plastic flow. Further information on this point should result from a comparison of the cratering behavior of pure aluminum with that of the aluminum-based alloy 2024-0 and of the cratering behavior of pure nickel with that of the nickel-based alloy Udimet 700. Udimet 700 in the aged condition is more resistant to plastic flow than in the solutioned condition (see Table 3.2). Comparison of the cratering behavior of pure nickel with that of Udimet 700 in each of these heat-treatment states should provide further information.

Table 1.1

Nominal Properties of the Selected Metals

<u>Metal</u>	<u>Melting Point, °C</u>	<u>Density, g/cm³</u>	<u>Sound Speed, cm/sec</u>
Tantalum	2996 ^(a)	16.6 ^(a)	4.235 x 10 ⁵ (b)
Zinc	420 ^(a)	7.133 ^(a)	4.170 x 10 ⁵ (c)
Iron	1536.5 ^(a)	7.874 ^(a)	5.850 x 10 ⁵ (c)
Nickel	1453 ^(a)	8.902 ^(a)	5.806 x 10 ⁵ (b)
Udimet 700	approx. 2400-2650	7.92 ^(d)	6.4 x 10 ⁵ (e)
Copper	1083 ^(a)	8.96 ^(a)	4.691 x 10 ⁵ (f)
Aluminum	657 ^(a)	2.71 ^(a)	6.318 x 10 ⁵ (f)

(a) Metals Handbook, American Society for Metals, Vol. I, 1961.

(b) Karl H. Schramm, Daten zur Schallgeschwindigkeit in reinen Metallen, Z. Metallk. 53, 729 (1962).

(c) L. Bergmann, Der Ultraschall, S. Hirzel, Stuttgart (1954).

(d) General Electric Flight Propulsion Division Material Properties Handbook, Vol. II.

(e) Calculated value.

(f) Measured by Carroll Tschiegg at the National Bureau of Standards [7].

2. DERIVATION OF THE CRATERING EQUATIONS

Equation (1.1) was derived with the use of elastic plane-wave theory. For background purposes, the derivation of elastic plane-wave particle velocities and stresses due to Saint-Venant [13] is reviewed.

2.1 Elastic Wave Theory Applied to the Impact of Rods

The elastic waves that travel through rods are plane waves. A fairly general case of the impact of rods is that two rods of different materials, each having a velocity of its own, approach and collide. A discussion of the effects of such a collision follows.

Interface Boundary Conditions

Let rods R and R', composed of materials M and M' and moving at velocities V and V' , respectively, where $V - V' > 0$, approach and collide. As soon as collision occurs, waves of compression, which originate at the impact interface, begin to move through each of the rods [13]. If a very short time interval, Δt , associated with the instant of impact is considered, the amounts of material of each rod that are traversed by the respective compressional waves are extremely small and it can be assumed that in this short time interval there is no gain or loss of momentum.

The distances that the compressional waves, which originate at the impact interface, move into the rods in the short time Δt are $c \Delta t$ and $c' \Delta t$, respectively. The situation is shown diagrammatically in Figure 2.1 for the case that $c > c'$, $V > V'$, and rods R and R' are moving along the x-axis.

Two boundary conditions must be met at the impact interface. First, in order that the bars simply remain in contact without one bar penetrating the other or one bar receding from the other, the material traversed by the compressional waves initiated in each rod must have the same

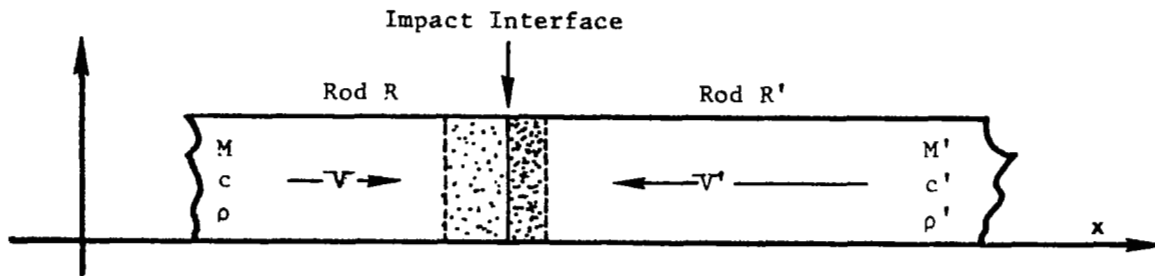


Figure 2.1. Schematic Representation of the Impact of Two Rods.

velocity (a common velocity). Secondly, the compressive force in the material of each rod traversed by the respective compressional waves must be equal because the equation for one-dimensional longitudinal elastic-wave motion is based on a balance of force across an element of a rod. The result of the second boundary condition is that there is no pressure difference across the impact interface.

Velocities

Let the common velocity, required by the first boundary condition, be v^* . To simplify the mathematical equations, let the rods each be cylindrical and of unit cross-sectional area. Conservation of momentum during the short time, Δt , requires that

$$c \Delta t \rho V + c' \Delta t \rho' V' = c \Delta t \rho v^* + c' \Delta t \rho' v^* \quad (2.1)$$

Dividing eq (2.1) by Δt and solving for the common velocity v^* produces

$$\begin{aligned} v^* &= (c \rho V + c' \rho' V') / (c \rho + c' \rho') \\ &= (z V + z' V') / (z + z') \end{aligned} \quad (2.2)$$

The common velocity given by eq (2.2) is equivalent to that found by Saint-Venant [13] who increased the generality of the case by considering rods with different cross-sectional areas.

The case in which one of the rods is at rest at the time that impact occurs is less general. If rod R' is chosen to be the rod at rest, then from conservation of momentum,

$$c \Delta t \rho V = c \Delta t \rho v^* + c' \Delta t \rho' v^*$$

and

$$v^* = c \rho V / (c \rho + c' \rho') = z V / (z + z') \quad (2.3)$$

Knowing the common velocity, v^* , the particle velocities in the compressed zones, v and v' , which are lost by rod R and gained by rod R', respectively, as a result of the impact, can be determined.

$$\begin{aligned} V - v &= v^* = (z V + z' V') / (z + z') \\ v &= z' (V - V') / (z + z') \end{aligned} \quad (2.4)$$

Similarly,

$$\begin{aligned} V' + v' &= v^* = (z V + z' V') / (z + z') \\ v' &= z (V - V') / (z + z') \end{aligned} \quad (2.5)$$

For the less general case, in which rod R' is at rest when the impact occurs,

$$v' = v^* = z V / (z + z') \quad (2.6)$$

and

$$\begin{aligned} V - v &= v^* = z V / (z + z') \\ v &= z' V / (z + z') \end{aligned} \quad (2.7)$$

Stresses

With the rods aligned along the x-axis as in Figure 2.1, unit shortenings $\partial u / \partial x$ and $\partial u' / \partial x$ are associated with the total shortenings, u and u' , due to compression in the two rods, respectively. According to the second boundary condition imposed, the compressive force in the compressed section of rod R is equal to the compressive force in the compressed section of rod R'. Because the compressive force is given by the product of the cross-sectional area, A , Young's modulus, Y , and the unit elongation [14], it follows that

$$A Y (\partial u / \partial x) = A' Y' (\partial u' / \partial x). \quad (2.8)$$

Because the unit shortening, $\partial u / \partial x$, is given [15] by

$$\partial u / \partial x = v / c, \quad (2.9)$$

and because for a rod,

$$Y = c^2 \rho = c z \quad (2.10)$$

the compressive force per unit area, or compressive pressure, σ , in the compressed zone of rod R is $(c^2 \rho/c) [z' (V - V') / (z + z')]$, and, with use of eq (2.6),

$$\sigma = z z' (V - V') / (z + z') = z' z (V - V') / (z + z') = \sigma' \quad (2.11)$$

For the less general case, in which rod R' is at rest when the impact occurs,

$$\sigma = z z' V / (z + z') = z' z V / (z + z') = \sigma' \quad (2.12)$$

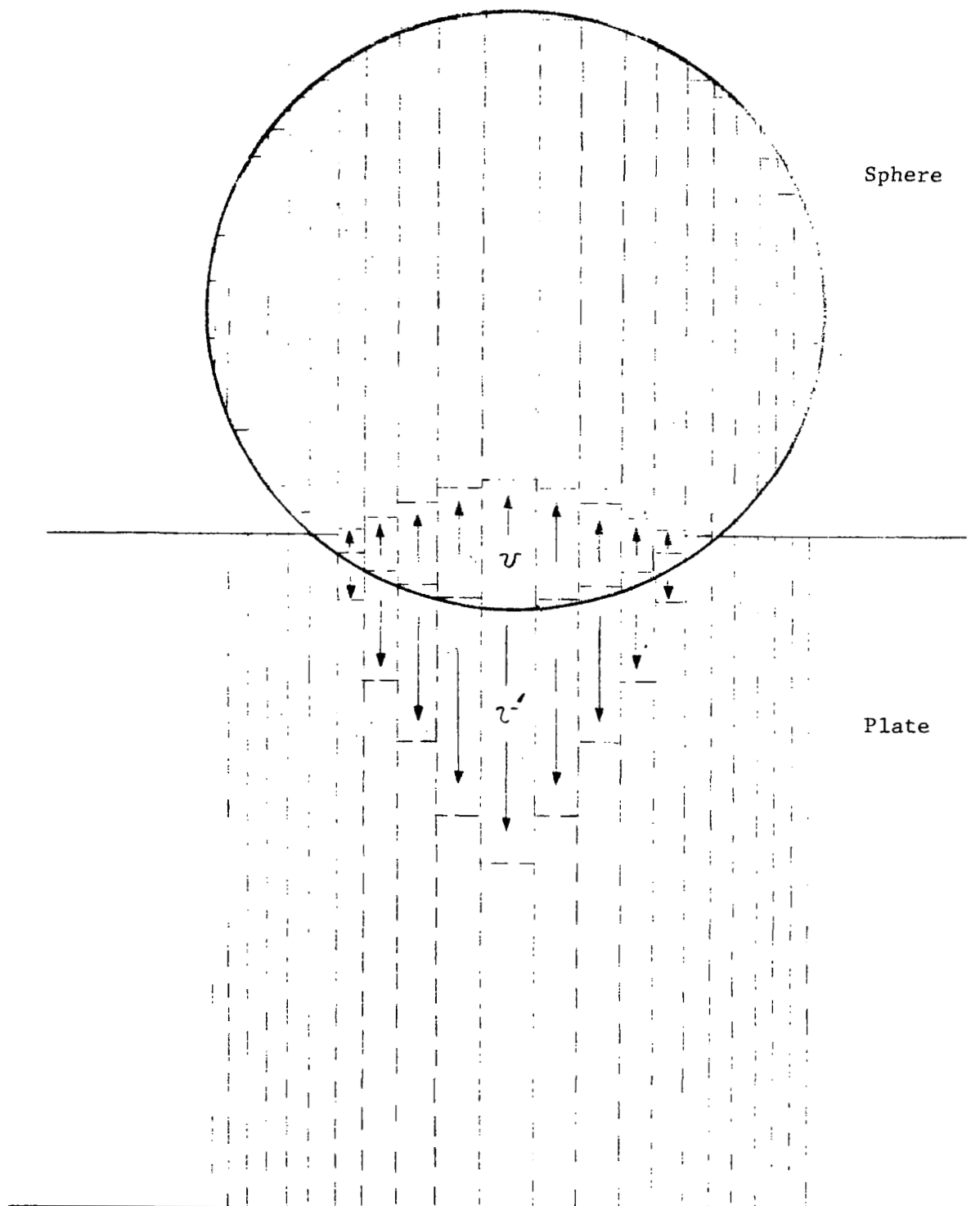
2.2 Derivation of Equation (1.1)

As noted above, the cratering equations are the same for impacts of liquid drops and impacts of steel spheres with the exception that the numerical coefficients, which were assessed from experimental data, are different. The original derivation of eq (1.1) was for the impact of a moving metal plate against a stationary liquid drop [6]. The derivation that follows is couched in terms of the impact of a moving steel sphere against a stationary metal plate.

At the instant that impact occurs between a moving steel sphere and a stationary metal plate, a pressure wave having a characteristic particle velocity, v , is developed in a core of metal through the projectile sphere and a pressure wave having a characteristic particle velocity, v' , is developed in a core of metal that extends through the target plate under the contact area between the sphere and the plate. The compressional wave spreads slightly as it moves through the thickness of the target plate; consequently, the core of metal under the contact area between the sphere and the plate has the shape of a frustrum of a cone.

For simplicity, the true situation is idealized in the following ways:

- (a) The curved surface of the sphere is regarded as the limit of fineness of the serrated surface of a stack of concentric cylinders (see Figure 2.2) and the compressional waves produced both in the sphere and in the target plate are regarded as plane waves in these cylinders.
- (b) The core of metal that extends through the thickness of the target plate under the contact area between the sphere and



R1354-1.1

Figure 2.2. Plane-Wave Idealization of the Impact Between a Steel Sphere and a Plate. (Cross-Sectional View)

the plate is regarded as a true cylinder (consisting of concentric cylinders) that is free to move in the impact direction but that is restrained laterally. A similar cylinder is assumed to exist through the diameter of the steel sphere.

The condition of restraint (the metal in the cylinders extending through both plate and sphere does not move laterally) has the consequence that the sound speeds that must be used for the steel of the sphere and for the metal of the target plate is the speed of sound in infinite medium given by eq (1.4). That this is the consequence of the condition of lateral restraint [6] is reviewed below⁽³⁾.

The condition of restraint is that there is no lateral motion. According to Hooke's law,

$$Y \epsilon_1 = \sigma_1 - \nu (2 \sigma_r) = \sigma_1 - 2\nu \sigma_r \quad (2.13)$$

where Y is Young's modulus of elasticity, ϵ_1 is the longitudinal strain, σ_1 is the longitudinal stress, ν is Poisson's ratio, and σ_r is the radial stress. Also,

$$Y \epsilon_r = \sigma_r - \nu (\sigma_1 + \sigma_r) = 0 \quad (2.14)$$

where ϵ_r is the radial strain. From eq (2.14),

$$\sigma_r = \nu \sigma_1 / (1 - \nu). \quad (2.15)$$

By substituting the expression for σ_r given by eq (2.15) into eq (2.13), it is found that

$$\sigma_1 = (1 - \nu) Y \epsilon_1 / (1 - 2\nu) (1 + \nu) \quad (2.16)$$

and, because for plane waves $c = (\sigma_1 / \rho \epsilon_1)^{1/2}$,

$$c = [Y (1 - \nu) / \rho (1 - 2\nu) (1 + \nu)]^{1/2} \quad (2.17)$$

This is the speed of sound in an infinite medium and, therefore, it is

⁽³⁾The proof that follows is due to Dr. John M. Frankland, former consultant for the Mechanics Section of the National Bureau of Standards.

demonstrated that the consequence of the condition of restraint is that the speed of sound in an infinite medium must be used for c and for c' in place of the speed of sound in a rod.

The physical model of cratering used in deriving eq (1.1) is that permanent movement occurs between the core of metal through the target plate under the contact area and the remainder of the metal of the target plate. The core of target metal moves in the impact direction. In the case of thin plates, the movement of this core of metal forms a bulge on the reverse face of the target plate. In the case of thick plates, the movement of the core of metal is absorbed by the metal through the thickness of the plate.

At very low velocities cratering does not occur because the shear strength of the target metal prevents permanent displacement between the core of metal under the impact area and the remainder of the metal of the target plate. To take account of this behavior, it is conceived that there is a threshold impact velocity, V_i , below which cratering does not occur. From eq (2.6), the plane-wave particle velocity in the target plate is $z V / (z + z')$ where z is acoustic impedance given by eq (1.2) and V is the relative impact velocity. Under the condition that the target plate is stationary, V is the velocity of the moving sphere that impinges against it. Primed quantities refer to the metal of the target plate; unprimed quantities refer to the steel of which the steel sphere is composed. The particle velocity that is effective in producing a crater in the target plate is expressed in terms of the velocity difference $V - V_i$ and is given by

$$v'_{\text{eff}} = z (V - V_i) / (z + z') \quad (2.18)$$

If the particles of solid in the core of target metal under the contact area move in the impact direction for a time t , the depth δ' of the crater produced in the metal plate will be given by

$$\delta' = v'_{\text{eff}} t \quad (2.19)$$

The impact cut-off time, t , is taken to be proportional to the time required for the pressure pulse developed in the steel sphere to move through the sphere, reflect as a tension wave from the trailing surface

of the sphere, and return to the impact surface. The impact cut-off time is then given by

$$t = k d / c \quad (2.20)$$

where k is a numerical proportionality constant, d is the diameter of the steel sphere, and c is the speed of sound in infinite medium for the steel of which the steel sphere is composed.

Substituting eqs (2.18) and (2.20) into eq (2.19), one finds that

$$\delta' = (k d / c) [z / (z + z')] \cdot [V - V_i] \quad (2.21)$$

Recourse to experimental crater-depth-versus-velocity plots for impacts of steel spheres against face-centered-cubic pure metals has indicated [7] that the numerical constant, k , is 17.5. Equation (2.21) is identical with eq (1.1) for the impact of liquid drops against metal plates except for the numerical constant.

Because z , z' , and c are constant properties of the steel of the sphere and of the metal of the target plate, crater depth for impacts of steel spheres against targets of a specific metal is given by

$$\delta' = k^* d [V - V_i] \quad (2.22)$$

where

$$k^* = k z / c (z + z') \quad (2.23)$$

Remembering that k is a numerical constant, the dimensions of the constant k^* are sec/cm. For firings with steel spheres of the same size,

$$\delta' = K [V - V_i] \quad (2.24)$$

where

$$K = k^* d \quad (2.25)$$

2.3 Derivation of Equation (1.3)

It remains to derive the expression for the intercept velocity, V_i , which, in the original treatment [6], was obtained through recourse to dimensional analysis. As noted above, the intercept velocity, V_i , expresses the boundary condition that there is a velocity below which

relative movement will not occur between the core of target metal and the remaining metal of the target plate. Within the metal, the boundary condition that governs whether or not this movement will occur is the criterion for initiation of plastic flow.

Let it be assumed that slip between the core of metal under the impact area and the remaining metal of the plate will occur when the strain energy per unit volume in the core of metal, which has been traversed by the elastic wave, becomes equal to the strain energy per unit volume that the target metal can accept without plastic flow.

The strain energy of deformation per unit volume in the elastic wave is given by [14] the quotient $\sigma'^2 / 2 Y'$. The strain energy per unit volume in the solid at the yield stress is given by $\sigma'_y \epsilon'_y / 2$, where sub-y refers to the yield point. Using eq (2.12) for the elastic-wave stress, σ' , and the assumption regarding the threshold velocity given above,

$$\left[z z' V_i / (z + z') \right]^2 (1 / 2 Y') = \sigma'_y \epsilon'_y / 2. \quad (2.26)$$

Multiplying eq (2.26) by 2 and substituting eq (2.9) for the unit shortening, ϵ'_y , produces the expression

$$\left[z z' V_i / (z + z') \right]^2 (1/Y') = \sigma'_y (v' / c'). \quad (2.27)$$

For the threshold condition, the particle velocity, v' , is given by eq (2.6) with $V = V_i$. Dividing both sides of eq (2.27) by this particle velocity, and multiplying both sides by c' , produces the equality

$$\left[z z' V_i / (z + z') \right] (z'c' / Y') = \sigma'_y. \quad (2.28)$$

If the explicit expression for Y' , given by eq (2.10), is substituted into eq (2.28), this equation reduces to

$$z z' V_i / (z + z') = \sigma'_y \quad (2.29)$$

from which

$$V_i = \sigma'_y (z + z') / z z'. \quad (2.30)$$

Table 2.1

Values of the Factor $(z_c / z'c')^{1/2}$ for Three Types of Projectile

Factor Target Metal	$(z_c / z'c')^{1/2}$ for waterdrops	$(z_c / z'c')^{1/2}$ for mercury drops	$(z_c / z'c')^{1/2}$ for steel spheres
Armco Iron	0.091	0.324	1.00
Pure Zinc	0.129	0.461	1.43
Nickel 270	0.089	0.317	0.98
Arc Cast Tantalum	0.090	0.321	0.99
Udimet 700, Aged	0.087	0.311	0.96
Udimet 700, Solutioned	0.087	0.311	0.96
1100-0 Aluminum	0.144	0.513	1.59
Electrolytic Tough Fitch Copper	0.106	0.380	1.18

With σ'_y set equal to E' , which was taken to be the dynamic compressive yield strength, eq (2.30) is identical with eq (1.3) except that the factor $(z_c/z'c')^{1/2}$ is missing. The physical significance of the factor $(z_c/z'c')^{1/2}$, which is required by the empirical equation for denting velocity, is not understood. Values of this factor for impacts of waterdrops, mercury drops, and steel spheres against eight metals are listed in Table 2.1. From the tabulation it can be seen that for steel-sphere impacts the value of this factor is essentially unity but for mercury-drop impacts it is about 0.3 and for waterdrop impacts it is about 0.1.

The values of the factor $(z_c / z'c')^{1/2}$ given in Table 2.1 indicate that this factor is essential when the modulus of elasticity of the striking ball is different from the modulus of elasticity of the metal of the target plate. This suggests that a coupling factor between the material of the striking ball and the metal of the target plate in addition to the presence of both z and z' in the elastic-wave stress σ' given by eq (2.12) may be needed.

In this connection it is noteworthy that if the condition is imposed that the strain energy of deformation per unit volume in the core of target metal being traversed by the elastic wave in the target plate is equal to the strain energy of deformation per unit volume in the core of material being traversed by the elastic wave in the striking sphere or drop, then

$$\sigma' = (Y'/Y)^{\frac{1}{2}} \sigma = (z'c'/zc)^{\frac{1}{2}} z z' V / (z + z') \quad (2.31)$$

Furthermore, if the condition for slip between the core of target metal and the remaining metal of the plate is taken to be that the stress difference between the metal core and the remaining metal of the plate becomes equal to the yield strength of the plate metal, then

$$(z'c'/zc)^{\frac{1}{2}} z z' V_i / (z + z') = \sigma'_y \quad (2.32)$$

and

$$V_i = [\sigma'_y (z + z') / z z'] (zc/z'c')^{\frac{1}{2}} \quad (2.33)$$

Equation (2.33) is identical with eq (1.3). However, there appears to be no theoretical justification for imposing the condition of equal strain energy of deformation per unit volume in the material both of the target and of the ball that is being traversed by elastic waves.

The theoretical reason for the need of the factor $(zc/z'c')^{\frac{1}{2}}$ remains to be found.

3. PREPARATION OF TEST SPECIMENS AND MEASUREMENT OF REQUIRED PROPERTIES

To obtain experimental cratering data to test further the equations that have been developed, additional steel-sphere firings were made against target plates of iron, tantalum, nickel, zinc, and Udimet 700 alloy. The preparation of test specimens and the measurement of required properties of the metals that were obtained for the study are described in this section.

3.1 Source and Chemical Composition Data for the Selected Metals

Iron

A single length of cold drawn, nominal 1-inch-diameter, round rod of Armco magnetic ingot iron (heat No. 66080) was purchased from the Lapham Hickey Steel Company at Chicago, Ill.

The certified test report submitted by the vendor indicates that the following elements could be present in the specified percentages: carbon, 0.025; manganese, 0.054; phosphorus, 0.006; sulfur, 0.011; silicon, trace; and copper, 0.062. Presuming that the balance is iron, the iron content is 99.842 percent.

For a further check on the purity of this metal, it was subjected to N.S.L. spectroscopic survey. The major impurities in percent were found to be: copper, 0.049; manganese, 0.003; cobalt, less than 0.005. The following elements were found in less than 0.001 percent: silver, aluminum, magnesium, nickel, chromium, vanadium, silicon, zirconium, sodium, tin, potassium, lithium, and molybdenum. The following elements were looked for and not detected: arsenic, boron, bismuth, calcium, columbium, cadmium, lead, antimony, strontium, barium, titanium, tungsten, and zinc. Carbon was determined separately using high-temperature combustion followed by conductimetric determination of

carbon dioxide⁽⁴⁾. Results obtained for two specimens of the metal were 30 and 85 ppm, respectively.

On the basis of the separate determination of carbon and of the spectroscopic results for manganese, cobalt, and copper in conjunction with the certified test results for phosphorus and sulfur, the iron content is 99.918 percent presuming that the balance is iron.

The reported processing history is that the 1-inch-diameter rod received was cold drawn from 1.0625-inch-diameter hot-rolled magnetic ingot iron bar. There was no process anneal on the hot-rolled metal or after cold drawing. Data on the as-received condition of the metal are as follows: structure, cold worked; grain size, approximately A.S.T.M. No. 5 to No. 6.

Tantalum

A single length of nominal 1-inch-diameter round rod of Haynes tantalum, A.S.T.M. Specification B-365-62T, was purchased from the Union Carbide Corporation at Kokomo, Ind. The heat was No. 81444.

The certified report of chemical analysis supplied by the vendor lists the following elements in the percentages specified: tungsten, less than 0.01; iron, less than 0.01; carbon, 0.001; silicon, less than 0.01; nickel, less than 0.005; columbium, 0.10; titanium, less than 0.01; oxygen, 0.0077; hydrogen, 0.0003; nitrogen, 0.0012; balance tantalum. On the basis of this analysis, the metal supplied is at least 99.845 percent tantalum.

The reported processing history of this tantalum metal is a 96 percent reduction in area. The as-received condition of the metal was

⁽⁴⁾ Determination of carbon was carried out by Mr. Harold Bradley of S.P.P.S. Chemistry and Physics Unit, General Electric Company, Evendale, Ohio.

as follows: structure, cold worked; hardness, 135 DPH (Brinell 118 equivalent).

Nickel

A single length of nominal 1-inch-diameter round rod of Nickel 270 (heat No. NP04A9H) was purchased from the Huntington Alloy Products Division of the International Nickel Company, Inc., at Huntington, W. Va.

The certified report of chemical analysis of the heat, which was supplied by the vendor, lists the following elements present in the specified percentages: carbon, 0.01; silicon, less than 0.001, manganese, less than 0.001; iron, less than 0.001; sulfur, less than 0.001; copper, less than 0.001; chromium, less than 0.001; titanium, less than 0.001; magnesium, less than 0.001; and cobalt, less than 0.001. Assuming that the balance is nickel, the metal is 99.981 percent nickel.

The basic processing history of the metal as supplied by the vendor is as follows. High purity nickel powder is compacted into a billet by isostatic pressing. The billet is sintered at 2000°F in hydrogen and the sintered billet is hot-rolled to 1.125-inch-diameter rod. This rod is centerless ground to uniform diameter and cold-drawn to a 1-inch diameter with approximately 16 percent reduction in area.

The metal received was in the cold-drawn condition. Mechanical properties supplied by the vendor are: tensile strength, 77,000 psi; 0.2 percent offset yield strength, 75,500 psi; elongation, 22 percent; reduction in area, 87 percent; hardness, 81 Rockwell B.

Zinc

The zinc metal, which was purchased from the Calnex Corporation at Campbell, O., consisted of 1.25-inch-diameter round rod. The metal

supplied was from one heat. The purity of the metal, as reported by Mr. John Stavich, is 99.997 percent zinc. The major impurities are: lead, 0.001 percent; cadmium, 0.0005 percent; and iron, 0.0015 percent.

The metal was cast into a billet and then extruded as 1.25-inch-diameter rod.

Udimet 700 Alloy

Udimet 700 alloy round rod, 1.125 inch in diameter and ordered to meet S.P.P.S. Specification 01-0065-00-A, was purchased from Allvac Metals Company at Monroe, N.C. The metal was supplied from one heat (heat No. 3812).

The certified percentage chemical composition of the alloy, which was supplied by the vendor, is as follows: carbon, 0.104; sulfur, 0.002; manganese, less than 0.02; silicon, 0.04; chromium, 14.47; molybdenum, 4.32; cobalt, 15.55; titanium, 3.18; aluminum, 4.28; boron, 0.012; zirconium, less than 0.02; iron, 0.31; copper, less than 0.02; phosphorus, 0.004; balance, nickel. On the basis of this report, the nickel content is about 42.33 percent.

The basic processing history of the wrought alloy is as follows. The constituent elements were melted in vacuum in an induction heated furnace. The resulting ingot was shaped into a cylindrical electrode and consumable-electrode vacuum-arc melted into a 12-inch-diameter ingot. This ingot was heated for 10 to 15 hours at 2025°F prior to rolling. It was hot-rolled to a 1.125-inch-diameter rod over the temperature range 1900-2025°F with numerous reheats to 2025°F. Finally, it was annealed for four hours at 1975°F and air cooled. The 2135°F solution anneal was omitted because a small grain size is needed in forging tie bolts and part of the Udimet 700 alloy was obtained for this purpose.

3.2 Preparation of Specimens

3.2.1 Machining

Twenty impact specimens to be used as targets for the steel-sphere firings, two tensile specimens for the determination of quasi-static yield strength, and one sound speed specimen were machined from each of the metals. In addition, one sound speed specimen was machined from a piece of the 52100 steel of which the steel spheres were fabricated.

Impact Specimens

The target plates are right circular cylinders having a diameter of 1.000 ± 0.016 inch and a length of 0.500 ± 0.016 inch. The impact face is flat to 0.001 inch total indicator reading. The impact face was given a 15-microinch finish at the time the target plates were machined; all other surfaces were finished to 125 microinch or better. The impact face was later polished as described below.

Tensile Test Specimens

Specimens for quasi-static tensile tests were machined to meet S.P.P.S. Drawing SK56162-862. These specimens are of small size. They have a 1-inch gauge length and a 0.160-inch gauge diameter.

Sound Speed Specimens

The sound speed specimens are right circular cylinders. The smallest of these specimens are one inch in size. The flat ends were given a surface finish of 32 rms or better. After finishing, the ends were flat to within 0.001 inch total indicator reading and perpendicular to the axis to within 0.001 inch. The corner radii did not exceed 0.080 inch.

3.2.2 Heat Treatment

It was necessary to make a decision as to what state the metals should be in for use as target plates in the firings. The criterion

adopted for annealing conditions to be used for the metals was a compromise between two requirements⁽⁵⁾. These requirements were that the maximum amount of cold work should be removed from the metals and that the grain size should be maintained as small as possible.

The first requirement is dictated by the need to test the metal in its most characteristic strength state. This requirement can be fulfilled satisfactorily by recrystallization alone. Most of the work in a metal is removed by recrystallization; after recrystallization is complete, there is essentially only an increase in grain size.

The second requirement is dictated by the fact that, if the grain size is large in comparison with the size of the impinging spheres, scatter may be introduced into the crater-depth data. Scatter is to be expected if the grain size is large in comparison with the sphere size because target areas covered by some impacts may lie wholly within single grains whereas those covered by other impacts may extend across one or more grain boundaries.

Because grain growth begins as soon as recrystallization is complete, the desired annealing conditions are those that will produce maximum recrystallization with minimum grain growth. Preliminary studies were carried out to determine the optimum processing conditions for the specimens of each of the metals to be used in the firings. The heat treatments that were selected on the basis of these studies are described below.

(5) The criterion selected was adopted at the suggestion of Dr. J.W. Semmel, Jr., Manager of S.P.P.S. Materials and Processes Unit, and of Dr. Cecil G. Dunn of the General Electric Research Laboratory, Schenectady, N.Y.

Iron

Recrystallization to a fine-grained structure was obtained when a specimen of the metal was heated for three hours at 1750°F, which is above the alpha-to-gamma transformation temperature⁽⁶⁾. All of the iron specimens (impact specimens, tensile test specimens, and sound speed specimen) were then heated in a Brew-type laboratory furnace at 1750°F in a vacuum of 6×10^{-6} mm mercury for three hours and furnace cooled. The grain size of the heat treated specimens, as determined by micro-examination at 100 X, was a uniform A.S.T.M. No. 4 to No. 5. The hardness of the heat treated specimens was found to be Rockwell F 75.4 (Brinell 70, equivalent) which is lower than the handbook value for fully annealed ingot iron.

Tantalum

Recrystallization was found to be not quite complete after a 1-hour heat treatment at a temperature of 2200°F; it was complete after heat treatment at 2300°F for the same length of time⁽⁶⁾. Uniform grain size was not achieved. All of the tantalum specimens (impact specimens, tensile test specimens, and sound speed specimen) were heat treated at 2350°F for one hour at a pressure less than 5×10^{-5} mm mercury. The grain size obtained was A.S.T.M. No. 1 with some grains as large as A.S.T.M. No. 0. The average of three Tukon microhardness measurements using a 100-g load was 94 DPH (Brinell < 89, estimated equivalent).

Nickel

It was found that heat treatment⁽⁷⁾ at 900°F for one hour produced a completely recrystallized structure with A.S.T.M. No. 6 grain size

(6) Mr. W.F. Zimmerman, Manager of S.P.P.S. Material Applications, and Mr. D.S. Engleby were in charge of the heat treatment process.

(7) Mr. L.B. Engel of S.P.P.S. Physical Metallurgy Unit took charge of the heat treatment of the nickel and Udimet 700 specimens. He also made a detailed study of the state of the metal in the zinc specimens using X-ray techniques.

and 62 Rockwell F hardness (Brinell 151, equivalent). Because of the difficulty that is encountered in controlling the Brew-type vacuum furnace at this low temperature, all of the nickel specimens (impact specimens, tensile test specimens, and sound speed specimen) were heat treated in air for one hour at 900°F in a Lindberg Hevi-Duty furnace. They were removed from the furnace and air cooled. The oxide layer was removed in the polishing operation.

Zinc

Metallographic examination⁽⁷⁾ of the surface layer of the metal revealed equiaxed grains of a size roughly equivalent to A.S.T.M. No. 6. The equiaxed character of the grains suggested that the metal in the surface layer had recrystallized as a result of heating during the surface grinding operation after the specimens were machined. After a 0.003-inch layer of the surface metal had been removed, metallographic examination revealed equiaxed grains of a size roughly equivalent to A.S.T.M. No. 2. The equiaxed character of these grains, in conjunction with their large size, suggested that this metal had annealed at a temperature in excess of its recrystallization temperature at the time that the zinc rod was extruded.

For an impact study it is important that the target metal be uniform from the surface inward. In order that the zinc metal be homogeneous from the surface inward, the small grained surface layer was removed from all of the zinc specimens (impact specimens, tensile test specimens, and sound speed specimen). This was accomplished with use of a combination of metallographic grinding and electropolishing.

Udimet 700 Alloy

It was specified that the Udimet 700 metal in the solutioned condition should have the smallest possible grain size in conjunction with

a uniform distribution of fine particles of γ' phase. By trial⁽⁷⁾ it was found that this condition is sufficiently realized in the standard heat treatment of Udimet 700. On the basis of this conclusion, enough of the Udimet 700 rod stock to make the required number of impact specimens, tensile test specimens, and sound speed specimen was solutioned at 2135^oF for four hours in a Lindberg Hevi-Duty furnace and air cooled⁽⁷⁾. The hardness of this metal was found to be Rockwell A 69 (Brinell 342, equivalent).

For fabrication of aged Udimet 700 specimens, a sufficient quantity of the Udimet 700 rod stock was given the usual preliminary partial heat treatment: heat at 2135^oF for four hours and air cool; heat at 1975^oF for four hours and air cool; heat at 1550^oF for 12 hours and air cool⁽⁸⁾. After the specimens (impact specimens, tensile test specimens, and sound speed specimen) were machined from this metal, they were given the following final heat treatment: heat at 1550^oF for 12 hours and air cool; heat at 1400^oF for 16 hours and air cool. The final heat treatment of the machined specimens was carried out at the General Electric Company, Evendale, O., with use of the Lindberg Hevi-Duty furnace⁽⁷⁾. The hardness of the aged Udimet 700 was found to be Rockwell A 68.3 (Brinell 332 equivalent).

3.2.3 Polishing

The impact face of the target specimens of each metal (except zinc) was polished⁽⁹⁾. The polishing procedure was carried out on a Struers mover and variable-speed wheel using a 500-g load at

(8) The preliminary heat treatment of large pieces of the metal was carried out at Honeycomb Products, Inc., Indianapolis, Ind.

(9) The polishing processes were carried out by Mr. H.J. Bauer of S.P.P.S. Metallography Unit.

100 rpm. The steps in polishing each metal are given below. The specimens were ultrasonically cleaned between each polishing step.

Iron

The iron impact specimens were received with a machine-ground surface so that metallographic grinding was not necessary. Step 1, four hours on nylon cloth with 45-micron diamond paste; Step 2, three hours on nylon cloth with 6-micron diamond paste; Step 3, four hours on polytech Pre-PS paper with 0.1-micron diamond paste.

Tantalum

The tantalum specimens were received with a machine-ground surface so that metallographic grinding was not necessary. Step 1, four hours on nylon cloth with 45-micron diamond paste; Step 2, twenty minutes on polytech Supreme cloth with 0.05-micron alumina in 30 percent hydrogen peroxide.

Nickel

Step 1, fifteen minutes on each 240-grit silicon carbide paper until flat using kerosene and paraffin lubricant; Step 2, fifteen minutes on each of two 320-grit silicon carbide papers using kerosene and paraffin lubricant; Step 3, repeat Step 2 but with 400-grit silicon carbide paper; Step 4, repeat Step 2 but with 600-grit silicon carbide paper; Step 5, two hours on nylon cloth with 45-micron diamond paste; Step 6, two hours on nylon cloth with 6-micron diamond paste; Step 7, four hours on polytech Pre-PS paper with 0.1-micron diamond paste.

Solutioned Udimet 700

Step 1, grind until flat on 50-grit silicon carbide paper using water lubricant; Step 2, repeat Step 1 but with 180-grit silicon carbide paper and grind until all 50-grit scratches are removed;

Step 3, fifteen minutes on each of two 240-grit silicon carbide papers using kerosene and paraffin lubricant; Step 4, two hours on nylon cloth with 45-micron diamond paste; Step 5, two hours on nylon cloth with 6-micron diamond paste; Step 6, two hours on polytech Pre-PS paper with 0.1-micron diamond paste.

Aged Udimet 700

Metallographic grinding was not necessary because a low-stress grinding technique had been employed to remove the lathe marks. Step 1, four hours on nylon cloth with 45-micron diamond paste; Step 2, two hours on nylon cloth with 6-micron diamond paste; Step 3, two hours on polytech Pre-PS paper with 0.1-micron diamond paste.

3.3 Determination of Infinite Medium Sound Speed

Specimens for the determination of infinite medium sound speed were fabricated (see Section 3.2) of Armco iron, zinc, nickel, tantalum, Udimet 700 solutioned, Udimet 700 aged, and 52100 steel. The 52100 steel was the same as that of which the spheres used in the firings were made; it was, furthermore, hardened to the same degree as the steel spheres.

These specimens were in most cases 1-inch right circular cylinders with polished ends. The specimens were sent to Mr. H.A.F. Rocha, Manager of the Nondestructive Testing Unit, General Electric Materials and Processes Laboratory, Schenectady, New York⁽¹⁰⁾.

A determination of sound speed consists of the measurement of the transit time of an ultrasonic pulse through a specimen which is maintained at room temperature ($72 \pm 2^{\circ}\text{F}$). The measurement is made with use of a

⁽¹⁰⁾The sound speed determinations were carried out by Mr. M.E. Auger.

pulse generator and a nanosecond time interval meter with associated electronic equipment. The speed of sound is found by dividing the axial distance⁽¹¹⁾ through the right circular cylinder used as specimen by the measured transit time of the ultrasonic pulse. The measured axial distance, transit time for the ultrasonic pulse, and speed of sound in infinite medium for each metal is entered in Table 3.1.

In detail, the procedure for measuring the transit time is as follows. A 0.5-inch-diameter Branson Type ZR search unit of 5 MHz resonant frequency is connected to a high-speed SCR pulser (thyristor). A 1-inch-diameter Branson Type ZR search unit, also of 5 MHz resonant frequency, is connected to a high-gain logarithmic amplifier. The two search units are coupled to the opposite end surfaces of a cylindrical specimen through thin oil films; they are firmly clamped to the test specimen.

The output of the SCR pulser is connected to the start channel of a nanosecond time interval meter (Eldorado Model 793) and the output of the logarithmic amplifier is connected to one of the inputs of an AND or time discriminator gate. The other input of the AND gate is connected to the variable-delay gating pulse of a pulse generator (III Model PG-2) which is suitably synchronized to the SCR pulser. The delay of the gating pulse is set to allow the AND gate to pass the sound pulse transmitted by the 0.5-inch-diameter Branson Type ZR search unit and received by the 1-inch-diameter Branson Type ZR search unit.

(11) The axial distance through each specimen was measured by Mr. L.B. Engel of S.P.P.S. Physical Metallurgy Unit, General Electric Company, Evendale, Ohio.

The output of the AND gate is connected to the stop channel of the nanosecond time interval meter. The measured time interval is recorded on a digital recorder (Hewlett-Packard Model 562A) and the last three digits are converted into analog voltage by a digital analog converter (Hewlett-Packard Model 562A-65L). The analog voltage is recorded on a Simpson Model 604 Multicorder.

The delay of the gating pulse of the pulse generator (III Model PG-2) is then adjusted to pass only the second (echo) pulse received by the 1-inch-diameter Branson Type ZR search unit (three transits) and the measured time interval required is recorded. The delay of the gating pulse of the pulse generator is then adjusted to pass only the third pulse received by the 1-inch-diameter Branson Type ZR search unit (five transits) and the measured time interval required is recorded. From the time interval measurements made, the transit time of the ultrasonic pulse through the specimen is calculated. Use of the transit times for the second and third pulses improves the accuracy of the sound speed measurement.

Table 3.1
Measured Speed of Sound in the Metals Used for the Firings

Metal	Specimen Length, cm	Sound Pulse Transit Time, nanosec.	Sound Speed, cm/sec
hardened 52100 steel	5.0800	8615 \pm 10	5.896 $\times 10^5$
Armco iron	2.5408	4325 \pm 10	5.874 $\times 10^5$
pure zinc	3.1686	7300 \pm 10	4.340 $\times 10^5$
nickel 270	2.5408	4495 \pm 10	5.652 $\times 10^5$
arc cast tantalum	2.5387	6220 \pm 10	4.081 $\times 10^5$
Udimet 700 aged	2.5397	4160 \pm 10	6.105 $\times 10^5$
Udimet 700 solutioned	2.5408	4165 \pm 10	6.100 $\times 10^5$

3.4 Tensile Properties of the Metals

The tensile specimens (see Section 3.2) of Armco iron, nickel, tantalum, zinc, Udimet 700 solutioned, and Udimet 700 aged were sent to Mr. J.R. Frey at the General Electric Company, Lynn, Mass., to be tested on a Tinius Olsen tensile testing machine that adjusts automatically to maintain a constant strain rate. This machine has a 120,000 lb capacity but it can be adjusted for use with small loads.

The specimens as sent had smooth ends. Because threaded ends are required for the testing machine, threads were ground on the ends of the specimens at the testing laboratory.

The tests were conducted⁽¹²⁾ at a speed of 0.005 inch per inch per minute to the 0.2 percent offset yield strength. After this point in the test was reached, the crosshead speed was increased to 0.1 inch per minute.

The data obtained were: 0.02 percent offset yield strength, 0.2 percent offset yield strength, ultimate tensile strength, percent elongation, and percent reduction in area. These data for each of the two specimens of each of the six metals are listed in Table 3.2. The tabulated values were obtained using the original cross-sectional areas of the test specimens.

Copies of the autographic recording of the stress-strain curves produced by the tensile tests were supplied by the testing laboratory.

⁽¹²⁾ The tests were carried out by Mr. J.J. Mulligan under the direction of Mr. G.R. Frey.

Table 3.2

Tensile Data for the Metals Used in the Firings

Metal	Ultimate Tensile Strength, psi	0.02 percent Offset Yield Strength, psi	0.2 percent Offset Yield Strength, psi	Elongation, percent	Reduction in Area, percent
Iron	43,410	22,220	20,640	52	73.55
Iron	43,100	21,920	22,180	52	72.80
Average	43,255	22,070	21,410	52	73.18
Nickel	51,520	9,310	10,950	70	90.0
Nickel	51,200	5,208	7,350	70	82.7
Average	51,360	7,259	9,150	70	86.4
Tantalum	35,320	27,080	22,930	68	85.1
Tantalum	34,230	21,380	22,510	70	84.4
Average	34,775	24,230	22,720	69	84.8
Zinc	14,810	4,485	6,755	8	6.7
Zinc	16,110	4,205	6,400	10	7.5
Average	15,460	4,345	6,578	9	7.1
U-700 sol'd.	195,000	115,000	124,250	27.0	25.39
U-700 sol'd.	194,100	101,500	122,700	24.0	21.40
Average	194,550	108,250	123,475	25.5	23.40
U-700 aged	200,600	116,200	129,400	19.0	16.92
U-700 aged	201,100	116,650	130,700	19.0	20.10
Average	200,850	116,425	130,050	19.0	18.51

3.5 Steel Spheres for Use in the Firings

Original plans for the collection of additional data to test the cratering equations (see Section 1.6) called for test firings with two sizes of steel spheres. The type and sizes of sphere selected were grade SGPL balls in the nominal sizes 3/32-inch and 5/32-inch diameter. For balls of this grade, the variation in sphericity in a jar lot does not exceed 0.000005 inch and the variation in diameter does not exceed 0.000010 inch.

Balls of this grade in these nominal sizes were purchased from Atlas Ball Division of SKF at Cincinnati, O. The actual average diameters of the balls were 0.093745 inch and 0.156215 inch.

The AISI 52100 chrome alloy steel of which the balls were made had the following percentage composition: carbon, 0.95 - 1.10; manganese, 0.25 - 0.45; silicon, 0.20 - 0.35; chromium, 1.30 - 1.60; phosphorus, 0.025; sulfur, 0.025; nickel, 0.35; copper, 0.25; molybdenum, 0.08.

These balls are hardened by a special heat treatment to Rockwell C 63-65. The structure of the steel after heat treatment is a fine martensite with no troosite or ferrite.

Due to a change in the gun to be used for the firings, it was not possible to use the nominal 5/32-inch-diameter balls. It was necessary to substitute 0.175-inch-diameter balls that were obtained from Industrial Tectonics, Inc., at Ann Arbor, Mich. These balls were also fabricated from AISI 52100 chrome alloy steel.

4. TEST FIRINGS AND MEASUREMENT OF CRATER DIMENSIONS

A sub-contract was issued to a reputable research institute to design and construct a gun and to make a total of 208 test firings under controlled conditions against specimen plates of iron, tantalum, nickel, zinc, and Udimet 700 alloy. It was specified that the gun must be equipped with a velocity-measuring system capable of determining the velocity of each shot to better than one per cent after the inaccuracies of all parts of the velocity-measuring system had been assessed.

Of the 208 data shots purchased, 128 were to be made at elevated temperatures. Consequently, it was also specified that the gun chamber must be capable of being evacuated to a pressure of 1×10^{-5} torr and that the gun must be equipped with a heater capable of raising the temperature of the metal specimen plates by various amounts up to a maximum temperature of 815°C (1500°F) in a uniform manner and with a total variation over the face of the plate of less than 8°C (15°F) after the plate has been mounted in the gun and after the vacuum environment has been established.

After an effort of approximately eight months, the gun that had been designed and constructed by the sub-contractor proved to be inadequate to make the test firings because the sphere trajectories could not be controlled sufficiently to insure impact of the sphere against the 1-inch-diameter circular specimen plate. The sub-contractor submitted a proposed research program describing three possible modifications of the gun as it then existed. Because the cost of each of the proposed alternate modifications plus the required firings approached the original cost of design and construction of the gun plus the required firings, it was considered advisable to reduce the scope of the experimental work as originally proposed to firings at room temperature only. The consent of the contracting agency for this change in the original scope of the work was obtained.

The required number of room-temperature test firings was purchased from Materials Development Laboratory of the General Electric Company at Evendale, O. The purchase order required that the accuracy

of the velocity measurements be ± 0.1 per cent on comparative velocity and ± 1.0 per cent on absolute velocity. The test firings were made under the direction of Mr. M. A. Miller, supervisor of materials testing.

4.1 Guns and Velocity-Measuring System

Test firings with 0.175-inch-diameter steel spheres were made with use of a Benjamin Model 317 air rifle having a 0.177-calibre rifled barrel. The pressure chamber of this gun had been modified to allow for direct connection to a compressed gas supply. Projectile velocity was controlled by changing the inlet gas pressure. A view of the mounted rifle is shown in Figure 4.1.

A brass smooth-bore insert barrel was fabricated for firing 0.0938-inch-diameter spheres. This barrel had a 0.175-inch outside diameter and could be inserted into the rifled barrel of the Benjamin Model 317 air gun. The insert barrel was made from tubing that had an initial inside diameter of 0.089-inch. This tubing was drilled, reamed, and honed with a 600-grit emery paper to a final inside diameter of 0.095-0.096 inch.

The velocity-measuring system consisted of two photocells located at points one foot apart. A Model 464T chronograph (Electronic Counters, Inc.) was connected in the photocell circuit. Two lumiline lamps directed light beams against the photocells; these light beams were focused into light screens that were about 1/16 inch thick. When a steel sphere, emerging from the end of the gun barrel, cut through the first light screen, the chronograph was started; when it cut through the second light screen, the chronograph was stopped.

4.2 Measurements of Crater Dimensions

A Federal Products Company Model Q6IS metric indicator and Model 35B-30 comparator were purchased for use in making measurements of crater depth. The indicator is graduated in 0.01 mm. A calibration chart showing calibration of the indicator for every 0.1 mm over the range of interest for the crater-depth measurements was obtained from the Federal Products Company.

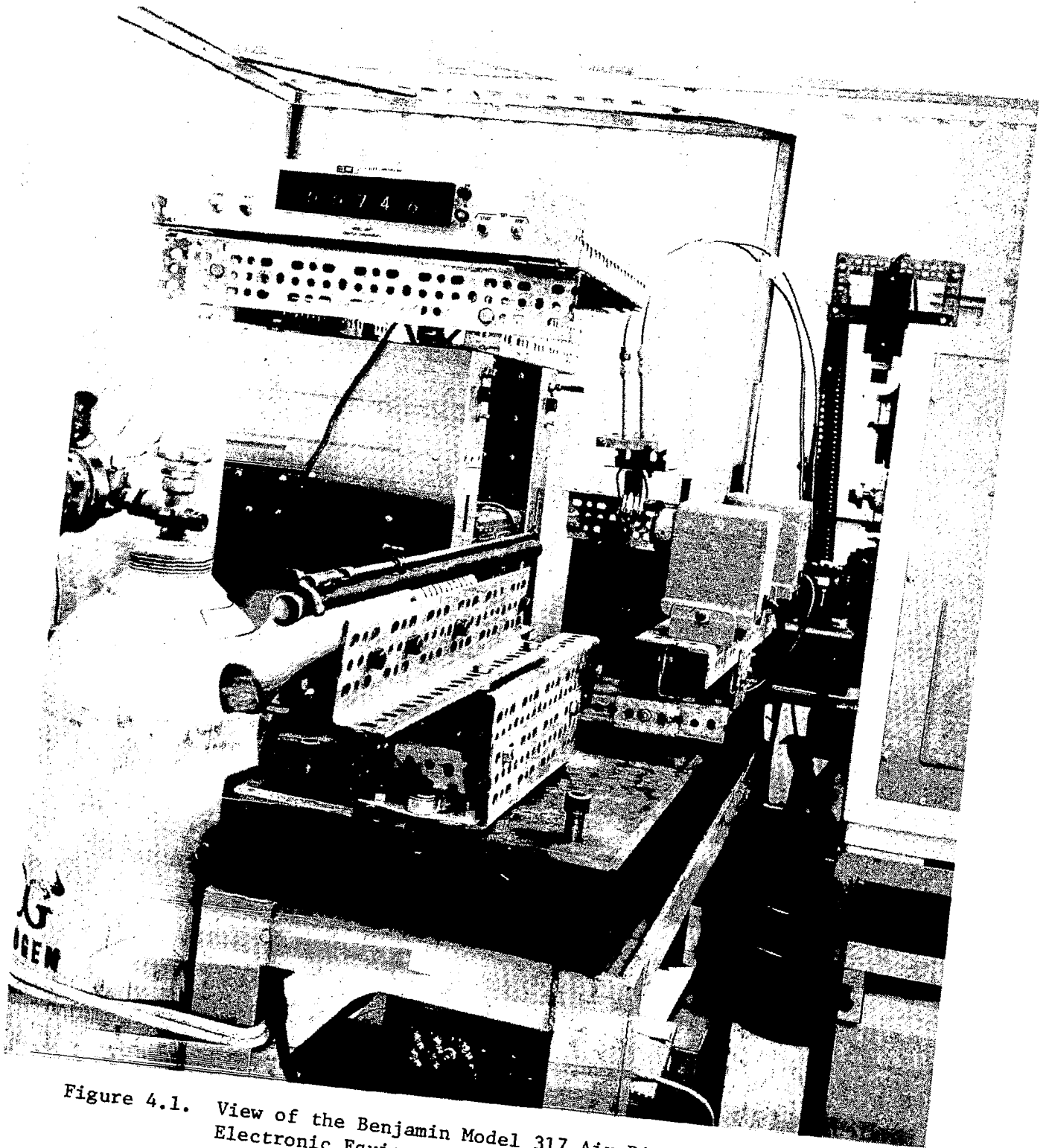


Figure 4.1. View of the Benjamin Model 317 Air Rifle and Associated Electronic Equipment.

To improve measurement accuracy, a mount to hold the impact face of the target specimen perpendicular to the direction of motion of the measuring probe was designed. The device was machined in one of the shops of the General Electric Company, Evendale, Ohio. To improve the accuracy with which craters produced by the small size balls could be measured, a special contact point was obtained from the Federal Products Company on special order.

Two procedures were used in making depth measurements. In one procedure, the dial indicator was read directly and the reading was corrected with reference to the calibration chart. With regard to this procedure, it was found by trial that a deviation as large as 0.004 mm could occur in five readings made on the same point when care was taken to lower the measuring probe to the surface very gently.

In the other procedure, the dial indicator was merely used to hold the measuring probe vertical. In this procedure the height of the top of the probe above a level surface was found by bringing the indicator hand of an electronic height gauge (Federal Electro-Check) to the zero position. This height was then read to an accuracy of ± 0.000010 inch on a Starrett height gauge.⁽¹³⁾

In each procedure, readings were made at points on the surface of the specimen that were undisturbed as a result of the cratering process. In the first procedure, four such readings were made; in the second procedure, two. These height readings were averaged and the crater depth was taken to be the difference between the average of the surface readings and a reading taken at the lowest point in the crater.

It was thought that the indicator readings for maximum depth might be affected by the process of moving the measuring probe to locate the point of greatest depth in a crater. To establish whether or not this was the case, measurements were made using two orders of precedence: (1) the surface readings were followed by the reading of

⁽¹³⁾ Measurements with use of the electronic height gauge and Starrett height gauge were made by Mr. James H. Gibbons of the Metrology Laboratory, General Electric Company, Evendale, Ohio.

maximum depth, and (2) the reading of maximum depth was followed by the surface readings. A statistical treatment⁽¹⁴⁾ of the variation in the depth values that resulted from the two orders of precedence yielded the result that the order of precedence was not significant.

Recorded values of crater depth are the average of two measurements. In most cases one of these measurements was made by each of the two procedures employed.

The diameters of some of the craters (see Table 4.1) were measured with use of the traveling microscope of a Brinell hardness testing machine. The impact face of the target specimen was held perpendicular to the optical axis of the instrument while a crater-diameter measurement was in progress by means of a special mount constructed for this purpose. Two measurements of crater diameter were made at an angle of roughly 90 degrees to one another in the plane of the crater mouth.⁽¹⁵⁾ The average of these two readings was recorded as crater diameter.

4.3 First Set of Cratering Data

The initial set of test firings was made against target plates of the four pure metals (nickel, zinc, tantalum, and iron) using 0.175-inch steel spheres, and the Benjamin Model 317 air gun with rifled barrel. The specimen plate used as target for each firing was mounted in the taped jaws of a vise. The cratering data for the four pure metals are listed in Table 4.1, the crater-depth data are plotted against velocity in Figure 4.2.

Inspection of Figure 4.2 shows that the crater-depth-versus-velocity plots for both nickel and zinc appear to be straight lines, as was expected from the earlier study [7]. The plots are inconsistent

⁽¹⁴⁾ This statistical treatment was devised by Dr. Gerald J. Hahn, statistician, Information Studies Branch, Information Sciences Laboratory, General Electric Research Laboratory, Schenectady, N.Y.

⁽¹⁵⁾ The measurements of crater diameter were made by Mr. R. C. Volmer, Materials Testing Unit, Materials Development Laboratory, General Electric Company, Evendale, Ohio.

Table 4.1

Initial Set of Cratering Data for the Four Pure Metals

Metal	Velocity, cm/sec	Average Crater Depth, cm	Average Crater Diameter, cm	Depth/Diameter Ratio --
iron	0.3322×10^4	0.0098	0.1481	0.0662
iron	0.6173×10^4	0.0186	0.1898	0.0980
iron	0.9810×10^4	0.0300	0.2483	0.1208
iron	1.304×10^4	0.0399	0.2826	0.1412
iron	1.653×10^4	0.0516	0.3220	0.1602
iron	1.958×10^4	0.0623	0.3516	0.1772
iron	2.283×10^4	0.0745	0.3820	0.1950
iron	2.748×10^4	0.0933	0.4153	0.2247
zinc	0.3319×10^4	0.0170	0.1602	0.1061
zinc	0.6173×10^4	0.0313	0.2111	0.1483
zinc	0.9854×10^4	0.0463	0.2554	0.1813
zinc	1.306×10^4	0.0621	0.2953	0.2103
zinc	1.657×10^4	0.0784	0.3264	0.2402
zinc	1.963×10^4	0.0934	0.3524	0.2650
zinc	2.275×10^4	0.1078	0.3721	0.2897
zinc	2.743×10^4	0.1340	0.4114	0.3257
nickel	0.6127×10^4	0.0348	0.2206	0.1578
nickel	0.9832×10^4	0.0537	0.2698	0.1990
nickel	1.303×10^4	0.0672	0.3042	0.2209
nickel	1.657×10^4	0.0842	0.3383	0.2489
nickel	1.959×10^4	0.0986	0.3570	0.2762
nickel	2.264×10^4	0.1125	0.3862	0.2913
nickel	2.748×10^4	0.136	0.4107	0.3311
tantalum	0.3320×10^4	0.0094	0.1446	0.0650
tantalum	0.6135×10^4	0.0184	0.1936	0.0950
tantalum	0.9851×10^4	0.0290	0.2462	0.1178
tantalum	1.312×10^4	0.0386	0.2986	0.1293
tantalum	1.654×10^4	0.0492	0.3509	0.1402
tantalum	1.960×10^4	0.0607	0.3958	0.1534
tantalum	2.276×10^4	0.0709	0.4286	0.1654

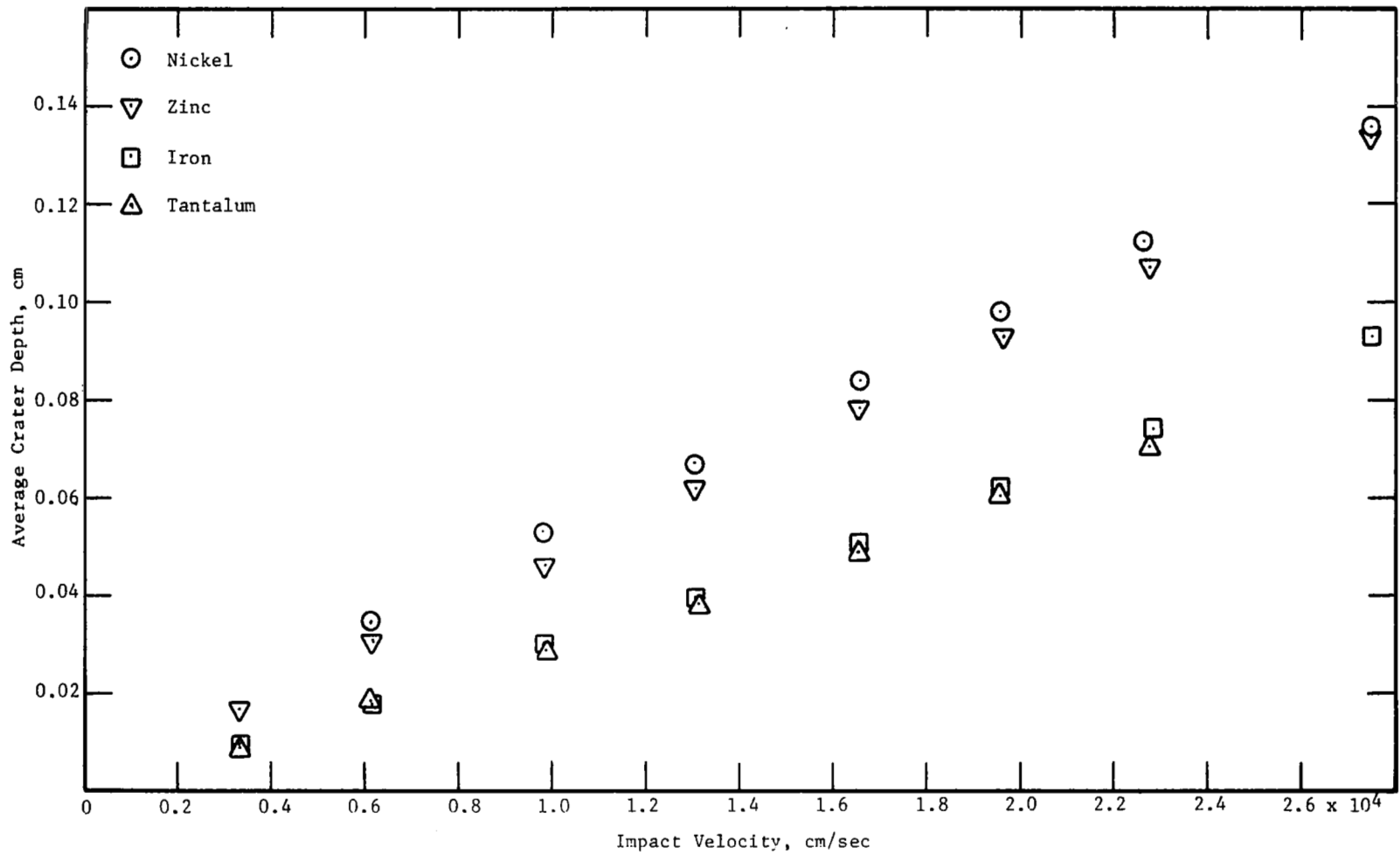


Figure 4.2. Crater-Depth-Versus-Velocity Plots for Impacts of 0.175-Inch Steel Spheres Against Plates of Nickel, Zinc, Iron, and Tantalum.

with those obtained in the earlier study [7] in that if best-fit lines are drawn for the data points these lines have positive intercepts on the crater-depth axis rather than positive intercepts on the velocity axis.

The feature of an intercept on the crater-depth axis is unreasonable in that it predicts a crater of measurable depth formed at zero velocity. If this feature is real, it can only mean that the cratering mechanism changes at very low velocities in such a way that the crater-depth-versus-velocity plot is either a curve or consists of two straight lines having different slopes. Because this behavior is different from what was observed in the past [6, 7], it was considered advisable to perform some diagnostic tests.

4.4 Diagnostic Tests

If the feature of an intercept on the crater-depth axis is an artifact, it could have resulted from a number of possible causes: the effect of reflected stress waves from the curved walls of the cylindrical target plates which differed in both size and shape from those used earlier [7], the way in which the target plates were gripped during the firings, the thickness of the target plates, spinning of the 0.175-inch-diameter spheres which were fired with the rifled-bore gun, and, possibly, a malfunction of some kind in the velocity-measuring system.

Reflected Stress Waves

That stress waves are reflected inward from the curved surface of transparent cylindrical plates of white sapphire that were struck by mercury drops was observed in the past [4]. What effect, if any, such waves may have when they reach a crater formed near the center of a metal plate is not known. In obtaining cratering data for steel-sphere impacts earlier [7], the plates of the metals being used as targets were 6-inch squares that were 1-inch thick. In planning the present experimental work, the targets were reduced to 1-inch-diameter, 1/2-inch-thick circular cylinders make it more convenient to place them in a closed vacuum system and heat them uniformly to high temperatures as well as to minimize scatter in the crater-depth-versus-

velocity plots by improving the accuracy with which the crater depths could be measured. The reduction in size also made it possible to give the surface of the target plates a uniform metallographic polish.

To make a test of the possibility that the crater depths may have been affected by reflected stress waves, a 1-inch diameter hole that was oversized by several mils was cut in a 6-inch-square 1-inch-thick plate of tool steel. After a depth of 0.523 ± 0.002 inch was reached, the diameter of the hole was reduced to 0.875 inch and the cut was continued through the tool steel plate. A 1-inch-diameter 1/2-inch-thick cylindrical specimen plate, when slipped into the hole, rested on the shoulder that formed where the diameter of the hole was reduced. The specimen plate could not move in the impact direction because of the shoulder on which it rested yet the rear face of the specimen plate remained a free surface.

The tool steel plate was heated in hot water and a nickel specimen, after being dipped in molten (approximately 195°F) Wood's metal, was slipped into the hole in the hot plate and firmly seated against the shoulder in the hole. The plate was then cooled to room temperature and a 0.175-inch-diameter steel sphere was fired against the nickel specimen. The nickel specimen was removed from the tool steel plate by heating the plate again in hot water and the same procedure was carried out using a second nickel specimen. The steel spheres that were fired at the nickel specimens impinged at different velocities. The depths of the craters produced in the nickel specimens were measured. The measured depths are listed in Table 4.2; they are plotted in Figure 4.3 against the velocities at which the spheres impinged. It can be seen from Figure 4.3 that these two points lie on the straight line which provides a best fit to the original data points for nickel.

The acoustic impedances of nickel, Wood's metal, and steel are 5.169×10^6 , 2.355×10^6 , and 4.547×10^6 g/cm²·sec, respectively. The layer of Wood's metal was extremely thin. Presuming that the acoustic-impedance mismatch between nickel and Wood's metal and that between Wood's metal and steel can be neglected, it appears to make

Table 4.2

Cratering Data for Diagnostic Firings

Metal	Velocity cm/sec	Average Crater Depth, cm	Average Crater Diameter, cm	Depth/Diameter Ratio --
A. Specimen soldered in tool steel block				
nickel	0.9373×10^4	0.0510	--	--
nickel	1.836×10^4	0.0928	--	--
B. Square specimen of size 0.794 by 0.794 inch				
nickel	1.517×10^4	0.0781	0.3236	0.2413
C. Square specimen of size 0.663 by 0.674 inch				
nickel	1.524×10^4	0.0782	0.3231	0.2420
D. Specimen bearing against rigidly gripped pipe				
nickel	0.2975×10^4	0.0186	--	--
nickel	0.7498×10^4	0.0416	--	--
nickel	1.162×10^4	0.0609	--	--
E. Specimen bearing against rigidly gripped pipe; shims for side support				
nickel	1.519×10^4	0.0776	0.3241	0.2394
F. Specimen standing on its curved contour with no support at all				
nickel	1.529×10^4	0.0784	0.3256	0.2408
G. Specimen of reduced thickness (approximately 0.16 inch thick)				
nickel	0.3423×10^4	0.0217	--	--
nickel	0.6523×10^4	0.0376	--	--
H. Steel spheres fired from a smooth-bore gun to minimize spin				
nickel ^(a)	1.108×10^4	0.0582	--	--
nickel	1.121×10^4	0.0580	--	--
nickel	1.548×10^4	0.0776	--	--
nickel	1.804×10^4	0.0902	--	--
I. Firings made at very low velocities				
nickel	0.08297×10^4	0.0064	0.1016	0.06299
nickel	0.1274×10^4	0.0084	0.1163	0.07223
nickel	0.1410×10^4	0.0094	0.1209	0.07775

(a) This specimen was of increased thickness (approximately 1 inch thick)

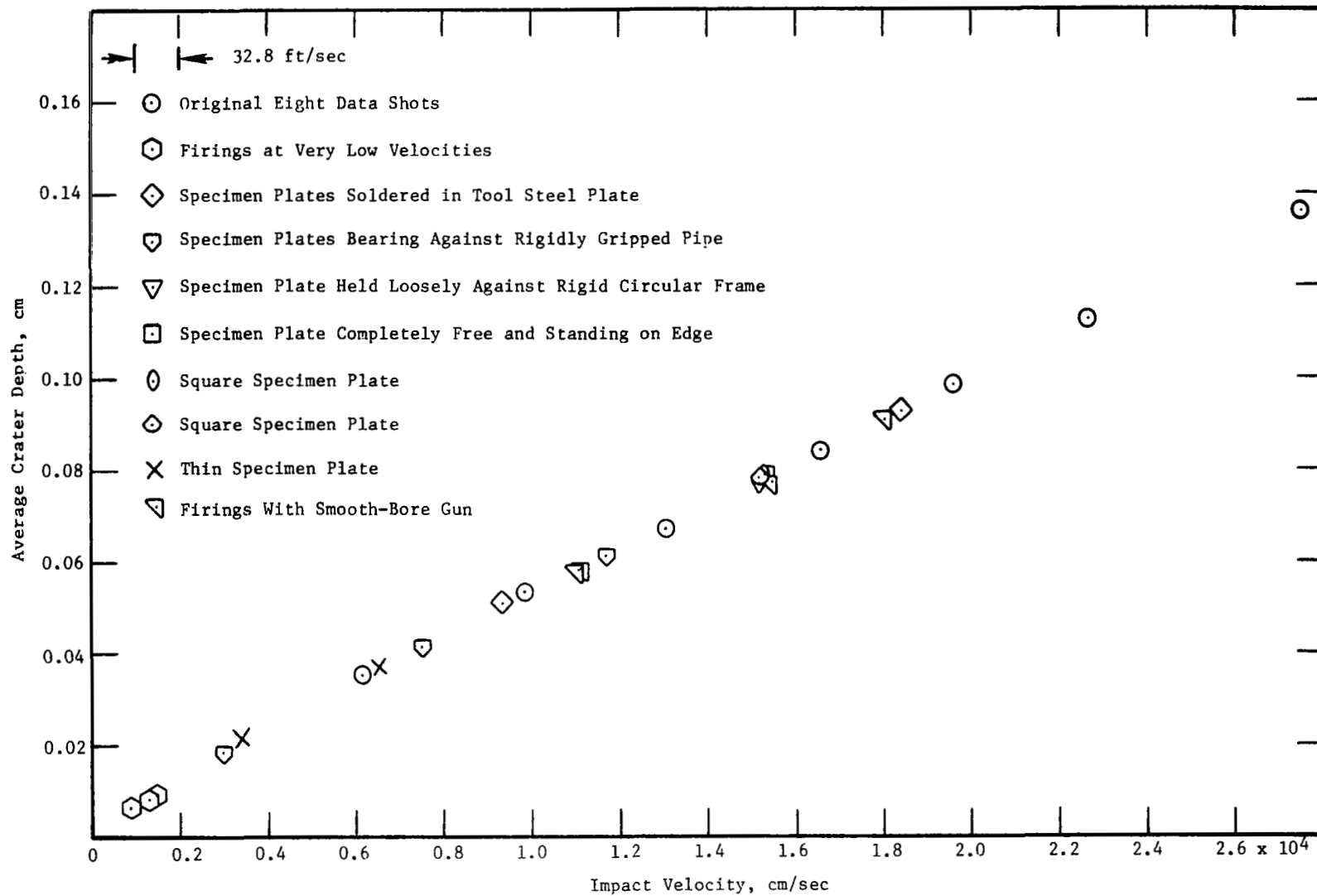


Figure 4.3. Crater-Depth-Versus-Velocity Plot for Craters Formed in Nickel Plates Under a Variety of Conditions.

no difference as far as crater depth is concerned whether the specimen is a 1-inch-diameter 1/2-inch-thick cylinder, or whether it is a 6-inch-square 1-inch-thick plate.

The possibility that reflected stress waves may affect the depth of impact craters was tested further with the use of two square nickel specimens of different sizes. The square specimens were cut out of cylindrical specimens and, consequently, had the same thickness. The larger square was 0.794 by 0.794 inch \pm 0.005 inch; the smaller square was 0.663 by 0.674 inch \pm 0.005 inch. The corners of the larger square were rounded in order to have a square specimen that was as large as possible.

These specimens were mounted in the taped jaws of a vise and a 0.175-inch-diameter steel sphere was fired against each. The depths of the craters that were produced were measured. The measured crater depths are listed in Table 4.2. They are plotted in Figure 4.3 against the velocities at which the spheres impinged. It can be seen from Figure 4.3 that these two points lie on the straight line which provided a best fit to the original data points for nickel. The conclusion drawn is that, as far as crater depth is concerned, for impacts of 0.175-inch-diameter steel spheres it makes no difference whether the specimen is a 1-inch diameter circular cylinder, a square that is 0.794 \pm 0.005 inch on a side, or a square that is 0.663 by 0.674 inch \pm 0.005 inch.

Specimen Mounting

As noted above, for the original data shots the specimen plates had been held in position by the taped jaws of a vise. This mounting was not absolutely rigid. It seemed possible that each specimen could have moved as a unit in the impact direction to some small extent when the impact against it occurred and that this may have affected the depths of the craters produced.

To test this possibility, a short section of 1-inch OD pipe was rigidly gripped in the bare jaws of the vise behind the 1-inch-diameter cylindrical specimen. The pipe provided a rigid restraining

frame for the specimen; this prevented the specimen from moving in the impact direction while it simultaneously maintained the rear face of the specimen as a free surface.

Firings at different velocities with 0.175-inch steel spheres were made against nickel specimens mounted in this way. The depths of the craters that resulted were measured. The measured crater depths are listed in Table 4.2. They are plotted against the velocities at which the spheres impinged in Figure 4.3. It can be seen from Figure 4.3 that these points also lie on the straight-line best-fit curve to the original data points for nickel and it can be concluded that movement of the specimen plate in the impact direction (if this occurred in the taped jaws of the vise) did not affect the depths of the craters that were produced in the original firings.

In view of the result that was obtained, a 0.175-inch steel sphere was fired against a nickel specimen that was mounted in the following way: the specimen was rested against a section of 1-inch OD pipe, which was rigidly gripped in the vise to prevent movement of the specimen plate in the impact direction, but the specimen plate itself was only loosely restrained with shims to prevent lateral movement. A 0.175-inch steel sphere was also fired against a nickel specimen plate that was standing on its curved edge without any restraint or support at all. The depths of the craters that were produced by these findings were measured. The measured crater depths are listed in Table 4.2. They are plotted in Figure 4.3 against the velocities at which the steel spheres impinged. It can be seen from Figure 4.3 that these two points also lie on the straight-line best-fit curve to the original data points for nickel.

The cratering results that were obtained using various types of gripping (including no gripping at all) make it possible to remove the qualification that the specimen should be given edge support only [6, 7]. No support or restraint in any direction is required. However, the reverse face of the specimen must be maintained as a free surface (that is, the specimen must not be backed up against a heavy rigid plate) [7].

Specimen Thickness

The selected 1/2-inch thickness of the specimen plates was scaled to the sizes of steel spheres to be used on the basis of previous work [6, 7]. To test the possibility that specimen thickness might provide an explanation for the seemingly anomalous data (intercept on the crater-depth axis) plotted in Figure 4.3, a nickel specimen was cut through its thickness so that two nickel specimens having thicknesses of approximately 0.2 and 0.3 inch, respectively, were obtained. The thinner of the two, which was 0.157 - 0.170 inch thick measured at the edge, was mounted in the taped jaws of the vise with edge support only; the rear face was maintained as a free surface. Two 0.175-inch steel spheres were fired against this specimen at velocities of 112.3 and 214 ft/sec, respectively. The depths of the craters that formed as a result of these impacts were measured. The measured depths of the craters are listed in Table 4.2; they are plotted against the velocities at which the steel spheres impinged in Figure 4.3. It can be seen from Figure 4.3 that the specified reduction in the thickness of the specimen plate does not affect the depth of crater produced. The conclusion that can be drawn from this test is that a plate thickness of roughly one sphere diameter is still acceptable for the cratering mechanism being considered.

Effect of Spin

It was thought that spinning of the steel spheres, which could be produced by the rifling in the barrel of the Benjamin Model 317 air gun, might affect crater depth; the spin of a spinning steel sphere might provide a rotary boring action that could result in a deeper crater at any arbitrary impact velocity than would be expected on the basis of the impact velocity alone.

To establish whether or not crater depth produced by spinning steel spheres differs from that produced by non-spinning steel spheres, a smooth-bore Crossman Model 760 Powermaster air gun was purchased. The pressure chamber of this rifle was modified to permit changing the projectile velocity by controlling the inlet gas pressure. Firings with 0.175-inch steel spheres were made against four specimens of each of the six metals for which cratering data were to be collected. One

of the four specimens was of double thickness. The depths of the craters were measured. For each of the six metals, it was found that the depths of craters produced by the smooth-bore gun, when plotted against velocity, fell on the same straight line as the depths of craters produced by the rifled-bore gun. The crater depths for the four nickel specimens, one of which was of double thickness, are listed in Table 4.2 and plotted in Figure 4.3.

The firings in Materials Development Laboratory had been purchased with a specification of ± 1.0 per cent on the accuracy of the measured velocities. However, elimination of the other possible causes of the anomolous intercept on the crater-depth axis, which appeared in plots of measured crater depth against measured impact velocity, suggested that the measured velocities might be in error.

4.5 Check of the Velocity-Measuring System

A thorough check of the electronics involved in the velocity-measuring system was carried out.⁽¹⁶⁾ Firings were made with 0.175-inch spheres and the output pulse of each light screen unit was observed on an oscilloscope. Both outputs were found to be zero-to-plus-fifty-volt pulses with an approximate six-millisecond decay time constant. The rise time of the output pulse was ten to twenty microseconds.

It was found that the output pulse from each unit would occasionally go negative. A schematic of the light screen unit showed that the output pulse is generated by triggering a thyatron. The trigger is obtained from the output of a vacuum tube amplifier located after the vacuum phototube. The cause of the occasional incorrect negative output pulse was traced to the thyatron which remained latched in the conducting state. A coupling network was changed to correct this condition and both light screen output pulses were then found to be consistent in direction and amplitude.

⁽¹⁶⁾ This check was made by Mr. John F. Wolfinger of Measurements Development Sub-operation, CANO-DTO, General Electric Company, Evendale, Ohio, assisted by Mr. Charles L. Burger.

The counter that had been used was removed and a counter-command generator was added to command a Hewlett-Packard timer. The counter-command generator receives the start light-screen output pulse and switches its output from zero to plus twelve volts. This output is held constant until the stop light-screen output is received at which time the generator output drops to zero. The generator output is the counter-command signal. To obtain correct operation of the generator for timing firings made with 0.175-inch spheres, it was necessary to attenuate the light screen output from a plus-fifty-volt peak to a plus-fifteen-volt peak.

A series of firings was made to obtain the velocities given to 0.175-inch spheres at nitrogen gas pressures from 5.5 to 500 psig. The two gauges that were used over this range of gas pressures were calibrated and the gauge pressures used for the firings were corrected. A plot of the velocities given to the spheres against the gauge pressures that were used for the firings is shown in Figure 4.4. It can be seen from Figure 4.4 that the plot of data obtained after checkout and adjustment of the velocity-measuring system extrapolates to the origin. However, the velocity-versus-gauge-pressure plot, which had been obtained for the system prior to checkout and adjustment, extrapolates to an intercept on the gauge-pressure axis. The intercept on the gauge-pressure axis in Figure 4.4 is the same kind of anomaly as the intercept on the crater-depth axis in Figure 4.2. Furthermore, the velocity difference between the curves of Figure 4.4 at pressures below 100 psig is about 50 ft/sec; this is a velocity difference sufficient to translate the straight-line nickel curve of Figure 4.2 to the right far enough to provide a substantial intercept on the velocity axis.

More data shots were fired on the basis of assurance that the system was working properly. However, plots of measured crater depth against measured impact velocity for the new data that were collected were as anomalous as the plots of Figure 4.2.

At the advice of two ballistics experts,⁽¹⁷⁾ metal screens were then

⁽¹⁷⁾ Mr. Wilfred J. Ferguson of Naval Research Laboratory, Washington, D.C., and Mr. H. F. Swift of the University of Dayton, Dayton, Ohio.

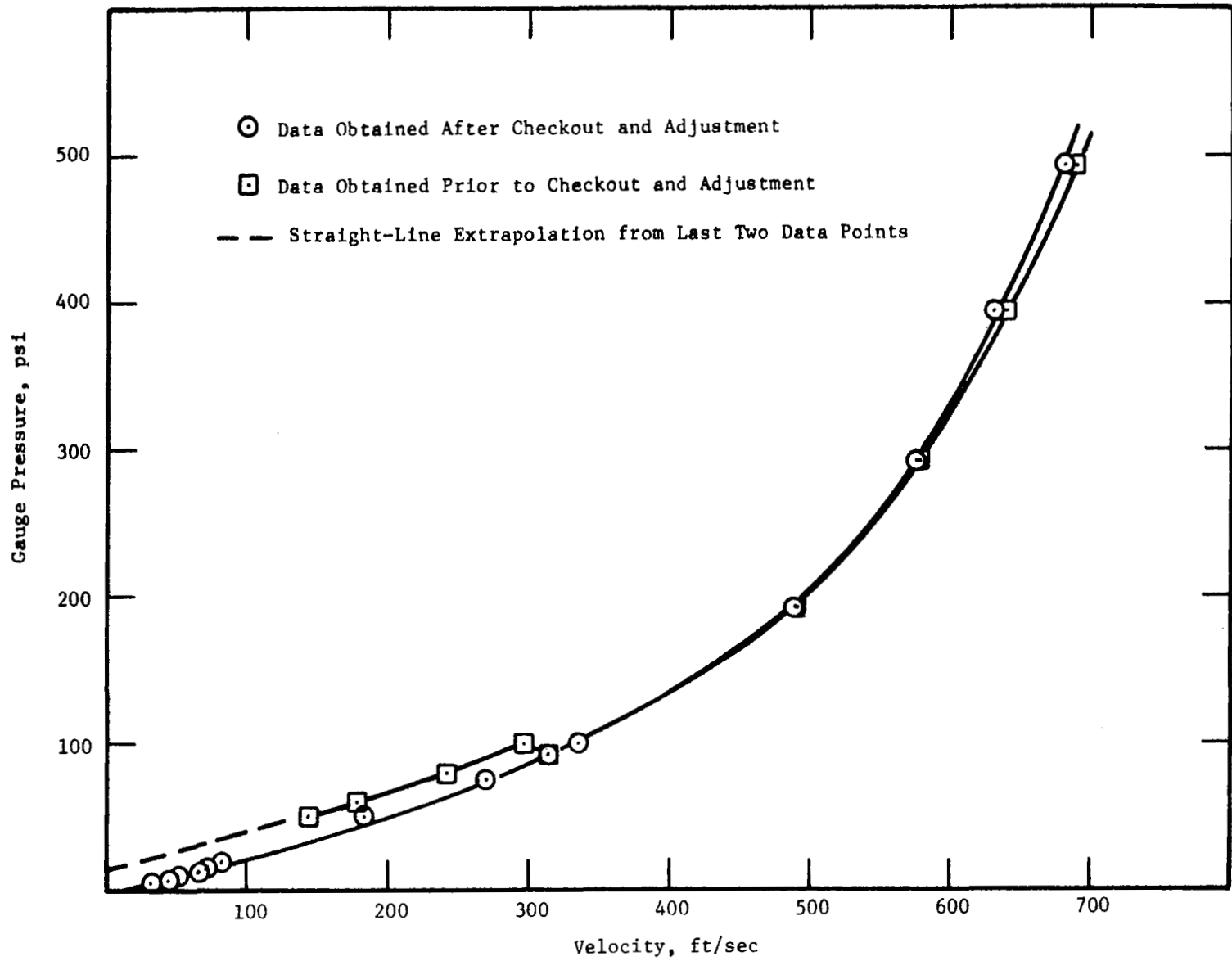


Figure 4.4. Velocities Acquired by 0.175-Inch Spheres at Arbitrary Gas Pressures.

introduced to measure the transit time of the sphere over the 1-foot base length. A metal screen was placed behind the light screen both at the beginning and at the end of the base length. Two chronographs were employed; the Hewlett-Packard timer was controlled by the metal screens and the Model 464T Chronograph (Electronic Counters, Inc.) was controlled by the light screens as before. Both chronographs were triggered by the passage of the sphere that struck the metal specimen plate.

The metal screens that were used were of two types. One type consisted of a continuous metal line printed on paper in the form of a grid.⁽¹⁸⁾ The grid spacing was of such a size that impact of a 0.175-inch sphere would break the circuit. Because the 0.0938-inch spheres were too small to break the circuit, a second type of screen was used for this sphere size. The second type of screen consisted of two very thin sheets of aluminum foil taped over each side of a hole in a thin plastic sheet. The distance between the aluminum foils was such that impact of a 0.0938-inch sphere would close the circuit.

The remaining data shots were fired with simultaneous double determination of the impact velocity. Two sets of data with simultaneous double determination of velocity were obtained over the entire velocity range; this range extended from about 50 ft/sec to about 900 ft/sec. The following analysis was made of these data. For each firing, the per cent of difference between the light-screen-measured and the metal-screen-measured velocity (taken with respect to the metal-screen-measured velocity) was determined and was plotted against the metal-screen-measured velocity. See Figure 4.5. In Figure 4.5, the points in the set of data that contained the smallest number of variables were connected with lines.

It can be seen from Figure 4.5 that there is a linear rise in the per cent of difference with increase in velocity to a velocity of 150 ft/sec. Because no firing was made at a velocity between 150 and

⁽¹⁸⁾ The metal-printed paper screens and the idea for construction of the metal-foil screens were contributed by Mr. H. F. Swift.

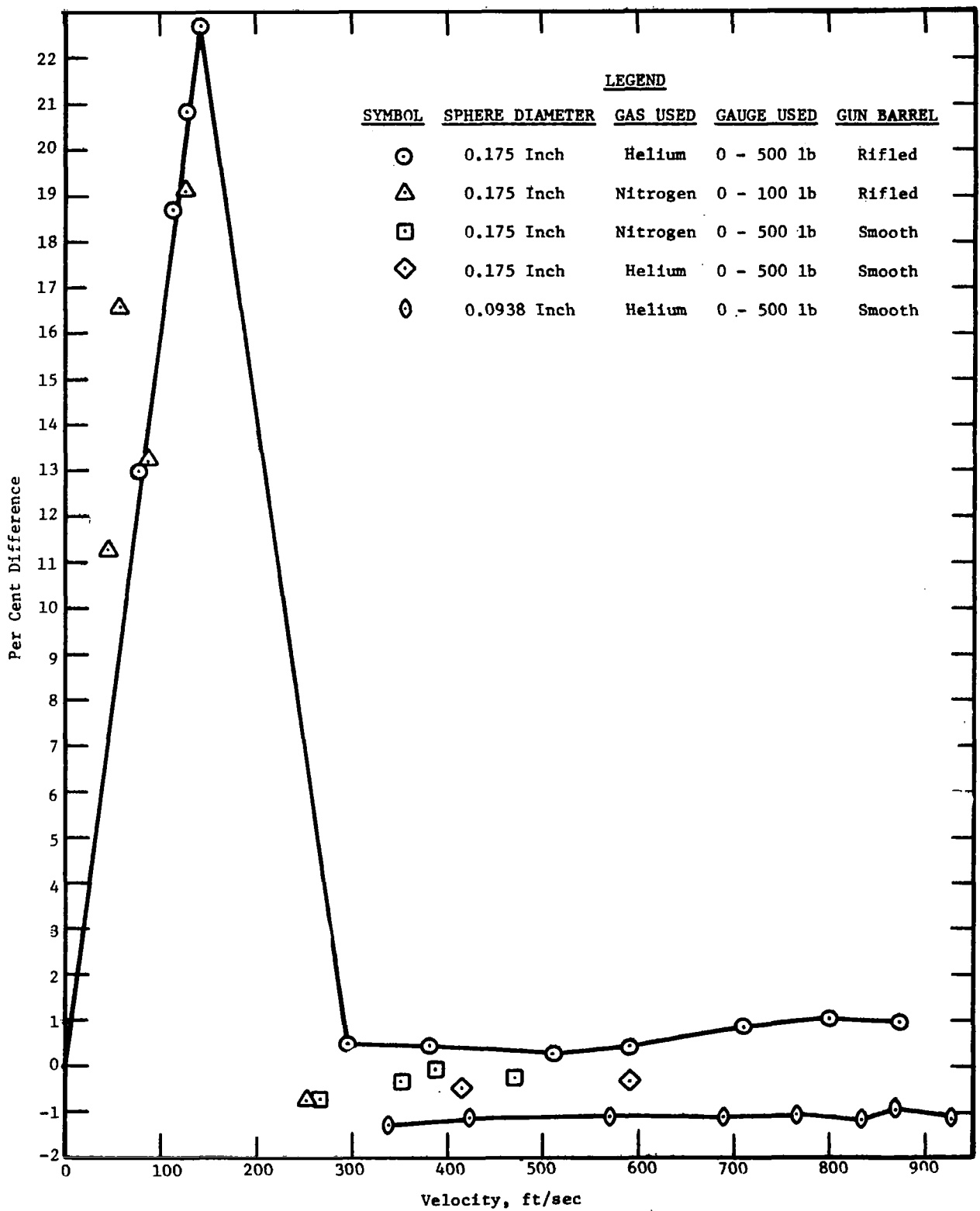


Figure 4.5. Comparison of Velocities Measured with Light Screens and Metal Screens.

250 ft/sec, it is not known whether or not 22.5 is the maximum per cent of difference. The behavior of the plot of Figure 4.5 at velocities below 250 ft/sec strongly suggests that the velocity-measuring technique employed may be subject to a systematic error in the low-velocity range.

It can be seen from Figure 4.5 that at velocities above 250 ft/sec the per cent of difference is not much greater than ± 1.0 even when the data for the 0.0938-inch sphere, for which the double-aluminum-foil type of screen was used, are considered. However, at velocities above 250 ft/sec, a curious form of behavior is evident. Except for the single point with triangular symbol plotted at a velocity of 252 ft/sec, the per cent of difference is negative for shots made with the smooth-bore gun and positive for shots made with the rifled-bore gun.

The velocity difference was always taken to be the metal-screen-measured velocity minus the light-screen-measured velocity. Consequently, the curious observation just cited means that for shots made with a smooth gun barrel, the light-screen-measured velocity is greater than the metal-screen-measured velocity but for shots made with a rifled gun barrel, the metal-screen-measured velocity is greater than the light-screen-measured velocity. Because the metal screens were located behind the light screens in every case, the light-screen-measured velocity should always be greater than the metal-screen-measured velocity.

Because the velocity-measuring system should be independent of the type of gun barrel employed, the curious behavior which has been described suggests that the velocity-measuring technique employed may also be subject to error in the high-velocity range.

In order to make a meaningful analysis of cratering data that are collected, it is essential to be certain that the measured velocities are correct. To test the accuracy of the velocity-measuring system, the measured velocities were compared with velocities that were measured by an independent method. The independent method selected was a ballistic pendulum.

The theory of the ballistic pendulum is well known [16]. A small projectile of known mass, which is moving at high velocity, gives all of its momentum to the pendulum when it impinges against the pendulum. If the pendulum block is constrained to move linearly in a single plane in the impact direction as a consequence of the impact, the velocity of the projectile prior to impact is found by conserving linear momentum. The velocity, v_1 , of the projectile prior to impact is given by [16]

$$v_1 = (m_2/m_1) (2gh)^{1/2} \quad (4.1)$$

where g is the acceleration due to gravity (locally, $g = 980.004$ cm/sec/sec), m_1 is the mass of the impinging projectile, m_2 is the mass of the pendulum plus projectile after impact, and h is the height of rise of the pendulum block as a consequence of the impact.

The height of rise, h , was calculated from the horizontal linear motion of the pendulum block in the impact direction and the length, d , of the vertical supporting string, which was calculated from the measured period of the pendulum. In terms of the period of the pendulum, T , the length of the vertical supporting string is given by

$$d = g T^2 / 4 \pi^2 \quad (4.2)$$

The height of rise of the pendulum block is given by

$$h = d - (d^2 - H^2)^{1/2} \quad (4.3)$$

where H is the measured horizontal motion of the pendulum that occurs as a result of the impact of the projectile against it.

The pendulum that was used consisted of a balsa wood block supported at three points by light-weight braided nylon cords.⁽¹⁹⁾ The arrangement of the supporting cords was designed to damp out all modes

⁽¹⁹⁾ The mode of support of the pendulum block and the method of measuring its horizontal motion were contributed by Mr. H. F. Swift of the University of Dayton, Dayton, Ohio, who supervised the collection of the experimental data. He was assisted by Mr. R. C. Volmer and Mr. L. B. Engel.

of motion of the pendulum block except simple translation in the impact direction. The frame from which the pendulum was hung was about five feet high.⁽²⁰⁾ During the firings that were made, the pendulum block was shielded from the gas blast of the firing and the end of the pendulum block was located far enough from the shield to avoid error due to a suction effect.

The horizontal motion of the pendulum that was caused by impact of a steel sphere was determined with use of a photographic technique. The pendulum block was sprayed with black paint and a very small flash light bulb and battery were fastened to the upper surface of it with black electrical resistance tape. A steel rule was mounted in such a way that the graduated surface of the rule was in a plane with the upper surface of the glowing filament of the flash light bulb. When a steel sphere was fired into the end of the pendulum block, the laboratory lights were turned off and the horizontal movement of the pendulum block as a result of the impact was photographed. When the pendulum block reversed its motion at the end of each maximum amplitude of swing, sufficient time elapsed to permit the light from the flash light bulb to mark the position of the pendulum with a bright spot against the dark background.

The extent of the horizontal displacements, for impacts of 0.175-inch-diameter spheres that impinged at velocities from about 75 to about 900 ft/sec, were obtained from measurements on the photographs. Measurements of the distance between the bright spots on the photographs, which mark the first and second maximum amplitude of the pendulum, were made by each of two observers with use of a travelling microscope. The magnifying factor was obtained from readings of ten points on the photograph of the steel rule by the same two observers using the same travelling microscope.

The measured horizontal motion for each firing was taken to be half of the distance between the first and second maximum amplitude

⁽²⁰⁾ The pendulum frame was obtained on loan from the Physics Department of the University of Cincinnati, Cincinnati, Ohio.

after this distance was reduced by the width of the filament. The measured horizontal motion for each firing was corrected for loss due to air drag and frictional resistance at the bearing points of the pendulum. To determine the logarithmic decrement, the pendulum was set in motion and the horizontal displacements of the first, tenth, and thirtieth periods were photographed and measured. The measured distance between the first and second maximum in the first period was found to be 1.91720 cm as measured on the scale of the travelling microscope; for the tenth period this distance was found to be 1.70685 cm. The logarithmic decrement is 1/9 of the logarithm of the ratio 1.91720/1.70685 or 0.00559. Horizontal motion during the test firings with the pendulum occurred over three fourths of a period. To a close approximation, the multiplying factor to correct for this amount of motion is 1.0097. The correction amounts to roughly one per cent.

Each sphere that was fired against the ballistic pendulum passed through two light screens that were located one foot apart. The occlusion of the first and second light screen by the sphere started and stopped a chronograph, respectively. The velocity of each sphere was calculated both from eq (4.1) and as the reciprocal of its transit time over the one-foot base length; these velocities are referred to below as the pendulum velocity and the chronograph velocity, respectively.

The chronograph velocity is plotted against the pendulum velocity in Figure 4.6. The straight line drawn in Figure 4.6 is a least squares fit to the plotted points obtained with use of a computer program⁽²¹⁾ which also yields the standard deviation of the slope and intercept. The linear equation found by the computer program is

$$v_c = 1.027 v_p + 83.7063 \quad (4.4)$$

(21) This computer program was constructed by Mr. Lars H. Sjodahl, Ceramic Materials Research, Nuclear Systems Programs, General Electric Company, Evendale, Ohio.

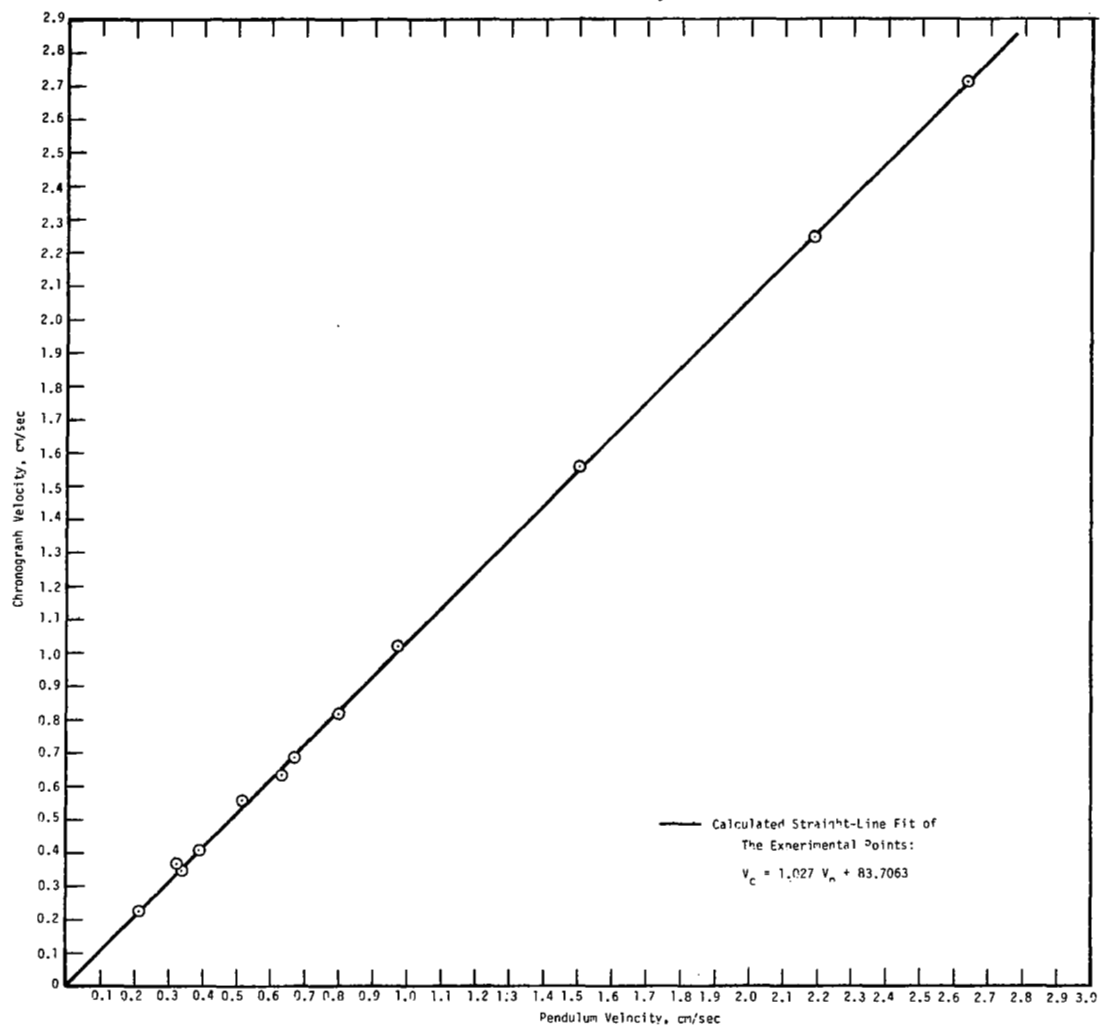


Figure 4.6. Plot of Chronograph Velocity Against Pendulum Velocity.

where V_c is the chronograph velocity in cm/sec and V_p is the pendulum velocity in cm/sec. The standard deviation of the slope of the line is ± 0.00591727 and the standard deviation of the intercept is ± 70.5972 cm/sec.

Taking twice the value of the standard deviation as a measure of 95 percent confidence, it can be seen that the slope of the straight line is known with a high degree of confidence (roughly, one percent) but the intercept is very poorly known. The intercept of the calculated best-fit line may be the result of scatter in the data. It is possible to impose on the least squares fit the condition that the line must pass through the origin; this would increase the slope by a small amount. However, it was considered preferable to accept eq (4.4) as the relation between the chronograph velocities and pendulum velocities.

From eq (4.4), and with consideration of the 95 per cent confidence limits on the slope, it appears that the chronograph velocities are from 1.7 to 3.7 percent high. Although the error in the chronograph velocities is not large, it was considered advisable to convert the chronograph velocities of the test firings into pendulum velocities with use of eq (4.4). The pendulum velocities contain only the measurement error which is less than ± 0.5 percent.

All of the measured velocities of the data shots that were made were corrected with use of eq (4.4). When the depths of the craters that were produced by the firings were plotted against the corrected velocities, it was found that the seemingly anomalous behavior of the crater-depth-versus-velocity plots was still evident. On the basis of the tests that had been made, this behavior was accepted as a real effect and an effort was made to understand it. Metallographic studies of the metal around impact craters in each of the selected metals were carried out, a study was made of the stress-strain behavior of the metals, and hardness measurements were made both below the crater and to the side of the crater edge.

5. FURTHER DIAGNOSTIC STUDIES

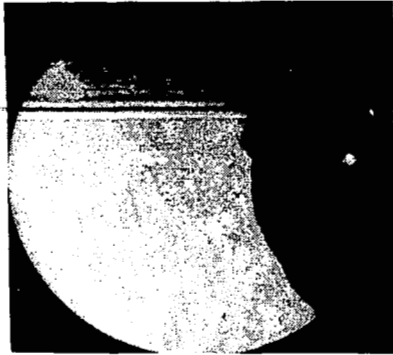
5.1 Appearance of the Surface Metal at the Rim of the Crater

If a metallic surface has a high polish prior to being deformed in some way, the existence of slip lines in the metal below the surface (plastic flow) can be detected by inspecting the surface itself; the ends of the slip lines are visible as microscopic ledges on the surface. With the exception of zinc, the specimens of the six metals that were selected for the steel-sphere-impact study were given a metallographic polish (see Section 3.2.3).

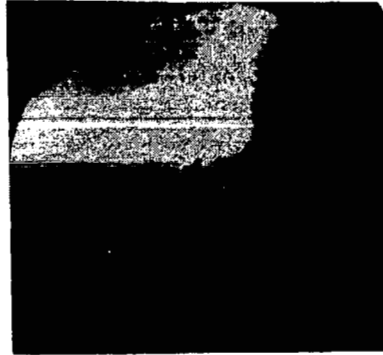
Inspection of the surface metal around the rims of craters produced in nickel specimens by impacts of 0.175-inch-diameter steel spheres at velocities of 1291, 2254, 3342, 3779, 4243, and 17465 cm/sec, respectively, was informative. From the micrographs shown in Figure 5.1, it can be seen that, although the surface metal near the rims of the craters produced at velocities below 4243 cm/sec is essentially featureless, there is a gradual development of surface irregularity with increase in velocity.

For impact velocities below 4243 cm/sec, the development of surface irregularity, which indicates that plastic flow of the metal around the crater produced by the impact has occurred, appears to be negligible in amount. The surface metal near the rim of the crater produced at a velocity of 17465 cm/sec, on the other hand, shows clear evidence that plastic flow has taken place in the metal around the crater; the metal grains are not only protruding from the surface but the individual grains are striated with microscopic ledges which indicate that slip has occurred.

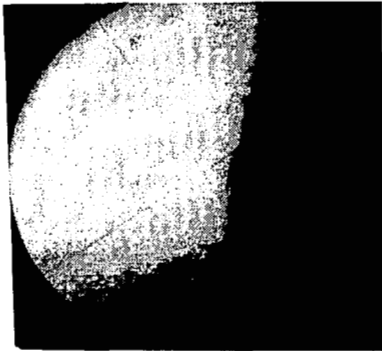
Micrographs of the surface metal around the rims of craters produced in the other five selected metals and in 1100-0 aluminum by impact of 0.175-inch steel spheres at velocities in the range of 1.72 to 1.75×10^4 cm/sec are shown in Figure 5.2. From these micrographs it can be seen that there is clear evidence of plastic flow in the metal around the craters that were produced in tantalum, iron, and the two heat-treatment states of Udimet 700. In the case of zinc and



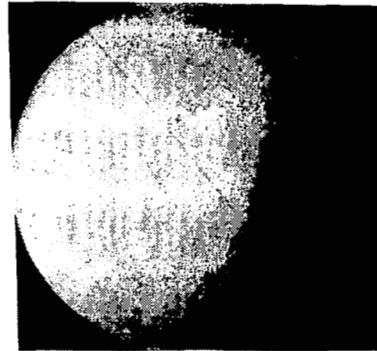
Velocity, 1291 cm/sec



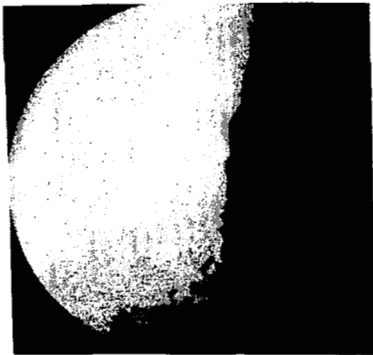
Velocity, 2254 cm/sec



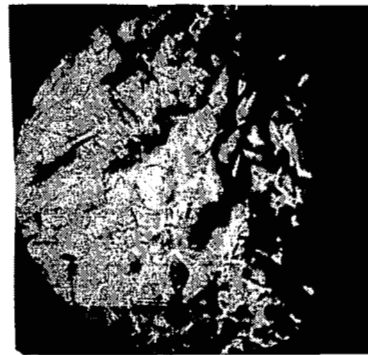
Velocity, 3342 cm/sec



Velocity, 3779 cm/sec



Velocity, 4243 cm/sec



Velocity, 17465 cm/sec

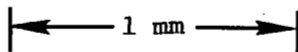


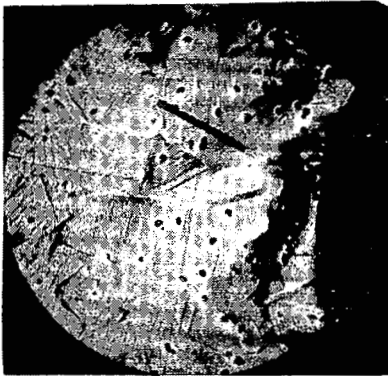
Figure 5.1. Surface Views of Nickel Specimens Near the Rim of the Crater.



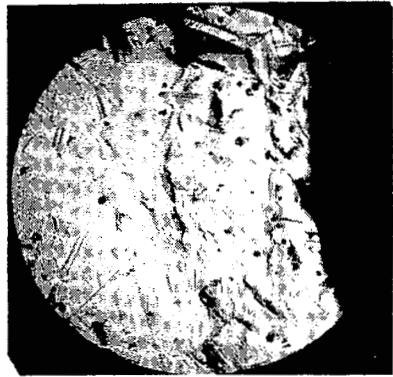
Aluminum, Velocity, 17406 cm/sec



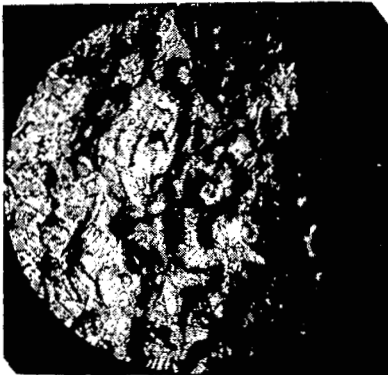
Zinc, Velocity, 17328 cm/sec



U-700 Aged, Velocity, 17153 cm/sec



U-700 Sol'ned, Velocity, 17182 cm/sec



Iron, Velocity, 17036 cm/sec



Tantalum, Velocity, 17066 cm/sec

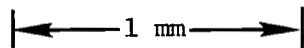


Figure 5.2. Surface Views of Selected Metals Near the Rim of the Crater.

1100-0 aluminum, there is no surface evidence which would indicate that plastic flow in the metal around the craters has occurred. It is noteworthy, however, that impact specimens of zinc and of 1100-0 aluminum were not given a metallographic polish.

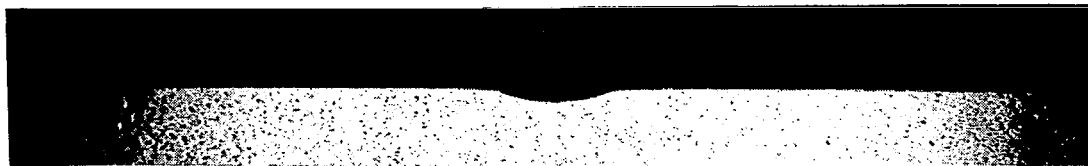
5.2 Studies of the Metal Around the Craters with Use of Cross-Sectional Cuts

To determine the relative microstructural response of the six metals that were selected for the steel-sphere-impact study, a cross-sectional cut was made of a crater produced in a specimen of each metal; a cross-sectional cut of an impact crater in 1100-0 aluminum was also made. To make comparison of the impact behavior of these metals more meaningful, the specimens that were selected for sectioning were chosen on the basis that the impact velocity used was in the range of 1.72 to 1.75×10^4 cm/sec. To be able to compare the impact behavior at low and at high velocity, a cross-sectional cut of an impact crater in nickel produced at a velocity of 3342 cm/sec was also made.

5.2.1 Gross Surface Contour

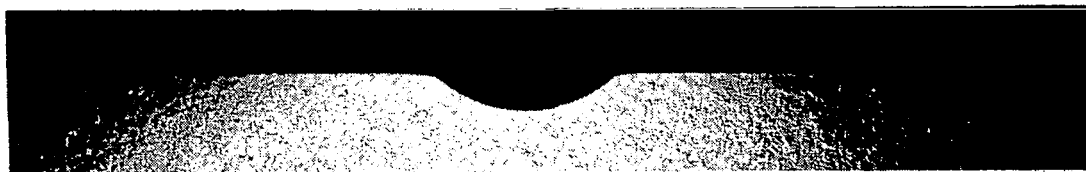
Surface views of the cross-sectional cuts of the specimens that were selected are shown in Figure 5.3. An interesting difference in crater contour is apparent in the crater cross sections shown in this figure. If a straight edge is laid across the surface of the metal in which the crater exists, it can be seen that in the case of nickel, zinc, and aluminum a collar of metal around the edge of the crater has been depressed with respect to the remaining surface metal of the specimen plate. This is shown schematically in sketch (a) of Figure 5.4. The magnitude of this effect is not equal; it is much less for aluminum than for nickel or zinc and it is very much less for nickel at an impact velocity of 3342 cm/sec than for nickel at an impact velocity of 17465 cm/sec. This suggests that this effect is a function both of the impact velocity and of material properties.

Using the same procedure, it can be seen that for tantalum, iron, and Udimet 700 a collar of metal around the edge of the crater has been



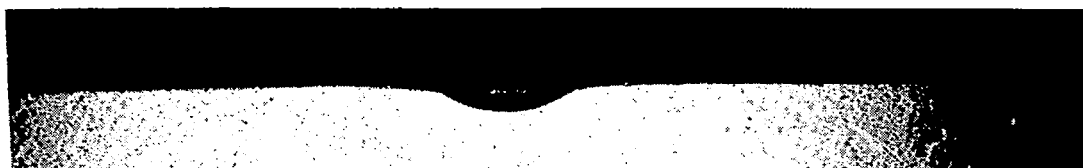
Nickel

Impact Velocity, 3342 cm/sec



Nickel

Impact Velocity, 17465 cm/sec



Zinc

Impact Velocity, 17328 cm/sec



Aluminum

Impact Velocity, 17406 cm/sec

1 mm → | ←

Figure 5.3. Surface Contrours Around the Impact Craters.



Tantalum

Impact Velocity, 17066 cm/sec



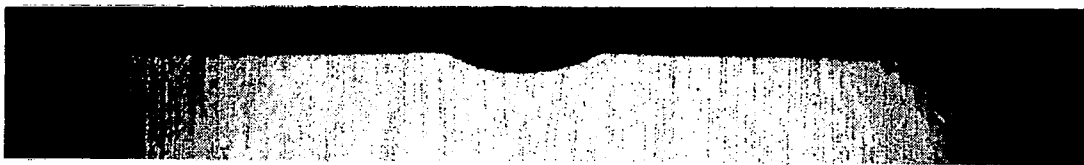
Iron

Impact Velocity, 17036 cm/sec



Udimet 700
Solutioned

Impact Velocity, 17182 cm/sec



Udimet 700
Aged

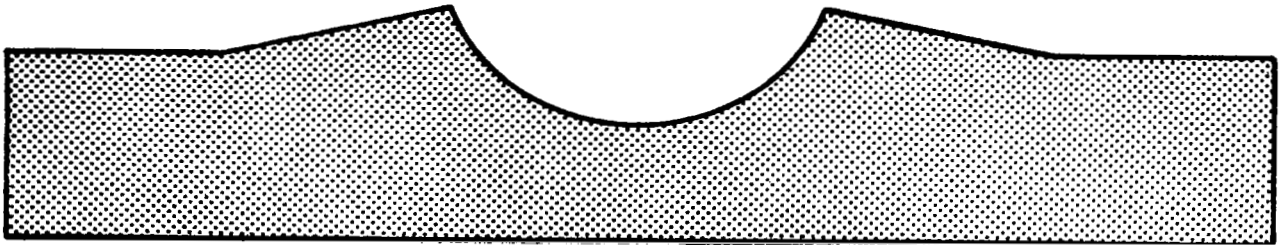
Impact Velocity, 17153 cm/sec

1 mm → | ←

Figure 5.3. Surface Contours Around the Impact Craters. (Cont.)



(a) Crater Contour: Nickel, Zinc, and Aluminum



(b) Crater Contour: Tantalum, Iron, and Udimet 700

Figure 5.4. Gross Surface Contour of the Craters.

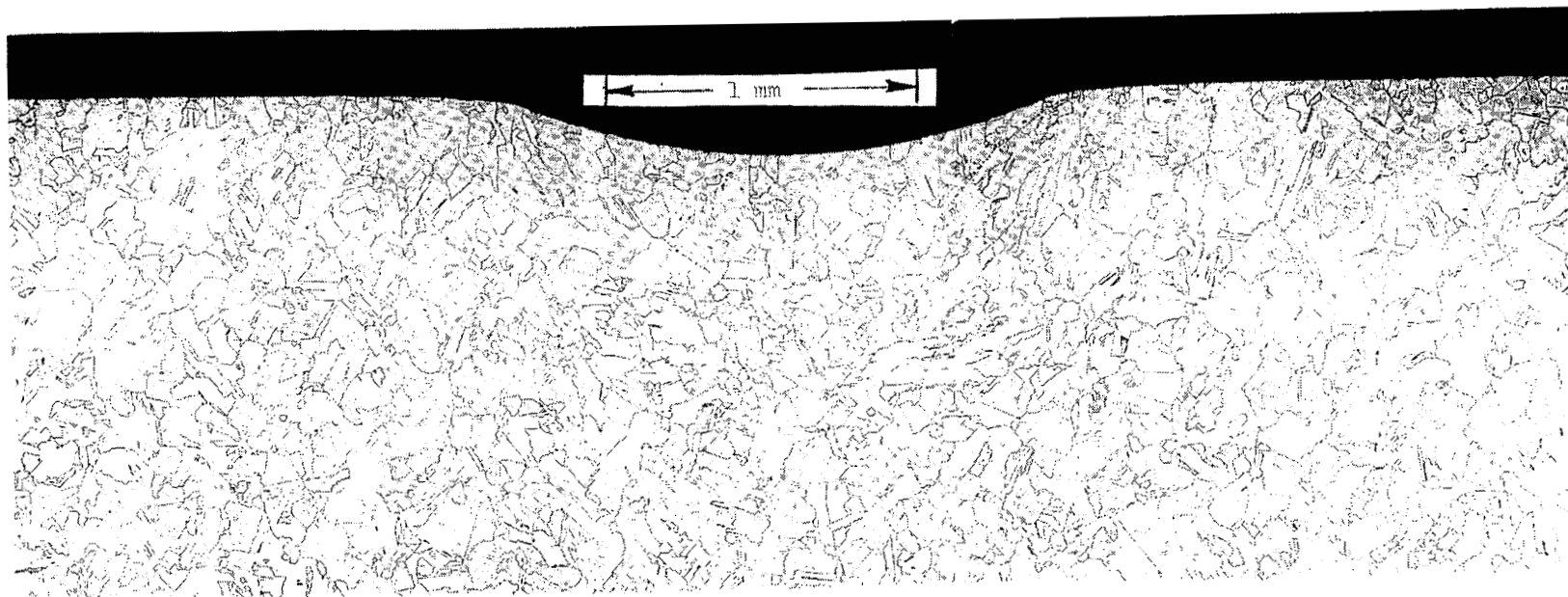
raised with respect to the remaining surface metal of the specimen plate. This is shown schematically in sketch (b) of Figure 5.4. The magnitude of this effect is considerably less in Udimet 700 than in tantalum and iron. Similar elevated collars of metal can be seen in cross sections of craters produced by impacts of steel spheres against specimen plates of annealed electrolytic tough pitch copper and of 2024-0 aluminum alloy that were produced in an earlier study [7]; the effect is more pronounced in 2024-0 aluminum than in copper.

5.2.2 Subsurface Microstructural Change

The cross-sectional cuts were given a metallographic polish and were etched to make the grain structure visible. Satisfactory results were obtained in the case of the six metals selected for use in the study; a good etched cross section of the crater in 1100-0 aluminum was not obtained.

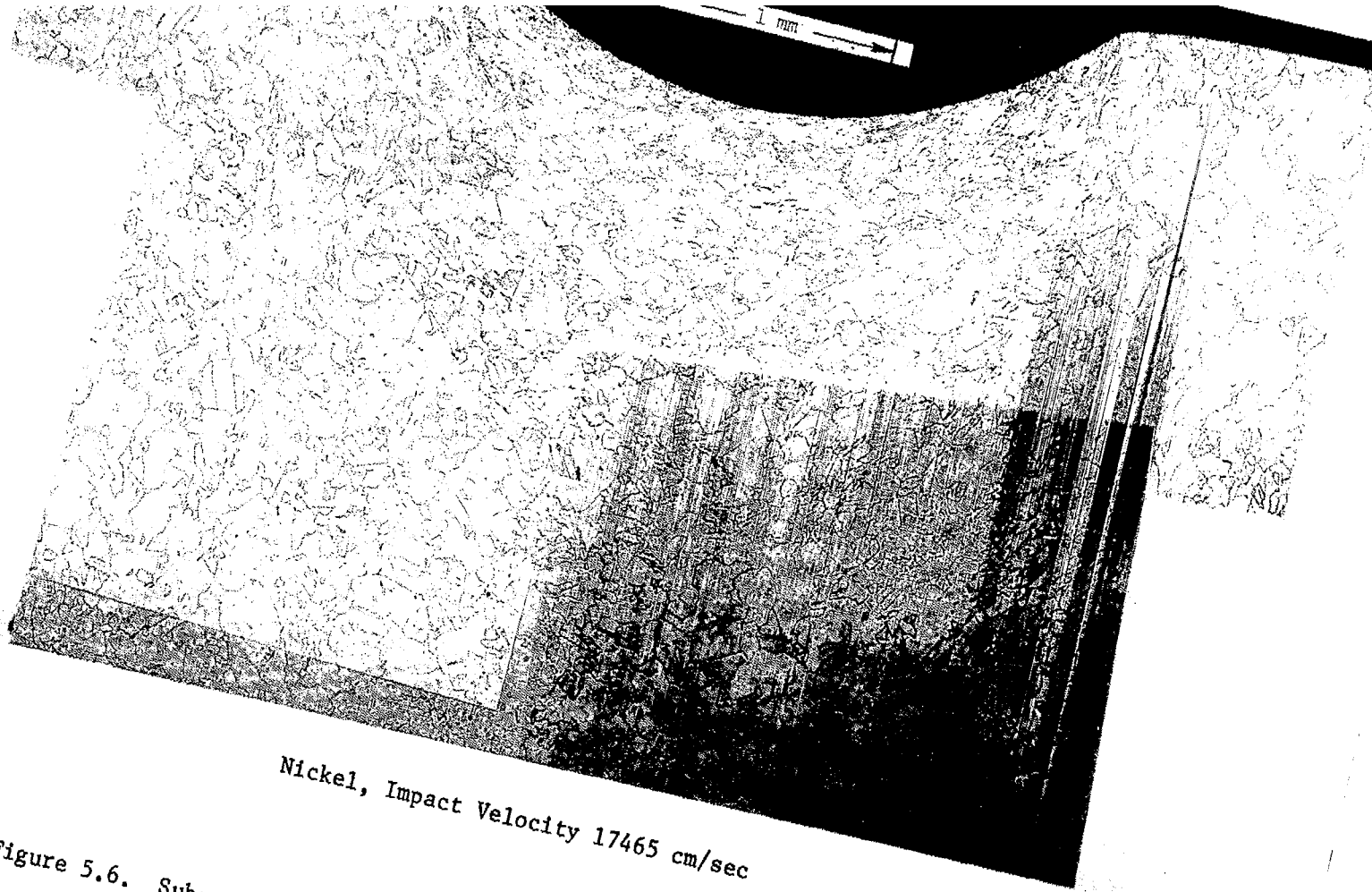
The cross sections of the craters produced in nickel by impacts of 0.175-inch steel spheres at velocities of 3342 and 17465 cm/sec are shown in the micrographs of Figures 5.5 and 5.6. From Figure 5.5 it can be seen that evidence of plastic flow in the metal is at most vanishingly small under the crater produced in nickel at a velocity of 3342 cm/sec. The situation is notably different in the metal around the crater produced in nickel at a velocity of 17465 cm/sec. From Figure 5.6 it can be seen that there is evidence of plastic distortion in the metal for a distance of about one crater diameter below this crater and to a small distance beyond the crater rim. These observations are in agreement with those pointed out in Section 5.1. The observations suggest that impact of a 0.175-inch steel sphere against nickel at 3342 cm/sec results in a pressure pulse that produces very little plastic distortion but that impact of a steel sphere of the same size against nickel at a velocity of 17465 cm/sec results in a pressure pulse that produces notable plastic distortion.

The cross section of the crater produced in zinc by impact of a 0.175-inch steel sphere at a velocity of 17328 cm/sec is shown in the micrograph of Figure 5.7. The metal around the inside surface of the



Nickel, Impact Velocity, 3342 cm/sec

Figure 5.5. Subsurface Microstructural Change in Nickel at a Low Velocity.



Nickel, Impact Velocity 17465 cm/sec

Figure 5.6. Subsurface Microstructural Change in Nickel at a High Velocity.

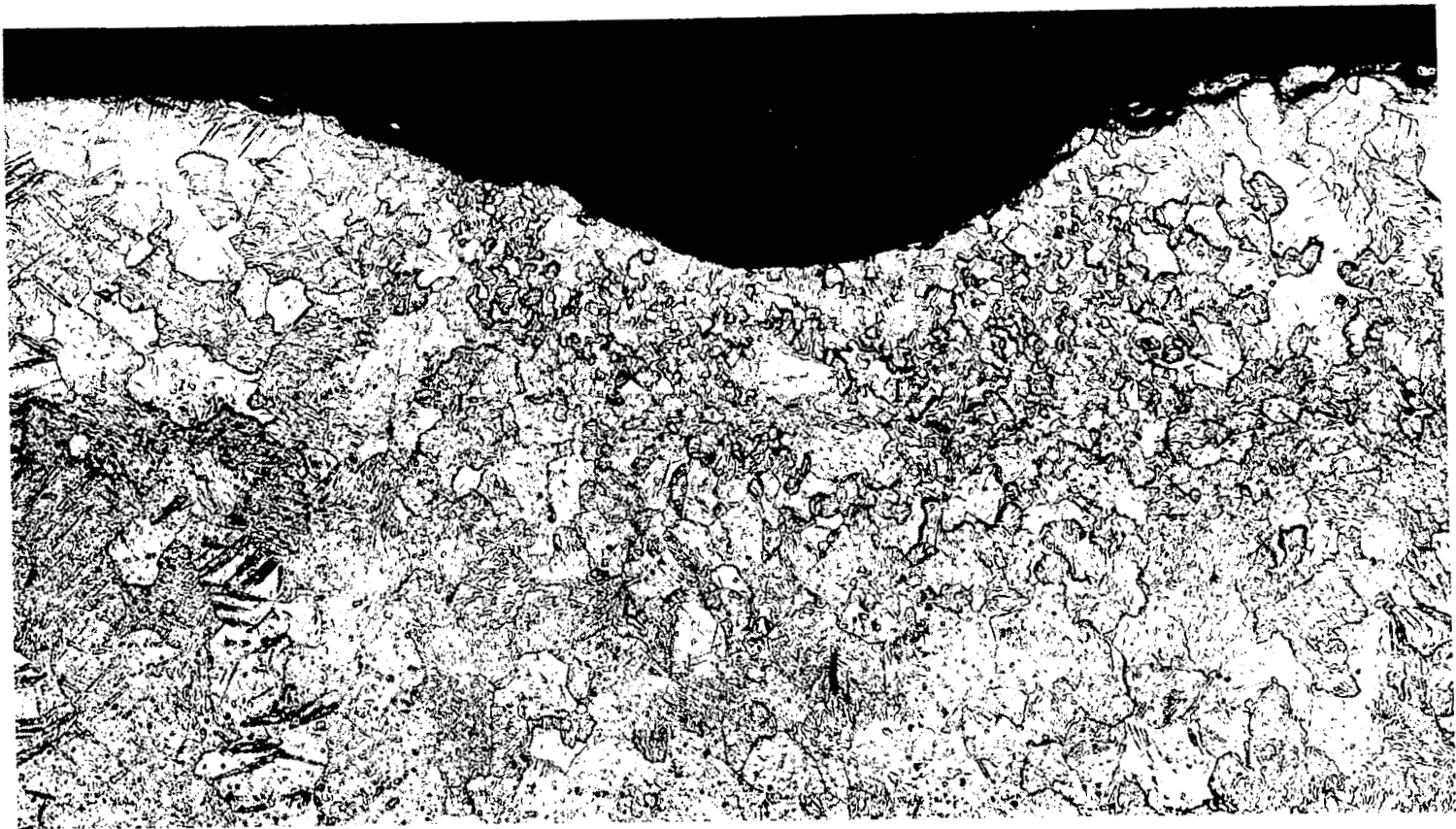


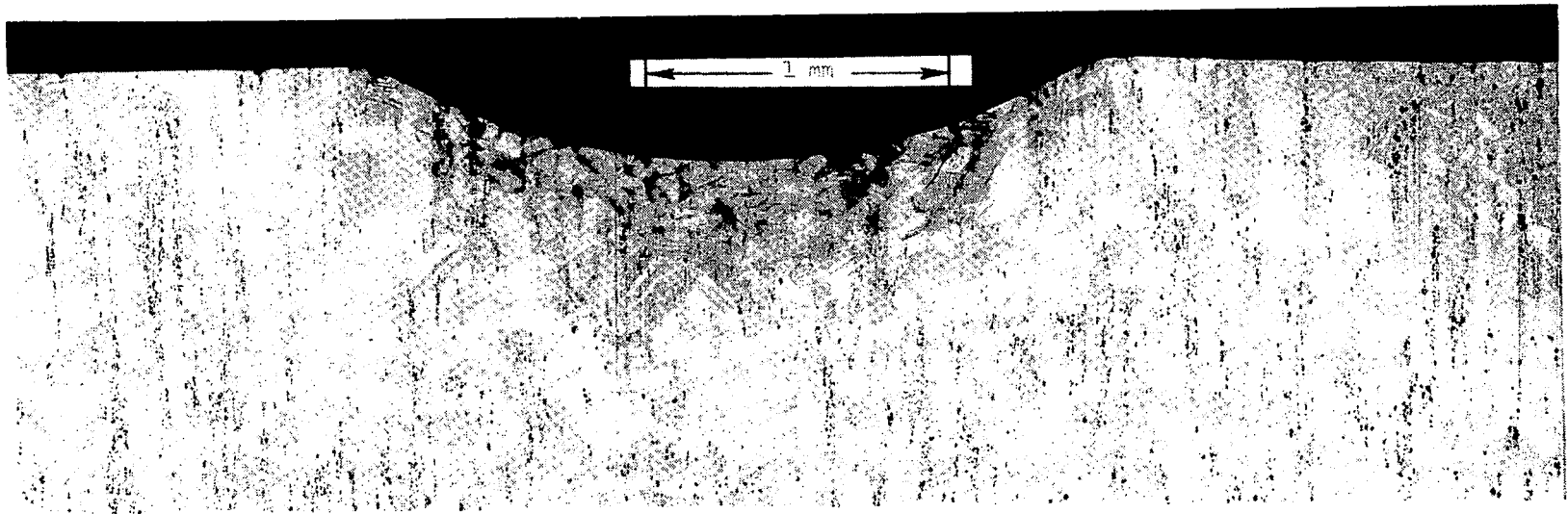
Figure 5.7. Zinc, Impact Velocity 17328 cm/sec.

crater was attacked during electro polishing with the result that the crater contour is no longer sharp. Comparison of the grain size in the metal around the crater with the grain size in the metal below the central part of the crater produced the information that the grains are of smaller size in the metal just below the crater. Reduction of grain size in zinc is produced as a result of machining; presumably the increase in temperature associated with the plastic flow produced in the machining process causes the metal to recrystallize in smaller grains. Although there is no clear evidence of plastic flow within the grains of zinc themselves, the change in grain size suggests that plastic flow did occur in zinc for impact of a 0.175-inch steel sphere at a velocity of 17328 cm/sec. This information was not obtained in the surface study discussed in Section 5.1 presumably because the zinc surface was not in a sufficiently high state of polish.

The cross section of the crater produced in Udimet-700-solutioned by impact of a 0.175-inch steel sphere at a velocity of 17182 cm/sec is shown in the micrograph of Figure 5.8. There is clear evidence of plastic flow in the metal below the surface of this crater; the metal grains are both distorted and striated with slip lines and/or twins. That plastic flow has occurred can also be seen in the displacement of the stringers of precipitate in the alloy immediately under the crater.

The cross section of the crater produced by impact of a 0.175-inch steel sphere against Udimet-700-aged at a velocity of 17153 cm/sec is shown in the micrograph of Figure 5.9. At first sight there appears to be no evidence of plastic flow in the metal below the crater shown in Figure 5.9. However, bending of the stringers of precipitate in the alloy under the bottom surface of the crater indicates that plastic flow has occurred; in addition, evidence of plastic flow in Udimet-700-aged was pointed out in Section 5.1. The fact that the stringers of precipitate appear to fan outward under the crater shown in Figure 5.9 suggests that there may have been some plastic flow in the radial direction.

From the evidence of plastic flow in the metal grains of Udimet-700-



Udimet 700 Solutioned, Impact Velocity 17182 cm/sec

Figure 5.8. Subsurface Microstructural Change in Udimet 700 Solutioned.



Udimet 700 Aged, Impact Velocity 17153 cm/sec

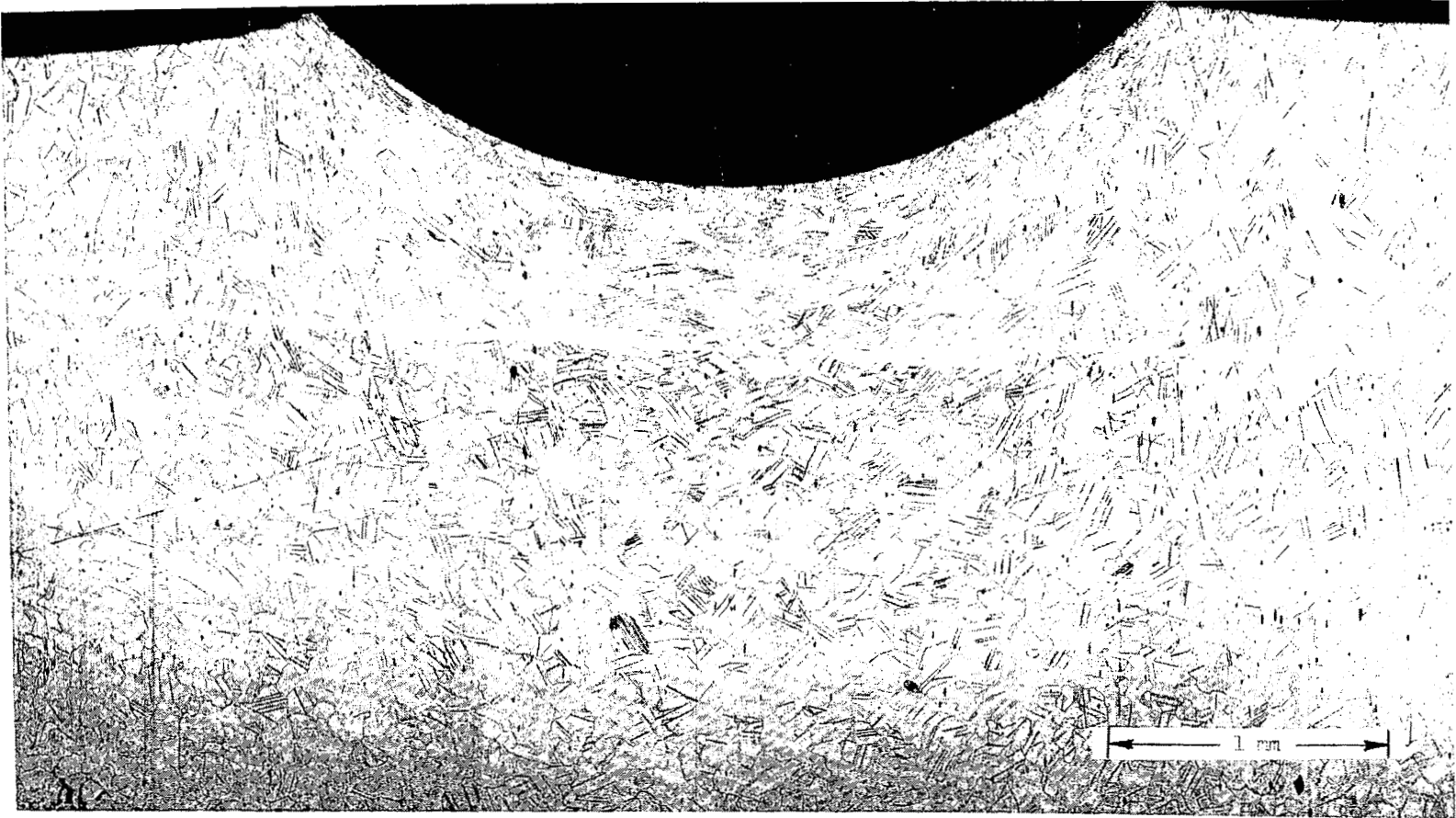
Figure 5.9. Subsurface Microstructural Change in Udimet 700 Aged.

solutioned in Figure 5.8 and from the distortion of the stringers of precipitate in Udimet-700-aged in Figure 5.9, it appears that plastic flow in the metal under the craters in Udimet 700 extends to a depth of only approximately one fourth of a crater diameter. Apparently, plastic flow does not extend to as great a depth below the crater in Udimet 700 as it does below the crater in nickel. The craters were produced by spheres of the same size at essentially the same velocity. This observation is in agreement with the difference in the yield strengths of these metals.

The cross section of the crater produced in Armco iron by impact of a 0.175-inch steel sphere at a velocity of 17036 cm/sec is shown in the micrograph of Figure 5.10. There is clear evidence of plastic flow to a depth of approximately one crater diameter below the surface of this crater and to a distance of roughly one half a crater diameter around the rim of the crater. It can also be seen that the surface of the metal is undulated at the rim of the crater which suggests that some plastic flow has occurred in the radial direction.

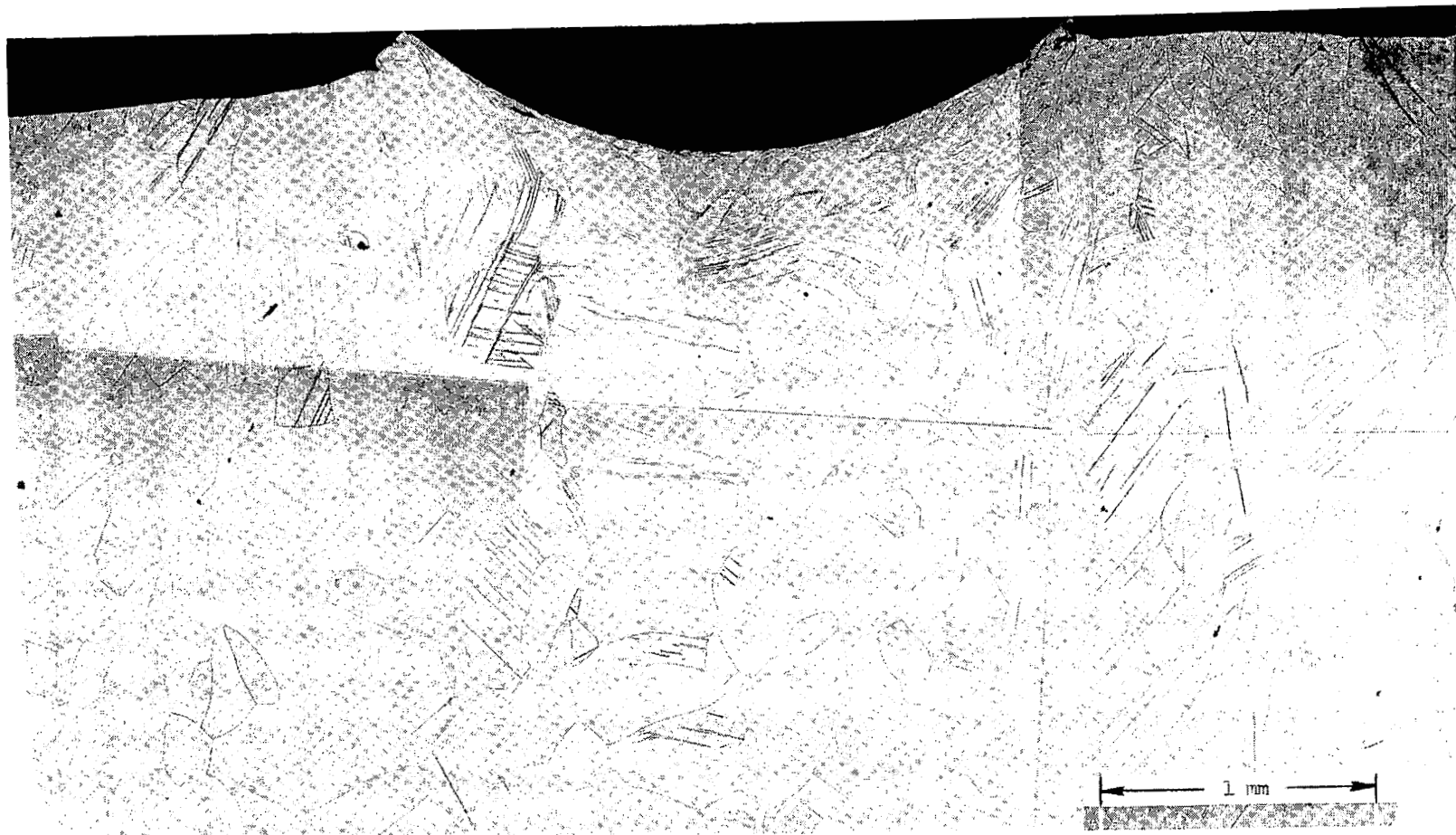
The cross section of the crater produced in tantalum by impact of a 0.175-inch steel sphere at a velocity of 17066 cm/sec is shown in the micrograph of Figure 5.11. In this micrograph also there is clear evidence of plastic flow in the metal grains to a depth of approximately one crater diameter and to a distance of roughly one half a crater diameter around the rim of the crater. It is interesting to note that the plastic flow does not appear to be continuous under the crater in tantalum at distances greater than half a crater diameter; in this respect the crater in tantalum differs from the crater formed in iron by impact of a steel sphere of the same size at essentially the same velocity.

From the standpoint of the moving-plug model of cratering, it is of special interest to note that grains which contain slip lines and/or twins extend downward from the rim of the crater in tantalum. This evidence of plastic flow at the periphery of the crater could mark the movement of the plug of metal under the crater with respect to the remaining metal of the specimen; the accumulation of more evidence from the



Iron, Impact Velocity 17036 cm/sec

Figure 5.10. Subsurface Microstructural Change in Iron.



Tantalum, Impact Velocity 17066 cm/sec

Figure 5.11. Subsurface Microstructural Change in Tantalum.

sectioning of a number of craters is needed to demonstrate that this observation is true in general. The positioning of the slip lines and/or twins and the appearance of surface undulations around the rim of the crater in tantalum shown in Figure 5.11 suggest that, as in the case of iron, some plastic flow has taken place in the radial direction.

To confirm the observations that have been pointed out in Figures 5.5 through 5.11, a micrograph at high magnification was made of the metal immediately below the bottom of the crater in each of the cross-sectional cuts. These micrographs are shown in Figures 5.12 through 5.15.

The micrographs in Figure 5.12 confirm the observations made with regard to nickel. There is no clear evidence of plastic flow in the nickel grains under the crater produced at an impact velocity of 3342 cm/sec. However, for the crater produced at an impact velocity of 17465 cm/sec, the grains of nickel immediately under the crater are flattened out perpendicular to the direction of impact.

The micrographs in Figure 5.13 confirm the observations made with regard to zinc. The grains of metal at the bottom of the crater are smaller than those of the zinc in its as-received condition. From the micrograph of the zinc in its as-received condition, it can be seen that twins existed in the metal prior to the impact of the steel sphere. Recrystallization due to heating as a result of the impact has removed the twins from the metal immediately under the impact crater.

The micrographs in Figure 5.14 confirm the observations made with regard to Udimet 700. Plastic flow has occurred in both solutioned and in aged Udimet 700 because for each of these heat-treatment states the grains of the metal immediately under the crater are striated with slip lines and/or twins. The striations on the grains of aged Udimet 700 are finer in texture than those on the grains of solutioned Udimet 700; this explains why they were not visible at low magnification.

The micrographs in Figure 5.15 confirm the observations made with regard to tantalum and iron. That plastic flow occurred in the metal

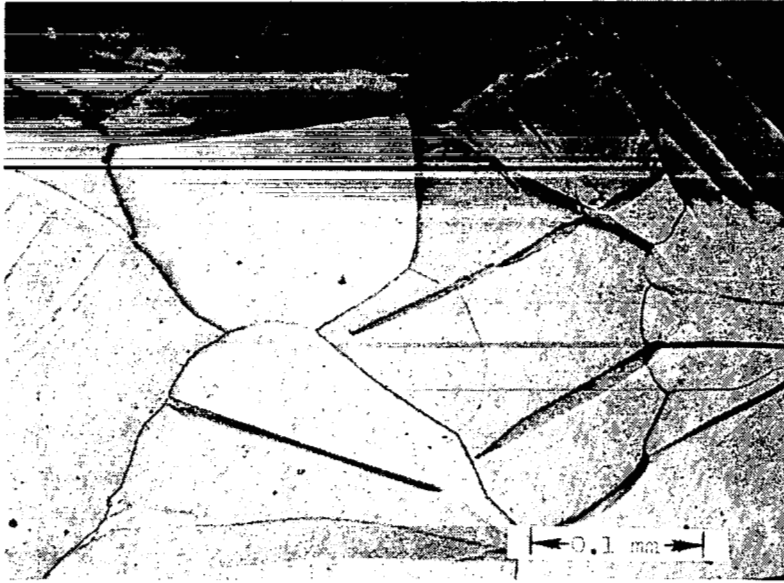


Nickel, Impact Velocity 3342 cm/sec



Nickel, Impact Velocity 17465 cm/sec

Figure 5.12. Microstructure of Nickel at the Bottom of the Crater.



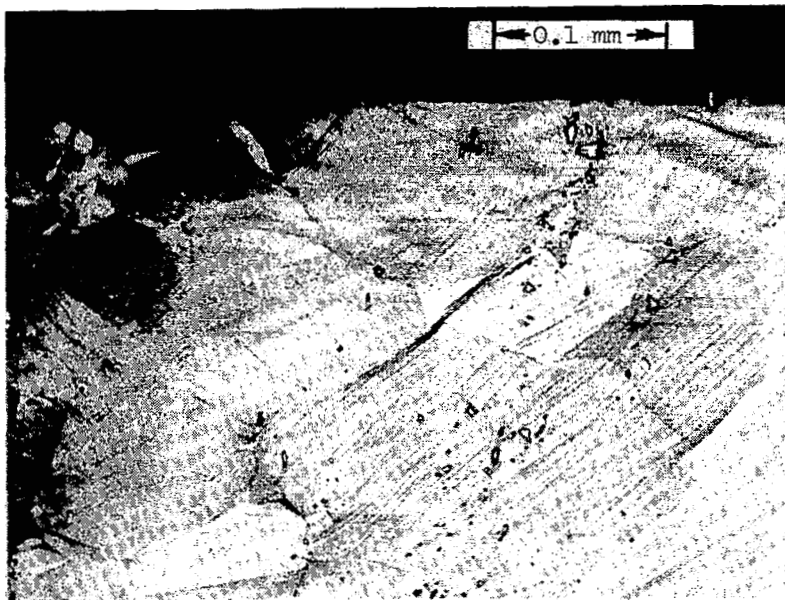
In the As-Received Condition



At the Bottom of the Crater

Impact Velocity, 17328 cm/sec

Figure 5.13. Change in the Microstructure of Zinc.

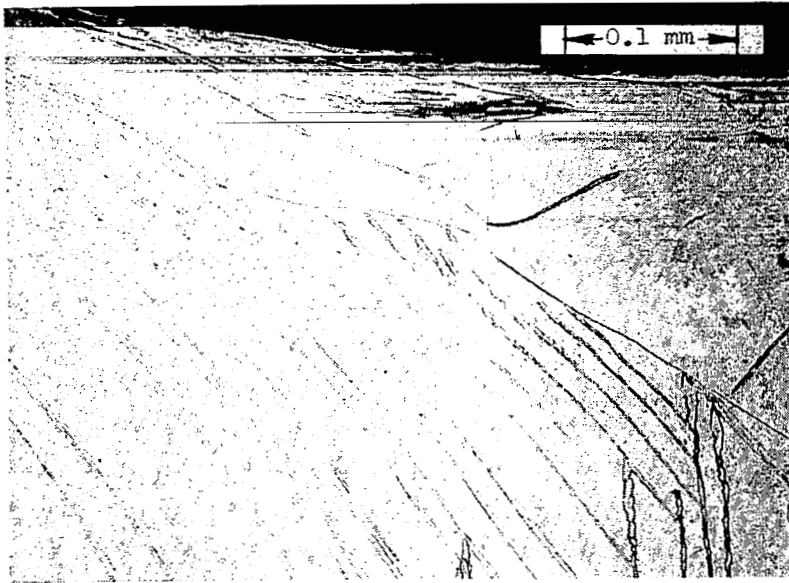


Udimet 700 Solutioned, Impact Velocity 17182 cm/sec



Udimet 700 Aged, Impact Velocity 17153 cm/sec

Figure 5.14. Microstructure of Udimet 700 at the Bottom of the Crater.



Tantalum, Impact Velocity 17066 cm/sec



Iron, Impact Velocity 17036 cm/sec

Figure 5.15. Microstructure of Tantalum and Iron at the Bottom of the Crater.

under the craters produced in each of these metals is substantiated by the clearly discernible slip lines and/or twins and by the fact that the grains close to the bottom of the crater are flattened out perpendicular to the direction of impact.

5.3 Information From Stress-Strain Behavior

Stress-strain behavior has been pointed out as an area of uncertainty with regard to the moving-plug model of cratering on which eqs (1.1) and (1.3) are based (see Section 1.5.2). The tensile properties of the six selected metals were determined for the heat-treatment states in which these metals were used as impact test plates (see Section 4.4) and copies of the autographic recording of the tests were obtained.

For each of the pure metals except nickel, at least one stress-strain curve was available for which the autographic recording had been carried as far as 0.004 inch per inch offset; in the case of nickel the stress-strain curves were in no case recorded beyond 0.003 inch per inch offset. The 0.2 and 0.4 percent offset yield strengths, the slopes of the stress-strain curves at these points, and the percentage change of these quantities are given in Table 5.1. Data for the 1100-0 aluminum that was used in an earlier study [7] are also given. In the case of Udimet 700 alloy, the extensometer was removed shortly after 0.002 inch per inch offset was reached. The data given for Udimet 700 in Table 5.1 were obtained from stress-strain curves⁽²²⁾ for a different heat of Udimet 700; the shapes of these stress-strain curves are similar to those of the curves obtained for the heat of Udimet 700 from which the impact test plates were made.

From the data of Table 5.1, it can be seen that for aluminum, nickel, and zinc the 0.4 percent offset yield strength is substantially higher than the 0.2 percent offset yield strength and that the slopes of the stress-strain curves at these points show little if any change. On the

(22) These curves were supplied on request by the Special Metals Corporation, New Hartford, New York.

TABLE 5.1 STRESS-STRAIN BEHAVIOR OF THE SELECTED METALS							
METAL QUANTITY	1100-0 ALUMINUM	NICKEL 270	PURE ZINC	UDIMET 700 SOLUTIONED	UDIMET 700 AGED	TANTALUM	ARMCO IRON
0.2 PERCENT OFFSET YIELD STRENGTH, psi	2,614	4,970	6,556	132,048	134,993	28,698	20,450
0.4 PERCENT OFFSET YIELD STRENGTH, psi	3,242	^a 5,805	7,730	135,484	138,675	22,584	19,335
CHANGE IN YIELD STRENGTH, percent	24.0	16.8	17.9	2.6	2.7	21.3	5.5
$d\sigma/d\epsilon$ AT 0.2 PER- CENT OFFSET, psi	414,000	895,000	735,000	2,455,000	2,455,000	-3,452,500	-1,222,500
$d\sigma/d\epsilon$ AT 0.4 PER- CENT OFFSET, psi	415,000	895,000	735,000	920,000	1,227,500	-1,332,500	147,500
CHANGE IN $d\sigma/d\epsilon$, percent	0.24	no change	no change	62.5	50	61	112

^a This value is the 0.3 percent offset yield strength. The extensometer was removed in every case for the four specimens that were pulled before the 0.4 percent offset yield point was reached.

basis of their stress-strain behavior, it can be expected that the impact behavior of these metals should be similar. It is known from an earlier study [7] that the crater-depth-versus-velocity plot for 1100-0 aluminum is a straight line and that, for the three sizes of steel spheres for which cratering data have been tabulated [7], the straight line is in every case given quite well by eqs (1.1) and (1.3) when the numerical coefficients for these equations are taken to be 17.5 and unity, respectively (see Section 1.4.1). On the basis of stress-strain behavior, it can be expected that the crater-depth-versus-velocity plots for nickel and zinc should also be found to be straight lines and that these straight lines should be given by eqs (1.1) and (1.3).

In the case of Udimet 700 both in the solutioned and in the aged condition, it can be seen from Table 5.1 that there is very little difference between the 0.2 and the 0.4 percent offset yield strengths. In addition, it can be seen that there is a decrease of 50 percent or more in the slopes of the stress-strain curves at 0.002 and 0.004 inch per inch offset. This stress-strain behavior is quite different from that of aluminum, nickel, and zinc. It may presage an approach to zero slope, which occurs before a sharp yield point, and may have a similar effect on the applicability of the moving-plug model of cratering (see Section 1.5.2). On the basis of its stress-strain behavior, it can be anticipated that the crater-depth-versus-velocity plot for Udimet 700 alloy may differ from that of the pure face-centered-cubic metals.

In the case of tantalum and iron, the 0.4 percent offset yield strength is lower than the 0.2 percent offset yield strength. The slopes of the stress-strain curves of both tantalum and iron are negative at 0.002 inch per inch offset; both of these metals display a sharp yield point. On the basis of this type of stress-strain behavior, it can be anticipated that the crater-depth-versus-velocity plots of both tantalum and iron may display a noticeable curvature or a change in slope (see Section 1.5.2).

Stress-strain curves of the seven selected metals are shown in Figures 5.16, 5.17, 5.18 and 5.19. The curves shown in these figures were selected as being representative; the curve for each metal is not in every case the same as the curve from which the data presented in Table 5.1 were obtained.

5.4 Information on Work-hardening Produced by the Impacts

Plastic flow in a metal is accompanied by work-hardening. It should, therefore, be possible to estimate the extent and the intensity or degree to which plastic flow occurred around the craters shown in Figures 5.5 through 5.11 by making Knoop microhardness determinations around the craters. The hardness analysis was restricted to a determination of hardness profiles in two directions. One series of Knoop microhardness determinations was made in a line extending into the metal below the bottom of the crater; a second series of Knoop microhardness determinations was made in a line extending into the metal outward from the crater side⁽²³⁾. The hardness values that were obtained are plotted against distance measured from the crater bottom and crater side (or center), respectively, in Figures 5.20 (a) and (b) through 5.27 (a) and (b).

It was considered essential that the line of hardness determinations made from the side of the crater be taken well below the surface of the specimen to avoid the interfering effect of surface hardness due to polishing. For all the metals except zinc, the depth below the surface was 10 mils. For zinc it was necessary to take the hardness readings at a distance of 20 mils below the surface because the loss of metal from the specimen cross section during electropolishing made it impossible to impress the hardness indenter at a distance of 10 mils below the surface without interference from the plastic material in which the specimen cross section was embedded.

(23) The hardness determinations were made by Mr. L. B. Engel and Mr. William Bohle, General Electric Company, Evendale, Ohio.

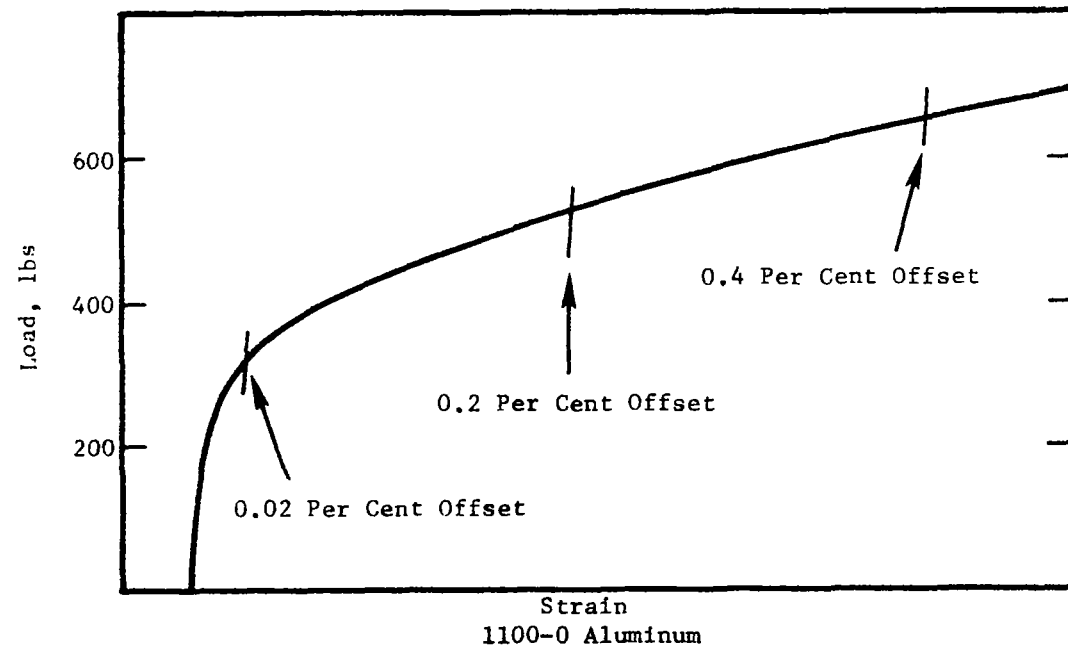
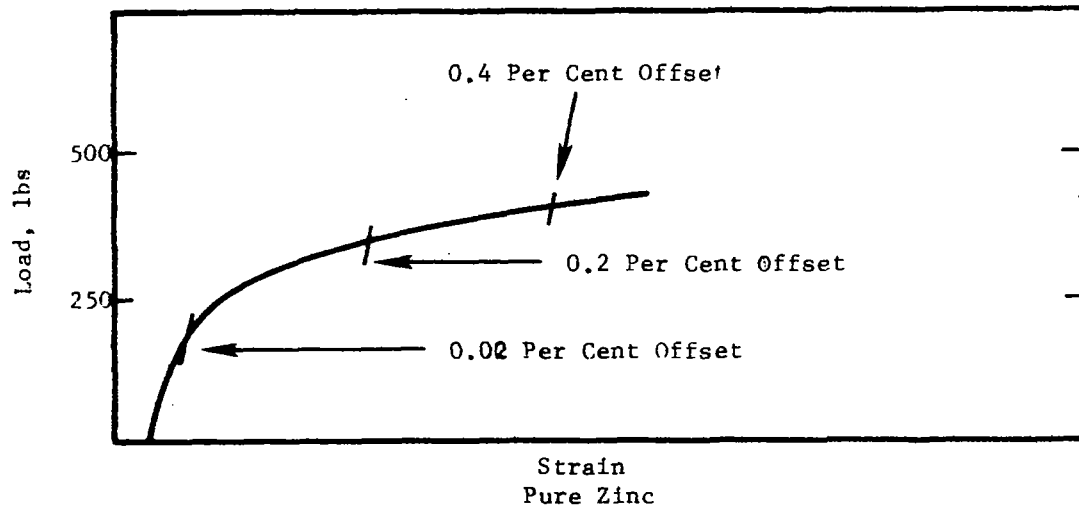
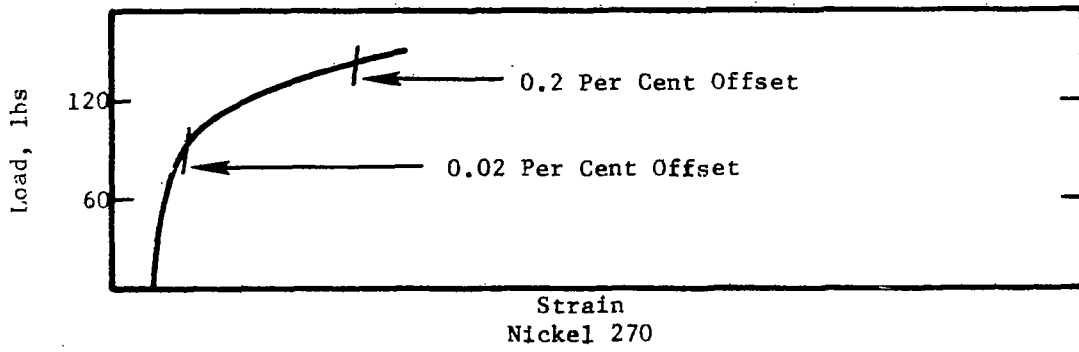
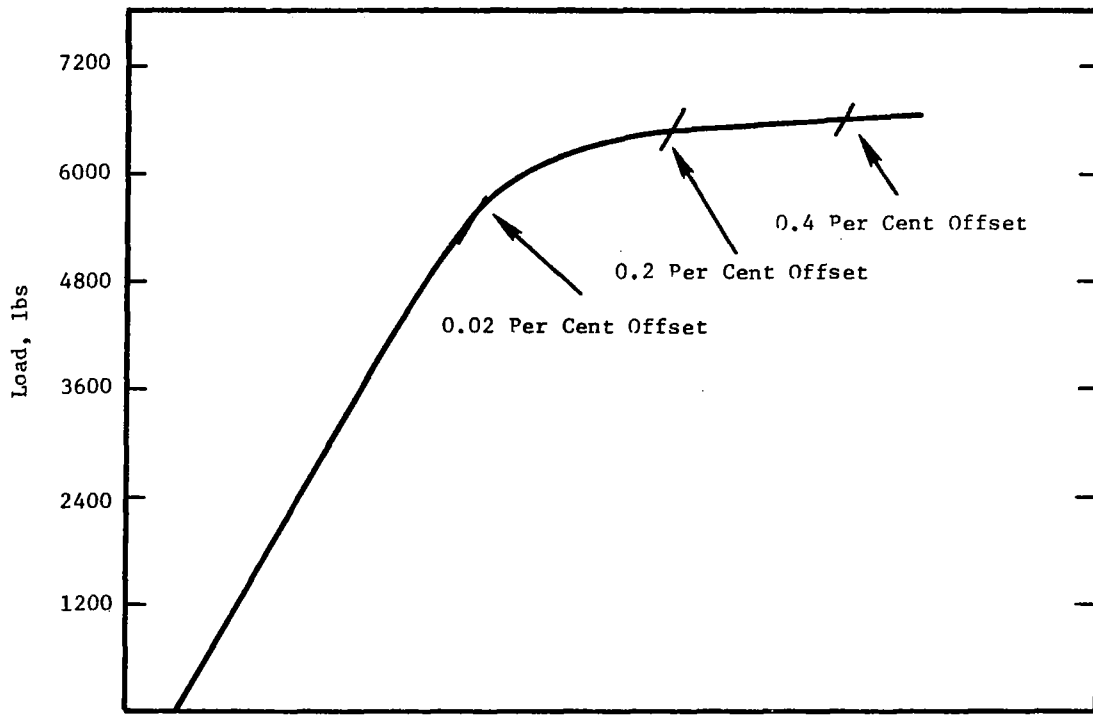
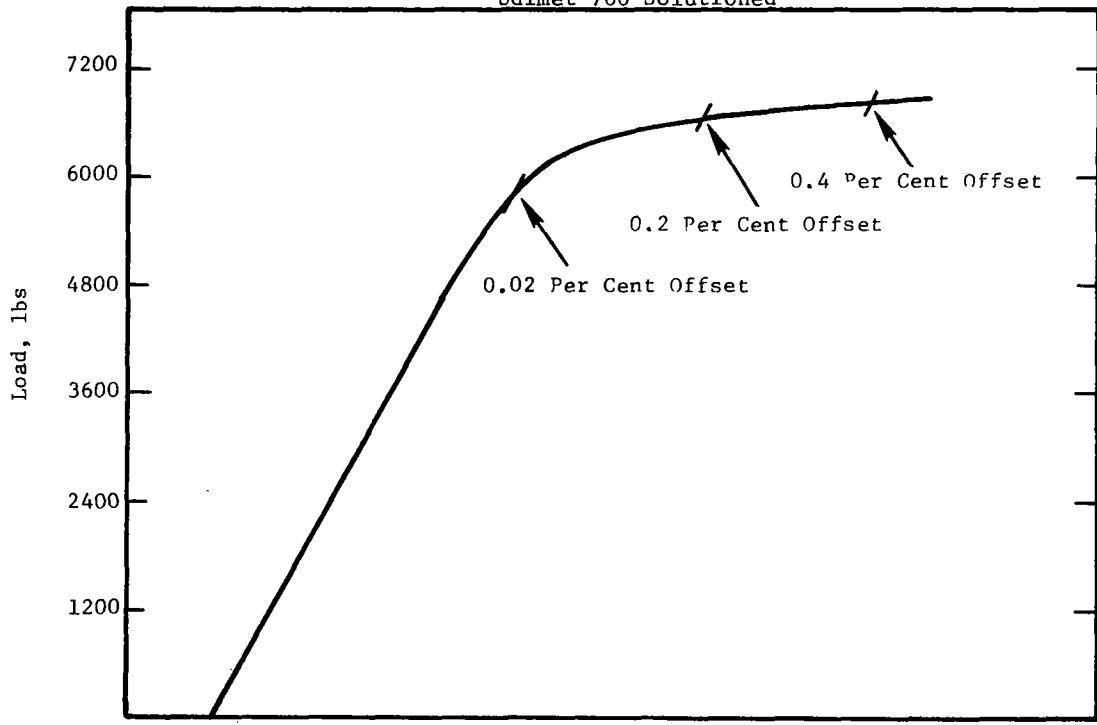


Figure 5.16. Stress-Strain Curves for Nickel, Zinc, and Aluminum.



Strain
Udimet 700 Solved



Strain
Udimet 700 Aged

Figure 5.17. Stress-Strain Curves for Udimet 700 in Two Heat-Treatment States.

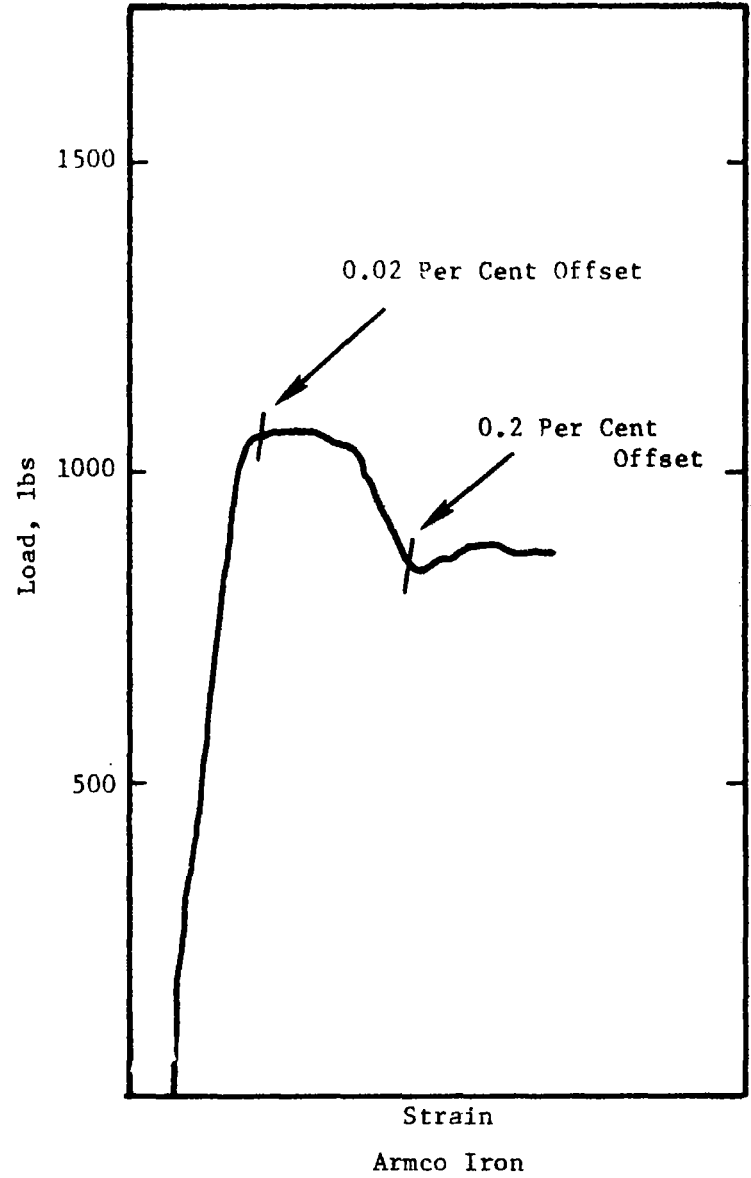
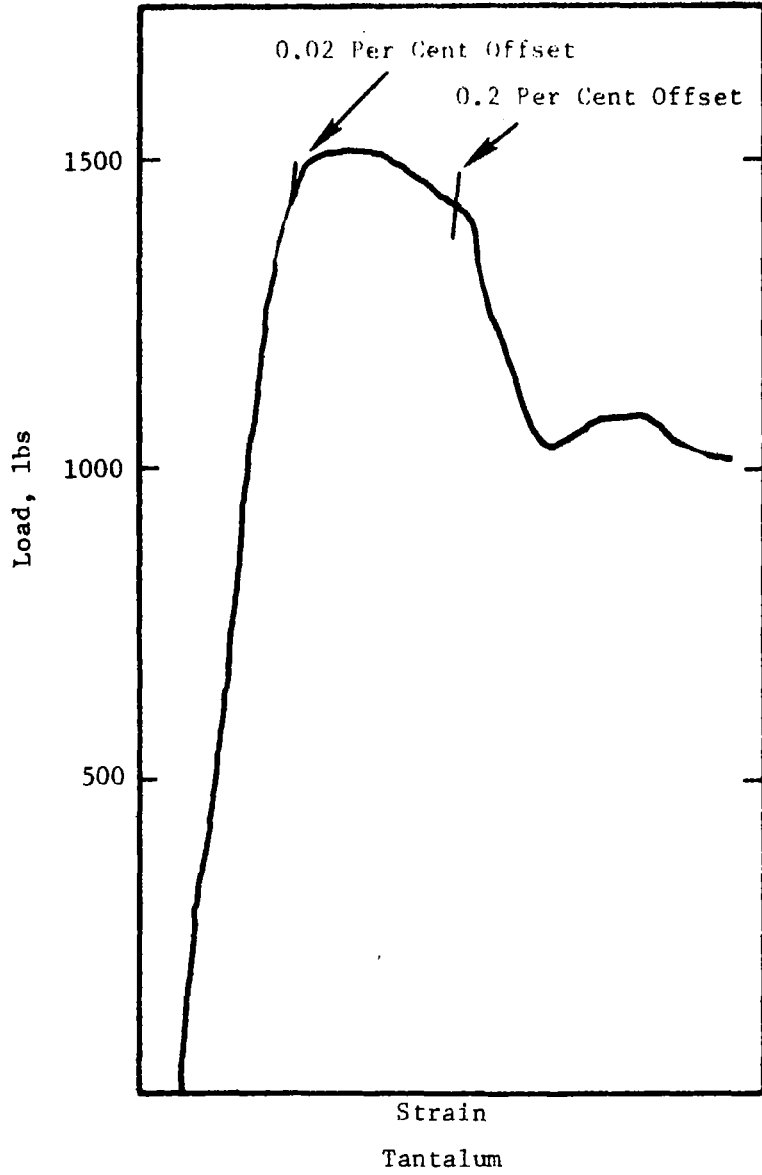


Figure 5.18. Stress-Strain Curves for Tantalum and Iron.

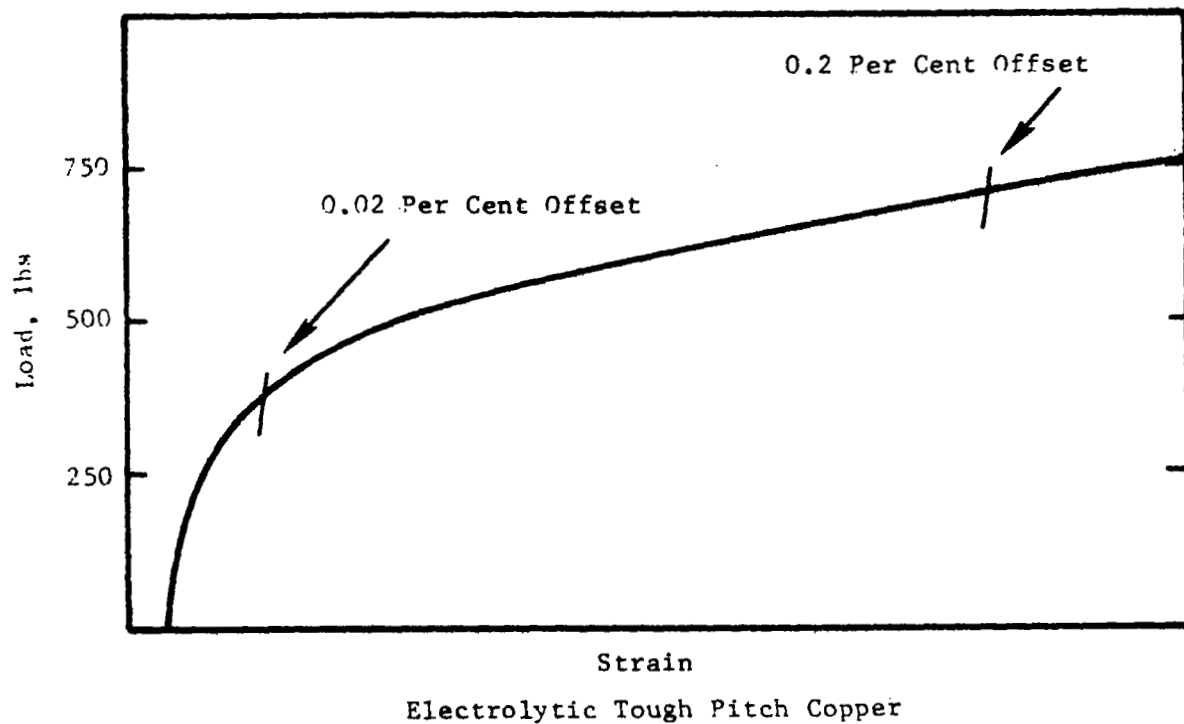


Figure 5.19. Stress-Strain Curve for Electrolytic Tough Pitch Copper.

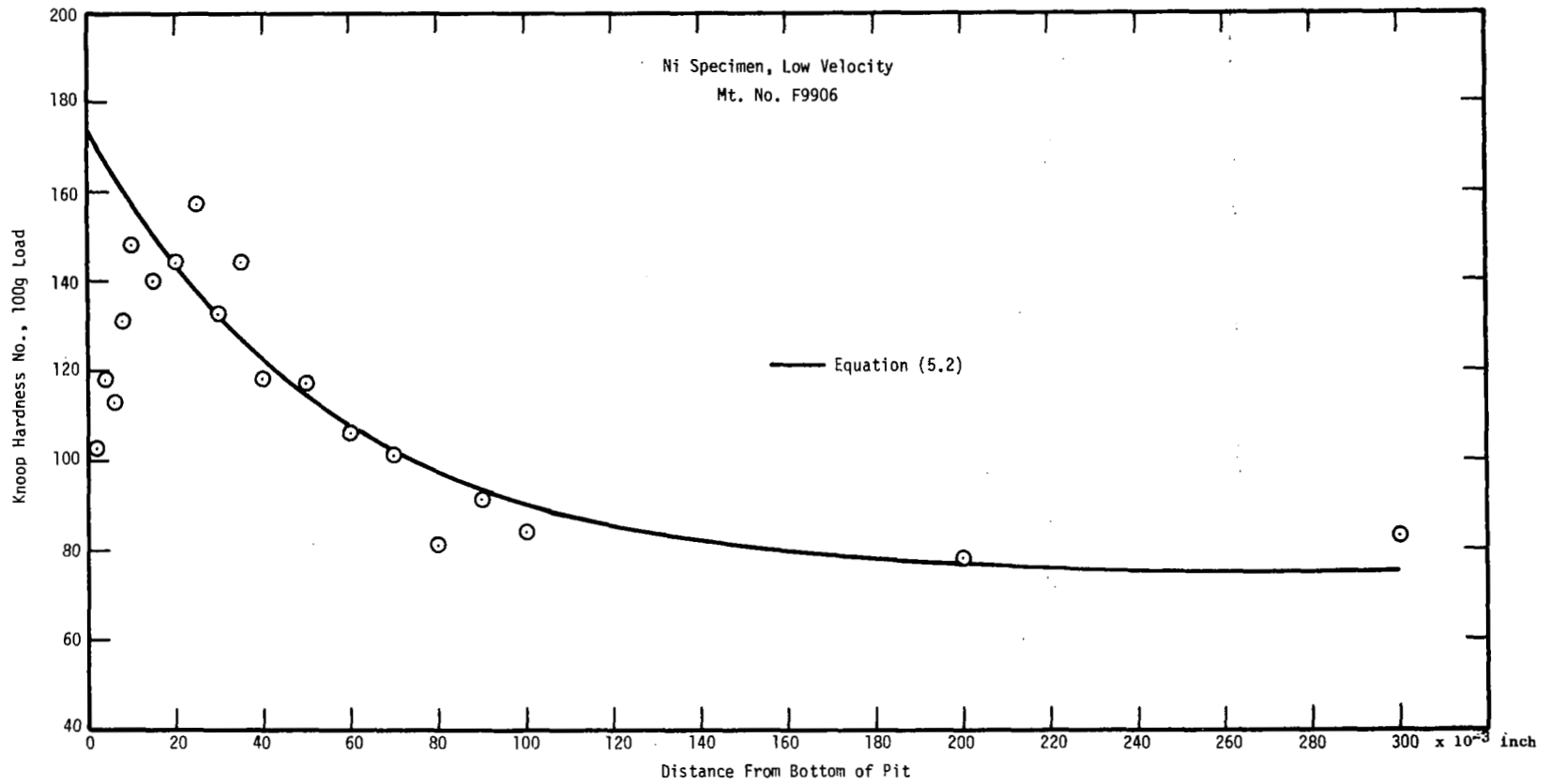


Figure 5.20a. Hardness Numbers Below a Crater Produced in Nickel. Impact Velocity 3342 cm/sec.

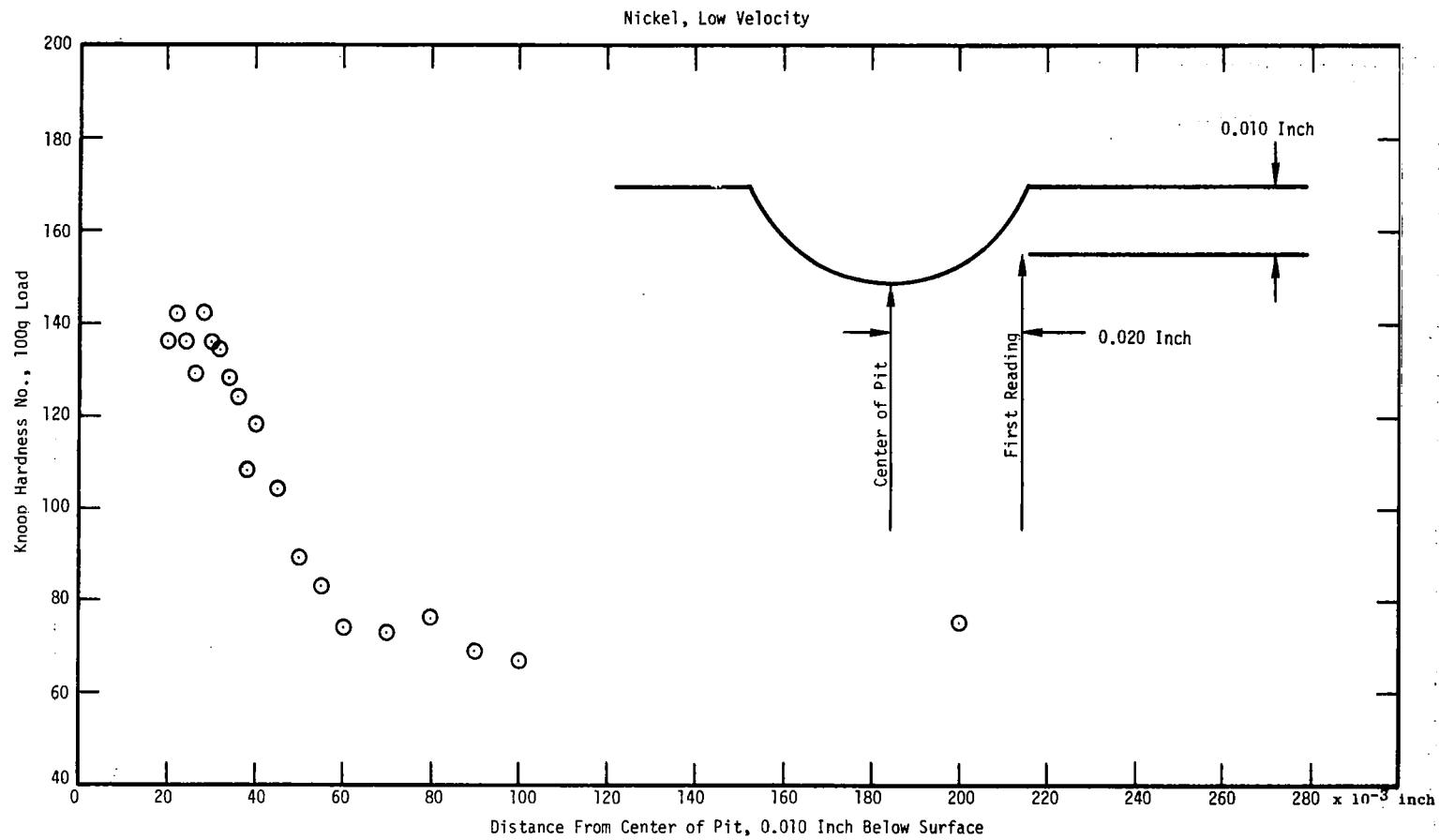


Figure 5.20b. Hardness Numbers Around a Crater Produced in Nickel. Impact Velocity 3342 cm/sec.

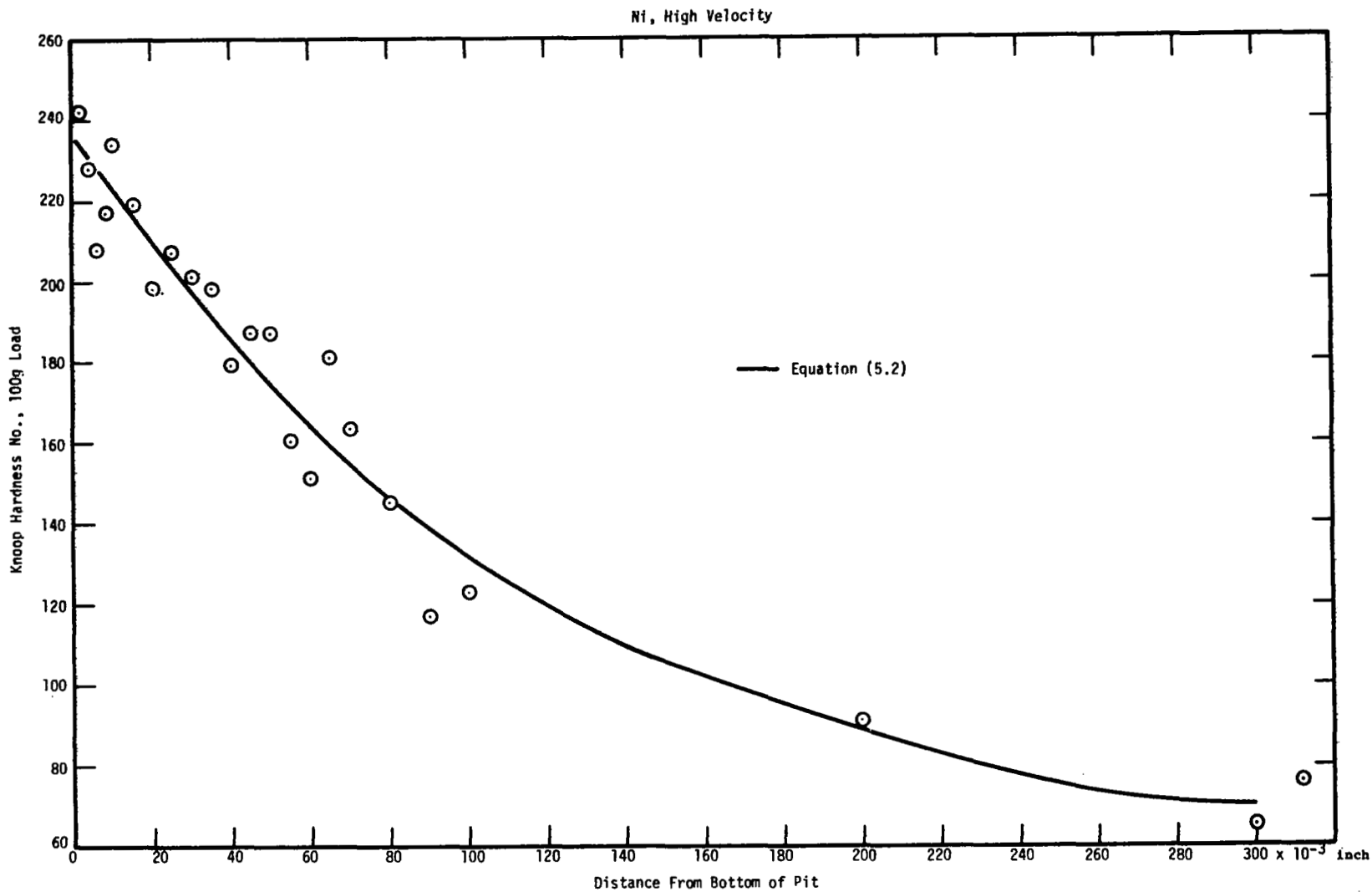


Figure 5.21a. Hardness Numbers Below a Crater Produced in Nickel. Impact Velocity 17465 cm/sec.

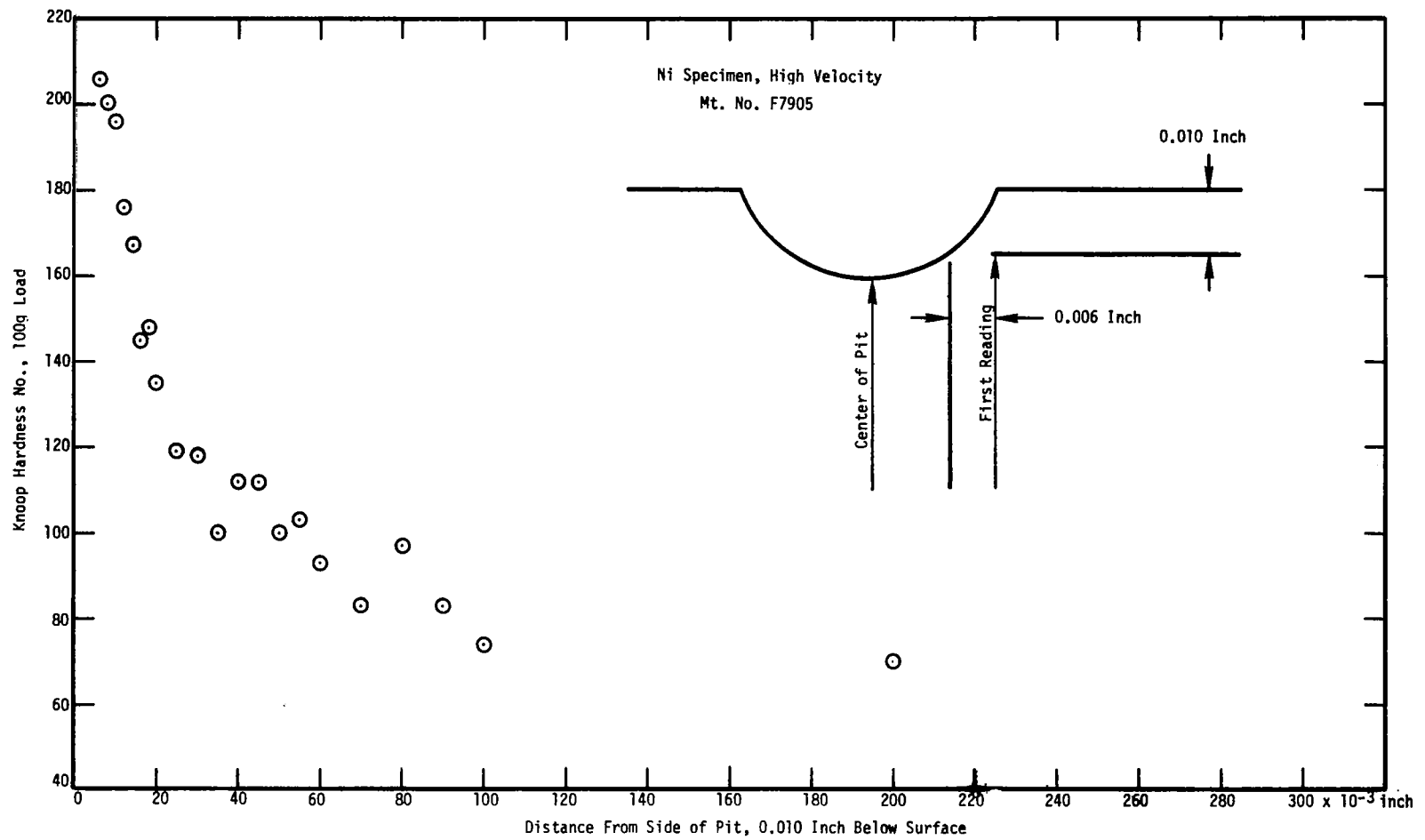


Figure 5.21b. Hardness Numbers Around a Crater Produced in Nickel. Impact Velocity 17465 cm/sec.

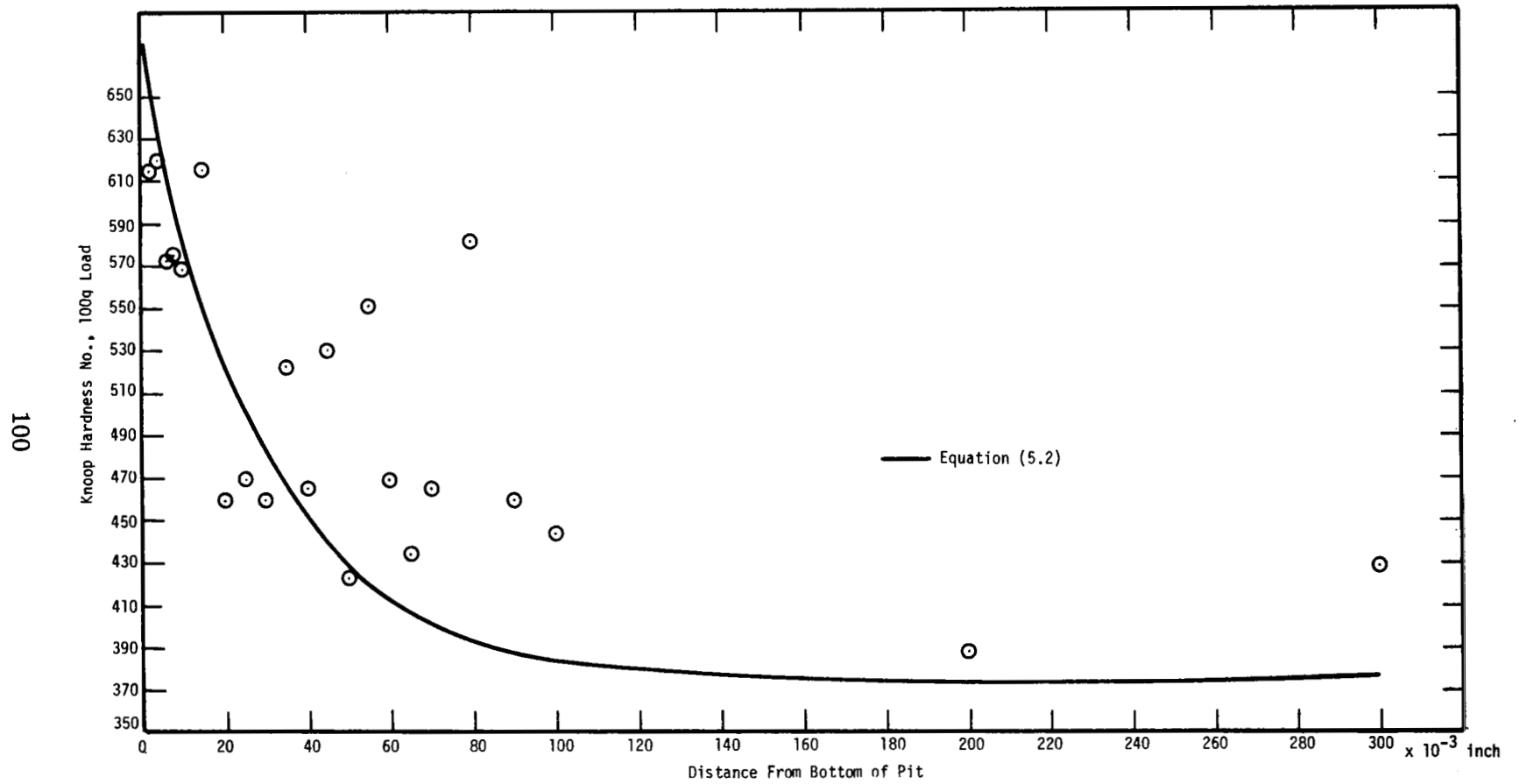


Figure 5.22a. Hardness Numbers Below a Crater Produced in Aged Udimet 700. Impact Velocity 17153 cm/sec.

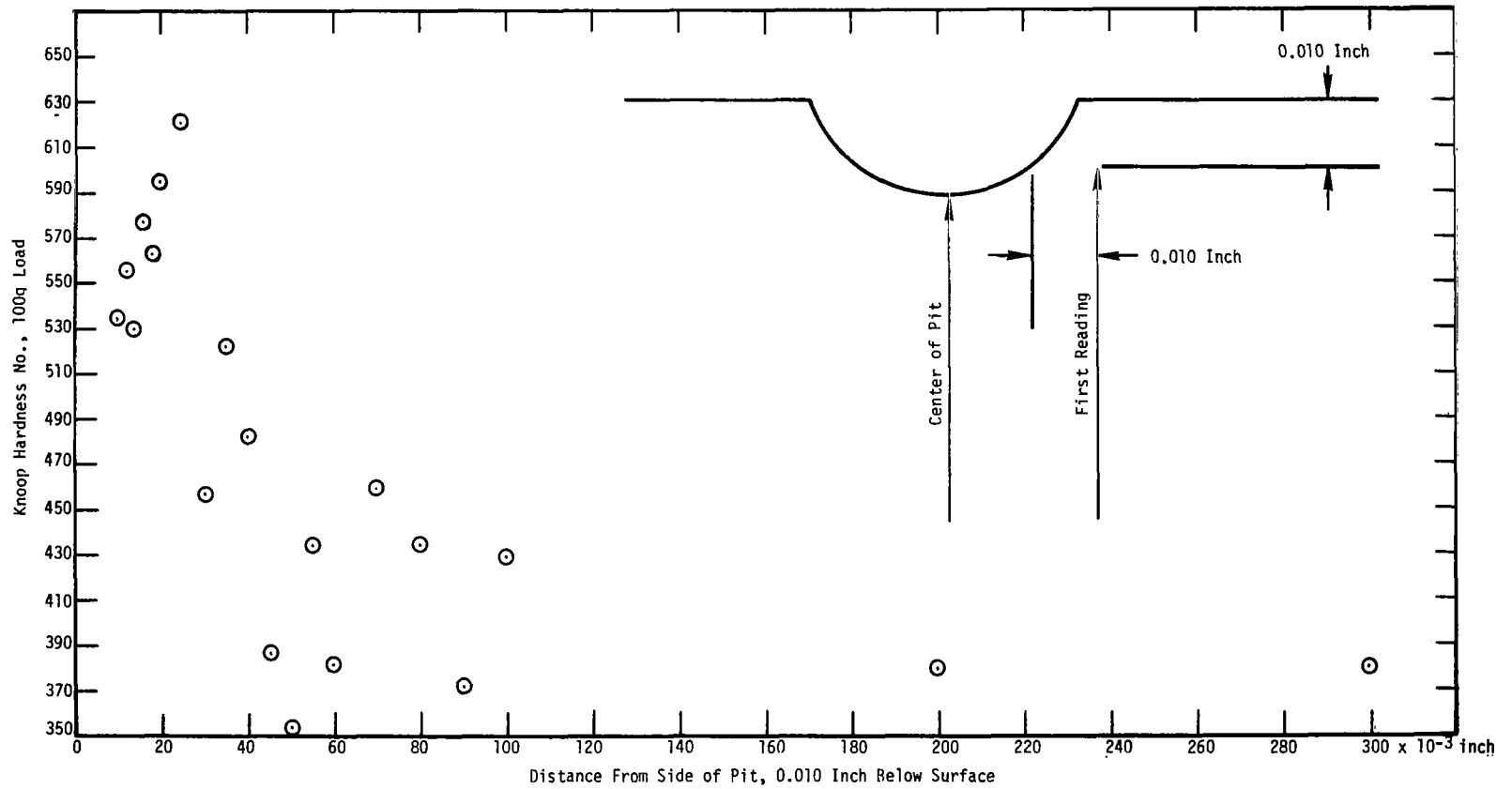


Figure 5.22b. Hardness Numbers Around a Crater Produced in Aged Udimet 700. Impact Velocity 17153 cm/sec.

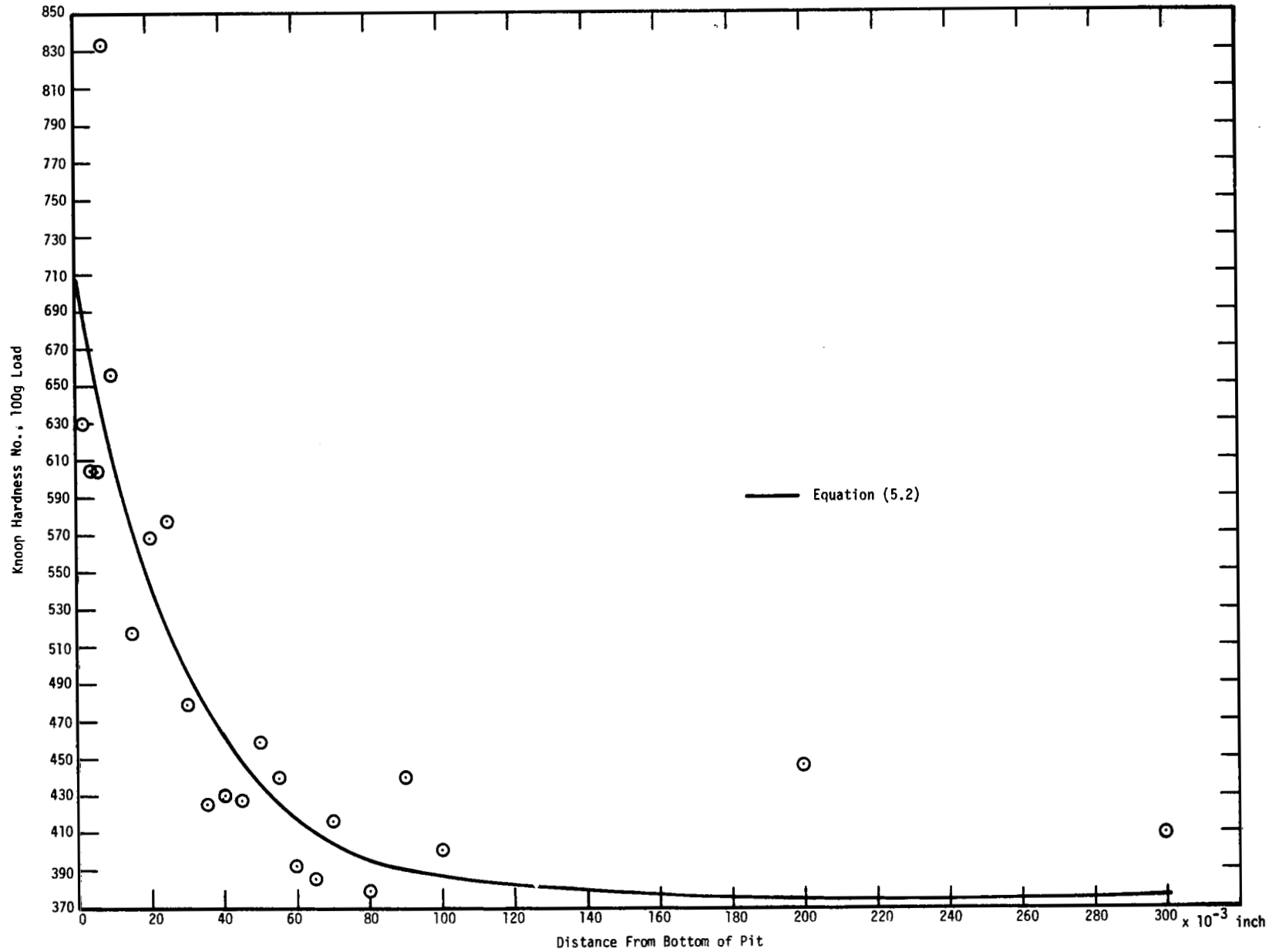


Figure 5.23a. Hardness Numbers Below a Crater Produced in Solved Udimet 700. Impact Velocity 17182 cm/sec.

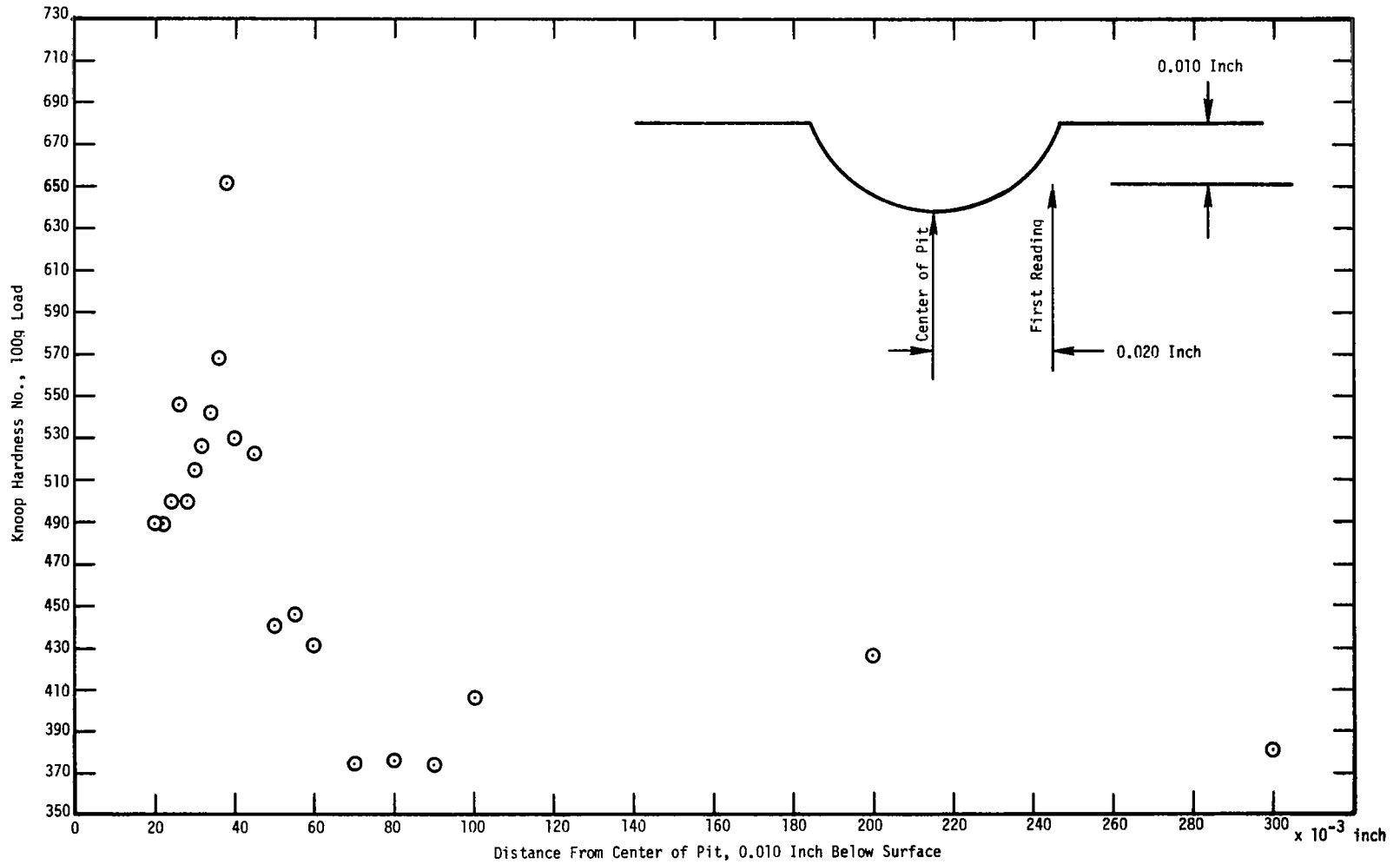


Figure 5.23b. Hardness Numbers Around a Crater Produced in Solutioned Udimet 700. Impact Velocity 17182 cm/sec.

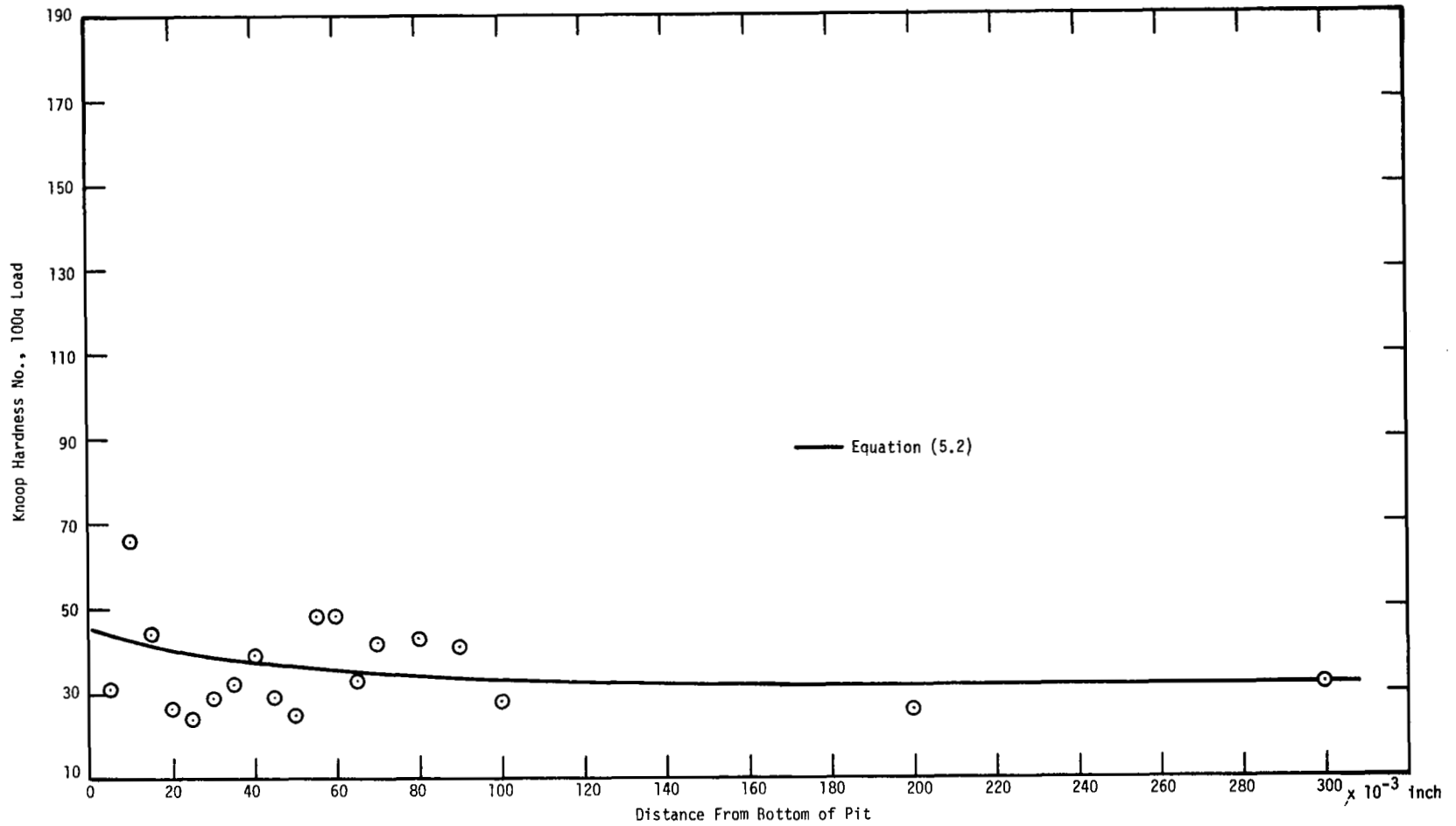


Figure 5.24a. Hardness Numbers Below a Crater Produced in Zinc. Impact Velocity 17328 cm/sec.

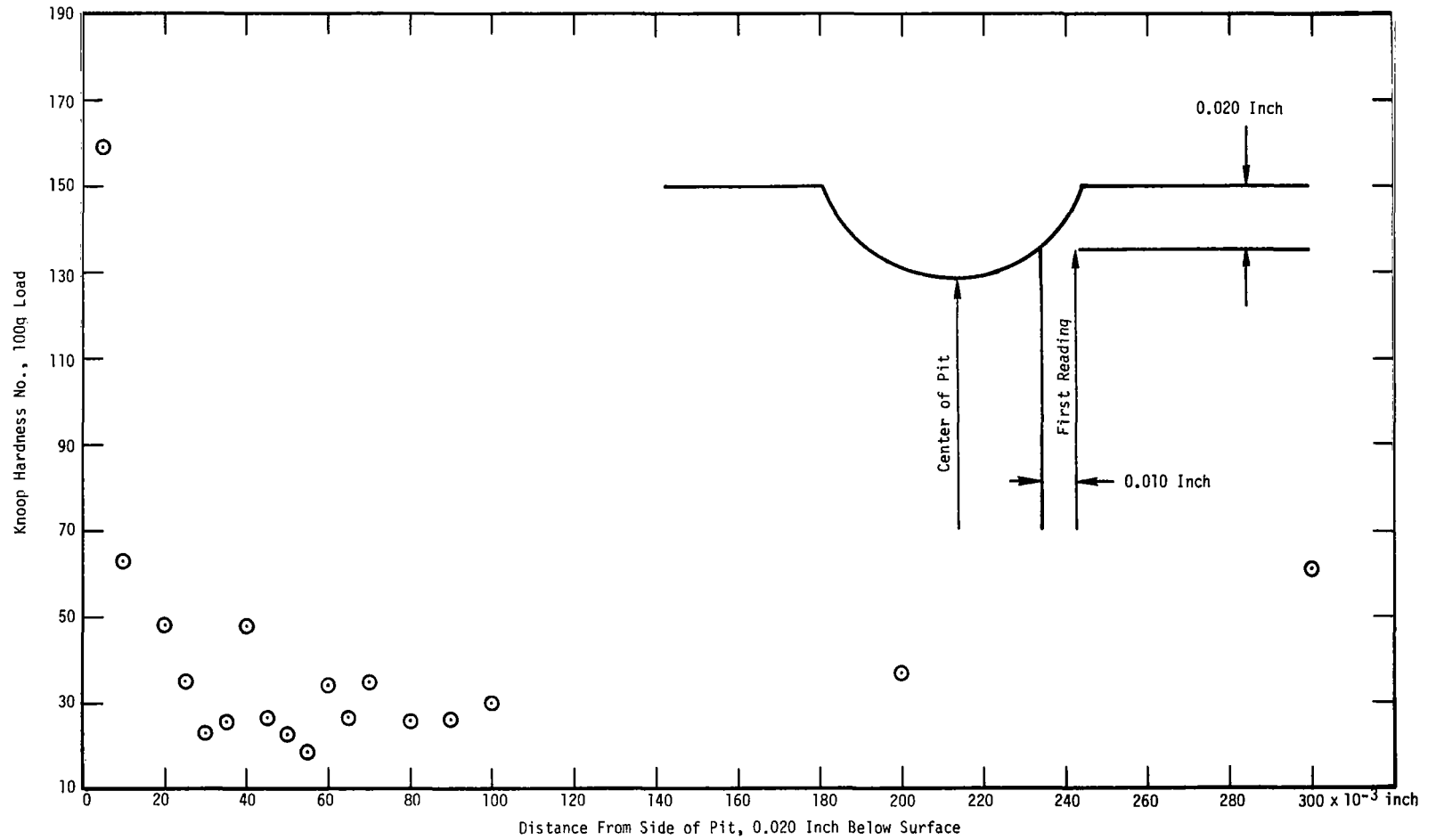


Figure 5.24b. Hardness Numbers Around a Crater Produced in Zinc. Impact Velocity 17328 cm/sec.

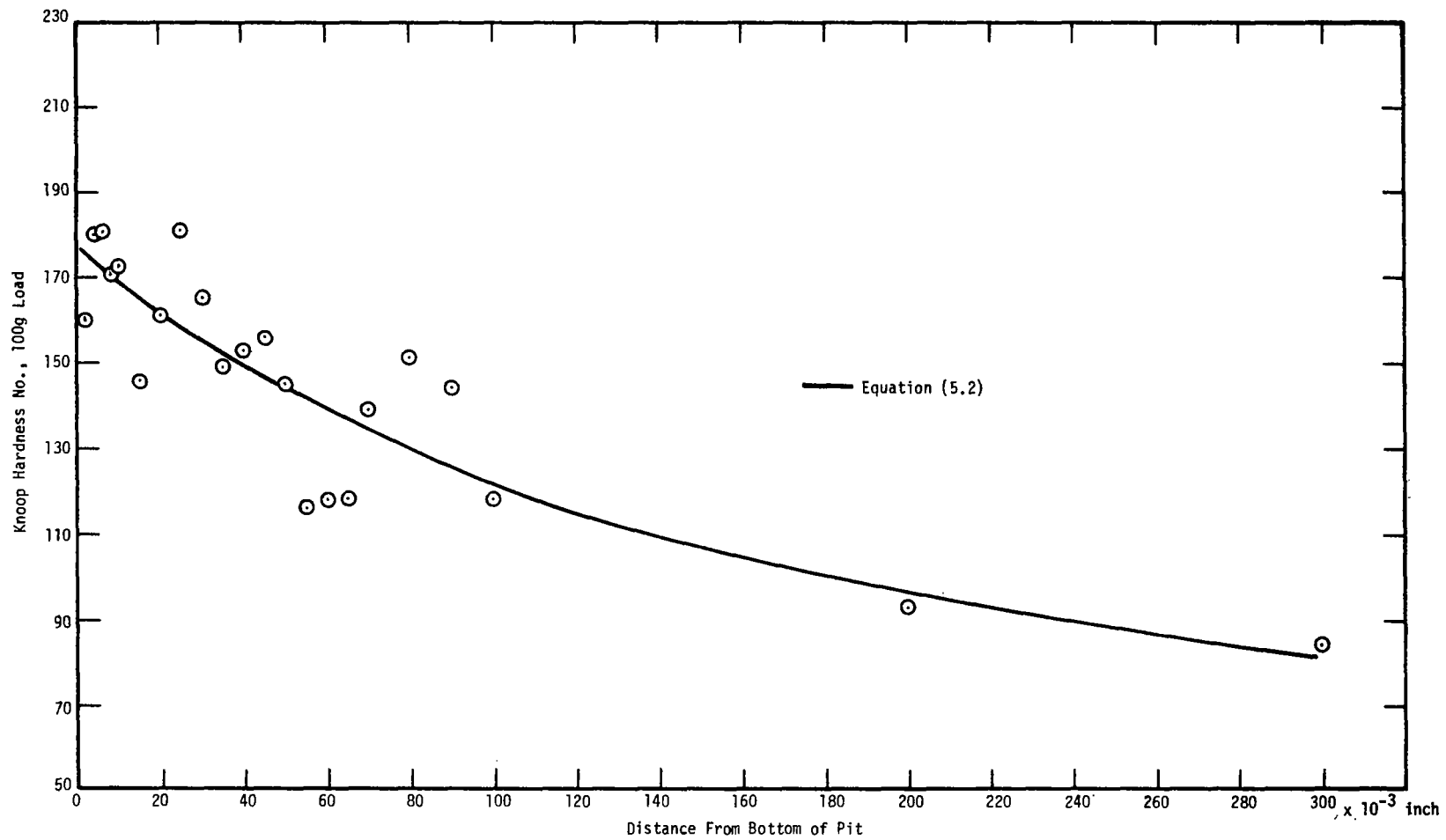


Figure 5.25a. Hardness Numbers Below a Crater Produced in Iron. Impact Velocity 17036 cm/sec.

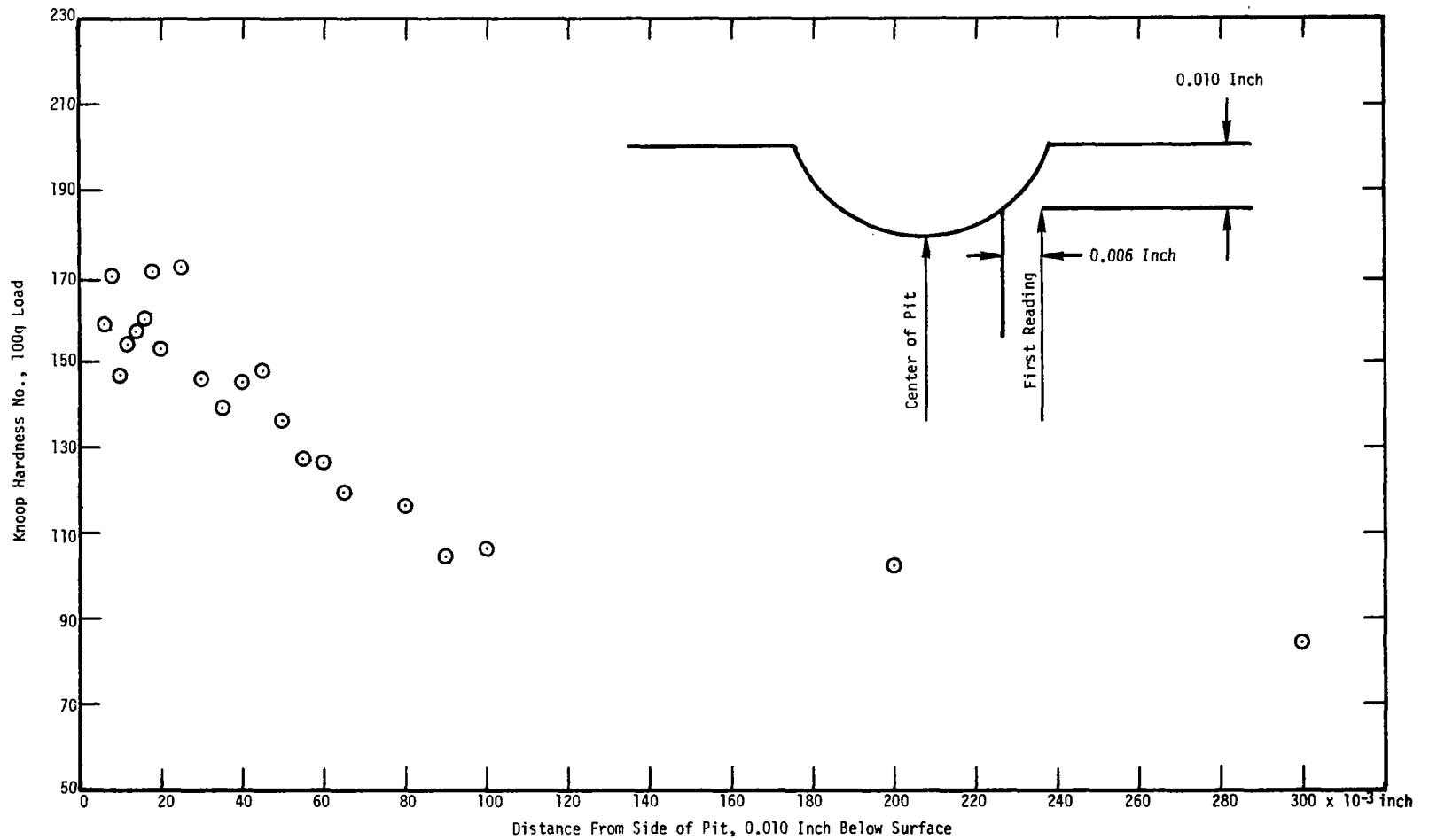


Figure 5.25b. Hardness Numbers Around a Crater Produced in Iron. Impact Velocity 17036 cm/sec.

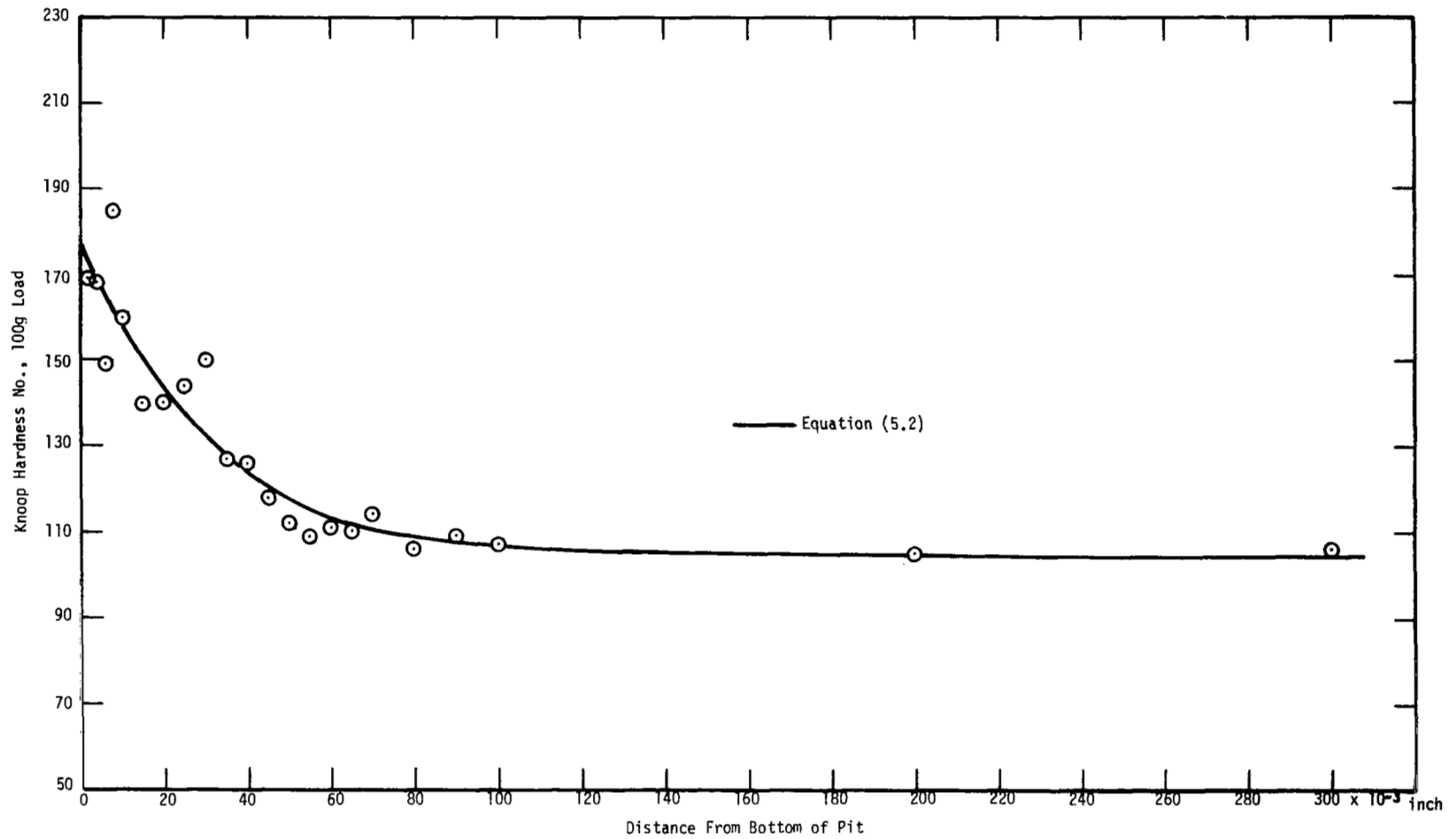


Figure 5.26a. Hardness Numbers Below a Crater Produced in Tantalum. Impact Velocity 17066 cm/sec.

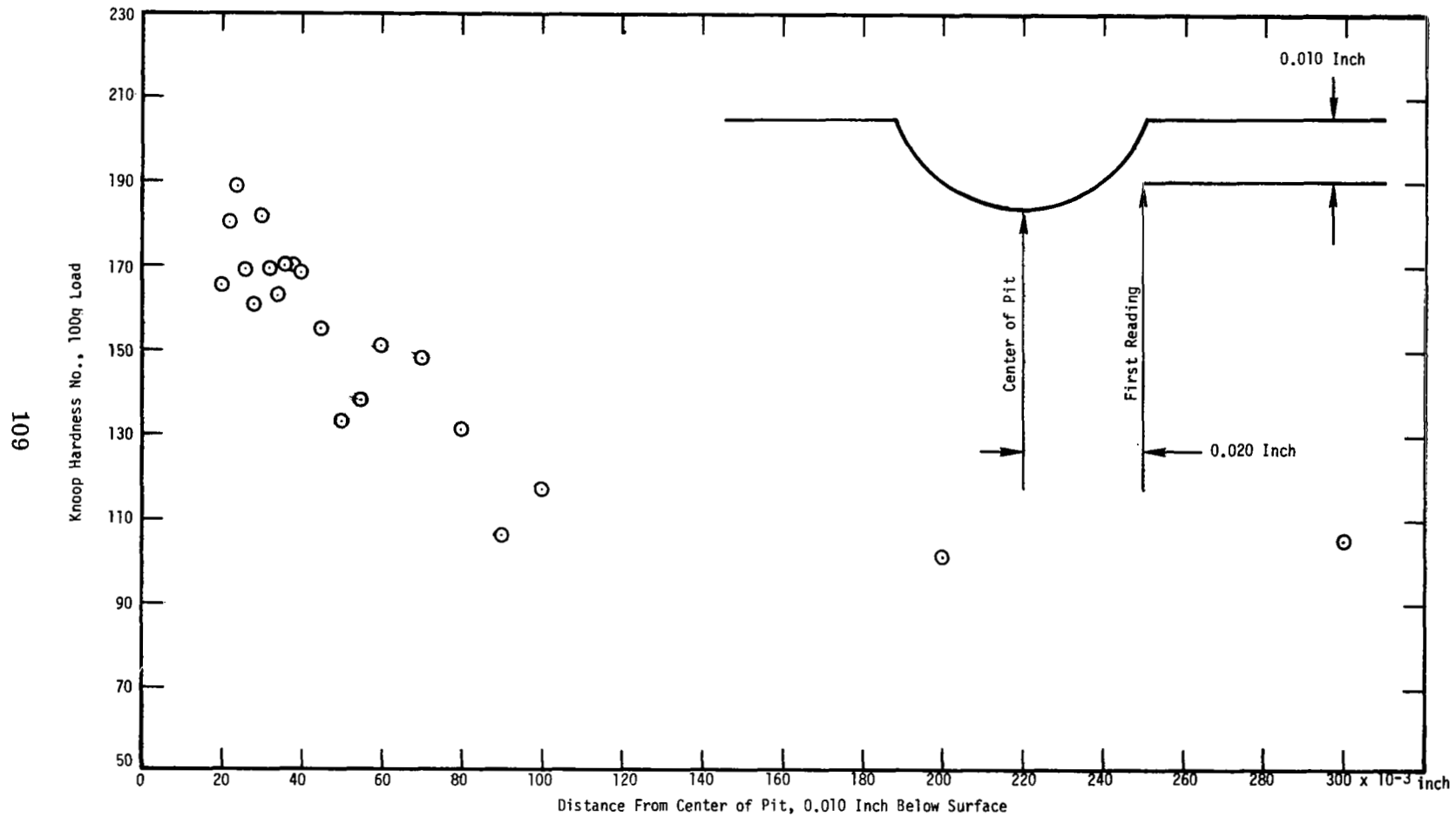


Figure 5.26b. Hardness Numbers Around a Crater Produced in Tantalum. Impact Velocity 17066 cm/sec.

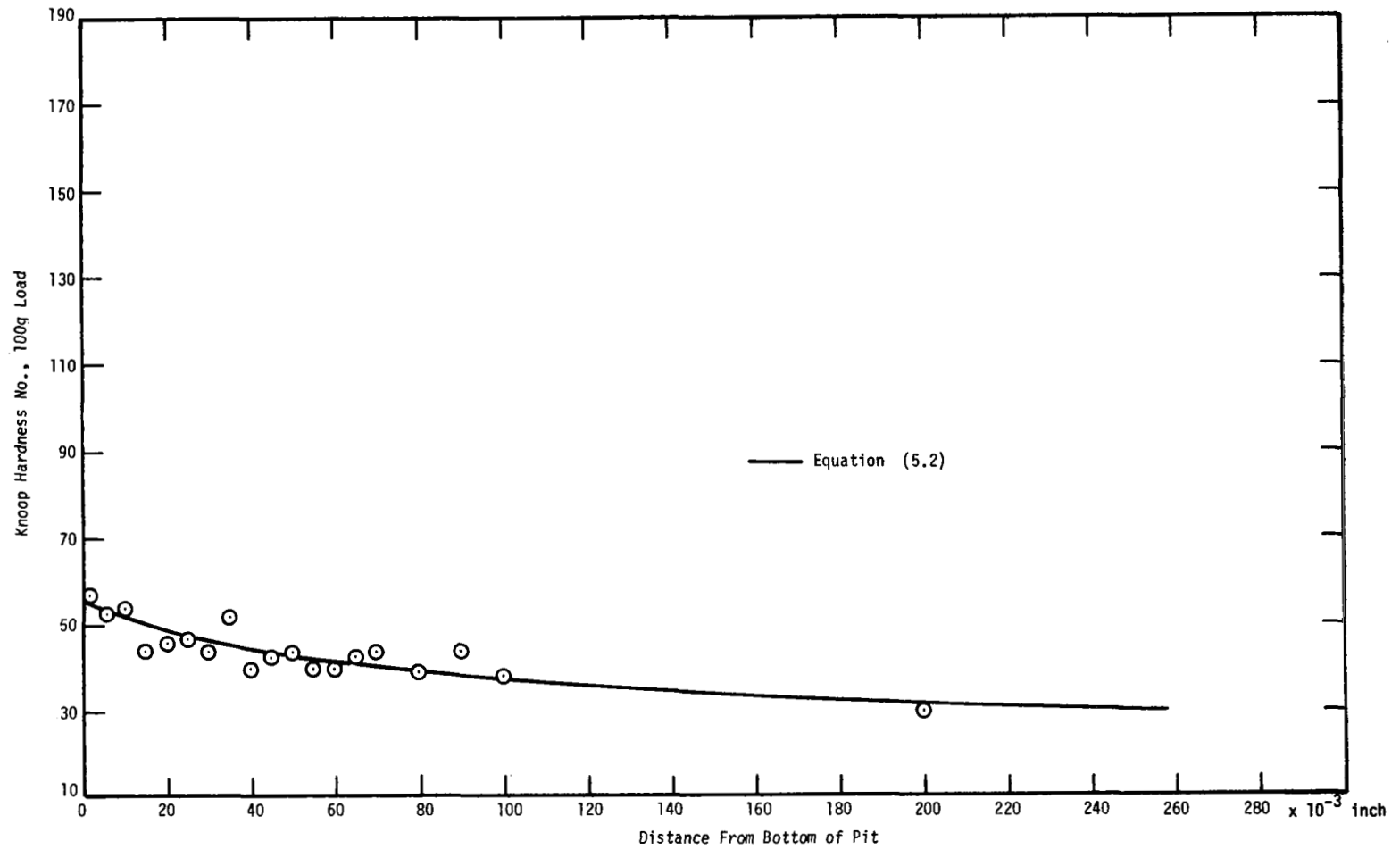


Figure 5.27a. Hardness Numbers Below a Crater Produced in Aluminum. Impact Velocity 17406 cm/sec.

III

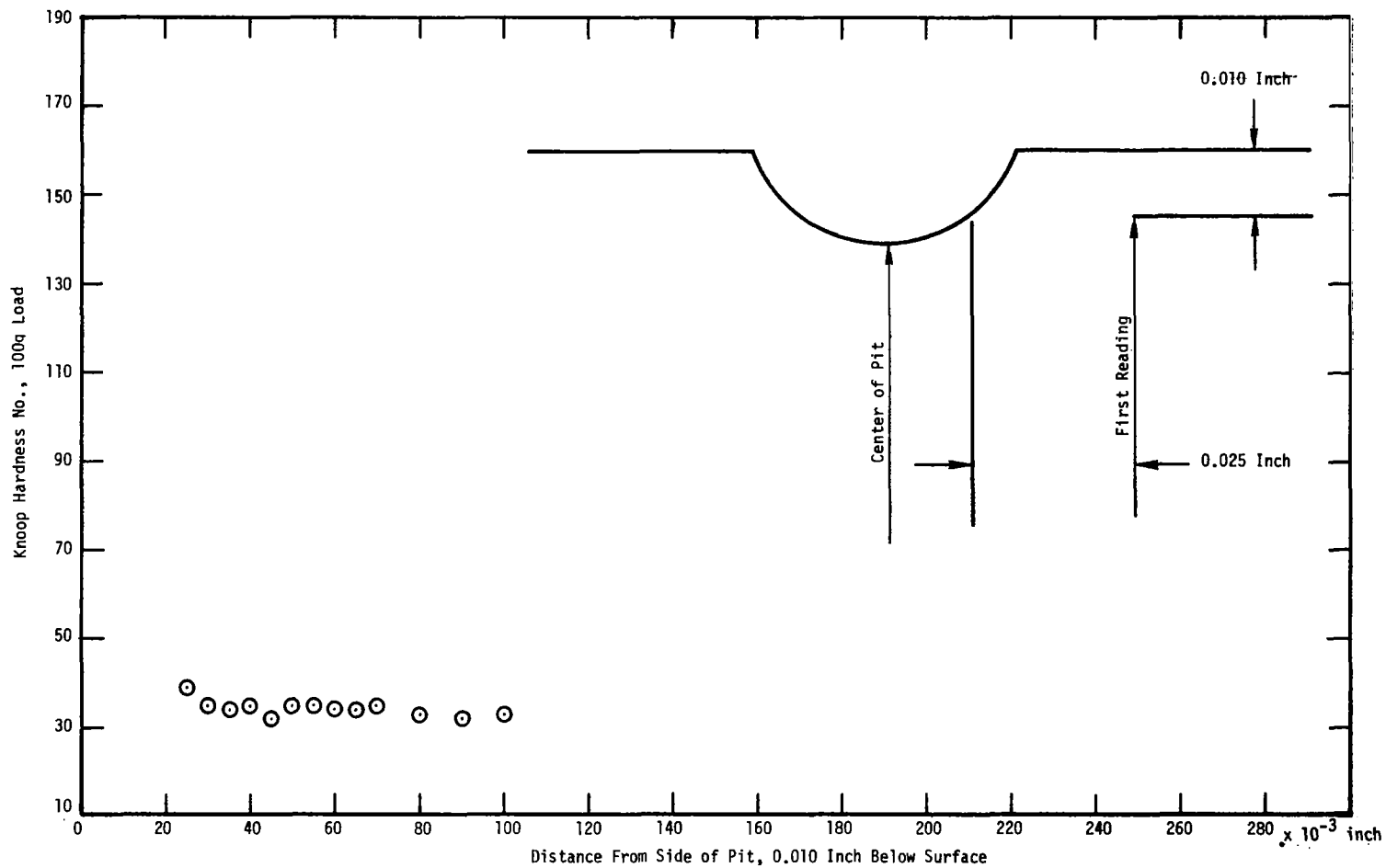


Figure 5.27b. Hardness Numbers Around a Crater Produced in Aluminum. Impact Velocity 17406 cm/sec.

For a different reason, it was considered essential that the starting points for both lines of hardness determinations be taken at some distance from the crater wall. If the cross-sectional cut has not been ground to the exact mid-point of the crater, a thin ledge of metal may exist near the edge of the crater. A hardness value obtained on this thin ledge of metal will be low because the ledge of metal will yield under the indenter.

Comparison of the calculated diameters with the measured diameters of the craters makes it possible to assess whether or not the cross-sectional cuts were ground to the maximum diameter of the crater. All of the craters, around which hardness determinations were made, were formed by impacts of 0.175-inch-diameter steel spheres. The diameters of the craters were calculated with use of the equation

$$d = 2 R \cos \left[\text{arc sin } \left\{ \frac{(R - \delta)}{R} \right\} \right] \quad (5.2)$$

where d is the crater diameter, R is the radius of the steel sphere that produced the crater, and δ is the depth of the crater below the original surface of the metal. The diameters of the craters as seen in the cross-sectional cuts were measured at the original surface of the metal. The calculated and the measured values of crater diameter are listed in Table 5.2.

From Table 5.2 it can be seen that for every metal except aged Udimet 700 the calculated diameter of the crater is greater than the measured diameter. It can be presumed that in the case of aged Udimet 700 the cross-sectional cut was ground to the true diameter of the crater. For the other metals, grinding of the cross section either overshot or undershot the true diameter of the crater. The most probable error in grinding a cross section to the true diameter of a crater is to grind too far.

Inspection of Figures 5.20 (a) through 5.27 (a) shows that the only case in which there is clear evidence of a rise to the maximum hardness below the crater is in Figure 5.20 (a). It can reasonably be presumed that the grinding of the cross section of the crater in nickel formed

TABLE 5.2

VALUES OF CRATER DEPTH AND DIAMETER

Metal	Impact Velocity, cm/sec	Crater Depth, cm	Measured Crater Diam., inch	Calculated Crater Diam.	
				cm	inch
Nickel	3342	0.0207	0.070	0.187	0.074
Nickel	17465	0.0910	0.115	0.359	0.141
U-700 Aged	17153	0.0355	0.098	0.241	0.095
U-700 Sol'ned.	17182	0.0369	0.094	0.245	0.097
Zinc	17328	0.0866	0.132	0.352	0.139
Iron	17036	0.0556	0.112	0.294	0.116
Tantalum	17066	0.0526	0.077	0.287	0.113
Aluminum	17406	0.1489	0.162	0.420	0.165

at a velocity of 3342 cm/sec was not carried far enough and that the fact that the first four values of hardness near the bottom of the crater are low is due to the existence of a thin ledge of metal that yielded under the indenter. On this basis, the first four values of hardness in Figure 5.20 (a) were not used in assessing the work-hardening behavior of nickel at this velocity.

The distance, D_{∞} , away from the crater bottom and crater side, at which the hardness numbers reach an asymptotic value, can be used to estimate the extent to which work-hardening occurred. Comparison of graph (a) with graph (b) for Figures 5.20 through 5.27 produced the observation that, for each of the metals except nickel, the hardening extends radially from the crater wall approximately as far as it extends from the bottom of the crater. The distance over which the hardening extends is roughly one crater diameter except in the case of iron. In iron the distance over which work-hardening extends is roughly three times as large as it is in the other metals. For nickel, the mass of work-hardened metal does not have spherical symmetry; it extends more than twice as far below the crater as it extends radially about it.

The rate at which work-hardening occurred and the intensity or degree to which it took place are more difficult to assess; the effort to assess these quantities was restricted to the loci of hardness numbers plotted against distance from the crater bottom. By trial it was found that these loci are very well given by the equation

$$H = H_{\infty} + (H_0 - H_{\infty}) e^{-K D} \quad (5.2)$$

which ⁽²⁴⁾ describes the decay of a variable H (such as hardness) with

(24) The applicability of this equation to impact hardening was suggested by Mr. Lars H. Sjodahl, Ceramic Materials Research, Nuclear Systems Programs, General Electric Company, Evendale, Ohio, on the basis of the observation that this equation has been found to give a good representation of other processes which reach asymptotic values. The machine solution of the equation that was used was constructed by Mr. Sjodahl.

distance, D , from an initial value, H_0 , to an asymptotic value, H_∞ . The quantity K is a rate constant with dimensions of reciprocal inches when the distance, D , is measured in inches.

A machine solution of eq (5.1) was constructed⁽²⁴⁾ which gives the hardness, H_0 , at the crater bottom, the hardness, H , at specific values of the distance, D , the slope of the hardness-versus-distance curve, dH/dD , at a distance of 15 mils from the crater bottom, the asymptotic hardness, H_∞ , the area under the hardness-versus-depth curve from the crater bottom to the depth at which the asymptotic value of hardness is reached, and the rate constant, K . The plots of calculated hardness against distance are shown in Figures 5.20 (a) through 5.27 (a); the other quantities are listed in Table 5.3.

The solution of eq (5.2) for Udimet 700 presented a problem. There are stringers of precipitated carbides in this alloy both in the aged and in the solutioned state; these carbides are very hard. If the hardness indenter should intercept a carbide particle, an abnormally high hardness value will be obtained. This is the reason for the large amount of scatter that appears in the data points plotted in Figure 5.22 (a) and (b) and in Figure 5.23 (a) and (b). The abnormally high hardness values reduced the slope of the calculated hardness-versus-distance curves for Udimet 700 with the result that the asymptotic values of hardness that were obtained from the solution of eq (5.2) were much too high.

The loci of eq (5.2) shown in Figures 5.22 (a) and 5.23 (a) were obtained by feeding the correct asymptotic value of hardness for Udimet 700, which both for the aged and for the solutioned state is a Knoop number of 375 with use of a 100-g load, into the machine solution. The loci of eq (5.2) shown in these figures are considered to be reasonable because the major scatter of the data points is above the calculated curve; this is to be expected on the basis of the presence of hard carbide particles in the alloy.

TABLE 5.3

DATA OBTAINED FROM THE SOLUTION OF EQUATION (5.2)

Metal	Impact Velocity, cm/sec	Rate Constant, K, inch ⁻¹	Maximum Hardness, H ₀ , hard. no.	Slope, dH/dD at 0.015 in. (hard. no.)/in.	Asymptotic Hardness, H _∞ , hard. no.	Area Under Hardness Curve (hard. no.)·in.
Nickel	3342	18.90	175.3	-1,429	74.85	5.311
Nickel	17465	8.757	237.2	-1,383	57.09	20.57
U-700 Aged	17153	35	668.1	-6,069	375	8.375
U-700 Sol'ned.	17182	35	716.3	-7,067	375	9.752
Zinc	17328	21.55	44.71	- 200.1	31.88	0.5955
Iron	17036	7.355	176.2	- 685.0	72.16	14.14
Tantalum	17066	33.89	177.7	-1,508	103.7	2.184
Aluminum	17406	10.70	53.44	- 220.2	29.27	2.258

The slope of the hardness-versus-distance curve gives the rate of decay of hardness with distance from the bottom of the crater. It is possible to convert distance below the crater to time with use of the group velocity of the plastic wave, which may be taken to be given by $[(d\sigma/d\varepsilon) / \rho]^{1/2}$ where σ is stress, ε is strain, and ρ is density. The group velocity of the plastic wave can be considered to be constant at an arbitrary value of stress [11]. Determination of the time rate of change in hardness was abandoned, however, because for two of the metals that were selected for the study of steel-sphere cratering (iron and tantalum) the slope of the stress-strain curve becomes negative after the yield point is reached (see Section 5.3).

It is interesting to note from Table 5.2 that the slope of the hardness-versus-distance curve is essentially the same for craters formed in nickel at velocities of both 3342 and 17465 cm/sec. This suggests that the slope, dH/dD , is independent of impact velocity and that it may be a function of material properties only. It would have been possible to assess the total integrated hardness that was produced around the craters in the metals (with the exception of nickel) by assuming that the mass of metal throughout which hardening occurred has spherical symmetry. This, however, was not done. The area under the hardness-versus-distance curve is the integrated hardness on a line extending into the metal from the center of the crater bottom. This integrated hardness provides an index to the intensity or degree to which hardening occurred.

From the tabulated values of the area under the hardness-versus-distance curve for craters produced by the same size of steel sphere fired at essentially the same velocity, it appears that the work-hardening ability of the metals due to impact is in the order: nickel > iron > Udimet 700 > (zinc, tantalum, and aluminum). Comparison of the area values for nickel at two velocities indicates that the degree of work-hardening produced varies as the impact velocity varies.

6. STATISTICAL ANALYSIS OF THE EXPERIMENTAL DATA

The cratering data that have been collected are the measured depths of craters produced by impacts of steel spheres against seven different metals at specific velocities. The procurement and preparation of the target specimens of the six metals (iron, nickel, tantalum, zinc, Udimet 700 solutioned, and Udimet 700 aged) originally selected for the current work have been described in sections 3.1 and 3.2; the determination of their properties has been discussed in sections 3.3 and 3.4. As an addition to the original scope of the current work, to provide a tie-in with steel-sphere cratering data collected earlier [7], cratering data were also collected for commercially pure aluminum. A large aluminum target plate, of the same size and dimensions and annealed under the same conditions as those used earlier [7], was employed.

For each set of cratering data (measured crater depth and corresponding measured impact velocity), the best-fit straight line and the best-fit parabola were calculated with use of a computer program⁽²¹⁾. The computer program yielded the standard deviation as a measure of the dispersion of the experimental points from the curves, the standard deviation of the slope and the standard deviation of the intercept. The program also printed out the value of an F-ratio (a measure of curvature) on the basis of which a decision could be made as to whether a straight-line fit or a parabolic fit was the more applicable.

The best-fit equations were calculated with crater depth as the dependent variable and impact velocity as the independent variable. Calculating the best-fit curve with crater depth as the dependent variable presumes that all the errors of measurement are in the measured values of crater depth and that no errors exist in the measured values of impact velocity. This, of course, is not the case. To make some compensation for this, the curve fitting was repeated using impact velocity

as the dependent variable and crater depth as the independent variable. The linear best-fit equations that resulted were averaged. The average best-fit equation, obtained in this way, was considered to be the most representative of the experimental data.

Two quantities of theoretical interest can be calculated from the linear best-fit equation. The general equation for this straight line [17] is

$$A V + B \delta' + C = 0 \quad (6.1)$$

where V is impact velocity and δ' is crater depth. When eq (6.1) is solved for δ' , the slope of the straight line is $(-A/B)$ and the crater-depth intercept, δ'_i , is $(-C/B)$. When eq (6.1) is solved for V , the intercept velocity, V_i , is $(-C/A)$. Because $-(-C/B)/(-A/B) = (-C/A)$, the intercept velocity of the best-fit equation can be found from the expression

$$V_i = -\delta'_i / (\text{slope of linear best-fit equation}). \quad (6.2)$$

The experimental value of the intercept velocity as found from eq (6.2) is the first quantity of theoretical interest that can be calculated from the linear best-fit equation.

The linear best-fit equation in intercept form [17] is

$$V/V_i + \delta'/\delta'_i = 1. \quad (6.3)$$

On transposing,

$$\delta'/\delta'_i = 1 - (V/V_i) = (V_i - V)/V_i,$$

and on multiplying throughout by -1 ,

$$(V - V_i)/V_i = -\delta'/\delta'_i = \delta'/(-\delta'_i)$$

} (6.4)

from which

$$\delta' = (-\delta'_i/V_i)(V - V_i). \quad (6.5)$$

On comparison of eq (6.5) with eqs (2.24) and (2.25) one finds that the constant k^* is given by

$$k^* = -\delta'_i/(V_i d) \quad (6.6)$$

where d is the diameter of the steel sphere. With use of eqs (6.2) and (6.6)

$$k^* = (\text{slope of the linear best-fit equation})/d \quad (6.7)$$

The experimental value of k^* as found from eq (6.7) is the second quantity of theoretical interest that can be calculated from the linear best-fit equation. Knowing the experimental value of the constant k^* , the experimental value of the numerical constant k of eq (2.21) can be calculated with use of eq (2.23). This is done in Section 7.4.

The results of the curve-fitting analysis and the discussion of these results are presented below organized under the lattice packing type of the metals or, in the case of alloys, under the lattice packing type of the major constituent.

6.1 Face-Centered-Cubic Metals and Alloys

The face-centered-cubic metals for which cratering data were subjected to statistical analysis are: 1100-0 aluminum, electrolytic tough pitch copper, nickel 270, the nickel based alloy Udimet 700 in both the solutioned and the aged condition, and the aluminum based alloy 2024-0 aluminum. The cratering data obtained with three sphere sizes for 1100-0 aluminum, electrolytic tough pitch copper, and 2024-0 aluminum were obtained in an earlier study [7] but had not been

subjected to statistical analysis. It will be of particular interest to make comparison between the cratering response of commercially pure nickel and the nickel based alloy Udimet 700 with the cratering response of commercially pure aluminum and the aluminum based alloy 2024-0 aluminum.

6.1.1 Commercially Pure Aluminum

Cratering data for impacts of 0.175-inch and 0.0938-inch spheres against 1100-0 aluminum were collected in the present study. Similar data for impacts of 0.5000-inch, 0.3125-inch, and 0.2188-inch steel spheres against 1100-0 aluminum were collected earlier [7]. The existing cratering data for the five sphere diameters are listed in Table 6.1. It is noteworthy that the largest sphere diameter for which cratering data exists is roughly five times the smallest sphere diameter. Results of statistical analysis of these data are presented in Table 6.2. Results for the 0.5000-inch-diameter spheres are discussed in detail below as a sample calculation.

The calculated curves for the 0.5000-inch spheres found from the computer program with crater depth, δ' , as dependent variable and impact velocity, V , as independent variable are as follows

$$\begin{aligned} \text{linear:} \quad \delta' &= 0.287915 \times 10^{-4} V - 0.0466872, \\ \text{parabolic:} \quad \delta' &= 5.39717 \times 10^{-10} V^2 + 1.12024 \times 10^{-5} V + 0.0853665. \end{aligned}$$

For the 12 available data points and 3 degrees of freedom, the value of 4.285 found for the F-ratio indicated that curvature was barely significant. See Appendix A. This finding eliminated further consideration of the parabolic best-fit curve.

Considering the linear best-fit equation, the standard deviation of the slope was found to be $\pm 0.0132893 \times 10^{-4}$ sec. Using twice the

Table 6.1

Cratering Data for Annealed Commercially Pure Aluminum

0.5000-inch-diam. Steel Spheres		0.3125-inch-diam. Steel Spheres		0.2188-inch-diam. Steel Spheres		0.175-inch-diam. Steel Spheres		0.0938-inch-diam. Steel Spheres	
Velocity, cm/sec	Crater Depth, cm	Velocity, cm/sec	Crater Depth, cm	Velocity, cm/sec	Crater Depth, cm	Velocity, cm/sec	Crater Depth, cm	Velocity, cm/sec	Crater Depth, cm
$\times 10^4$		$\times 10^4$		$\times 10^4$		$\times 10^4$		$\times 10^4$	
0.887	0.2235	0.7163	0.1102	0.9784	0.0998	0.1320	0.0084	0.7848	0.0348
1.055	0.2723	0.9723	0.1460	1.018	0.1041	0.1693	0.0107	1.275	0.0554
1.295	0.3294	1.265	0.1920	1.049	0.1072	0.2508	0.0223	1.545	0.0654
1.558	0.3746	1.414	0.2121	1.411	0.1481	0.3171	0.0293	2.005	0.0898
1.609	0.3917	1.490	0.2245	1.457	0.1514	0.3677	0.0327	2.039	0.0934
1.759	0.4483	1.506	0.2344	1.704	0.1798	0.4271	0.0271	2.310	0.1059
1.807	0.4658	1.530	0.2342	1.871	0.1986	0.6374	0.0558	2.377	0.1079
2.009	0.5263	1.646	0.2530	2.140	0.2291	0.7398	0.0636	2.422	0.1088
2.082	0.5565	1.661	0.2558	2.146	0.2334	0.7760	0.0659	2.530	0.1145
2.121	0.6083	1.783	0.2758	2.576	0.2906	1.034	0.0888	2.829	0.1310
2.128	0.5542	1.789	0.2751	2.865	0.3442	1.139	0.0974		
2.414	0.6556	1.862	0.2967	3.103	0.3726	1.218	0.1034		
		1.993	0.3172			1.224	0.1028		
		2.137	0.3406			1.384	0.1182		
		2.423	0.3780			1.741	0.1489		
						1.774	0.1559		

Table 6.2

Results of Statistical Analysis of the Cratering Data Obtained for Commercially Pure Aluminum

SECTION A. Linear Best-Fit Equation for Crater Depth as a Function of Impact Velocity

SPHERE DIAM., inch	SLOPE OF LINE, 10^{-4} sec		CRATER-DEPTH INTERCEPT, cm		VELOCITY INTERCEPT, $\frac{\text{cm}}{\text{sec}}$			F- RATIO	STD. DEV.	NUMBER OF POINTS
	Value Found	95% Confidence Range	Value Found	95% Confidence Range	Value Found	95% Confidence Range				
0.5000	0.2879	0.2613 to 0.3145	-0.04669	-0.09409 to 0.0007202	1622	119.5 to 3124	4.285	0.0205	12	
0.3125	0.1623	0.1569 to 0.1676	-0.01193	-0.02084 to -0.003017	735.1	209.4 to 1261	1.546	0.0043	15	
0.2188	0.1271	0.1204 to 0.1339	-0.03156	-0.04496 to -0.01817	2483	1551 to 3414	53.710	0.0081	12	
0.175	0.08753	0.08474 to 0.09031	-0.002219	-0.004960 to 0.000523	253.5	-52.95 to 559.9	0.071	0.0029	16	
0.0938	0.04729	0.04548 to 0.04910	-0.004450	-0.008252 to -0.000649	941	171.6 to 1710	3.210	0.0017	10	

SECTION B. Average Linear Best-Fit Equation

SPHERE DIAM., inch	SLOPE OF LINE, sec	CRATER-DEPTH INTERCEPT, cm	VELOCITY INTERCEPT, cm/sec	Constant, k^* , sec/cm
0.5000	0.290982×10^{-4}	-0.0519838	0.1786×10^4	0.2291×10^{-4}
0.3125	0.162540×10^{-4}	-0.0123902	0.07623×10^4	0.2048×10^{-4}
0.2188	0.127593×10^{-4}	-0.0323956	0.2539×10^4	0.2296×10^{-4}
0.175	0.0876822×10^{-4}	-0.00234788	0.0268×10^4	0.1973×10^{-4}
0.0938	0.0473616×10^{-4}	-0.00458994	0.0969×10^4	0.1988×10^{-4}

value of the standard deviation for 95 percent confidence, it was found that the slope could have a value from 0.261336×10^{-4} to 0.314494×10^{-4} sec. The standard deviation of the crater-depth intercept, δ'_i , was found to be ± 0.0237037 cm. Using twice the value of the standard deviation for 95 percent confidence, it was found that the crater-depth intercept could have a value from -0.0940946 to 0.0007202 cm.

It is noteworthy that one limit of the 95-percent-confidence range for the crater depth intercept, δ'_i , is positive in sign with the consequence that the corresponding value of the velocity intercept calculated from eq (6.2) will be negative in sign. From this circumstance, it appears that, when the velocity intercept is small, inaccuracies in the collection of the experimental data can produce a standard deviation of the crater-depth intercept large enough to bring negative values of the intercept velocity within the range of 95 percent confidence. However, a negative value of the velocity intercept has no physical significance. It would imply that a crater of measurable depth forms at zero impact velocity as was pointed out in Section 4.3.

The best-fit straight line found with crater depth as the independent variable and impact velocity as the dependent variable is

$$\delta' = 0.294048 \times 10^{-4} V - 0.0572803.$$

The average of this equation with the best-fit linear equation found with crater depth as the dependent variable and impact velocity as the independent variable is

$$\delta' = 0.290982 \times 10^{-4} V - 0.0519838. \quad (6.8)$$

Equation (6.8) is considered to be the most representative best-fit equation for this set of data. Using eq (6.8), the value of the constant k^* , found with use of eq (6.7), is 0.2291×10^{-4} sec/cm and the value of the intercept velocity, V_i , found from eq (6.2), is 0.1786×10^4 cm/sec.

For each sphere size, with the exception of the 0.2188-inch spheres, the F-ratio indicated that the data were fit better by a straight line than by a parabola. It can be seen from Section A of Table 6.2 that for every sphere size the 95-percent-confidence range for the slope is small in comparison with the value of the slope itself; this means that the slope is known with an acceptable degree of certainty. It can also be seen that for every sphere size the 95-percent confidence range both for the crater-depth intercept and for the velocity intercept is large in comparison with the values of these intercepts; this means that the crater-depth intercept and the velocity intercept are known with only a very low degree of certainty.

In Section B of Table 6.2, the slope, crater-depth intercept, velocity intercept, and the constant k^* found from the average best-fit equation are given. The values of these quantities as given in Section B are considered to be the most representative for the respective sphere sizes. By inspection of the values of the velocity intercept and of the constant k^* it can be seen that these quantities are not functions of the sphere size because there is no trend in the values of these quantities with sphere size. Consequently, it is to be expected that there is a value for each of these quantities that is characteristic of steel-sphere impacts against 1100-0 aluminum.

The average of the five entries for each of these quantities should provide the most representative value. However, inspection of the statistical measures shows that the experimental data are not of uniform quality. The value of the standard deviation, which measures the dispersion of the points around the best-fit straight line, is more than 10 times larger for the 0.5000-inch spheres than for the 0.0938-inch spheres and nearly 5 times larger for the 0.2188-inch spheres than for the 0.0938-inch spheres. Furthermore, the F-ratio, which is a measure of whether or not there is significant curvature,

is so high for the 0.2188-inch spheres that curvature is highly significant. Because it is unreasonable to suppose that the cratering curve for one sphere size is parabolic if the corresponding curves for impacts of four other sizes of spheres against the same metal are unquestionably straight lines, the highly significant curvature found for the 0.2188-inch spheres appears to be the result of inaccuracies in data collection.

These observations are very likely related to the fact that the constant k^* is 0.23×10^{-4} sec/cm for the 0.5000-inch and for the 0.2188-inch spheres whereas the value of this constant is about 0.20×10^{-4} sec/cm for the other three sizes of spheres. This is a 15 percent difference. Similarly, the intercept velocity is substantially higher for the 0.5000-inch and 0.2188-inch spheres than for the other three sizes of spheres. The 95-percent-confidence range for the intercept velocity of the 0.2188-inch spheres lies completely above the corresponding range for the 0.3125-inch and 0.175-inch spheres and almost completely above the corresponding range for the 0.0938-inch spheres.

The fact that the value of the constant k^* obtained for 0.2188-inch and that obtained for 0.5000-inch spheres, which are in close agreement among themselves, are about 15 percent higher than the values of the constant k^* obtained for 0.0938-inch, 0.175-inch, and 0.3125-inch spheres, which are also in close agreement among themselves, is disturbing. The data for the 0.3125-inch, 0.2188-inch, and 0.5000-inch spheres were collected in the same laboratory, with use of the same velocity-measuring technique, and with use of 1100-0 aluminum target plates that had been cut from a single large plate and that had been annealed under the same conditions.

Second Analysis of the Data for 1100-0 Aluminum

It appeared that scatter in the data points might be responsible for the lack of agreement between the values of the intercept velocity and the values of the constant k^* in Table 6.2. To investigate this possibility, data points for each sphere size that showed a wide degree of scatter were eliminated and the curve-fitting process was repeated. The data points that were deleted are marked with crosses in Figure 6.1. The results of the second curve fitting are given in Table 6.3. The best-fit curves are plotted with the experimental data in Figure 6.1.

From Table 6.3 it can be seen that the values of the standard deviation for the 0.5000-inch, 0.3125-inch, and 0.2188-inch spheres are strongly reduced from what they were in Table 6.2; they compare favorably with the values of standard deviation reported for 0.175-inch and 0.0938-inch spheres in Table 6.2. This is a measure of the reduction in scatter that was accomplished by dropping the data points marked with crosses in Figure 6.1.

The reduction in scatter was accompanied by improvement in the general agreement of the data. The anomalous F-ratio reported for the 0.2188-inch spheres in Table 6.2 has a value in Table 6.3 which compares favorably with those of the other sphere sizes and indicates that the data for the 0.2188-inch spheres are fit by a straight line. The values of the constant k^* for 0.5000-inch and 0.2188-inch spheres, which are higher than those found for the other sphere sizes in Table 6.2, are seen to compare favorably with those of the other sphere sizes in Table 6.3.

The values of the intercept velocity for 0.5000-inch and 0.2188-inch spheres, which were excessively high in Table 6.2, compare favorably with those of the other sphere sizes in Table 6.3. The average value of the intercept velocity for the three largest sphere sizes

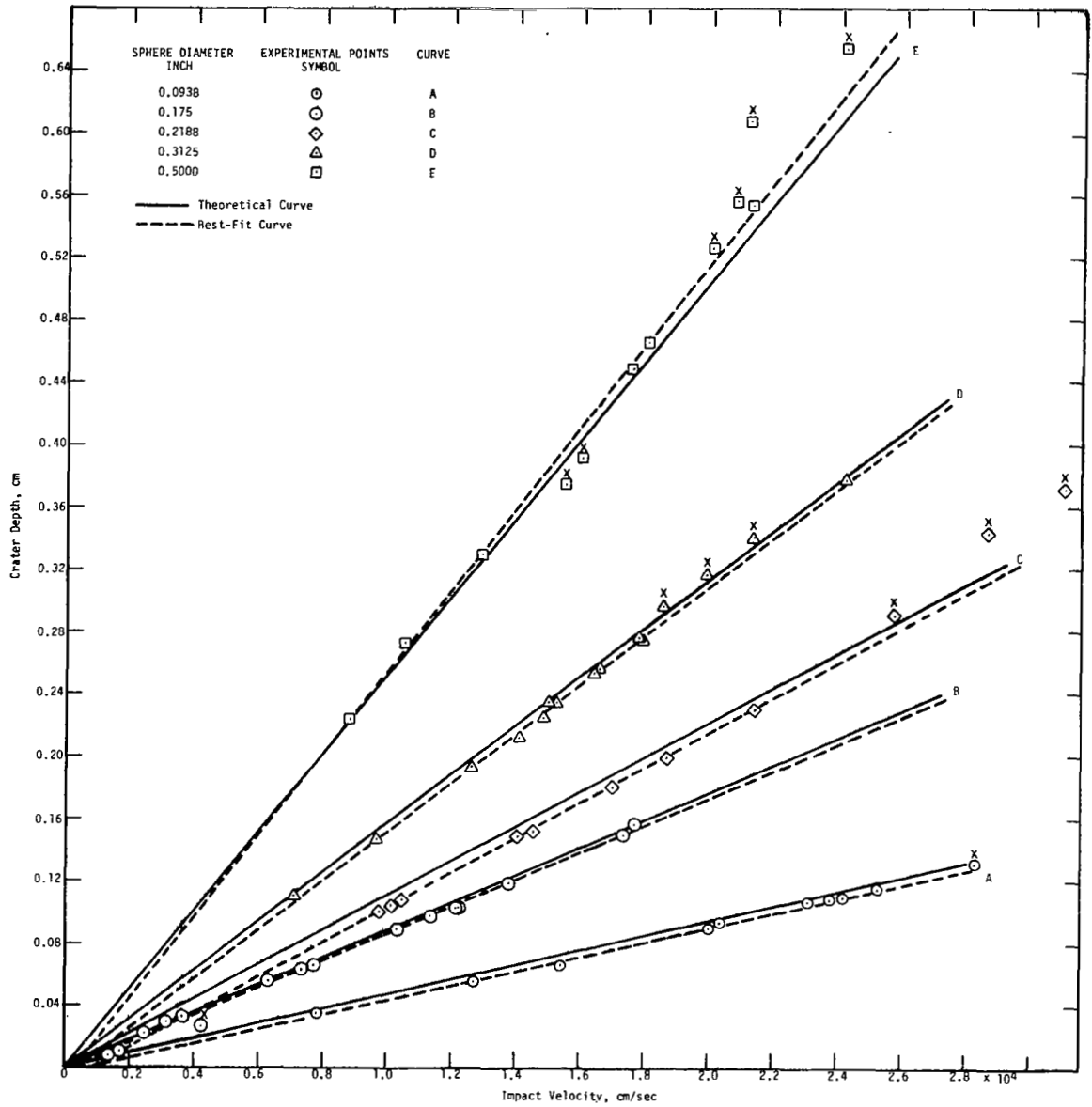


Figure 6.1. Theoretical Curves and Experimental Data for Impacts of Steel Spheres Against 1100-0 Aluminum.

Table 6.3

Results of Second Statistical Analysis of the Cratering Data Obtained for Commercially Pure Aluminum

SECTION A. Linear Best-Fit Equation for Crater Depth As a Function of Impact Velocity

SPHERE DIAM., Inch	SLOPE OF LINE, 10^{-4} sec		CRATER-DEPTH INTERCEPT, cm		VELOCITY INTERCEPT, $\frac{\text{cm}}{\text{sec}}$		F- RATIO	STD. DEV.	NUMBER OF POINTS
	Value Found	95% Confidence Range	Value Found	95% Confidence Range	Value Found	95% Confidence Range			
0.5000	0.2629	0.2557 to 0.2701	-0.009114	-0.02030 to 0.002070	346.7	-69.63 to 762.9	1.69	0.0039	6
0.3125	0.1580	0.1543 to 0.1617	-0.006971	-0.01282 to -0.001124	441.2	81.19 to 801.3	3.54	0.0026	12
0.2188	0.1126	0.1105 to 0.1148	-0.01113	-0.01458 to -0.007686	988.4	700.5 to 1276.	3.76	0.0014	9
0.175	0.08670	0.08485 to 0.08856	-0.000973	-0.00285 to 0.000905	112.2	-102.4 to 326.7	0.05	0.0019	15
0.0938	0.04677	0.04478 to 0.04876	-0.003625	-0.00761 to 0.000359	775.1	-45.21 to 1595.	1.34	0.0017	9

SECTION B. Average Linear Best-Fit Equation

SPHERE DIAM., inch	SLOPE OF LINE, sec	CRATER-DEPTH INTERCEPT, cm	VELOCITY INTERCEPT, cm/sec	Constant, k^* , sec/cm
0.5000	0.263024×10^{-4}	-0.00926133	0.0352110×10^4	0.207106×10^{-4}
0.3125	0.158102×10^{-4}	-0.00713731	0.0451437×10^4	0.199184×10^{-4}
0.2188	0.112686×10^{-4}	-0.0111867	0.0992732×10^4	0.202763×10^{-4}
0.175	0.0867682×10^{-4}	-0.001028324	0.0118514×10^4	0.195204×10^{-4}
0.0938	0.0468412×10^{-4}	-0.00376728	0.0804266×10^4	0.196604×10^{-4}

(earlier data [7]) in Table 6.3 is 599 cm/sec and the difference between the largest and the smallest value is 641 cm/sec. Similarly, the average value of the intercept velocity for the two smallest sphere sizes (current data) in Table 6.3 is 461 cm/sec and the difference between these values is 686 cm/sec.

The closeness of the average values and of the differences between largest and smallest value indicates that the two sets of data, which were collected at different times and under different circumstances, are of comparable quality. However, the difference between the largest and smallest value for each of the two sets of data is larger than the average value. This indicates that the average value is of doubtful reliability.

The experimental error is certainly reduced by taking the average of the values found. However, for four of the sphere sizes, cratering data were collected only at velocities above 7000 cm/sec. See Table 6.1. The intercept velocities obtained from these four sets of data were found by extrapolating over a substantial velocity range. This large extrapolation may be contributing to the disparity in the values of intercept velocity found for these four sphere sizes. Only for 0.175-inch spheres were cratering data collected below 7000 cm/sec, and, for this sphere size, nearly half of the data points were obtained in this low velocity range.

The intercept velocity found with use of 0.175-inch spheres is 119 cm/sec. Very little extrapolation is involved in obtaining this value of the intercept velocity as can be seen from Figure 6.1. From this standpoint, it appears to be more reliable than the average value of intercept velocity based on high-velocity impacts. It is noteworthy that the value of the velocity intercept for the 15 data points for 0.175-inch spheres in Table 6.3 B is less than half the value of the velocity intercept for 16 data points for 0.175-inch spheres in

Table 6.2 B. This shows that one data point, which is substantially out of line with the others, can change the value of the intercept velocity by a factor of two when the intercept velocity is small in size.

Search for a Change in Slope

Inspection of the data points for 0.175-inch spheres in Figure 6.1 suggests that the five points at the lowest velocities might conceivably be fit by a line with a steeper slope than that which would fit the remaining data points. If this were found to be the case, it would be in agreement with the observation (see Section 5.4) that 1100-0 aluminum does work-harden to a very small extent and that it may, consequently, become more resistant to crater formation as impact velocity is increased.

To test this possibility, best-fit straight lines were calculated for the data points below 4000 cm/sec and for the data points above 4000 cm/sec; the data point marked with a cross in Figure 6.1 was not used. The slopes and intercepts of the best-fit lines that were obtained are given in Table 6.4. The values of the F-ratios in Table 6.4 A indicate that the five data points below 4000 cm/sec and all 15 data points are best fit by straight lines: the F-ratio for the 10 points above 4000 cm/sec indicates significant curvature. The tabulated values of the standard deviation indicate that the scatter of the points about the lines is low.

Comparison of the values of slope, crater-depth intercept, velocity intercept, and constant k^* for the group of 10 data points above 4000 cm/sec with the values obtained for all 15 data points (see Table 6.4 B) shows that they are closely similar. This suggests that the addition or subtraction of the points below 4000 cm/sec is of little

Table 6.4

Results of Statistical Analysis of the Data Obtained for Impacts of 0.175-inch Spheres Against 1100-0 Aluminum

SECTION A. Linear Best-Fit Equation for Crater Depth As a Function of Impact Velocity

DATA POINTS CONSIDERED	SLOPE OF LINE, 10^{-4} sec		CRATER-DEPTH INTERCEPT, cm		VELOCITY INTERCEPT, cm/sec		F-RATIO	STD. DEV.
	Value Found	95% Confidence Range	Value Found	95% Confidence Range	Value Found	95% Confidence Range		
5 below 4000 cm/sec	0.1096	0.0952 to 0.1240	-0.006432	-0.002649 to -0.01021	587	313.1 to 860.5	0.806	0.0014
10 above 4000 cm/sec	0.08675	0.08401 to 0.08949	-0.001127	-0.004485 to +0.00223	130	-253.2 to 513.1	6.259	0.0016
All 15 data points	0.08670	0.08485 to 0.08856	-0.000973	-0.002851 to +0.000905	112	-102.4 to 326.7	0.0456	0.0019

132

SECTION B. Average Linear Best-Fit Equation

DATA POINTS CONSIDERED	SLOPE OF LINE, sec	CRATER-DEPTH INTERCEPT, cm	VELOCITY INTERCEPT, cm/sec	CONSTANT, k^* sec/cm
5 below 4000 cm/sec	0.110320×10^{-4}	-0.00660764	0.0598952×10^4	0.248189×10^{-4}
10 above 4000 cm/sec	0.0868344×10^{-4}	-0.00122861	0.0141489×10^4	0.195353×10^{-4}
All 15 data points	0.0867682×10^{-4}	-0.001028324	0.0118514×10^4	0.195204×10^{-4}

consequence and implies that these points should not be treated separately. The velocity intercept of 599 cm/sec for the five points below 4000 cm/sec is close to the average value of 618 cm/sec which was found when all points of both 0.175-inch and 0.0938-inch spheres were considered (see Table 6.2), but the constant k^* found for the five points below 4000 cm/sec is out of agreement with the values found when all points of both sphere sizes were considered. In view of the observations that have been made, it appears to be more likely that the points below 4000 cm/sec do not comprise a separate group.

Analysis of Liquid-Drop Cratering Data

Some mercury-drop cratering data exist for 1100-0 aluminum [6] and these data do provide a check on the use of eq (7.3) (see Section 7.5) to calculate liquid-drop denting velocities. These mercury-drop cratering data for 1100-0 aluminum were fitted with straight lines with use of the computer program⁽²¹⁾. The results of the analysis are given in Table 6.5. The tabulated values of standard deviation are reasonably low with the exception of the value for 0.15-cm mercury drops which is notably higher than the other values. The values obtained for F-ratio in conjunction with the number of data points indicate that the data are best fit with straight lines.

Consideration of the width of the 95 percent confidence range of the slopes of the lines in comparison with the values found indicates that the slopes of the lines are reasonably well known. Consideration of the width of the 95 percent confidence range of the velocity intercepts in comparison with the values found indicates that the velocity intercepts are known with somewhat less certainty than the slopes.

Consideration of the width of the 95 percent confidence range of the velocity intercepts in Tables 6.2, 6.3, 6.4, and 6.5 in comparison with the values found shows that the velocity intercepts for the

Table 6.5

Results of Analysis of Mercury-Drop Cratering Data for 1100-0 Aluminum

SECTION A. Linear Best-Fit Equation for Crater Depth As a Function of Impact Velocity

DROP DIAM. cm	SLOPE OF LINE, 10^{-4} sec		CRATER-DEPTH INTERCEPT, cm		VELOCITY INTERCEPT, $\frac{\text{cm}}{\text{sec}}$		F- RATIO	STANDARD DEVIATION	NUMBER OF POINTS
	Value Found	95% Confidence Range	Value Found	95% Confidence Range	Value Found	95% Confidence Range			
0.1	0.02529	0.02406 to 0.02653	-0.03360	-0.03893 to -0.02826	13282	11704 to 114860	0.0142	0.005999	21
0.15	0.04306	0.04008 to 0.04605	-0.05306	-0.06621 to -0.03991	12321	9983 to 14659	0.0172	0.014318	21
0.285	0.06120	0.05269 to 0.06970	-0.05337	-0.07038 to -0.03636	8721	7009 to 10433	4.3890	0.008865	8

SECTION B. Average Linear Best-Fit Equation

DROP DIAM. cm	SLOPE OF LINE, sec	CRATER-DEPTH INTERCEPT, cm	VELOCITY INTERCEPT, cm/sec	CONSTANT, k^* sec/cm
0.1	0.0254363×10^{-4}	-0.0341336	13419.2	0.254363×10^{-4}
0.15	0.0435536×10^{-4}	-0.0549630	12619.6	0.290357×10^{-4}
0.285	0.0620836×10^{-4}	-0.0550182	8861.95	0.217837×10^{-4}

mercury-drop cratering data are known with considerably more certainty than the velocity intercepts for the steel-sphere cratering data. On the basis of the relatively small amount of experimental data available, the reason for this appears to be that the velocity intercepts of the mercury-drop cratering data are large numbers and that the lowest velocities at which data were collected are reasonably close to the value of the intercept velocity. The amount of extrapolation involved is, consequently, less for the liquid-drop cratering data.

It can be seen from Table 6.5 B that there is a trend in the values of velocity intercept as drop diameter increases. However, the trend is in the reverse direction from that found in liquid-drop cratering data for copper (see Table 6.10) and this suggests that the trend is without real significance. However, the observation should be checked further.

6.1.2 Nickel 270

The cratering data obtained for nickel 270 with use of 0.175-inch and 0.0938-inch spheres are listed in Table 6.6. The special circumstances that were employed in the diagnostic firings (see Section 4.4) made with 0.175-inch spheres against specimens of nickel 270 are also recorded in this table. It is noteworthy that, although the data accumulated with use of these special circumstances fall on a curve with the other data points for nickel (see Figure 4.3), some instances of a lower depth at a higher velocity (velocity-depth inversions) appear when these data are entered into the total compilation of cratering data for nickel 270. Some of these inversions may be significant.

In particular, the 0.17-inch-thick specimen that was struck at a pendulum velocity of 3251 cm/sec developed a crater which is 0.001 cm deeper than the crater developed in the standard 0.5-inch-thick

Table 6.6

Cratering Data for Nickel 270

Measured Velocity, cm/sec	Corrected Velocity, cm/sec	Crater Depth, cm	Special Circumstances
-----Sphere Diameter 0.4445 cm (0.175 in.)-----			
829.7	726.381	0.0064	Very low velocity produces very shallow crater and taxes depth measurement techniques employed
1274	1159.	0.0084	
1410	1291.43	0.0094	
2399	2254.42	0.0138	
2975	2815.28	0.0186	Specimen backed by rigidly gripped pipe
3427	3251.5	0.0217	Specimen about 0.17 in. thick
351	3342.06	0.0207	
3965	3779.25	0.0229	
4441	4242.74	0.0256	
6523	6270.	0.0376	Specimen about 0.17 in. thick
6579	6324.53	0.0365	
7498	7219.37	0.0416	Specimen backed by rigidly gripped pipe
8989	8671.17	0.0473	
9373	9045.08	0.0510	Impact specimen soldered in steel block
11080	10707.2	0.0582	Smooth-bore gun; specimen 1 in. thick
11210	10833.8	0.0580	Smooth-bore gun employed
11600	11213.5	0.0608	
11620	11233.	0.0609	Specimen backed by rigidly gripped pipe
13031	12606.9	0.0672	
15170	14689.7	0.0781	Square specimen 0.794 in. by 0.794 in.
15190	14709.1	0.0776	Pipe support with side shims
15240	14757.8	0.0782	Square specimen 0.663 in. by 0.674 in.
15290	14806.5	0.0784	
15480	14991.5	0.0776	Smooth-bore gun employed
15560	15069.4	0.0796	
16565	16048.	0.0842	
18020	17464.7	0.0910	
18040	17484.2	0.0902	Smooth-bore gun employed
18360	17795.8	0.0928	Impact specimen soldered in steel block
19589	18992.5	0.0986	
21710	21057.7	0.105	

Table 6.6 (cont.)

Cratering Data for Nickel 270

Measured Velocity, cm/sec	Corrected Velocity, cm/sec	Crater Depth, cm	Special Circumstances
-----Sphere Diameter 0.4445 cm (0.175 in.)-----			
22645	21968.2	0.1125	
24460	23735.4	0.120	
26667	25884.4	0.131	
27484	26679.9	0.136	
-----Sphere Diameter 0.2383 cm (0.0938 in.)-----			
1521	1399.51	0.0063	
3507	3333.29	0.0146	
5175	4957.44	0.0158	
6370	6121.03	0.0196	
7915	7625.41	0.0232	
9267	8941.86	0.0268	
10330	9976.92	0.0291	
11773	11382.	0.0308	
12890	12469.6	0.0351	
14890	14417.	0.0404	
14930	14456.	0.0434	
1744C	16900.	0.0450	
18020	17464.7	0.0475	
20920	20288.5	0.0536	
21010	20376.1	0.0542	
23360	22664.4	0.0599	
24230	23511.5	0.0632	
25420	24670.2	0.0674	
26570	25790.	0.0692	
28250	27425.8	0.0740	

specimen when this specimen was struck at a velocity 90 cm/sec (2.7 percent) higher. The reliability of the observation appears to be substantiated by the fact that a crater-depth inversion of the same magnitude occurs for the 0.17-inch-thick specimen struck at a pendulum velocity of 6,270 cm/sec. Here the shallower crater was formed at a velocity 55 cm/sec (0.9 percent) higher. Because only two thin specimens were tested and because the same type of inversion occurred for each, it appears that the crater depth of data points for which the plate thickness is only one sphere diameter or less may not be entirely comparable with the crater depth of data points obtained with the standard specimens which had a thickness of nearly three times the 0.175-inch-diameter spheres. It is noteworthy, however, that both the differences in depth and the differences in velocity are near or below the limit of reliability of the measuring techniques employed. Furthermore, the tentative conclusion is based on the evidence of only two cases.

Conversely, the craters produced by 0.175-inch spheres fired with the smooth-bore gun at pendulum velocities of 14992 and 17484 cm/sec are consistently shallow by about 0.001 cm when compared with craters produced by the same sphere size fired with the rifled-bore gun at velocities that were 185 cm/sec (1.2 percent) and 19 cm/sec (0.1 percent) lower, respectively. On the evidence of these two instances, it appears that craters produced with the rifled-bore gun may be deeper than, and consequently not comparable with, craters produced with the smooth-bore gun. Again, as in the case of the inversions that occurred for the thin specimens, the evidence is restricted to two cases and the differences in both depth and velocity are near or below the limit of reliability of the measuring techniques employed.

There are two other depth inversions; these are probably not significant. The crater produced in the square specimen at a pendulum velocity of 14690 cm/sec is 0.0005 cm deeper than the crater produced

in the standard specimen with pipe support and side shims at a velocity 19 cm/sec (0.1 percent) higher. No inversion occurred with the other square specimen or with two specimens that were backed by a rigidly gripped pipe. Also, the craters produced by firings of 0.175-inch spheres at pendulum velocities of 10,707 and 10,834 cm/sec with use of the smooth-bore gun also show a depth inversion; the 1-inch-thick specimen developed a crater at 10,707 cm/sec that was 0.0002 cm deeper than the crater developed in the 0.5-inch-thick specimen at a velocity 127 cm/sec (1.2 percent) higher. It is very doubtful that a difference of 0.0002 cm in depth is significant.

On the basis of the inversions that it was thought might be significant, it was decided to exclude the data obtained with the thin specimens and the data obtained with the smooth-bore gun from the analysis of the data for nickel 270. With use of a computer program⁽²¹⁾, best-fit straight lines were calculated for the remaining cratering data for nickel obtained with 0.175-inch spheres and for the cratering data obtained with 0.0938-inch spheres. The slopes and intercepts of these curves are given in Tables 6.7 and 6.8.

From Table 6.7 A it can be seen that the F-ratio, which is a measure of curvature, is 23.8 for the curve fit of the 29 data points obtained for 0.175-inch spheres. The magnitude of the F-ratio indicates that there is significant curvature in the best-fit line for these points. The negative sign of the x^2 term of the parabolic equation given by the computer program indicates that the curvature is concave toward the velocity axis. The value of the standard deviation is 0.0012; the smallness of this value indicates that there is very little scatter in the data points about the line.

From Table 6.8 A it can be seen that the F-ratio for the curve fit of the 20 data points obtained with use of 0.0938-inch spheres is

Table 6.7

Results of Statistical Analysis of Cratering Data Obtained for Nickel 270 Using 0.175-inch Spheres

SECTION A. Linear Best-Fit Equation for Crater Depth as a Function of Impact Velocity

DATA POINTS CONSIDERED	SLOPE OF LINE, 10^{-4} sec		CRATER-DEPTH INTERCEPT, cm		VELOCITY INTERCEPT, $\frac{\text{cm}}{\text{sec}}$		F-RATIO	STANDARD DEVIATION
	Value Found	95% Confidence Range	Value Found	95% Confidence Range	Value Found	95% Confidence Range		
4 below 6500 cm/sec	0.05931	0.05572 to 0.06289	0.0005587	-0.0006895 to 0.001807	-94.2	-310.2 to 121.8	2.17	0.00026
20 above 6500 cm/sec	0.04788	0.04715 to 0.04862	0.007101	0.005849 to 0.008353	-1483	-5891 to 2925	0.047	0.00089
All 29 data points	0.04936	0.04877 to 0.04995	0.004430	0.003585 to 0.005275	-897.5	-1078 to -717.1	23.8	0.0012

SECTION B. Average Linear Best-Fit Equation

DATA POINTS CONSIDERED	SLOPE OF LINE, sec	CRATER-DEPTH INTERCEPT, cm	VELOCITY INTERCEPT, cm/sec	CONSTANT, k^* sec/cm
4 below 6500 cm/sec	0.0593598×10^{-4}	0.000540258	-0.00910141×10^4	0.133543×10^{-4}
20 above 6500 cm/sec	0.0479100×10^{-4}	0.00706017	-0.147363×10^4	0.107784×10^{-4}
All 29 data points	0.0493862×10^{-4}	0.00440142	-0.0891225×10^4	0.111105×10^{-4}

Table 6.8

Results of Statistical Analysis of Cratering Data Obtained for Nickel 270 Using 0.0938-inch Spheres

SECTION A. Linear Best-Fit Equation for Crater Depth as a Function of Impact Velocity

DATA POINTS CONSIDERED	SLOPE OF LINE, 10^{-4} sec		CRATER-DEPTH INTERCEPT, cm		VELOCITY INTERCEPT, $\frac{\text{cm}}{\text{sec}}$		F-RATIO	STANDARD DEVIATION
	Value Found	95% Confidence Range	Value Found	95% Confidence Range	Value Found	95% Confidence Range		
2 below 6500 cm/sec	0.03266	--- ---	-0.0003898	--- ---	119.4	--- ---	---	---
16 above 6500 cm/sec	0.02533	0.02431 to 0.02636	0.003603	0.001714 to 0.005493	-1422	-2223 to -622.0	1.2	0.00126
All 20 data points	0.02518	0.02444 to 0.02592	0.003921	0.002694 to 0.005149	-1557	-2086 to -1029	0.623	0.00128

141

SECTION B. Average Linear Best-Fit Equation

DATA POINTS CONSIDERED	SLOPE OF LINE, sec	CRATER-DEPTH INTERCEPT, cm	VELOCITY INTERCEPT, cm/sec	CONSTANT, k^* sec/cm
2 below 6500 cm/sec	0.0326576×10^{-4}	-0.0003898	0.01194×10^4	0.137072×10^{-4}
16 above 6500 cm/sec	0.0254046×10^{-4}	0.00347730	-0.136877×10^4	0.106629×10^{-4}
All 20 data points	0.0252270×10^{-4}	0.00384962	-0.152599×10^4	0.105884×10^{-4}

0.623. The magnitude of this F-ratio indicates that curvature in the best-fit line is not significant for this sphere size. The value of the standard deviation is comparable in magnitude to that found for 0.175-inch spheres and indicates that there is very little scatter of the data points about the line.

From Tables 6.7 A and 6.8 A it can be seen that the intercept velocity is negative for both sphere sizes when all of the data points are considered. It was pointed out in Section 4.3 that, providing there is no serious error in the measurements, a negative intercept velocity (positive intercept on the crater-depth axis) indicates that the crater-depth-versus-velocity plot must bend. It is either a curve or it consists of two straight lines that have different slopes.

It is of distinct interest to note that significant curvature is indicated by the F-ratio only for the 0.175-inch spheres. That the curvature detected is concave toward the velocity axis signifies that penetration efficiency is reduced. It is possible that the curvature which has been found may be the result of work-hardening of the nickel targets as the steel-sphere impacts occurred. It was pointed out in Section 5.3 that, of the metals used as targets for the steel-sphere firings, the work-hardenability of nickel is the greatest and that of aluminum is the least. No meaningful curvature was found for the crater-depth-versus-velocity plots of 1100-0 aluminum (see Section 6.1.1).

Inspection of a plot of the data points for nickel suggested that the change in slope may occur at a velocity of about 6500 cm/sec. For each sphere size, the data points below this velocity and the data points above this velocity were considered as independent sets of data. With use of the computer program, each of these sets of data points was fitted with a straight line.

The calculated best-fit equations that were obtained for data points below 6500 cm/sec were considered to be unsatisfactory because each equation had a positive intercept on the crater-depth axis. It was thought that the measured depths might be high because, in a soft metal, the pointed plunger of the dial gauge pierces the metal at the bottom of a crater during a measurement. The percentage error introduced in this way is larger in shallow craters produced at low velocities than in deep craters produced at high velocities. The crater depths suspected of being high were progressively rejected and the curve fitting was repeated until a positive value of intercept velocity within the range of 95 percent confidence was obtained. The slopes and intercepts of the lines that were considered acceptable are given in Tables 6.7 and 6.8. The lines are plotted in Figure 6.2.

The values of F-ratio given for the lines below and above 6500 cm/sec indicate that there is no significant curvature in these lines. The values of the standard deviation for the curves below and above 6500 cm/sec indicate that the scatter of the points about the lines is less for each sphere size than when all of the points for each size were considered. Reduction in the magnitude of the standard deviation is the result of removing the curvature from the lines. That the reduction in scatter is greater for the 0.175-inch than for the 0.0938-inch spheres was to be expected because significant curvature was found only for the data obtained with 0.175-inch spheres.

For 0.175-inch spheres, the ratio of the slope of the line below 6500 cm/sec to the slope of the line above 6500 cm/sec is 1.24. This corresponds to a 24 percent reduction in slope. The corresponding ratio for 0.0938-inch spheres is 1.29 which corresponds to a 29 percent reduction in slope. That the crater-depth-versus-velocity plot for the smaller sphere size was subject to a greater percentage reduction in slope may or may not be meaningful; the best-fit equation below 6500 cm/sec for the data obtained with 0.0938-inch spheres is based on only two points.

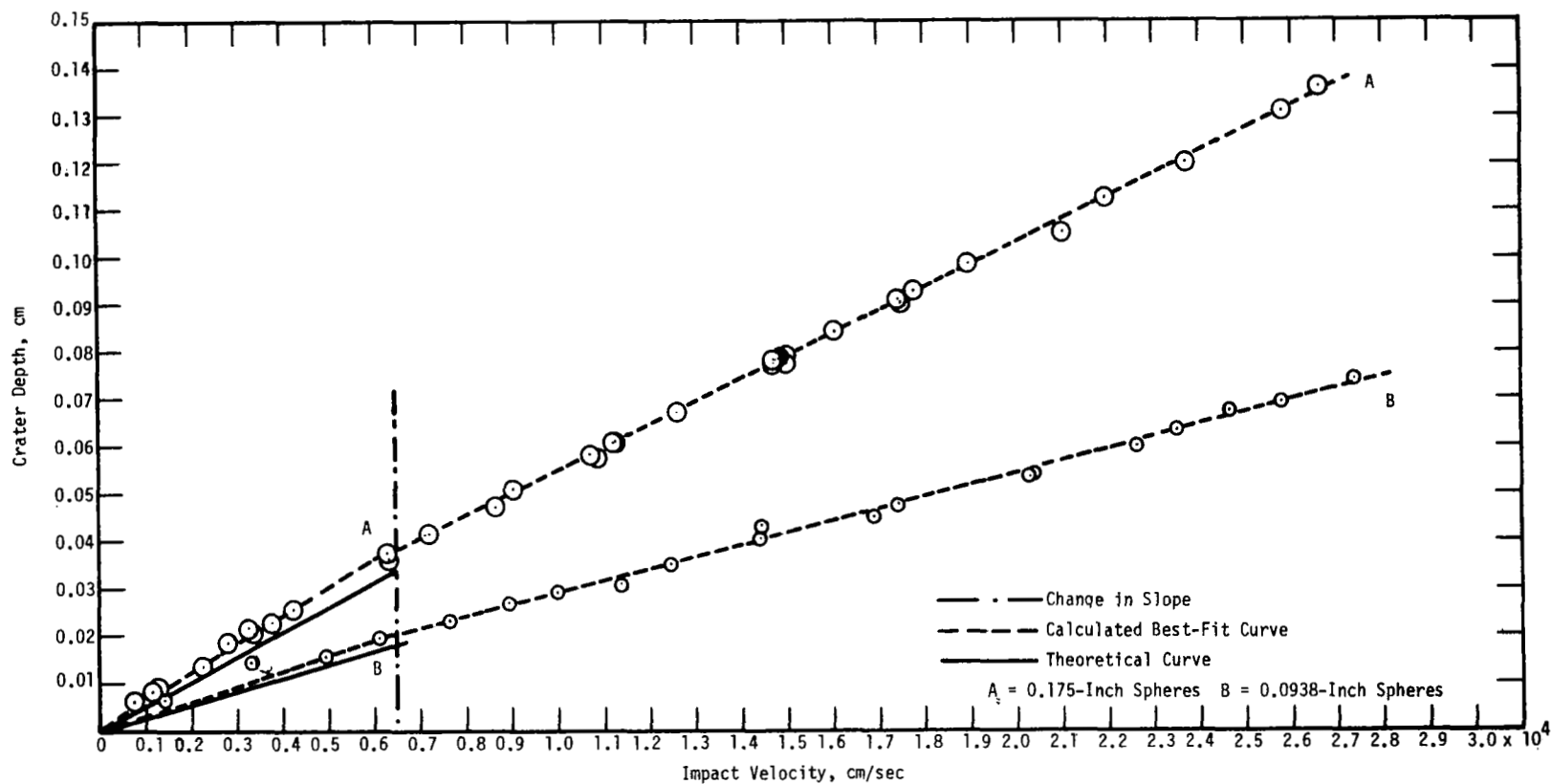


Figure 6.2. Theoretical Curves and Experimental Data for Impacts of Steel Spheres Against Nickel 270.

6.1.3 Electrolytic Tough Pitch Copper

Copper was not one of the metals chosen for the current study of cratering by means of steel-sphere impacts. However, some steel-sphere-impact data for electrolytic tough pitch copper were obtained in an earlier study [7]; these data had not been subjected to statistical analysis. In an effort to obtain more evidence to establish the experimental value of the constant k for face-centered cubic metals (see Section 7.4), an analysis of these data was made. The results are given in Table 6.9.

From the value of the F -ratio and number of points given in Table 6.9 A, the cratering data for 0.5000-inch and 0.2188-inch spheres are fit best by straight lines. On the other hand, the value of the F -ratio in conjunction with the number of points for 0.3125-inch spheres indicates that curvature is highly significant. From the values of standard deviation given in Table 6.9 A, it can be seen that there is a large amount of scatter of the data points about the best-fit lines for the 0.5000-inch and 0.2188-inch spheres. On the other hand, the standard deviation for the 0.3125-inch spheres indicates relatively little scatter.

The value of the intercept velocity for each sphere size is negative in Table 6.9 A; in Table 6.9 B, the only positive value of intercept velocity is for the 0.5000-inch spheres for which scatter in the data points is very high. The fact that the intercept velocity for the 0.3125-inch spheres, for which the value of the standard deviation is the lowest, is negative in Table 6.9 B suggests that the copper did work-harden under the impacts and that the slopes and intercepts of the lines given in Table 6.9 B may not be representative. This conclusion is supported by the finding of highly significant curvature for the 0.3125-inch spheres.

Table 6.9

Results of Statistical Analysis of Steel-Sphere Cratering Data Obtained for Electrolytic Tough Pitch Copper

SECTION A. Linear Best-Fit Equation for Crater Depth As a Function of Impact Velocity

SPHERE DIAM., inch	SLOPE OF LINE, 10^{-4} sec		CRATER-DEPTH INTERCEPT, cm		VELOCITY INTERCEPT, $\frac{\text{cm}}{\text{sec}}$		F- RATIO	STD. DEV.	NUMBER OF POINTS
	Value Found	95% Confidence Range	Value Found	95% Confidence Range	Value Found	95% Confidence Range			
0.5000	0.1783	0.1569 to 0.1997	0.008037	-0.03863 to 0.05471	-451	-3117 to 2216	0.129	0.0407	20
0.3125	0.1078	0.1043 to 0.1112	0.005001	-0.0008887 to 0.01089	-464	-1025 to 96.28	6.80	0.0031	9
0.2188	0.07464	0.06526 to 0.08403	0.005249	-0.01606 to 0.02656	-703	-3644 to 2237	2.48	0.0109	17

SECTION B. Average Linear Best-Fit Equation

SPHERE DIAM., inch	SLOPE OF LINE, sec	CRATER-DEPTH INTERCEPT, cm	VELOCITY INTERCEPT, cm/sec	CONSTANT, k^* , sec/cm
0.5000	0.184122×10^{-4}	-0.0035645	0.0193594×10^4	0.144978×10^{-4}
0.3125	0.107846×10^{-4}	0.00484820	-0.0449548×10^4	0.135869×10^{-4}
0.2188	0.0768548×10^{-4}	0.00038396	-0.00499591×10^4	0.138290×10^{-4}

If the velocity at which a change of slope due to work-hardening is taken to be 9020 cm/sec, two data points at or below this velocity are available for 0.3125-inch spheres and for 0.5000-inch spheres. The straight line calculated for the two data points obtained with 0.3125-inch spheres is

$$\delta = 0.118612 \times 10^{-4} V - 0.00235293 \quad (6.9)$$

from which the intercept velocity is 198 cm/sec, the constant k^* is 0.149432×10^{-4} sec/cm, and the constant k calculated from eq (2.23) is 16.85. This value of the constant k compares favorably with the values of this constant found for 1100-0 aluminum and nickel (see Table 7.8). It is noteworthy that the value of the constant k calculated with use of the value of the constant k^* given in Table 6.9 B for impacts of 0.3125-inch spheres against copper is 15.32.

The average best-fit equation found for the seven data points obtained at velocities above 9020 cm/sec for impacts of 0.3125-inch spheres against copper is

$$\delta = 0.109983 \times 10^{-4} V + 0.000339393. \quad (6.10)$$

The ratio of the slope of the best-fit line below 9020 cm/sec to the slope of the best-fit line above 9020 cm/sec is 1.078. This corresponds to a 7.8 percent reduction in slope as a consequence of work-hardening. This is from 1/6 to 1/7 of the reduction in slope observed in the case of nickel 270. It is regrettable that copper was not among the metals considered in the study of Section 5.4.

The straight line calculated for the two data points obtained below a velocity of 9020 cm/sec with 0.5000-inch spheres is

$$\delta = 0.291803 \times 10^{-4} V - 0.03637$$

from which the velocity intercept is 1246 cm/sec, the constant k^* is 0.229766×10^{-4} sec/cm, and the constant k calculated from eq (2.23) is

25.91. This value of the constant k is widely different from those found for 1100-0 aluminum and nickel 270 (see Table 7.8) and this suggests that the two data points at velocities below 9020 cm/sec for impacts of 0.5000-inch spheres against copper are probably subject to the same high degree of scatter found for all of the data points of this sphere size (see values of standard deviation in Table 6.9 A).

Based on the two data points obtained at velocities below 9020 cm/sec for impacts of 0.3125-inch spheres against copper, the value of the steel-sphere denting velocity for electrolytic tough pitch copper is 198 cm/sec, the value of the constant k^* for the low-velocity branch of the crater-depth-versus-velocity curve is 0.149432×10^{-4} sec/cm, and the value of the constant k calculated from eq (2.23) is 16.85 for the low-velocity branch of the crater-depth-versus-velocity curve.

Data for copper are plotted in Figure 6.3.

Analysis of Liquid-Drop Cratering Data

The waterdrop denting velocity and the mercury-drop denting velocity for copper can be calculated from the steel-sphere denting velocity. This is done in Section 7.5.1. Because cratering data were collected for impacts of both waterdrops and mercury drops against target plates of electrolytic tough pitch copper from the same heat and annealed at the same temperature, a comparison can be made between the experimentally determined waterdrop and mercury-drop denting velocities and the values calculated from the steel-sphere denting velocity. See Section 7.5.1.

The cratering data that were tabulated earlier [7] for mercury-drop and waterdrop impacts were fitted with straight lines with use of the computer program⁽²¹⁾. The results of the analysis are given in Table 6.10. The tabulated values of standard deviation are reasonably low with the exception of the value for 0.2-cm mercury drops which is higher than the other values. The values obtained for the F-ratio in conjunction with the number of data points indicate that curvature is not significant for the 0.2-cm mercury drops and waterdrops. However, the F-ratio found for 0.1-cm mercury drops indicates that curvature is significant.

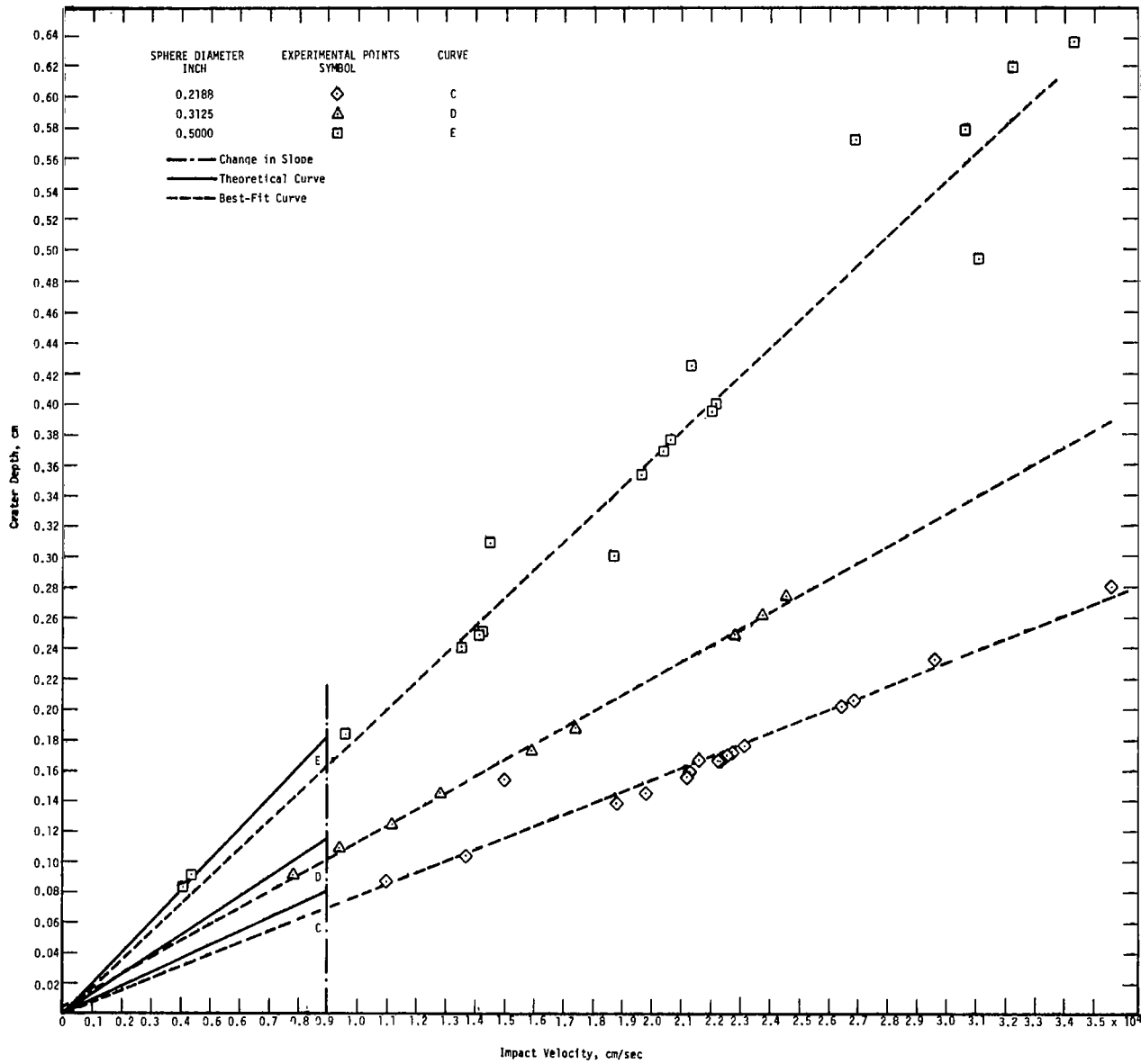


Figure 6.3. Theoretical Curves and Experimental Data for Impacts of Steel Spheres Against Electrolytic Tough Pitch Copper.

Table 6.10

Results of Analysis of Liquid-Drop Cratering Data for Electrolytic Tough Pitch Copper

SECTION A. Linear Best-Fit Equation for Crater Depth As a Function of Impact Velocity

DROP DIAM., cm	SLOPE OF LINE, 10^{-4} sec		CRATER-DEPTH INTERCEPT, cm		VELOCITY INTERCEPT, $\frac{\text{cm}}{\text{sec}}$		F- RATIO	STD. DEV.	NUMBER OF POINTS
	Value Found	95% Confidence Range	Value Found	95% Confidence Range	Value Found	95% Confidence Range			
	-----DATA FOR MERCURY DROPS-----								
0.1	0.01472	0.01393 to 0.01550	-0.01221	-0.01680 to -0.007622	8295	5570 to 11021	7.497	0.0052	27
0.2	0.03449	0.03138 to 0.03759	-0.03036	-0.04289 to -0.01783	8804	5911 to 11697	0.872	0.0108	30
	-----DATA FOR WATERDROPS-----								
0.2	0.003509	0.001630 to 0.005389	-0.01230	-0.02429 to -0.0003221	35058	18980 to 51137	0.200	0.0035	10

SECTION B. Average Linear Best-Fit Equation

DROP DIAM., cm	SLOPE OF LINE, sec	CRATER-DEPTH INTERCEPT, cm	VELOCITY INTERCEPT, cm/sec	CONSTANT, k^* , sec/cm
	-----DATA FOR MERCURY DROPS-----			
0.1	0.0148482×10^{-4}	-0.0128966	8685.63	0.148482×10^{-4}
0.2	0.0354626×10^{-4}	-0.0341077	9617.94	0.177313×10^{-4}
	-----DATA FOR WATERDROPS-----			
0.2	$0.00451602 \times 10^{-4}$	-0.0186080	41204.4	0.0225801×10^{-4}

Consideration of the width of the 95 percent confidence range of the slopes of the lines in comparison with the values found indicates that the slopes of the lines are reasonably well known for the mercury-drop data. However, the slope is known with much less certainty for the waterdrop data. Consideration of the width of the 95 percent confidence range of the velocity intercepts in comparison with the values found indicates that the velocity intercepts for the mercury-drop data are known with less certainty than the slopes of the lines. In the case of the waterdrop data, the velocity intercept is known to about the same degree of certainty as the slope of the line.

Consideration of the width of the 95 percent confidence range of the velocity intercepts in comparison with the values found in Tables 6.9 and 6.10 shows that the velocity intercepts for the liquid-drop cratering data are known with considerably more certainty than the velocity intercepts for the steel-sphere cratering data. The reason for this appears to be that the velocity intercepts of the liquid-drop cratering data are large numbers and that the lowest velocities at which data were collected are reasonably close to the value of the intercept velocity.

6.1.4 Solutioned Udimet 700 Alloy

The cratering data obtained for solutioned Udimet 700 alloy with use of 0.175-inch and 0.0938-inch spheres are listed in Table 6.11. The special circumstances that were employed are also recorded in this table.

Two velocity-depth inversions occur in this set of data points. Among the firings made with 0.175-inch spheres using the smooth-bore gun, the 0.0236-cm-deep crater produced in a 1-inch-thick specimen of solutioned Udimet 700 was formed at a higher velocity than the 0.0243-cm-deep crater produced in a standard 0.5-inch-thick specimen. However, from Table 6.6 it can be seen that the 0.0582-cm-deep crater produced in a 1-inch-thick specimen of nickel was formed at a lower

Table 6.11
Cratering Data for Solutioned Udimet 700

Measured Velocity, cm/sec	Corrected Velocity, cm/sec	Crater Depth, cm	Special Circumstances
-----Sphere Diameter 0.4445 cm (0.175 inch)-----			
11290	10911.7	0.0243	Smooth-bore gun employed
11310	10931.2	0.0236	Smooth-bore gun; specimen 1 inch thick
15320	14835.7	0.0319	Smooth-bore gun employed
17730	17182.4	0.0369	Smooth-bore gun employed
21450	20804.6	0.0440	
24130	23414.1	0.0498	
26640	25858.1	0.0542	
-----Sphere Diameter 0.2383 cm (0.0938 inch)-----			
1378	1260.27	0.0014	
1440	1320.64	0.0012	
2772	2617.62	0.0028	
5358	5135.63	0.0058	
6257	6011.	0.0065	
6395	6145.37	0.0073	
7946	7655.59	0.0088	
10700	10337.2	0.0107	
13170	12742.3	0.0146	
14700	14232.	0.0154	
15120	14641.	0.0162	
16110	15605.	0.0182	
18390	17825.	0.0196	
18610	18039.2	0.0213	
23910	23199.9	0.0248	
26160	25390.7	0.0282	
28750	27912.7	0.0320	

velocity than the 0.0580-cm-deep crater produced in a standard 0.5-inch-thick specimen. On the basis of this evidence, it was concluded that velocity-depth inversions involving specimens of 1-inch and 0.5-inch thickness are the result of experimental error and are not related to the specimen thickness. The data point obtained with use of the 1-inch-thick specimen was used in determining the best-fit curve for impacts of 0.175-inch steel spheres against targets of solutioned Udimet 700 alloy.

A velocity-depth inversion also occurs in the two lowest velocity firings made with 0.0938-inch spheres. The craters produced by these firings are so shallow that the depth-measuring techniques that were employed were probably inadequate for their measurement. Curve fitting was carried out both with and without these data points.

In the case of two nickel specimens, the craters produced by firings of 0.175-inch spheres with the smooth-bore gun were found to be shallow by about 0.001 cm compared with craters produced by the same size of sphere fired with the rifled-bore gun. Because more than 50 percent of the data points for impacts of 0.175-inch spheres against solutioned Udimet 700 were obtained with use of the smooth-bore gun it was possible to assess the significance of this observation. Best-fit curves were calculated separately for the smooth-bore firings against solutioned Udimet 700 and for the rifled-bore firings.

The average equations found are:

For smooth-bore firings: $\delta = 0.0200255 \times 10^{-4} V + 0.00237701$

For rifled-bore firings: $\delta = 0.0202437 \times 10^{-4} V + 0.00204616$

These equations are closely similar. For a velocity of 1×10^4 cm/sec, the depth of crater produced by the smooth-bore gun is 0.0224 cm and that produced by the rifled-bore gun is 0.0223 cm. It was concluded that differences of 0.0001 cm in the depths of craters produced by smooth-bore and rifled-bore firings are not significant and that these firings should not be treated separately.

The slope and intercept of the best-fit straight line found with impact velocity as the independent variable for all seven impacts of 0.175-inch steel spheres against solutioned Udimet 700 are given in Table 6.12 A. The F-ratio obtained in conjunction with the number of data points indicates that curvature is not significant. However, not only the intercept velocity but both of the 95 percent confidence limits on the intercept velocity are negative. The slope and intercept of the average best-fit equation for all seven impacts of 0.175-inch steel spheres against solutioned Udimet 700 are given in Table 6.12 B. This equation, which is considered to be the most representative of the data points, is plotted with a dashed line in Figure 6.4. The intercept velocity of the average equation is also negative in sign.

The finding of a negative intercept velocity suggests that solutioned Udimet 700 may be behaving like nickel, which is its major constituent. Unfortunately, no cratering data at velocities below 1.091×10^4 cm/sec were collected for impacts of 0.175-inch spheres against solutioned Udimet 700. Had firings at lower velocities been made, significant curvature may have been found in the best-fit curve for all of the data points, the slope of the low-velocity section of the cratering curve may have been found to be higher than the slope reported for the seven data points in Table 6.12, and the velocity intercept of the low-velocity section of the cratering curve may have been found to be positive. This is speculation; the actual locus of the cratering curve for solutioned Udimet 700 using 0.175-inch spheres can only be known by collecting more cratering data.

The slope and intercept of the best-fit straight line found with impact velocity as the independent variable for all 17 data points obtained with firings of 0.0938-inch steel spheres against solutioned Udimet 700 are given in Table 6.12 A. The F-ratio obtained for the 17 data points in conjunction with the number of data points indicates that there is no significant curvature. However, the cratering data

TABLE 6.12

Results of Statistical Analysis of Data Obtained for Steel-Sphere Impacts Against Solutioned Udimet 700

SECTION A. Linear Best-Fit Equation for Crater Depth As a Function of Impact Velocity

DATA POINTS CONSIDERED	SLOPE OF LINE, 10^{-4} sec		CRATER-DEPTH INTERCEPT, cm		VELOCITY INTERCEPT, $\frac{\text{cm}}{\text{sec}}$		F-RATIO	STD. DEV.	NUMBER OF POINTS
	Value Found	95% Confidence Range	Value Found	95% Confidence Range	Value Found	95% Confidence Range			
-----DATA FOR 0.175-inch SPHERES-----									
All Points	0.02040	0.01996 to 0.02083	0.001700	0.0008931 to 0.002508	-834	-1247 to -421	0.2007	0.00032	7
-----DATA FOR 0.0938-inch SPHERES-----									
All Points	0.01124	0.01088 to 0.01160	-0.000079	-0.0006114 to 0.000454	70	-402 to 542	0.0037	0.00060	17
6 below 6500 cm/sec	0.01173	0.01077 to 0.01270	-0.000232	-0.0006471 to 0.000184	197	-142 to 537	0.0903	0.00025	6
11 above 6500 cm/sec	0.01127	0.01052 to 0.01203	-0.000150	-0.001518 to 0.001218	133	-1072 to 1339	0.0196	0.00075	11

SECTION B. Average Linear Best-Fit Equation

DATA POINTS CONSIDERED	SLOPE OF LINE, sec	CRATER-DEPTH INTERCEPT, cm	VELOCITY INTERCEPT, cm/sec	CONSTANT, k^* , sec/cm
-----DATA FOR 0.175-inch SPHERES-----				
All Points	0.0204029×10^{-4}	0.00169019	-828.407	0.0459008×10^{-4}
-----DATA FOR 0.0938-inch SPHERES-----				
All Points	0.0112626×10^{-4}	-0.00010558	93.7244	0.0472718×10^{-4}
6 below 6500 cm/sec	0.0117738×10^{-4}	-0.000246666	209.504	0.0494174×10^{-4}
11 above 6500 cm/sec	0.0113298×10^{-4}	-0.000247686	218.615	0.0475538×10^{-4}

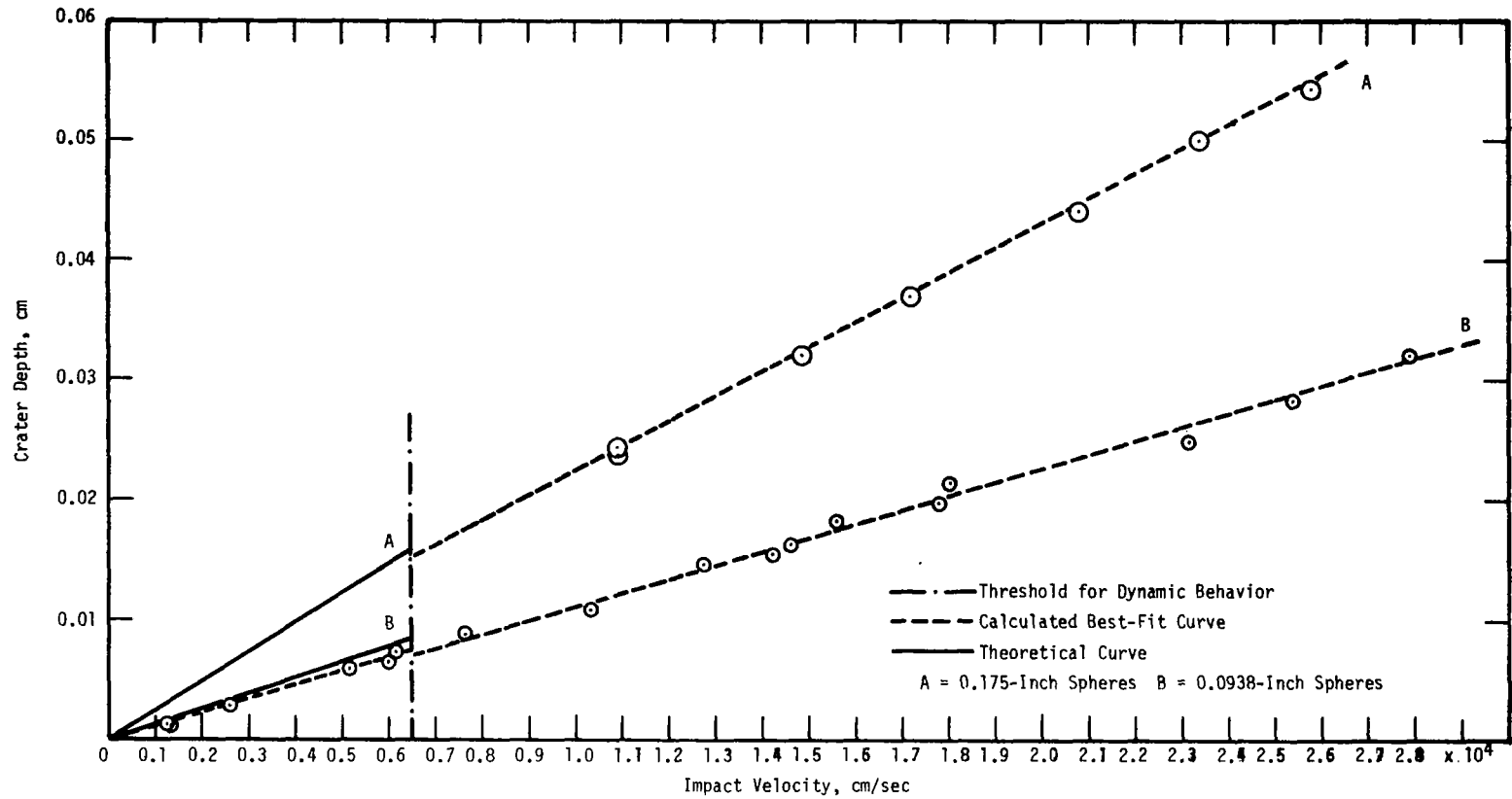


Figure 6.4. Theoretical Curves and Experimental Data for Impacts of Steel Spheres Against Solutioned Udimet 700 Alloy.

obtained for impacts of 0.0938-inch spheres against nickel also showed no significant curvature. In view of the possibility (see above) that solutioned Udimet 700 may be behaving like nickel, curve fitting was performed separately on the data points above and below 6500 cm/sec as was done in the case of nickel. The slopes and intercepts of the best-fit lines that were obtained are also given in Table 6.12 A. The values of F-ratio obtained, in conjunction with the number of data points used in determining each line, indicates that there is no significant curvature in either velocity range. The average equations given in Table 6.12 B are plotted with dashed lines in Figure 6.4.

If a change in slope of the cratering curve is characteristic of solutioned Udimet 700, it is more likely that it is due to work-hardening than to a dynamic elevation in yield strength because the change in slope is a decrease rather than an increase. However, there is some evidence that suggests that some elevation in yield strength may occur. Although the velocity intercept for the best-fit line of the data points obtained with 0.0938-inch spheres below 6500 cm/sec is substantially higher than that of the best-fit line for all of the data points, the velocity intercept for the best-fit line of the data points above 6500 cm/sec is higher than that of the data points below 6500 cm/sec. This suggests that the high-velocity branch of the cratering curve may be translated to the right along the velocity axis with respect to the low-velocity branch and that an elevated dynamic yield strength may be involved.

The ratio of the slope of the best-fit line below 6500 cm/sec to the slope of the best-fit line above 6500 cm/sec for 0.0938-inch spheres is 1.04. This corresponds to a 4 percent reduction in slope. In the case of impacts of 0.0938-inch spheres against nickel, the reduction in slope was 29 percent. If the reduction in slope is the result of work-hardening, it would be expected that the slope of the nickel curve would be reduced more than that of the solutioned Udimet 700 curve because nickel work-hardens more than solutioned Udimet 700

(see Section 5.4). The ratio of 4 percent reduction found for solutioned Udimet 700 to 29 percent reduction found for nickel is 0.14. The value of this ratio compares with that of the ratio of the asymptotic hardnesses of solutioned Udimet 700 and nickel. The asymptotic hardnesses of solutioned Udimet 700 and nickel (see Table 5.2) are 375 and 57.09, respectively. The ratio of 57.09 to 375 is 0.15. Comparison of the values of these ratios suggests that the change in slope of the crater-depth-versus-velocity plots of two metals due to work-hardening may vary inversely as their asymptotic hardnesses.

In summary, the cratering behavior of solutioned Udimet 700 is not known with a high degree of assurance. Although the data collected with 0.0938-inch spheres suggest that the cratering curve for solutioned Udimet 700 may have a change in slope due to work-hardening, as was found in the case of nickel, no low-velocity data collected with 0.175-inch spheres (or with spheres of any substantially larger diameter) are available to substantiate this possibility. In addition, there is some evidence which suggests that an elevated dynamic yield strength may be involved. However, there are no independent data, such as determinations of tensile yield strength at reduced temperatures, to substantiate the evidence.

6.1.5 Aged Udimet 700 Alloy

The cratering data obtained for aged Udimet 700 alloy with use of 0.175-inch and 0.0938-inch spheres are listed in Table 6.13. The special circumstances that were employed are also recorded in this table. There are no velocity-depth inversions in this set of data points. The data points are plotted in Figure 6.5 using the same scale as that employed for solutioned Udimet 700 in Figure 6.4.

From Figure 6.5 it can be seen that, as in the case of solutioned Udimet 700, no data points for impacts of 0.175-inch spheres were obtained in the low-velocity range. Furthermore, it can be seen that,

Table 6.13
Cratering Data for Aged Udimet 700

Measured Velocity, cm/sec	Corrected Velocity, cm/sec	Crater Depth, cm	Special Circumstances
-----Sphere Diameter 0.4445 cm (0.175 inch)-----			
11100	10726.7	0.0223	Smooth-bore gun; specimen 1 in. thick
11300	10921.4	0.0224	Smooth-bore gun employed
15420	14933.1	0.0306	Smooth-bore gun employed
17700	17153.2	0.0355	Smooth-bore gun employed
21360	20716.9	0.0429	
24130	23414.1	0.0489	
26670	25987.3	0.0549	
-----Sphere Diameter 0.2383 cm (0.0938 inch)-----			
1540	1418.01	0.0015	
2615	2464.75	0.0034	
3596	3419.95	0.0045	
6251	6005.15	0.0055	
7787	7500.77	0.0076	
10690	10327.5	0.0112	
13300	12868.8	0.0140	
14800	14329.4	0.0153	
16330	15819.2	0.0181	
16720	16198.9	0.0184	
18530	17961.3	0.0198	
18800	18224.2	0.0208	
24020	23307.	0.0254	
24110	23394.6	0.0260	
26570	25790.	0.0290	
28410	27581.6	0.0312	

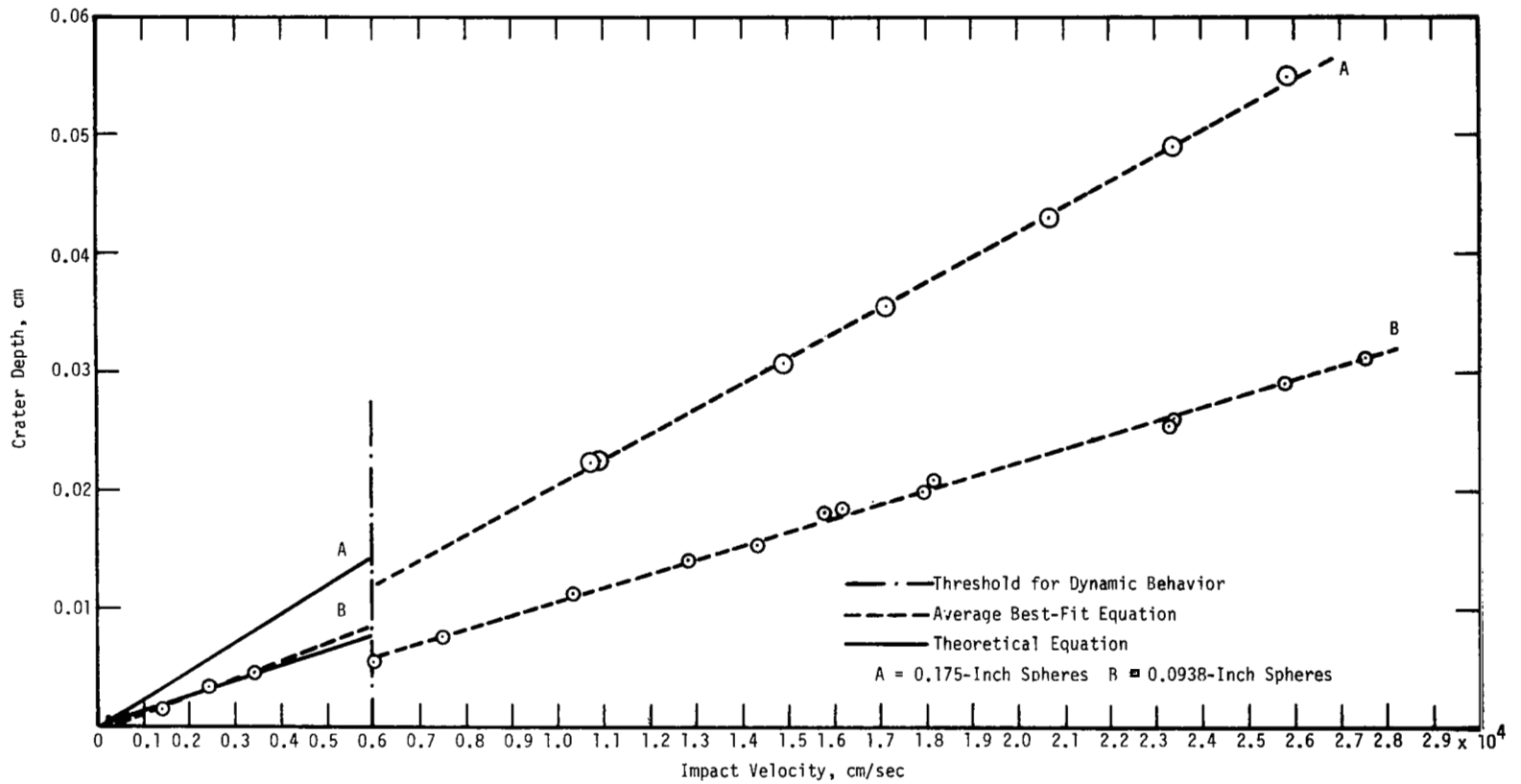


Figure 6.5. Theoretical Curves and Experimental Data for Impacts of Steel Spheres Against Aged Udimet 700 Alloy.

in the case of data points obtained with 0.0938-inch spheres, the point obtained at a velocity of 6005 cm/sec appears to belong to the high-velocity rather than to the low-velocity branch of the crater-depth-versus-velocity plot.

The slope and intercept of the best-fit straight line calculated with impact velocity as the independent variable for the seven data points obtained with use of 0.175-inch steel spheres are given in Table 6.14 A. The F-ratio, which is a measure of curvature, is 17.6. This value of the F-ratio for the seven data points considered indicates significant curvature. This is surprising in view of the fact that no significant curvature was found in the case of impacts of 0.175-inch spheres against solutioned Udimet 700. The sign of the x^2 term in the parabolic equation is positive which means that the curvature is convex toward the velocity axis. This type of curvature is opposite to that which was found in the case of nickel. The intercept velocity found from the crater-depth intercept and slope of the best-fit line is positive in sign and equal to 494 cm/sec. The finding of a positive velocity intercept for impacts of 0.175-inch spheres against aged Udimet 700 is again different from what was found in the analysis of the data collected for impacts of 0.175-inch spheres against solutioned Udimet 700.

The differences that have been cited suggest that the cratering behavior of aged Udimet 700 may be complicated by the instability that is characteristic of the aged condition of this alloy. It is quite possible that phase precipitation as a result of impact may be initiated in aged Udimet 700 as impact velocity is increased [18]. The precipitation of sigma phase in its characteristic basket-weave structure may tend to inhibit plastic flow of the metal and it is possible that inhibition of plastic flow in a metal may be associated with curvature in the crater-depth-versus-velocity plot (see Section 1.5.1). As part of a future study, it would be of interest to look for sigma phase in cross-sectional cuts of craters produced at increasing velocities.

Table 6.14

Results of Statistical Analysis of Data Obtained for Steel-Sphere Impacts Against Aged Udimet 700

SECTION A. Linear Best-Fit Equation for Crater Depth As a Function of Impact Velocity

DATA POINTS CONSIDERED	SLOPE OF LINE, 10^{-4} sec		CRATER-DEPTH INTERCEPT, cm		VELOCITY INTERCEPT, $\frac{\text{cm}}{\text{sec}}$		F-RATIO	STD. DEV.	NUMBER OF POINTS
	Value Found	95% Confidence Range	Value Found	95% Confidence Range	Value Found	95% Confidence Range			
-----DATA FOR 0.175-inch SPHERES-----									
All Points	0.02141	0.02087 to 0.02194	-0.001057	-.00205 to -.0000656	494	43 to 945	17.6	0.00039	7
-----DATA FOR 0.0938-inch SPHERES-----									
All Points	0.01122	0.01087 to 0.01158	-.0001624	-.000743 to 0.000418	145	-369 to 658	1.42	0.00058	16
3 below 6000 cm/sec	0.01504	0.01122 to 0.01886	-.0005268	-.001508 to 0.000454	350	-218 to 919	0	0.00027	3
13 above 6000 cm/sec	0.01165	0.01127 to 0.01202	-.001013	-.001693 to -.000333	870	312 to 1427	2.13	0.00044	13

SECTION B. Average Linear Best-Fit Equation

DATA POINTS CONSIDERED	SLOPE OF LINE, sec	CRATER-DEPTH INTERCEPT, cm	VELOCITY INTERCEPT, cm/sec	CONSTANT, k^* , sec/cm
-----DATA FOR 0.175-inch SPHERES-----				
All Points	0.0214138×10^{-4}	-0.00107153	500.392	0.0481750×10^{-4}
-----DATA FOR 0.0938-inch SPHERES-----				
3 below 6000 cm/sec	0.0151572×10^{-4}	-0.000556296	367.018	0.0636184×10^{-4}
13 above 6000 cm/sec	0.0116656×10^{-4}	-0.00104119	892.530	0.0489633×10^{-4}
All Points	0.0112414×10^{-4}	-0.000190239	169.231	0.0471828×10^{-4}

Curve fitting of the data points obtained in firings of 0.0938-inch spheres against aged Udimet 700 was carried out for all of the available 16 data points. The slope and intercept of the straight-line equation found with impact velocity as the independent variable are given in Table 6.14 A. The values of F-ratio obtained, in conjunction with the number of data points, indicate that curvature is not significant. This result is the same as that obtained for impacts of 0.0938-inch spheres against both solutioned Udimet 700 and nickel. This consistent observation suggests that work-hardening produced by impacts of 0.0938-inch spheres may be less extensive than that produced by impact of 0.175-inch spheres. Unfortunately, the study of Section 5.4 was not extended to include the smaller sphere size. This is another area that needs further investigation and it is suggested that a study of work-hardening produced by impacts of the smaller spheres should be made.

Curve fitting was also carried out considering that the three data points obtained below 6000 cm/sec may be fit by one straight line and that the remaining 13 data points may be fit by a different straight line. The calculated slopes and intercepts of the best-fit equations that were obtained, with impact velocity as the independent variable, are given in Table 6.14 A. The values of F-ratio found in obtaining these equations, in conjunction with the number of data points on which each equation is based, indicate that curvature is not significant. The slopes and intercepts of the average equations found for the groups of data points considered are given in Table 6.14 B. These equations are plotted with dashed lines in Figure 6.5.

The 95 percent confidence limits on the slope of the line found for the three data points at lowest velocities extend to ± 25.4 percent of the value found. This percentage range, in comparison with the range of ± 8.2 percent for impacts of 0.0938-inch spheres against solutioned Udimet 700 below 6500 cm/sec, indicates that the slope of the best-fit

line for aged Udimet 700 below 6000 cm/sec is known with less certainty than the slope of the best-fit line for solutioned Udimet 700 in this velocity range.

The ratio of the slope of the best-fit line below 6000 cm/sec to the slope of the best-fit line above 6000 cm/sec is 1.30. This corresponds to a 30 percent reduction in slope which compares closely with the 29 percent reduction in slope found in the cratering curve for impacts of 0.0938-inch spheres against nickel. This reduction in slope, as in the case of nickel and solutioned Udimet 700, may be the result of work-hardening. If this is the case, there is no ready explanation for the difference in the extent of reduction in slope for solutioned Udimet 700 and aged Udimet 700 because their work-hardening characteristics are similar (see Table 5.3) and, in addition, the tentative association of the extent of reduction in slope with the asymptotic hardness of a metal (see Section 6.1.4) is rendered questionable. It is possible that phase precipitation as a result of impact may contribute to the reduction in slope in the case of aged Udimet 700.

Inspection of the velocity intercepts given in Table 6.14 B shows that the value obtained for points below 6000 cm/sec is higher than the value obtained for all of the data points considered together. However, the value obtained for the data points above 6000 cm/sec is very much larger than that obtained for the data points below 6000 cm/sec. This suggests that the high-velocity branch of the cratering curve for aged Udimet 700 may be translated to the right along the velocity axis with respect to the low-velocity branch and that aged Udimet 700 may have an elevated dynamic yield strength.

In summary, the cratering behavior of aged Udimet 700, like that of solutioned Udimet 700, is not known with a high degree of certainty. There is a change in slope (decrease) of the crater-depth-versus-velocity plot as impact velocity is increased. This change in slope may be due

to work-hardening or to the effect of phase precipitation as the result of impact. Similarly, there is some evidence which suggests that aged Udimet 700 may have an elevated dynamic yield strength. More experimental evidence is needed to substantiate these possibilities. The extent of phase precipitation as the result of impact should be determined by studying cross-sectional cuts of craters produced in aged Udimet 700 at increasing velocities, and the possibility of an elevated dynamic yield strength should be explored by pulling tensile specimens at reduced temperatures.

6.1.6 Aluminum Based Alloy 2024-0 Aluminum

It was considered desirable to be able to compare the cratering response of pure aluminum and of an aluminum based alloy with that of nickel and a nickel based alloy. No cratering data for an aluminum based alloy were collected in the present study but cratering data for impacts of 0.5000-inch, 0.3125-inch, and 0.2188-inch steel spheres against 2024-0 aluminum were collected in an earlier study and have been tabulated [7]. These data, which are plotted in Figure 6.6, had never been subjected to a statistical analysis. Results of a statistical analysis of these data, which has been made in connection with the current study, are presented in Table 6.15.

From the value of the F-ratio and the number of data points for each sphere size, it was found that the data points for 0.5000-inch and 0.2188-inch spheres are fit best by straight lines. However, as in the case of electrolytic tough pitch copper (see Section 6.1.3), the F-ratio of the best-fit line for the 0.3125-inch spheres indicates significant curvature. However, in contrast with what was found in the case of electrolytic tough pitch copper, the standard deviation found for the 0.3125-inch spheres is not lower than that found for the other two sphere sizes.

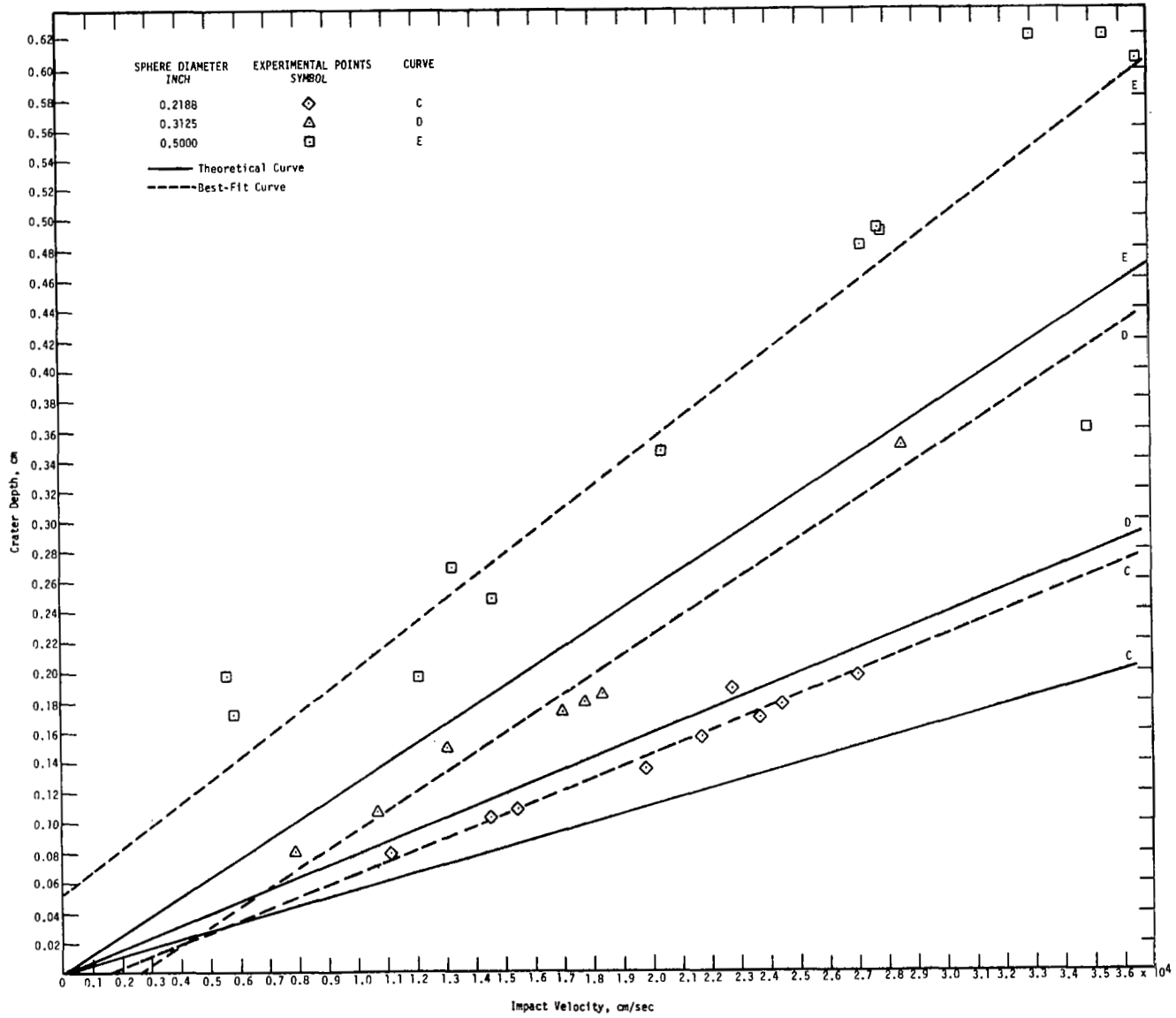


Figure 6.6. Theoretical Curves and Experimental Data for Impacts of Steel Spheres Against 2024-O Aluminum Alloy.

Table 6.15

Results of Statistical Analysis of the Cratering Data Obtained for 2024-0 Aluminum Alloy

SECTION A. Linear Best-Fit Equation for Crater Depth as a Function of Impact Velocity

SPHERE DIAM., inch	SLOPE OF LINE, 10^{-4} sec		CRATER-DEPTH INTERCEPT, cm		VELOCITY INTERCEPT, $\frac{\text{cm}}{\text{sec}}$		F- RATIO	STD. DEV.	NUMBER OF POINTS
	Value Found	95% Confidence Range	Value Found	95% Confidence Range	Value Found	95% Confidence Range			
0.5000	0.1362	0.09890 to 0.1736	0.083897	-0.009915 to 0.1777	-6158	-10240 to 1003	0.0027	0.0731	13
0.3125	0.1270	0.1079 to 0.1461	-0.03066	-0.06374 to 0.002431	2414	-166.4 to 5907	8.004	0.0157	7
0.2188	0.07710	0.06485 to 0.08935	-0.008642	-0.03396 to 0.01668	1121	-1867 to 5237	0.0014	0.0091	9

SECTION B. Average Linear Best-Fit Equation

SPHERE DIAM. inch	SLOPE OF LINE, sec	CRATER-DEPTH INTERCEPT, cm	VELOCITY INTERCEPT, cm/sec	CONSTANT, k^* , sec/cm
0.5000	0.150310×10^{-4}	0.0520184	(-0.3461×10^4)	0.118354×10^{-4}
0.3125	0.128810×10^{-4}	-0.0335595	0.2605×10^4	0.162280×10^{-4}
0.2188	0.0788060×10^{-4}	-0.0120584	0.1530×10^4	0.141801×10^{-4}

From the values of standard deviation given in Table 6.15, there is a large amount of scatter in the data; the standard deviation for each sphere size is larger than that found for the corresponding sphere sizes in the case of commercially pure aluminum (see Table 6.2). It is possible that the less homogeneous metallographic structure of an alloy in comparison with the structure of a pure metal may account in part for greater scatter in the cratering data of an alloy. However, comparison of the values of standard deviation found for two sphere sizes in the data for commercially pure nickel (see Tables 6.7 and 6.8) with those found for the same two sphere sizes in the data for the nickel based alloy Udimet 700 shows that the scatter is less for the nickel based alloy than for nickel. This suggests that the large amount of scatter that exists in the data for 2024-0 aluminum may be at least in part due to the techniques of data collection that were used.

It is informative to note that the value of the standard deviation decreases as the sphere size decreases (see Table 6.15). Two considerations suggest that this trend may be related to the data collection techniques that were employed. First, on impact large spheres intercept more grains in the target metal than small spheres intercept. On the basis of this consideration, cratering data for large spheres should show less scatter than those for small spheres. Secondly, in the case of a soft metal the pointed plunger, which is attached to a dial gauge and used to measure the crater depths, can pierce the metal at the bottom of a crater. This effect is more important in the relatively shallow craters produced by small spheres at any given impact velocity than in the deeper craters produced by larger spheres at this velocity. On the basis of this consideration, cratering data for large spheres should also show less scatter than those for small spheres.

Rejecting the anomalous negative value of the intercept velocity found for 0.5000-inch spheres, and basing the average value of this quantity on the data for 0.3125-inch and 0.2188-inch spheres, the

experimental value of the intercept velocity for impacts of steel spheres against 2024-0 aluminum alloy is 0.2×10^4 cm/sec (65.6 ft/sec). From the large difference in the intercept velocities for these sphere sizes in Table 6.15 B, it can be seen that the average value is unreliable. The velocity intercept is determined by a different method in Section 7.1.

Only three data points (two with use of 0.5000-inch and one with use of 0.3125-inch spheres) were collected at velocities below 10,000 cm/sec. This makes it impossible to know whether or not a low-velocity branch of the cratering curve, which has a higher value of slope than the values given in Table 6.15, exists for impacts of each sphere size used against 2024-0 aluminum. More cratering data in the low-velocity range will have to be collected to establish whether or not the cratering curve for 2024-0 aluminum changes slope as a result of work-hardening.

Comparison of the slope of the average best-fit straight line (see Section 3 of Table 6.2) of the alloy with that of the pure metal yields the following information. The ratio of the slope found for the alloy to that found for the pure metal is 0.5166 for 0.5000-inch spheres, 0.7925 for 0.3125-inch spheres, and 0.6176 for 0.2188-inch spheres. The value of the ratio for the 0.5000-inch spheres is considered to be unreliable because of the negative intercept velocity associated with the slope of the best-fit line for cratering data obtained for impacts of spheres of this size against 2024-0 aluminum. The average of this ratio, based on the other two sphere sizes, is 0.705.

Furthermore, the average value of the constant k^* , based only on the values found for 0.3125-inch and 0.2188-inch spheres, is 0.1520×10^{-4} sec/cm. Introducing this experimentally determined value for k^* into eq (2.23), it is found that the numerical constant k for steel-sphere impacts against 2024-0 aluminum is 12.396. The average value of the constant k for commercially pure aluminum is 16.19 (see Table 7.8).

As far as eq (2.21) is concerned, k is a numerical constant and should not be found to vary. From the statistical analysis of the cratering data for copper, the value of the constant k does not vary for pure face-centered-cubic metals. The fact that the constant k is different for a pure face-centered-cubic metal and for one of its alloys suggests that a dimensionless quotient may be missing from eq (2.21) and that this quotient is unity for pure face-centered-cubic metals. This dimensionless quotient may be related to the inhibition of plastic flow which is produced by the addition of alloying constituents. The question is considered further in Section 7.4.

6.2 Hexagonal Close-Packed Metals

Cratering data were collected for only one hexagonal close-packed metal; this metal is high-purity zinc. These data, which are for impacts of 0.175-inch and 0.0938-inch spheres, are listed in Table 6.16. Inspection of the data obtained with 0.0938-inch spheres yields the information that the three firings which resulted in craters having depths of 0.0158, 0.0157, and 0.0158 cm, respectively, appear to be involved in velocity inversions. However, inspection of the plot of the cratering data for zinc shown in Figure 6.7 suggested that a change in slope may occur in the velocity range over which these points were collected.

Curve fitting with use of the computer program⁽²¹⁾ was performed first on all 12 data points obtained for 0.175-inch spheres and for all 20 data points obtained for 0.0938-inch spheres. The results are given in Tables 6.17 and 6.18. From Table 6.17, it can be seen that the F-ratio for 0.175-inch spheres is 12.87 for the 12 data points. This value of the F-ratio for 12 data points indicates highly significant curvature; the curvature is convex toward the velocity axis. From Table 6.18 it can be seen that the F-ratio for 0.0938-inch spheres is 4.900 for 20 data points. This value of the F-ratio for 20 data points indicates that curvature is significant.

Table 6.16

Cratering Data for High-Purity Zinc

Measured Velocity cm/sec	Corrected Velocity, cm/sec	Crater Depth,	Special Circumstances
----- Sphere Diameter 0.4445 cm (0.175 inch) -----			
3319	3150.24	0.017	
6173	5929.21	0.0313	
9854	9513.43	0.0463	
11080	10707.2	0.0522	Smooth-bore gun; specimen 1 in. thick
11310	10931.2	0.0531	Smooth-bore gun employed
13060	12635.1	0.0621	
14850	14378.1	0.0702	Smooth-bore gun employed
16570	16052.9	0.0784	
17880	17328.4	0.0866	Smooth-bore gun employed
19630	19032.4	0.0934	
22750	22070.4	0.1078	
27430	26627.4	0.134	
----- Sphere Diameter 0.2383 cm (0.0938 inch) -----			
1360	1242.74	0.0036	
1520	1398.53	0.006	Not used in curve fit below 9000 $\frac{\text{cm}}{\text{sec}}$
2990	2829.89	0.0088	Not used in curve fit below 9000 "
5270	5049.95	0.0158	Not used in curve fit below 9000 "
5880	5643.91	0.0157	
6010	5770.49	0.0158	
7990	7698.44	0.0217	
10920	10551.4	0.0279	
11920	11525.1	0.0302	
14890	14417.	0.0368	
15070	14592.3	0.0378	
15340	14855.2	0.0383	
17660	17114.2	0.0432	
20310	19694.5	0.0501	
22930	22245.7	0.0563	
23870	23160.9	0.0583	
24060	23346.	0.0596	
25790	25030.5	0.0653	
26370	25595.2	0.0664	
28490	27659.5	0.0724	

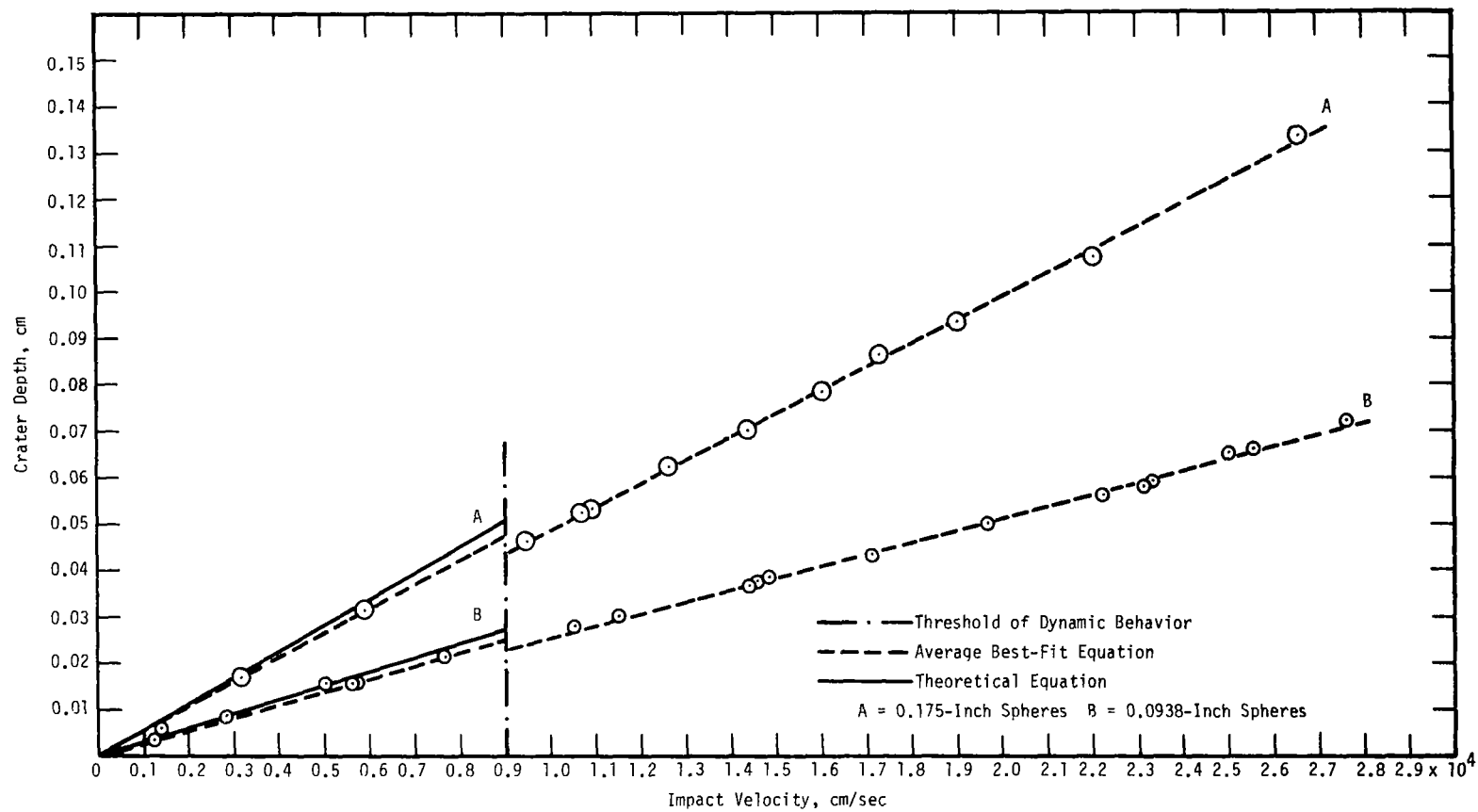


Figure 6.7. Theoretical Curves and Experimental Data for Impacts of Steel Spheres Against High-Purity Zinc.

Table 6.17

Results of Statistical Analysis of Cratering Data Obtained for Pure Zinc Using 0.175-inch Spheres

SECTION A. Linear Best-Fit Equation for Crater Depth as a Function of Impact Velocity

DATA POINTS CONSIDERED	SLOPE OF LINE, 10^{-4} sec		CRATER-DEPTH INTERCEPT, cm		VELOCITY INTERCEPT, $\frac{\text{cm}}{\text{sec}}$		F-RATIO	STANDARD DEVIATION
	Value Found	95% Confidence Range	Value Found	95% Confidence Range	Value Found	95% Confidence Range		
2 below 9000 cm/sec	0.05146	--- ---	0.0007895	--- ---	-153.4	--- ---	---	---
10 above 9000 cm/sec	0.05062	0.04944 to 0.05180	-0.002220	-.004197 to -.0002423	438.5	57.6 to 819.4	2.304	0.0009703
All 12 data points	0.04932	0.04809 to 0.05054	0.0001756	-.001710 to 0.002062	- 35.6	-418.8 to 347.6	12.87	0.0013545

SECTION B. Average Linear Best-Fit Equation

DATA POINTS CONSIDERED	SLOPE OF LINE, sec	CRATER-DEPTH INTERCEPT, cm	VELOCITY INTERCEPT, cm/sec	CONSTANT, k^* sec/cm
2 below 9000 cm/sec	0.0514578×10^{-4}	0.000789522	-0.0153431×10^4	0.115766×10^{-4}
10 above 9000 cm/sec	0.0506498×10^{-4}	-0.00226342	0.0446876×10^4	0.113948×10^{-4}
All 12 data points	0.0493556×10^{-4}	0.000122420	-0.00248037×10^4	0.111036×10^{-4}

Table 6.18

Results of Statistical Analysis of Cratering Data Obtained for Pure Zinc Using 0.0938-inch Spheres

SECTION A. Linear Best-Fit Equation for Crater Depth as a Function of Impact Velocity

DATA POINTS CONSIDERED	SLOPE OF LINE, 10^{-4} sec		CRATER-DEPTH INTERCEPT, cm		VELOCITY INTERCEPT, $\frac{\text{cm}}{\text{sec}}$		F-RATIO	STANDARD DEVIATION
	Value Found	95% Confidence Range	Value Found	95% Confidence Range	Value Found	95% Confidence Range		
4 below 9000 cm/sec	0.02783	0.02664 to 0.02901	.00003906	.0006265 to .0007046	-14.04	-253.8 to 225.7	3.394	0.0002805
13 above 9000 cm/sec	0.02573	0.02489 to 0.02656	-.0000019	-.001666 to .0016619	0.731	-645.9 to 647.4	21.617	0.0008221
All 20 data points	0.02499	0.02450 to 0.02547	.00158964	.0007956 to .0023836	-636.2	-964.5 to -307.8	4.900	0.0009233

174

SECTION B. Average Linear Best-Fit Equation

DATA POINTS CONSIDERED	SLOPE OF LINE, sec	CRATER-DEPTH INTERCEPT, cm	VELOCITY INTERCEPT, cm/sec	CONSTANT, k^* , sec/cm
4 below 9000 cm/sec	0.0278398×10^{-4}	0.0000326310	0.00117210×10^4	0.116850×10^{-4}
13 above 9000 cm/sec	0.0257639×10^{-4}	-0.000073092	0.00283699×10^4	0.108137×10^{-4}
All 20 data points	0.0250088×10^{-4}	0.00156000	-0.0623780×10^4	0.104968×10^{-4}

Inspection of plots of the data points in Figure 6.7 with the help of a straight edge was informative. It suggested that the curvature indicated by the F-ratios may be the result of a displacement of data points obtained above 9000 cm/sec. The displacement is such that extrapolations of the curves for these data points intersect the velocity axis at a higher value of impact velocity than is found for extrapolations of the curves that fit the data below 9000 cm/sec. No change in the density or sound speed of the metals is expected to take place; consequently, with reference to eq (2.33), the displacement of the cratering curve suggests that at velocities above 9000 cm/sec zinc may have an elevated dynamic yield strength. The F-ratio for the 0.0938-inch spheres indicated that curvature was just significant and, for this sphere size, the displacement of the points above 9000 cm/sec with respect to the points below 9000 cm/sec is much less marked.

Curve fitting of the data points above and below 9000 cm/sec was performed for each sphere size. In the case of the data points obtained at velocities below 9000 cm/sec with 0.0938-inch spheres, three data points at velocities of 1398.53, 2829.89, and 5049.95 cm/sec were deleted because in the plot of Figure 6.7 these points show considerable scatter with respect to the other data points below 9000 cm/sec. The results of the curve fitting are given in Tables 6.17 and 6.18.

From the tabulated data, it can be seen that for each size of sphere there is very little difference in the slopes of the best-fit lines above and below 9000 cm/sec; for 0.175-inch and 0.0938-inch spheres, the changes in slope are 1.6 and 7.5 percent decreases, respectively. On the other hand, it can be seen that for each size of sphere there is a marked increase in the velocity intercept for the data points above 9000 cm/sec as compared with the velocity intercept for the data points below 9000 cm/sec. This is the result of the displacement of the high-velocity branch with respect to the low-velocity branch of the cratering curve and points to the possibility that zinc

may have an elevated dynamic yield strength for impacts delivered at velocities above 9000 cm/sec. More will be said about this in Section 7.

In the case of the 10 data points collected with use of 0.175-inch spheres above 9000 cm/sec, the value of 2.304 for the F-ratio indicates that curvature is not significant. Because only two data points were collected with the use of 0.175-inch spheres below 9000 cm/sec, curvature in the low-velocity branch of the cratering curve cannot be assessed. On the basis of the available information, it appears that the curvature which was found when all 12 data points were curve fitted together was produced by a displacement between two straight lines.

The value of 3.394 found for the F-ratio of the 4 data points collected with 0.0938-inch spheres below 9000 cm/sec also indicates that curvature is not significant. However, the F-ratio for the data points collected with 0.0938-inch spheres above 9000 cm/sec has a value which indicates that curvature is highly significant. To clarify this anomalous observation, more cratering data for zinc above 9000 cm/sec should be collected with use of 0.0938-inch spheres.

The experimental value of the constant k for high purity zinc can be calculated from eq (2.23) with use of the experimental value of the constant k^* . On substituting the values of the constant k^* given in Tables 6.17 and 6.18 into eq (2.23), the values of the constant k were found to be as follows: for 0.175-inch spheres below 9000 cm/sec, k is 11.41; for 0.0938-inch spheres below 9000 cm/sec, k is 11.52; for 0.175-inch spheres above 9000 cm/sec, k is 11.24; for 0.0938-inch spheres above 9000 cm/sec, k is 10.66. The average value of the constant k below 9000 cm/sec is 11.46 and the average value of the constant k above 9000 cm/sec is 10.95.

On the basis of the average values of the constant k above and below 9000 cm/sec, the decrease in slope is 4.5 percent. A decrease in slope was ascribed to work-hardening of the target metal (see Section 6.1.4) and it was suggested that the change in slope of two

metals due to work-hardening may vary inversely as their asymptotic hardness (see Section 6.1.6). The ratio of 4.5 percent reduction found for zinc to 29 percent reduction found for nickel is 0.16. The asymptotic hardness of nickel is 57.09 and that of zinc is 31.88. The ratio of the asymptotic hardnesses for nickel and zinc is not the same as the ratio of the reductions in slope as was found in considering nickel and solutioned Udimet 700 (see Section 6.1.6). Perhaps agreement could not logically be expected in view of the fact that zinc and nickel differ in lattice packing type whereas Udimet 700 is a nickel-based alloy with the same lattice packing type as its major constituent.

6.3 Body-Centered-Cubic Metals

Cratering data were collected for two body-centered-cubic metals. These metals are Armco iron and arc-cast tantalum.

6.3.1 Armco Iron

Cratering data for impacts of 0.175-inch and 0.0938-inch steel spheres against Armco iron are listed in Table 6.19. Inspection of the data for 0.0938-inch spheres in Table 6.19 shows the presence of two velocity-depth inversions. The 0.024-cm-deep crater was formed at a lower velocity than the shallower 0.0226-cm-deep crater and the 0.0453-cm-deep crater was formed at a lower velocity than the shallower 0.045-cm-deep crater. The craters that are 0.0226 cm and 0.0453 cm deep appear to be out of line with the other data points; they were not considered in determining the best-fit curve for the data.

Curve fitting with use of the computer program⁽²¹⁾ was performed first on all 12 data points obtained with use of 0.175-inch spheres and on 18 data points obtained with use of 0.0938-inch spheres. The results are given in Tables 6.20 and 6.21. From Table 6.20 it can be seen that the F-ratio for 0.175-inch spheres is 115.37 for the 12 data points. This value of the F-ratio for 12 data points indicates highly

Table 6.19
Cratering Data for Armco Iron

Measured Velocity, cm/sec	Corrected Velocity, cm/sec	Crater Depth, cm	Special Circumstances
-----Sphere Diameter 0.4445 cm (0.175 inch)-----			
3322	3153.16	0.0098	
6173	5929.21	0.0186	
9810	9470.59	0.03	
10870	10502.7	0.0334	Smooth-bore gun; specimen 1 in. thick
11300	10921.4	0.0349	Smooth-bore gun employed
13040	12615.7	0.0399	
15290	14806.5	0.048	Smooth-bore gun employed
16530	16013.9	0.0516	
17580	17036.3	0.0556	Smooth-bore gun employed
19580	18983.7	0.0623	
22830	22148.3	0.0745	
27480	26676.	0.0933	
-----Sphere Diameter 0.2383 cm (0.0938 inch)-----			
1362	1244.69	0.0019	
1416	1297.27	0.0022	
2902	2744.2	0.0054	Not used in curve fit below 10550 cm/sec
3757	3576.72	0.0074	Not used in curve fit below 10550 cm/sec
6182	5937.97	0.0095	
6317	6069.42	0.01	
7878	7589.38	0.0124	
10620	10259.3	0.0166	
12170	11768.5	0.0202	
14450	13988.6	0.024	
14770	14300.2	0.0226	Not used in curve fitting processes
15309	14825.	0.0255	
17620	17075.3	0.0298	
20710	20084.	0.0348	
23060	22372.2	0.0396	
23990	23180.4	0.0402	
24310	23589.4	0.0408	

Table 6.19 (Cont'd.)

Measured Velocity, cm/sec	Corrected Velocity, cm/sec	Crater Depth, cm	Special Circumstances
25870	25108.4	0.0453	Not used in curve fitting processes
26620	25906.8	0.045	
26460	27630.3	0.0494	

Table 6.20

Results of Statistical Analysis of Cratering Data for Armco Iron Using 0.175-inch Spheres

SECTION A. Linear Best-Fit Equation for Crater Depth As a Function of Impact Velocity

DATA POINTS CONSIDERED	SLOPE OF LINE, 10^{-4} sec		CRATER-DEPTH INTERCEPT, cm		VELOCITY INTERCEPT, $\frac{\text{cm}}{\text{sec}}$		F-RATIO	STANDARD DEVIATION
	Value Found	95% Confidence Range	Value Found	95% Confidence Range	Value Found	95% Confidence Range		
4 below 10550 cm/sec	0.03210	0.03185 to 0.03235	-.0003672	-.0005602 to -.0001741	114.4	55.04 to 173.7	23.32	0.0000720
8 above 10550 cm/sec	0.03705	0.03553 to 0.03858	-.0069618	-.0097111 to -.0042125	1878.8	1210.98 to 2546.7	68.22	0.0010350
All 12 data points	0.03507	0.03382 to 0.03632	-.003179	-.005108 to -.001249	906.4	385.4 to 1427.4	115.37	0.0013893

SECTION B. Average Linear Best-Fit Equation

DATA POINTS CONSIDERED	SLOPE OF LINE, sec	CRATER-DEPTH INTERCEPT, cm	VELOCITY INTERCEPT, cm/sec	CONSTANT, k^* , sec/cm
4 below 10550 cm/sec	0.0321005×10^{-4}	-0.000367497	0.0114483×10^4	0.0722171×10^{-4}
8 above 10550 cm/sec	0.0371007×10^{-4}	-0.00704348	0.189848×10^4	0.0834661×10^{-4}
All 12 data points	0.0351238×10^{-4}	-0.00325698	0.0927286×10^4	0.0790187×10^{-4}

Table 6.21

Results of Statistical Analysis of Cratering Data for Armco Iron Using 0.0938-inch Spheres

SECTION A. Linear Best-Fit Equation for Crater Depth as a Function of Impact Velocity

DATA POINTS CONSIDERED	SLOPE OF LINE, 10^{-4} sec		CRATER-DEPTH INTERCEPT, cm		VELOCITY INTERCEPT, $\frac{\text{cm}}{\text{sec}}$		F-RATIO	STANDARD DEVIATION
	Value Found	95% Confidence Range	Value Found	95% Confidence Range	Value Found	95% Confidence Range		
6 below 10550 cm/sec	0.01624	0.01590 to 0.01658	-.000003051	-.0002182 to -.0002121	1.88	-130.6 to 134.3	0.180	0.0001358
10 above 10550 cm/sec	0.01799	0.01743 to 0.01855	-.00113240	-.0022937 to 0.00002894	629.3	2.93 to 1255.8	1.158	0.0004535
All 18 data points	0.01757	0.01721 to 0.01794	-.00030991	-.0008853 to 0.00026550	176.34	-148.0 to 500.7	6.526	0.0006682

SECTION B. Average Linear Best-Fit Equation

DATA POINTS CONSIDERED	SLOPE OF LINE, sec	CRATER-DEPTH INTERCEPT, cm	VELOCITY INTERCEPT, cm/sec	CONSTANT, k^* , sec/cm
6 below 10550 cm/sec	0.0162448×10^{-4}	-0.00000498994	0.000307172×10^4	0.0681833×10^{-4}
10 above 10550 cm/sec	0.0180109×10^{-4}	-0.00116752	0.0648230×10^4	0.0755960×10^{-4}
All 18 data points	0.0175896×10^{-4}	-0.000329775	0.0187483×10^4	0.0738277×10^{-4}

significant curvature; the curvature is convex toward the velocity axis. From Table 6.21 it can be seen that the F-ratio for 0.0938-inch spheres is 6.526 for 18 data points. This value of the F-ratio for 18 data points indicates that curvature is significant.

Inspection of plots of the data points in Figure 6.8 suggested that the curvature indicated by the F-ratios may be the result of an increase in slope of the best-fit lines for the data points obtained at velocities above 10550 cm/sec. As a consequence of the increase in slope, extrapolations of the curves for these data points intersect the velocity axis at a higher value of impact velocity than is found for extrapolations of the curves that fit the data below 10550 cm/sec. Because no change in the density or sound speed of the metals is expected to take place, reference to eq (2.33) suggests that the increase in slope of the cratering data at velocities above 10550 cm/sec may be associated with an elevated dynamic yield strength.

Curve fitting of the data points above and below 10550 cm/sec was performed for each sphere size. In the case of data points obtained at velocities below 10550 cm/sec with 0.0938-inch spheres, two additional data points, at velocities of 2744.2 and 3576.72 cm/sec, were deleted because in the plot of Figure 6.8 these data points show considerable scatter with respect to the other data points below 10550 cm/sec. The results of the curve fitting are given in Tables 6.20 and 6.21.

From the tabulated data, it can be seen that, for each sphere size, there is a notable increase in the slope of the line; in the case of the data for 0.175-inch spheres, it is 15.6 percent and in the case of the data for 0.0938-inch spheres it is 10.9 percent. These percentage changes are higher than the percentage changes reported for zinc and they are increases rather than decreases as was found in the case of zinc. As a consequence of these increases in slope, there is a marked increase in the velocity intercept for the data points collected at

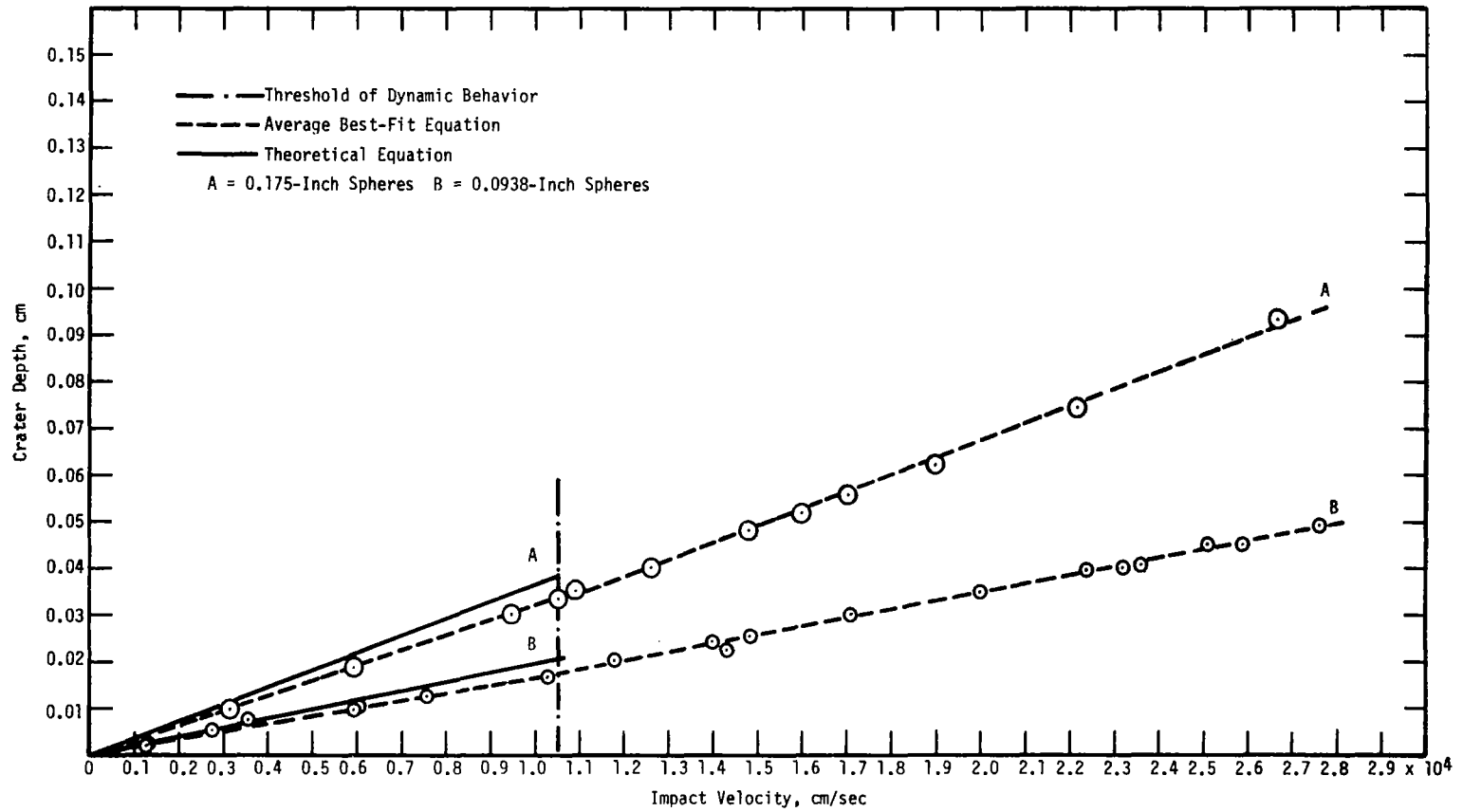


Figure 6.8. Theoretical Curves and Experimental Data for Impacts of Steel Spheres Against Armco Iron.

velocities above 10550 cm/sec with respect to the data points collected at velocities below 10550 cm/sec for each sphere size. As noted above, this result points to the possibility that iron may have an elevated dynamic yield strength for impacts delivered at velocities above 10550 cm/sec. See Section 7 for a further discussion of this point.

In the case of the data collected with 0.175-inch spheres, the F-ratio for the points that were collected below 10550 cm/sec is 23.32 and that for the points collected above 10550 cm/sec is 68.22. For the number of data points considered, the value of the F-ratio for the points collected below 10550 cm/sec indicates that curvature is not significant but that for the data points collected above 10550 cm/sec indicates that curvature is highly significant. This observation is the same as that made in the case of impacts of 0.0938-inch spheres against both zinc and aged Udimet 700 in the high-velocity branches of their cratering curves.

In the case of the data collected for impacts of 0.0938-inch spheres against iron, the value of the F-ratio for the 6 points below 10550 cm/sec is 0.180. This value of the F-ratio is not significant for the number of points considered. Similarly, for the 10 data points collected above 10550 cm/sec, the value of the F-ratio is 1.158 and this value of the F-ratio for the number of points considered is also not significant.

The finding of no curvature in either the low-velocity or the high-velocity branch of the cratering curve in the case of the small sphere size suggests that the finding of highly significant curvature in the high-velocity branch for 0.175-inch spheres may possibly be accidental. Inspection of the plot of the data in Figure 6.8 indicates that if the single point obtained at a velocity of 26676 cm/sec were to be deleted the curvature would vanish. It is possible that this data point is subject to error or even that it may mark the onset of a further increase in yield strength accompanied by a further increase in slope. For

clarification, more data should be collected for iron in this velocity range.

The experimental values of the constant k can be calculated from eq (2.23) with use of the experimental values of the constant k^* . Substitution of the values of the constant k^* given in Tables 6.20 and 6.21 produced the following values of the constant k for iron: for 0.175-inch spheres below 10550 cm/sec, k is 8.53; for 0.0938-inch spheres below 10550 cm/sec, k is 8.06; for 0.175-inch spheres above 10550 cm/sec, k is 9.86; for 0.0938-inch spheres above 10550 cm/sec, k is 8.93. The average value of the constant k below 10550 cm/sec is 8.3 and the average value of the constant k above 10550 cm/sec is 9.4. The change in the average value of the constant k represents a 13.3 percent increase in slope.

6.3.2 Tantalum

Cratering data for impacts of 0.175-inch and 0.0938-inch steel spheres against tantalum are listed in Table 6.22. Inspection of the data for 0.0938-inch spheres in Table 6.22 shows the presence of two velocity-depth inversions. The agreement of these data points with the other data points collected was considered to be sufficiently good to include them in the curve-fitting procedure.

Curve fitting with use of the computer program⁽²¹⁾ was performed first on all 11 data points obtained with use of 0.175-inch spheres and on all 18 data points obtained with use of 0.0938-inch spheres. The results are given in Tables 6.23 and 6.24. From Table 6.23, the F-ratio for 0.175-inch spheres is 16.9997 for the 11 data points, and from Table 6.24, the F-ratio for 0.0938-inch spheres is 20.815 for the 18 data points. Both of these values of F-ratio, for the numbers of points considered, indicate that curvature is highly significant.

Inspection of plots of the data points in Figure 6.9 suggested that, as in the case of iron, the curvature indicated by the F-ratios may be

Table 6.22

Cratering Data for Tantalum

Measured Velocity, cm/sec	Corrected Velocity, cm/sec	Crater Depth, cm	Special Circumstances
-----Sphere Diameter 0.4445 cm (0.175 inch)-----			
3320	3151.21	0.0094	
6135	5892.2	0.0184	
8851	9510.51	0.0290	
10810	10541.7	0.0318	Smooth-bore gun employed
11210	10833.8	0.0331	Smooth-bore gun; specimen 1 in. thick
13120	12693.6	0.0386	
15360	14874.7	0.0462	Smooth-bore gun employed
16540	16023.7	0.0492	
17610	17065.5	0.0526	Smooth-bore gun employed
19600	19003.2	0.0607	
22760	22080.1	0.0709	
-----Sphere Diameter 0.2383 cm (0.0938 inch)-----			
1413	1294.35	0.0018	
1493	1372.24	0.0027	
3086	2923.36	0.0055	Not used in curve fit below 18000 cm/sec
3597	3420.93	0.0074	Not used in curve fit below 18000 cm/sec
6012	5772.44	0.0088	
6084	5842.55	0.0089	
7716	7431.64	0.0122	
7807	7520.25	0.0118	
10030	9684.8	0.0156	
13250	12820.2	0.0215	
14612	14146.3	0.0232	
15202	14720.8	0.0241	
16720	16198.9	0.0266	
17420	16880.5	0.0277	
24000	23287.5	0.0404	
24060	23346.	0.0403	
26390	25614.7	0.0453	
28410	27581.6	0.0480	

Table 6.23

Results of Statistical Analysis of Cratering Data for Arc-Cast Tantalum Using 0.175-inch Spheres

SECTION A. Linear Best-Fit Equation for Crater Depth As a Function of Impact Velocity

DATA POINTS CONSIDERED	SLOPE OF LINE, 10^{-4} sec		CRATER-DEPTH INTERCEPT, cm		VELOCITY INTERCEPT, $\frac{\text{cm}}{\text{sec}}$		F-RATIO	STANDARD DEVIATION
	Value Found	95% Confidence Range	Value Found	95% Confidence Range	Value Found	95% Confidence Range		
9 below 18000 cm/sec	0.03093	0.03038 to 0.03148	-.0003178	-.0009770 to 0.0003414	102.7	-108.7 to 314.1	1.048	0.000358
2 above 18000 cm/sec	0.03315	-----	-.002296	-----	692.6	-----	-----	-----
All 11 data points	0.03221	0.03123 to 0.03318	-.001489	-.002851 to -.0001276	462.4	52.5 to 872.4	16.9997	0.000870

SECTION B. Average Linear Best-Fit Equation

DATA POINTS CONSIDERED	SLOPE OF LINE, sec	CRATER-DEPTH INTERCEPT, cm	VELOCITY INTERCEPT, cm/sec	CONSTANT, k^* , sec/cm
9 below 18000 cm/sec	0.0309430×10^{-4}	-0.000327353	0.0105792×10^4	0.0696130×10^{-4}
2 above 18000 cm/sec	0.0331502×10^{-4}	-0.00229608	0.0692629×10^4	0.0745786×10^{-4}
All 11 data points	0.0322406×10^{-4}	-0.00153222	0.0475245×10^4	0.0725323×10^{-4}

Table 6.24

Results of Statistical Analysis of Cratering Data for Arc-Cast Tantalum Using 0.0938-inch Spheres

SECTION A. Linear Best-Fit Equation for Crater Depth As A Function of Impact Velocity

DATA POINTS CONSIDERED	SLOPE OF LINE, 10^{-4} sec		CRATER-DEPTH INTERCEPT, cm		VELOCITY INTERCEPT, $\frac{\text{cm}}{\text{sec}}$		F-RATIO	STANDARD DEVIATION
	Value Found	95% Confidence Range	Value Found	95% Confidence Range	Value Found	95% Confidence Range		
12 below 18000 cm/sec	0.01660	0.01618 to 0.01703	-.0003196	-.0007788 to 0.0001396	192.5	-79.8 to 464.8	1.861	0.000384
4 above 18000 cm/sec	0.01836	0.01552 to 0.02120	-.002324	-.009432 to 0.004783	1266	-2409.5 to 4941.5	15.348	0.000506
All 18 data points	0.01738	0.01685 to 0.01791	-.0005741	-.001356 to 0.0002082	330.3	-111.5 to 772.08	20.815	0.000934

SECTION B. Average Linear Best-Fit Equation

DATA POINTS CONSIDERED	SLOPE OF LINE, sec	CRATER-DEPTH INTERCEPT, cm	VELOCITY INTERCEPT, cm/sec	CONSTANT, k^* , sec/cm
12 below 18000 cm/sec	0.0166152×10^{-4}	-0.000332404	0.0200060×10^4	0.0697379×10^{-4}
4 above 18000 cm/sec	0.0184709×10^{-4}	-0.00259865	0.140689×10^4	0.0775267×10^{-4}
All 18 data points	0.0174130×10^{-4}	-0.000613463	0.0352302×10^4	0.0730865×10^{-4}

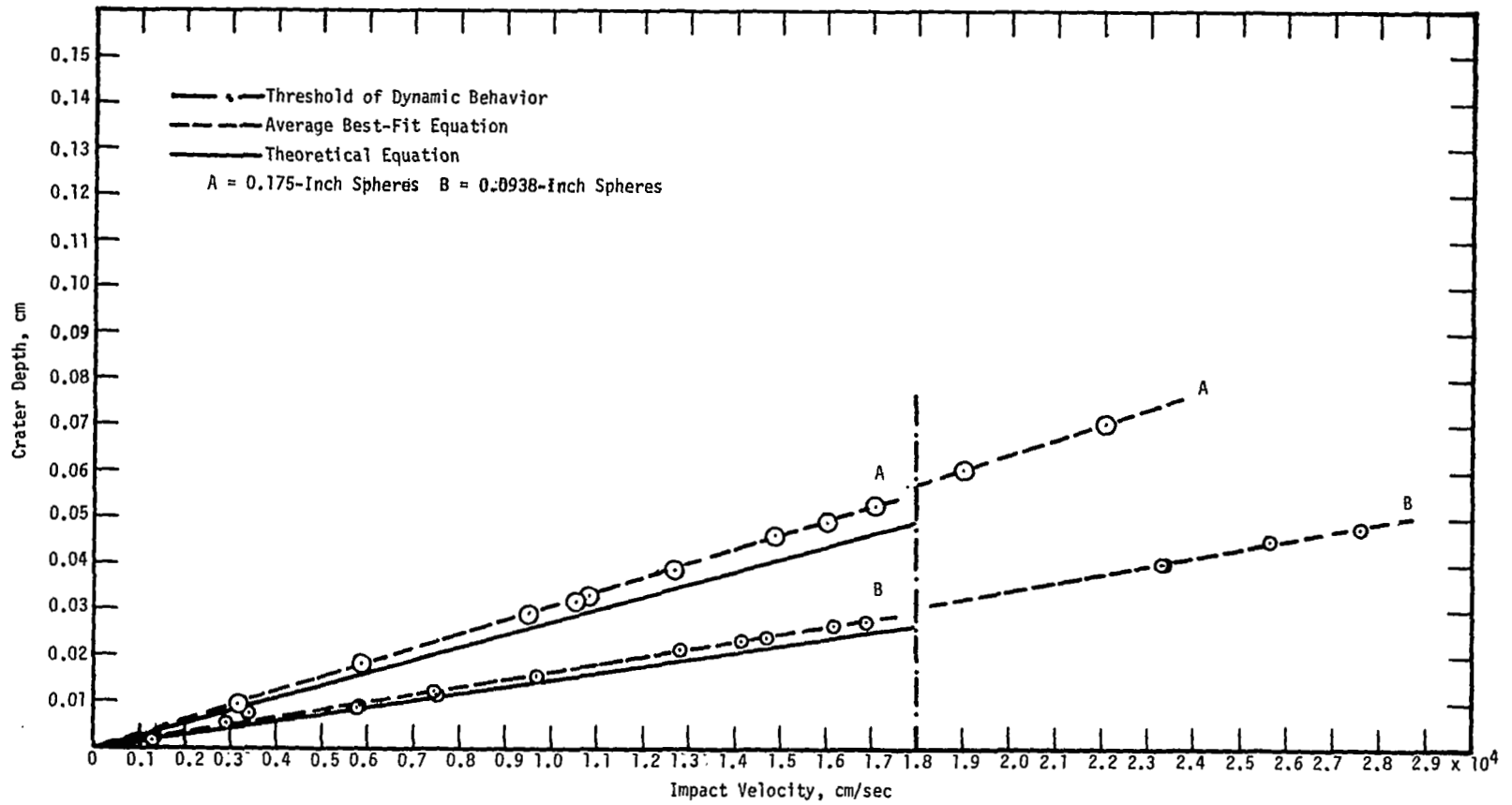


Figure 6.9. Theoretical Curves and Experimental Data for Impacts of Steel Spheres Against Tantalum.

the result of an increase in slope of the cratering curve. In the case of tantalum, the increase in slope occurs in the best-fit line for data points obtained at velocities above 18000 cm/sec. As a consequence of the increase in slope, extrapolations of the curves that fit the data points obtained at velocities above 18000 cm/sec intersect the velocity axis at a higher value of impact velocity than is found for extrapolations of the curves that fit the data below 18000 cm/sec. As in the case of iron, reference to eq (2.33) suggests that the increase in slope of the cratering curve at velocities above 18000 cm/sec may be associated with an elevated yield strength in view of the fact that no change in the density or sound speed of the metal is expected to take place.

Curve fitting of the data points above and below 18000 cm/sec was performed for each sphere size. In the case of data points obtained at velocities below 18000 cm/sec with 0.0938-inch spheres, two data points, at velocities of 2923.36 and 3420.93 cm/sec, were deleted because in the plot of Figure 6.9 these two points show noticeable scatter with respect to the other data points below 18000 cm/sec. The results of the curve fitting are given in Tables 6.23 and 6.24.

From the tabulated data it can be seen that for each sphere size there is a notable increase in the slope of the line; in the case of the data for 0.175-inch spheres it is 7.1 percent and in the case of the data for 0.0938-inch spheres it is 11.2 percent. As a consequence of the increases in slope, there is a marked increase in the velocity intercept of each sphere size for the data points collected at velocities above 18000 cm/sec with respect to the data points collected at velocities below 18000 cm/sec. As noted above, this finding points to the possibility that tantalum may have an elevated dynamic yield strength for impacts delivered at velocities above 18000 cm/sec. See Section 7 for a further discussion of this point.

In the case of the data collected for impacts of 0.175-inch spheres against tantalum, the value of the F-ratio for the points that were collected below 18000 cm/sec is 1.048. For the 9 data points considered, this value of the F-ratio indicates that curvature is not significant. Because only two points were considered at velocities above 18000 cm/sec, curvature in the high-velocity branch of the cratering curve cannot be assessed.

In the case of the data collected for impacts of 0.0938-inch spheres against tantalum, the value of the F-ratio for the 12 points below 18000 cm/sec is 1.861. This value of the F-ratio for the number of points considered indicates that curvature is not significant. For the 4 data points above 18000 cm/sec, the value of the F-ratio is 15.348; for 4 data points this value of the F-ratio indicates that curvature is not significant. Consequently, in the case of tantalum, no curvature is indicated in either the high-velocity or the low-velocity branch of the cratering curve for either size of sphere that was used.

The experimental values of the constant k can be calculated from eq (2.23) with use of the experimental values of the constant k^* . Substitution of the values of the constant k^* given in Tables 6.23 and 6.24 produced the following values of the constant k for tantalum: for 0.175-inch spheres below 18000 cm/sec, k is 10.14; for 0.0938-inch spheres below 18000 cm/sec, k is 10.16; for 0.175-inch spheres above 18000 cm/sec, k is 10.87; for 0.0938-inch spheres above 18000 cm/sec, k is 11.29. The average value of the constant k below 18000 cm/sec is 10.15 and the average value of the constant k above 18000 cm/sec is 11.08. It is noteworthy that, because the value of 10.87 for 0.175-inch spheres above 18000 cm/sec is based on only two data points, the value of the constant k above 18000 cm/sec may be closer to the value of 11.29 found with the 0.0938-inch spheres.

7. OBJECTIVES AND RESULTS

7.1 Steel-Sphere Denting Velocities of the Selected Metals

The first objective of the study that has been carried out was to determine the threshold velocity required to dent the selected metals by impact of steel spheres at room temperature. In planning the study, it was thought that this objective would be realized by obtaining the velocity intercepts of the crater-depth-versus-velocity plots. Unfortunately, one of the results of the statistical analysis described in Section 6 is that intercepts of crater-depth-versus-velocity plots are too poorly known to be of value in establishing reliable values of denting velocity.

In the limited time that was left to complete the study after this result of the statistical analysis became clear, recourse was taken to the method of obtaining denting velocity that was used by Davies [19]. However, because this attempt to obtain more accurate values of the denting velocities of the metals was restricted to a very limited period of time at the end of the study, the procedures used were considerably less refined than those employed by Davies.

7.1.1 Steel-Sphere Denting Velocities by the Method of Davies

Small, approximately half-inch thick test plates of the metals were prepared and annealed under the same conditions that were used for the impact specimens; tested impact specimens were used as test plates wherever this was feasible. One face of each test plate was given a minimum degree of polish and a 5/32-inch steel sphere was dropped against the polished surface from various heights.

For small distances, the fall height was determined by allowing the steel sphere to fall off the edge of a gauge block (or of several gauge blocks stacked one upon another) placed on the polished surface of the

test plate. For larger heights, the steel sphere was allowed to fall off the edge of a hole in a metal plate that was clamped to a rigid support. The perforated plate was adjusted until it was level to a bubble gauge; the height of the top surface of the plate above the polished surface of the test plate was determined by sighting across the plate to a steel rule the end of which was bearing against the polished surface of the test plate. An effort was made to minimize the horizontal velocity component of the steel sphere as it passed over the edge of the gauge block or over the edge of the perforation in the metal plate.

The indentations produced by the falling spheres were viewed with use of a microscope at low magnification. The reality of the craters was established by changing the focus of the microscope. A change in focus in one direction caused the craters to become spots of light; a change in focus in the opposite direction caused the craters to become dark circular spots.

Fall heights of 50, 25, and 15 mils were tried for 1100-0 aluminum. For the 50- and 25-mil fall heights, craters which showed the light-to-dark transition with a change in focus of the microscope could be seen. A view of the craters produced at the 25-mil fall height is shown in Figure 7.1. For the 15-mil fall height the craters, if any were produced, could not be located with assurance. Marks that were observed seemed to be only surface deformations; they did not show the light-to-dark transition with a change in focus of the microscope.

A fall height of 100 mils was first tried for 2024-0 aluminum. A view of the craters produced is shown in Figure 7.1. Although the craters produced were not well defined, they did show the light-to-dark transition with a change in focus of the microscope. An effort was made to detect a crater at a fall height of 75 mils. If any craters were produced at this fall height, they could not be located even by changing the microscope focus to look for light-to-dark transitions. A fall height of 150 mils was also tried; two very distinct craters were produced.

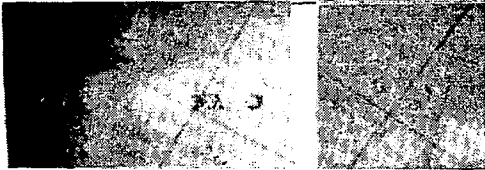
Fall heights of 100, 75, 50, and 25 mils were tried for electrolytic tough pitch copper. Four craters that were produced by the 50-mil fall and that showed the light-to-dark transition with a change of



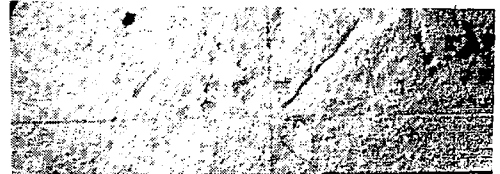
1100-0 Aluminum
Fall Height 0.0635 cm



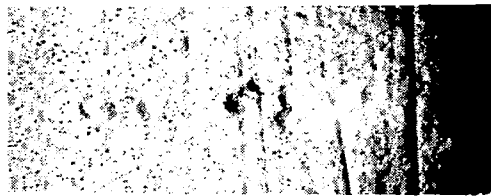
Armco Iron
Fall Height 0.635 cm



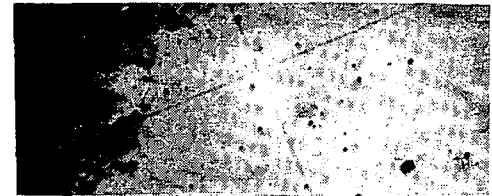
Nickel 270
Fall Heights 0.0635 and 0.0381 cm



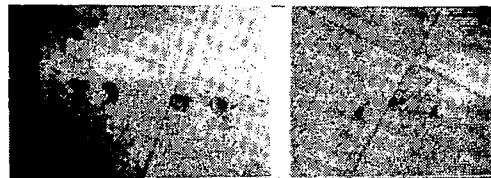
Arc Cast Tantalum
Fall Height 0.762 cm



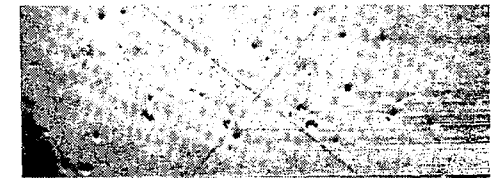
0.999 Zinc
Fall Height 0.127 cm



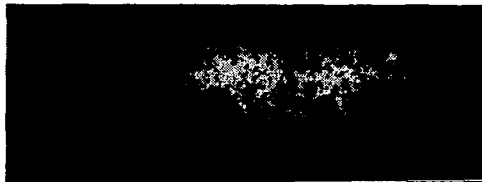
Udimet 700 Solutioned
Fall Height 1.95 cm



Electrolytic Tough Pitch Copper
Fall Heights 0.127 and 0.0635 cm



Udimet 700 Aged
Fall Height 2.10 cm



2024-0 Aluminum
Fall Height 0.254 cm



Magnification Key
Each Division = 1/2 mm

Figure 7.1. Views of Dents at Specified Fall Heights for the Metals Considered.

focus of the microscope are shown in Figure 7.1. Two well-defined craters that were produced by the 25-mil fall height are also shown; these craters are considerably smaller than those produced by the 50-mil fall.

Fall heights of 50, 25, and 15 mils were tried for nickel. Photographs of the craters that were produced by the 25- and 15-mil falls are shown in Figure 7.1. The very small craters produced by the 15-mil fall showed the light-to-dark transition with change in focus of the microscope.

Zinc recrystallizes as a result of mechanical working but it was necessary to polish the specimen to determine the denting velocity of the metal. It is not known to what extent the presence of a fine-grained re-crystallized surface layer of metal may have affected the denting fall height that was found. A view of craters produced at a 50-mil fall height are shown in Figure 7.1.

The minimum fall heights for iron and tantalum are larger than those found for the metals considered so far. To get sufficient height, gauge blocks were rubbed together to get good surface contact and stacked; the steel sphere was rolled off the edge of the gauge block at the top of the stack. Views of craters that were produced are shown in Figure 7.1.

To determine the large fall height required to dent Udimet 700, the movable perforated plate was used. In the case of aged Udimet 700, surface marks were produced at a fall height of 1.85 and 1.7 cm. However, these marks appeared to be without depth because they exhibited no shadow or light-to-dark transition. Views of craters formed in aged and solutioned Udimet 700 at fall heights that were judged to be close to those that would correspond to the denting velocities of these heat-treatment states of Udimet 700 are shown in Figure 7.1. In the case of solutioned Udimet 700, two craters that are smaller than the rest can be seen at the right of the micrograph. These smaller craters may have been produced by bounces of the steel sphere after its first impact and this suggests that the reported fall height may be too large.

The denting velocities were calculated from the heights of fall with use of the equation for falling bodies neglecting air resistance, that is, the denting velocity was taken to be given by

$$v_i = (2 g s)^{\frac{1}{2}} \quad (7.1)$$

where s is the fall height and g is the acceleration due to gravity; the local value of g is 980.004 cm/sec/sec. The velocities required to produce the craters in the selected metals, which are shown in Figure 7.1, are listed in Table 7.1.

Table 7.1

Steel-Sphere Denting Velocities of the Selected Metals

Metal	Fall Height, cm	Denting Velocity, cm/sec
1100-C Aluminum	0.0635	11.2
Nickel 270	0.0635	11.2
C.999 Zinc	0.127	15.8
Copper (electrolytic tough pitch)	0.127	15.8
2024-C Aluminum	0.254	22.3
Armco Iron	0.635	35.3
Arc Cast Tantalum	0.762	38.6
Udimet 700 Solutioned	1.95	61.8
Udimet 700 Aged	2.10	64.2

There is a feature inherent in the method of Davies [19] which makes it somewhat open to question. This feature is that a crater of microscopic dimensions is formed in a polished surface. If the depth of the crater that is produced is comparable to the thickness of the polish layer, then the denting velocity that is found is characteristic of the polish layer rather than of the bulk metal. The following check was made of this.

With recourse to the magnification key for the micrographs shown in Figure 7.1, the diameters of the larger craters are approximately 0.01 cm. Presuming that the craters are spherical indentations, their depth can be determined from the expression

$$(d/2)^2 = \delta (D - \delta) \quad (7.2)$$

where d is the crater diameter, D is the diameter of the spherical indenter, and δ is the crater depth. Because the diameter of the steel sphere that was dropped to produce the indentations was 5/32 inch (0.3967 cm), the crater depth corresponding to a crater diameter of 0.01 cm is 0.000063 cm (0.000025 inch).

The very thin surface layer work-hardening due to polishing can extend to 0.00002 or 0.00003 cm [20]. This is roughly half of the calculated depth of the larger craters shown in Figure 7.1. It can be hoped, therefore, that roughly half of the depths of the craters shown in Figure 7.1 were formed in metal that was not disturbed by the surface polishing operations which are necessary to make the craters visible.

The measured values of denting velocity given in Table 7.1 are certainly closer to the true denting velocities of the selected metals than the values that were obtained from the velocity intercepts of the crater-depth-versus-velocity plots. Nevertheless, because of the lack of refinement with which the method was carried out, they can be regarded only as improved approximations. For a specimen of armor plate WTN, having a yield strength of about 152,000 psi, Davies [19] found an average minimum fall height of 0.38 cm. The 0.2 percent offset yield strength of Udimet 700 is about 125,000 psi. Consequently, if the more refined techniques used by Davies had been employed, it could be expected that Udimet 700 might be found to have a minimum fall height as low as 0.32 cm. On comparing this value with the observed fall height for Udimet 700 in Table 7.1, it appears that the denting velocity given in Table 7.1 for Udimet 700 is too large by at least a factor of six.

7.1.2 Steel-Sphere Denting Velocities from the Energy Per Unit Volume Required for Flow

The denting velocity of a metal for impacts of steel spheres (see eq. (1.3) of Section 1) is

$$V_i = E' (z + z') / (\rho c' z'^3)^{1/2} \quad (7.3)$$

where V_i is the steel-sphere denting velocity, E' is the energy per unit volume required for flow, ρ is density, c is sound speed, and z is acoustic impedance; primed quantities refer to the target metal and unprimed

quantities refer to the steel of which the steel spheres are composed. The denting velocity can be calculated from eq (7.3) if the energy per unit volume required for flow can be assessed.

An effort was made to assess the energy per unit volume required for flow from the stress-strain curves of the selected metals. Copies of the autographic recording of the stress-strain curves produced by the tensile tests of the selected metals were supplied by the testing laboratories. The area under the stress-strain curve of each metal to the proportional limit, the 0.02 percent offset yield strength, and the 0.2 percent offset yield strength was determined by counting squares. The energy per unit volume per square was found from the load in pounds per division, the elongation in inch per inch per division, and the original cross-sectional area of the test specimen in square inches. The area (in squares) under the stress-strain curve up to any arbitrary point multiplied by the energy per unit volume per square is the energy per unit volume accepted by the test specimen up to the point selected.

In this way, the energies per unit volume accepted by each of the selected metals up to the proportional limit, the 0.02 percent offset yield strength, and the 0.2 percent offset yield strength were determined. The values of these quantities that were found for each of two test specimens, as well as the average value of each quantity, are given in Table 7.2. Accidental differences in the test specimens and/or their mounting in the test machine affect the onset of plastic flow. From the values of percent deviation from the average, given in Table 7.2 for iron, tantalum, nickel, and zinc, it can be seen that the percent deviation from the average in the energy per unit volume to the 0.2 percent offset yield strength is less for each of the four metals than the percent deviation in the energy per unit volume up to the proportional limit or up to the 0.02 percent offset yield strength. Presumably, this is due to size of the areas involved.

The energy per unit volume accepted by each of the selected metals up to the 0.2 percent offset yield strength is plotted against the 0.2 percent offset yield strength in Figure 7.2. Curve fitting of the nine data points was performed with use of the computer program⁽²¹⁾. The

Table 7.2

Energy per Unit Volume to Three Points on the Stress-Strain Curve^(a)

Energy per unit volume to Specimen	Proportional Limit, dyn/cm ²	0.02 Percent Offset Yield Strength, dyn/cm ²	0.2 Percent Offset Yield Strength, dyn/cm ²
Iron No. 1	8.296×10^5	1.265×10^6	3.874×10^6 (b)
Iron No. 2	5.757×10^5	9.126×10^5	3.723×10^6 (b)
Average	7.026×10^5	1.089×10^6	3.799×10^6
% Deviation from Avg.	18	16	2.0
Tantalum No. 1	8.380×10^5	1.479×10^6	4.212×10^6
Tantalum No. 2	7.733×10^5	1.260×10^6	4.224×10^6
Average	8.056×10^5	1.370×10^6	4.218×10^6
% Deviation from Avg.	4.0	8.0	0.14
Nickel No. 1	7.409×10^4	1.935×10^5	1.507×10^6
Nickel No. 2	2.427×10^4	1.517×10^5	1.374×10^6
Average	4.918×10^4	1.726×10^5	1.441×10^6
% Deviation from Avg.	50.6	12.1	4.6
Zinc No. 1	3.411×10^4	1.266×10^5	9.795×10^5
Zinc No. 2	3.201×10^4	1.380×10^5	9.479×10^5
Average	3.306×10^4	1.323×10^5	9.637×10^5
% Deviation from Avg.	3.2	4.3	1.6

(a) The stress-strain curves were obtained by J.J. Mulligan under the direction of G.R. Frey at the General Electric Company, Lynn, Massachusetts.

(b) The extensometer was unfortunately removed slightly before the 0.2 percent offset yield strength was reached. The effect of the ambiguity involved is negligibly small as far as the values given here are concerned.

Table 7.2 Continued

Energy per unit volume to Specimen	Proportional Limit, dyn/cm ²	0.02 Percent Offset Yield Strength, dyn/cm ²	0.2 Percent Offset Yield Strength, dyn/cm ²
Udimet 700 Solutioned No. 1	10.33 x 10 ⁶	1.556 x 10 ⁷	3.309 x 10 ⁷
Udimet 700 Solutioned No. 2	7.408 x 10 ⁶	1.243 x 10 ⁷	3.219 x 10 ⁷
Average	8.869 x 10 ⁶	1.400 x 10 ⁷	3.264 x 10 ⁷
Udimet 700 Aged No. 1	9.055 x 10 ⁶	1.358 x 10 ⁷	3.141 x 10 ⁷
Udimet 700 Aged No. 2	9.647 x 10 ⁶	1.530 x 10 ⁷	3.493 x 10 ⁷
Average	9.351 x 10 ⁶	1.444 x 10 ⁷	3.317 x 10 ⁷
1100-0 Aluminum No. 1(c)	5.198 x 10 ³	3.205 x 10 ⁴	3.197 x 10 ⁵
Copper (tough pitch) No. 1(c)	1.172 x 10 ³	2.972 x 10 ⁴	4.285 x 10 ⁵
Copper (tough pitch) No. 2(c)	3.054 x 10 ³	4.036 x 10 ⁴	4.863 x 10 ⁵
Average	2.113 x 10 ³	3.504 x 10 ⁴	4.574 x 10 ⁵
2024-0 Aluminum No. 1(c)	17.08 x 10 ⁴	4.549 x 10 ⁵	2.095 x 10 ⁶
2024-0 Aluminum No. 2(c)	5.934 x 10 ⁴	3.664 x 10 ⁵	1.973 x 10 ⁶
Average	11.51 x 10 ⁴	4.106 x 10 ⁵	2.034 x 10 ⁶

(c) The stress-strain curves were obtained by Lafayette Irwin, Mechanics Section, National Bureau of Standards. See Reference [7].

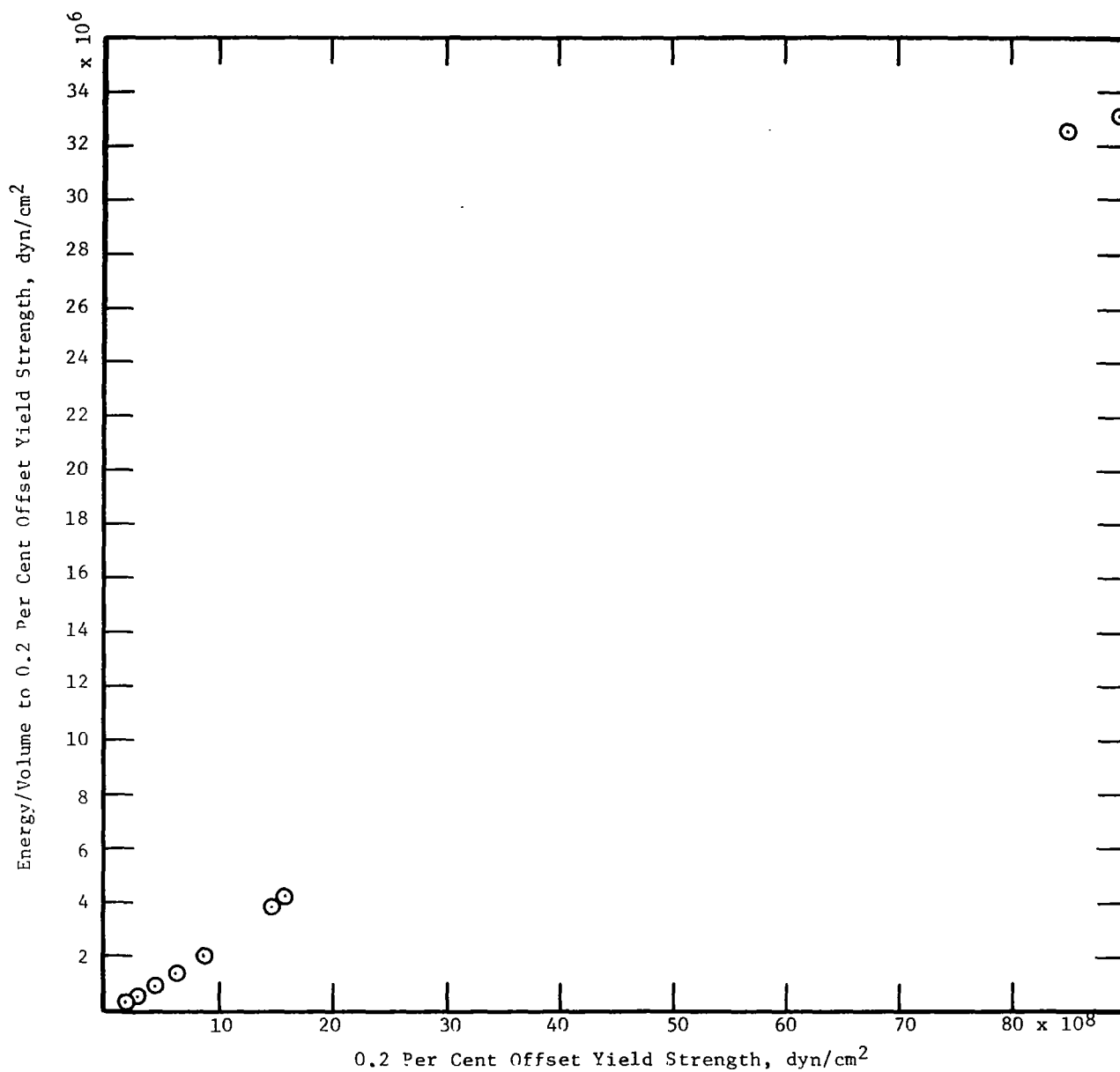


Figure 7.2. Plot of the Energy Per Unit Volume up to the 0.2 Per Cent Offset Yield Strength Against the 0.2 Per Cent Offset Yield Strength.

F-ratio of 10.31 that was obtained for the nine data points indicated that curvature was significant. The parabolic equation found for the nine data points by the curve fitting program is

$$Y = -379517 + 2.80699 \times 10^{-3}X + 1.13868 \times 10^{-13} X^2 \quad (7.4)$$

where Y is the energy per unit volume up to the 0.2 percent offset yield strength and X is the 0.2 percent offset yield strength.

It was thought that the curvature found may have been produced by the two points at the extreme upper right of the plot in Figure 7.2. These points are for Udimet 700 aged and Udimet 700 solutioned. Curve fitting with the computer program was performed a second time with the two points for Udimet 700 excluded. Six of the remaining seven data points are for pure metals; the remaining data point is for the relatively simple alloy 2024-0 aluminum. For the seven data points, the F-ratio was found to be 8.60 which indicates that curvature is also significant for the seven data points.

Values of denting velocity for the selected metals were calculated with use of eq (7.3) and the average energy per unit volume accepted by the metal up to the 0.2 percent offset yield strength given in Table 7.2. Other data needed for the calculation are given in Table 7.3. The calculated values of denting velocity found in this way for the selected metals are given in Table 7.4.

The values of denting velocity given in Table 7.4 are thought to be of the right order of magnitude. The value of 13.5 cm/sec for the denting velocity of aged Udimet 700 in Table 7.4 is roughly 1/5 of the value of 64.2 given for Udimet 700 in Table 7.1. It was pointed out at the end of Section 7.1.1 that, on the basis of the fall height found by Davies [19] for armor plate WTN, the denting velocity of Udimet 700 given in Table 7.1 is too large by about a factor of six. The fact that the calculated values of denting velocity for Udimet 700 in Table 7.4 are roughly one fifth of the values of denting velocity given for Udimet 700 in Table 7.1 suggests both that the calculated denting velocities given in Table 7.4 are of the right order of magnitude and that the energy per unit volume assessed up to the 0.2 percent offset yield strength is a good approximation of the flow energy per unit volume for cratering.

Table 7.3

Sound Speed, Density, and
Acoustic Impedance of the Metals Considered

Metal	Sound Speed, cm/sec	Density, g/cm ³	Acoustic Impedance, g/cm ² .sec
hardened 52100 steel	5.896 x 10 ⁵ (a)	7.81 ^(c)	4.605 x 10 ⁶
Armco iron	5.874 x 10 ⁵ (a)	7.874 ^(c)	4.625 x 10 ⁶
pure zinc	4.340 x 10 ⁵ (a)	7.133 ^(c)	3.096 x 10 ⁶
nickel 270	5.652 x 10 ⁵ (a)	8.902 ^(c)	5.031 x 10 ⁶
arc-cast tantalum	4.081 x 10 ⁵ (a)	16.6 ^(c)	6.774 x 10 ⁶
Udimet 700, aged	6.105 x 10 ⁵ (a)	7.92 ^(d)	4.835 x 10 ⁶
Udimet 700, solutioned	6.100 x 10 ⁵ (a)	7.92 ^(d)	4.831 x 10 ⁶
commercially pure aluminum	6.318 x 10 ⁵ (b)	2.713 ^(e)	1.714 x 10 ⁶
electrolytic tough pitch copper	4.691 x 10 ⁵ (b)	8.96 ^(c)	4.203 x 10 ⁶
2024-0 aluminum alloy	6.370 x 10 ⁵ (b)	2.768 ^(e)	1.763 x 10 ⁶

(a) Measured by H.A.F. Rocha, Manager of Nondestructive Testing Unit, General Electric Materials and Processes Laboratory, Schenectady, New York.

(b) Measured by C.E. Tschiegg, Sound Section, National Bureau of Standards, Washington, D.C.

(c) Data from Metals Handbook, American Society for Metals, 1961, Vol. I.

(d) General Electric Flight Propulsion Division Material Properties Data Handbook, Vol. II.

(e) Data from Aluminum Company of America.

Table 7.4

Calculated Values of Denting Velocity for the Selected Metals

Metal	Denting Velocity, cm/sec
Armco Iron	1.65
0.999 Zinc	0.74
Nickel 270	0.59
Arc-Cast Tantalum	1.52
Udimet 700 Aged	13.5
Udimet 700 Solutioned	13.3
1100-0 Aluminum	0.41
Copper (electrolytic tough pitch)	0.24
2024-0 Aluminum	2.48

This is a useful finding. The 0.2 percent offset yield strength is the yield strength that is commonly recorded in the literature and eq (7.4) provides a means of calculating the energy per unit volume from it.

It is hoped that it will be possible to measure the denting velocities of the selected metals again with use of a falling steel sphere and the refined techniques employed by Davies [19]. The test sections should be highly polished optical flats formed on thick plates of the metals. Care should be taken to remove all traces of grease from the steel sphere and from the highly polished test sections. With use of a fine thread, the steel sphere should be made the bob of a pendulum and, with the highly polished test section oriented into the vertical plane, the vertical fall height should be determined by the horizontal displacement of the pendulum bob. This horizontal displacement can be accurately measured and the pendulum can be caught by hand before a second impact (bounce) occurs. The optical methods employed by Davies should be used to detect the presence of a crater as the result of an impact and a large number of trials should be made to establish as exactly as possible the minimum fall height that is required to produce a detectable crater.

7.2 Denting Velocity at Elevated Temperatures

The second objective of the study that has been carried out was to determine the threshold velocity required to dent two of the selected metals by impact of steel spheres at four elevated temperatures. To determine denting velocity with firings at elevated temperatures the gun must be equipped with a heater capable of raising the temperature of the metal impact specimen to these temperatures. In addition, the gun chamber must be capable of being evacuated to a pressure of approximately 1×10^{-5} torr to prevent the formation of an oxide layer on the impact specimens; formation of an oxide layer would affect the value of the denting velocity that was measured.

It was pointed out in Section 4.7 that a sub-contract was issued to a reputable research institute to design and construct a gun having these capabilities. The gun that was designed and constructed by the sub-contractor proved to be inadequate to make the test firings because the sphere trajectories could not be controlled sufficiently to insure impact of the sphere against the 1-inch-diameter circular specimen plate. As a consequence of the failure of the sub-contractor to produce a usable gun, it was not possible to make the firings at elevated temperatures.

It is possible, however, to calculate the denting velocity of a metal at elevated temperatures. To be able to calculate values of acoustic impedance given by eq (1.2), and infinite medium sound speed given by eq (1.4), for a metal at elevated temperatures, it is necessary to know the density, elastic modulus, and Poisson's ratio of the metal at these temperatures.

High-temperature densities can be computed by calculating the unit volume at the desired elevated temperature. The high-temperature densities of Udimet 700 found in this way are listed in Table 7.5. In obtaining these high-temperature densities, the reported [21] values of the mean coefficient of thermal expansion for Udimet 700 over the temperature range considered was used.

To obtain values of the infinite medium sound speed at elevated temperatures, the values of Young's modulus, Poisson's ratio, and the density at the desired elevated temperatures were fed into eq (1.4). For Udimet

Table 7.5

Elevated-Temperature Data for Udimet 700 and Calculated Values of Elevated-Temperature Denting Velocity of This Alloy

Section A. Elevated-Temperature Properties				
Temp., °F	Density, ρ' , g/cm ³	Sound Speed, c' , cm/sec	Acoustic Impedance, z' , g/(cm ² .sec)	Yield Strength, E' , dyn/cm ²
68	7.916	6.365×10^5	5.038×10^6	8.412×10^9 (a)
200	7.892	6.344×10^5	5.006×10^6	----
400	7.858	6.270×10^5	4.927×10^6	----
600	7.822	6.186×10^5	4.839×10^6	----
800	7.786	6.050×10^5	4.710×10^6	7.963×10^9 (a)
1000	7.745	5.942×10^5	4.602×10^6	7.791×10^9 (a)
1200	7.701	5.805×10^5	4.470×10^6	7.653×10^9 (a)
1400	7.651	5.697×10^5	4.358×10^6	7.515×10^9 (a)
1600	7.593	5.524×10^5	4.194×10^6	5.516×10^9 (a)
1800	7.523	5.715×10^5	4.299×10^6	2.896×10^9 (a)

Section B. Elevated-Temperature Energy per Unit Volume Required for Flow and Denting Velocity

Temperature, °F	Energy per Unit Volume Required for Flow, dyn/cm ²	Denting Velocity, cm/sec
800	2.919×10^7	12.24
1000	2.840×10^7	12.30
1200	2.777×10^7	12.52
1400	2.715×10^7	12.68
1600	1.857×10^7	9.16
1800	0.870×10^7	4.12

(a) Aircraft Engine Group Material Properties Data Handbook, General Electric Company, Evendale, Ohio, See Vol. II.

700, Poisson's ratio, ν , over the desired temperature range was calculated using reported values [21] of Young's modulus and modulus of rigidity at the desired elevated temperatures

After values of infinite medium sound speed, c' , and density, ρ' , were calculated at the desired elevated temperature, the values of acoustic impedance for Udimet 700 at these temperatures were found from eq (1.2). A summary of the high-temperature properties needed to calculate high-temperature values of the denting velocity of Udimet 700 are listed in Table 7.5. Reported values [21] of 0.2 percent offset yield strength are also listed.

The energy per unit volume up to the yield strength of Udimet 700 was calculated with use of eq (7.4) for six elevated temperatures. These values are listed in Section B of Table 7.5. The values of denting velocity were then calculated with use of eq (7.3) using the calculated high-temperature values of energy per unit volume required for flow and the high-temperature values of density, sound speed, and acoustic impedance given in Table 7.5. The calculated high-temperature values of denting velocity for Udimet 700 are also listed in Section B of Table 7.5.

From the values of steel-sphere denting velocity for Udimet 700 given in Table 7.5, it can be seen that the denting velocity increases very slightly from 800°F to 1400°F. This very slight increase may or may not be meaningful. The steel-sphere denting velocity of Udimet 700 suffers a sharp decline at temperatures higher than 1600°F. The changes in sound speed and acoustic impedance with increase in temperature are gradual as can be seen from Section A of Table 7.5. Consequently, the sharp decline in denting velocity can only be due to a sharp reduction in yield strength of this alloy from which the energy per unit volume required for flow was calculated. That a sharp drop in the yield strength of Udimet 700 occurs at 1500°F can be seen from Figure 7.3. From the values of steel-sphere denting velocity for Udimet 700 given in Table 7.5, it can be seen that denting velocity is very little affected by an increase in temperature until a strong reduction in yield strength occurs.

Plans for the study that has been carried out included the measurement of the denting velocity of nickel 270 at elevated temperatures.

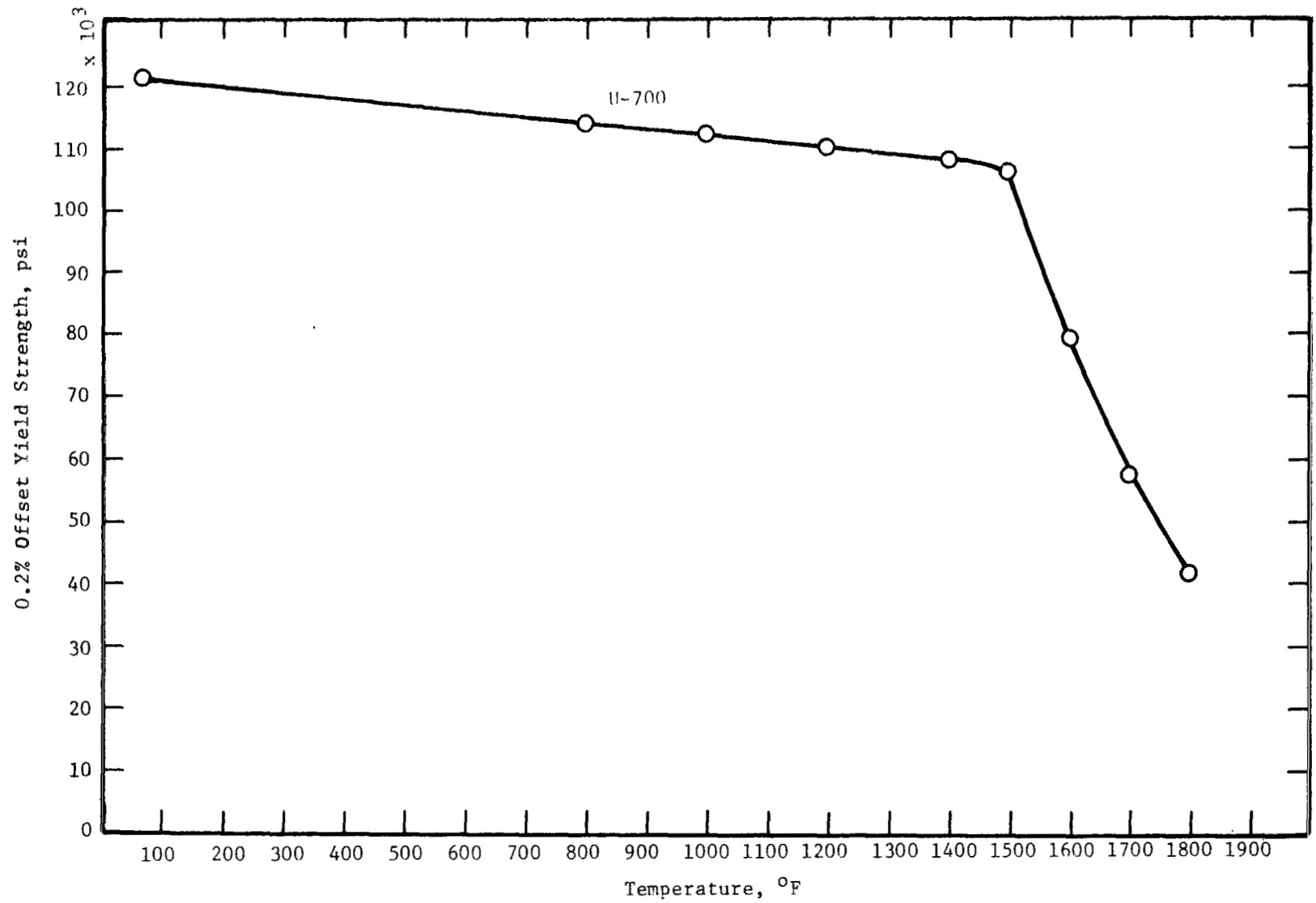


Figure 7.3. Yield Strength of Udimet 700 With Increase in Temperature. [21]

Elevated-temperature values of denting velocity for nickel 270 were not calculated because the time limit for completing the work of the study had expired.

7.3 Dynamic Yield Strengths of the Selected Metals

The third objective of the study that has been carried out was to calculate the dynamic yield strengths of the selected metals from the threshold velocities required to dent them. Evidence for an elevated dynamic strength must be sought in the results of the statistical analysis of Section 6. No displacement of the crater-depth-versus-velocity plot and no change in its slope at high velocities with respect to its slope at low velocities was observed for the face-centered-cubic metals 1100-0 aluminum, 2024-0 aluminum, and electrolytic tough pitch copper. This observation leads to the conclusion that no dynamic elevation in the yield strength of these metals occurs. The values of the slope of the line and of the velocity intercept for the low-velocity and high-velocity branch of the crater-depth-versus-velocity plots of the other selected metals are given in Table 7.6. The changes in these quantities and the signs of the changes are also given in this table.

From Table 7.6 it can be seen that the change in slope that occurred is negative for the face-centered-cubic and hexagonal-close-packed metals but is positive for the body-centered-cubic metals. The decrease in slope sustained by nickel, Udimet 700, and zinc means that the efficiency of penetration is reduced. In the case of nickel, and possibly in the case of Udimet 700, this may be the result of work-hardening. Zinc, however, has a very low work-hardening capacity (see Section 5.4).

In the case of nickel the high-velocity section of the crater-depth-versus-velocity plot branches off the low-velocity section without evidence of a displacement or translation along the impact-velocity axis (see Figure 6.2). In the case of solutioned Udimet 700, aged Udimet 700, and zinc, the high-velocity section of the curve is displaced to the right along the impact-velocity axis with respect to the low-velocity section (see Figures 6.4, 6.5, and 6.7). This displacement is associated with a larger denting velocity and, consequently, with an elevated dynamic yield strength.

Table 7.6

Characteristics of the Low-Velocity and High-Velocity Branches of the Crater-Depth-Versus-Velocity Plots

Metal	Lattice Packing Type	Critical Velocity, cm/sec	Sphere Diam. inch	Slope of Line, 10^{-4} sec			Intercept Velocity, cm/sec			Evidence of Dynamic Yield Strength
				Low Velocity Branch	High Velocity Branch	Change in Slope	Low Velocity Branch	High Velocity Branch	Change in Intercept Velocity	
Nickel 270	fcc	6500	0.175	0.05936	0.04791	-0.01145	zero	zero	zero	-
Nickel 270	fcc	6500	0.0938	0.03266	0.02540	-0.00726	119	zero	-119	-
U-700 Sol'n.	fcc	6500	0.0938	0.01177	0.01133	-0.00044	210	219	+ 9	+
U-700 Aged	fcc	6000	0.0938	0.01516	0.01167	-0.00349	367	893	+526	+
0.999 Zinc	hex	9000	0.175	0.05146	0.05065	-0.00081	zero	447	+447	+
0.999 Zinc	hex	9000	0.0938	0.02784	0.02576	-0.00208	12	28	+ 16	+
Armco Iron	bcc	10550	0.175	0.0321	0.03710	+0.00500	114	1898	+1784	+
Armco Iron	bcc	10550	0.0938	0.01624	0.01801	+0.00177	3	648	+645	+
Tantalum	bcc	18000	0.175	0.03094	0.03315	+0.00221	106	693	+587	+
Tantalum	bcc	18000	0.0938	0.01662	0.01847	+0.00185	200	1407	+1207	+

In the case of Armco iron (see Figure 6.8) and of tantalum (see Figure 6.9), the slope of the high-velocity section of the crater-depth-versus-velocity plot is increased with respect to that of the low-velocity section. The increase in slope is associated with an increase in the efficiency of penetration. In the case of Armco iron and tantalum, the increase in slope of the high-velocity section with respect to that of the low-velocity section is associated with a larger denting velocity and, consequently, with an elevated dynamic yield strength.

Bennett and Sinclair [22] have reported that in the low-temperature range, the engineering yield strength of polycrystalline body-centered-cubic metals can change by a factor of 10 or more with serious consequences appearing in the form of brittle fracture. They state that for each metal there is a temperature region where the yield strength rises rapidly with small decreases in temperature or with increases in loading or strain rate. They state further that regions of extreme dependence of yield stress on rate and temperature are generally not observed in face-centered-cubic metals but that some hexagonal-close-packed metals exhibit a rate- and temperature sensitive yield behavior that is not as pronounced as that of the body-centered-cubic metals.

Fractures in pipelines, pressure vessels, ships, and in numerous structural members have been traced directly to the change in mode of failure (from ductile failure of the low-strength state to brittle fracture of the high-strength state) and to the inability to predict the change in strength accurately [22]. The reason for the elevation in strength is not known although a number of failure models have been proposed. Bennett and Sinclair [22] state that it is likely that interstitial atoms are associated in some way with the yield behavior of the body-centered-cubic metals. Hahn, Gilbert, and Jaffee [23] report that the solubilities of interstitial elements in Group V-A metals (vanadium, columbium, and tantalum) are much greater than in Group VI-A metals (chromium, molybdenum, and tungsten). They report also that increased strain rate reduces the tolerance for interstitials.

The denting velocity which corresponds to the dynamic strengths of these metals can only be assessed as the intercept velocity of the crater-

depth-versus-velocity plot. The analysis of Section 6 has shown that the intercept velocity is very poorly known. Consequently, the elevated dynamic yield strength that will be calculated from the intercept velocity will also be known with little certainty.

The average of the intercept velocities of the high-velocity sections of the crater-depth-versus-velocity plots found with the two sizes of steel spheres that were used are given in Table 7.7. From eq (7.3), the energy per unit volume required for flow, E' , is given by

$$E' = V_i (\rho c' z')^{\frac{3}{2}} / (z + z') \quad (7.5)$$

where V_i is the denting velocity or intercept velocity, ρ is density, c is sound speed, and z is acoustic impedance; primed quantities refer to the target metal and unprimed quantities refer to the steel of which the steel spheres are composed. The elevated dynamic values of E' for solutioned Udimet 700, aged Udimet 700, zinc, iron, and tantalum (found with use of eq (7.5), the average elevated dynamic values of intercept velocity given in Table 7.7, and the values of sound speed and acoustic impedance given in Table 7.3) are given in Table 7.7. Values of dynamic yield strength back calculated from the dynamic energy per unit volume required for flow with use of eq (7.4) and the quadratic formula are also given in Table 7.7.

The values of dynamic yield strength that are given in Table 7.7 are larger than the static yield strengths of these metals (see Tables 3.2 and 7.10). In the case of solutioned Udimet 700, the factor of increase is 6.8. In the case of aged Udimet 700, the factor of increase is 14. These factors of increase are close to the factor of 10 reported by Bennett and Sinclair [22]. In the case of zinc, iron, and tantalum, the factor of increase is about 100. This is a very large factor of increase. In view of the poorness with which the values of intercept velocity are known, it should be checked by a different method such as the determination of yield strength at reduced temperature.

Two pieces of further research are suggested by the results that have been reported in this section. The first of these is that the denting velocity and cratering behavior of pure molybdenum and of a molybdenum-

Table 7.7

Dynamic Denting Velocity, Dynamic Energy per Unit Volume
Required for Flow, and Dynamic Yield Strength

Metal	High-Velocity Range, cm/sec	Average Intercept Velocity, cm/sec	Energy per Unit Volume Required for Flow dyn/cm ²	Dynamic Yield Strength, dyn/cm ²
Sol'ned. Udimet 700	above 6500	219	5.37901×10^8	5.752×10^{10}
Aged Udimet 700	above 6000	893	2.19605×10^9	1.271×10^{11}
0.999 Zinc	above 9000	238	3.09957×10^8	4.132×10^{10}
Armco Iron	above 10550	1273	2.93824×10^9	1.488×10^{11}
Arc Cast Tantalum	above 18000	1050	2.90444×10^9	1.479×10^{11}

based alloy such as TZM or TZC should be determined with use of steel-sphere firings. Molybdenum is a body-centered-cubic metal of Group VI-A. In view of the postulated role of interstitials in the development of the dynamic strengths that have been observed, and in view of the report that the Group VI-A metals have a lower solubility for interstitials than the Group V-A metals, it would be of interest to compare the high-velocity cratering response of molybdenum with that of tantalum. It would also be of interest to know to what extent the molybdenum-based alloys are subject to embrittlement under high rates of loading because these alloys are being considered as possible materials of construction for high-speed alkali-metal-vapor turbine blades.

The second piece of research suggested by the results that have been reported is a search for an improved method of determining the velocity intercept of a crater-depth-versus-velocity plot.

7.4 Test of the Cratering Equation

The fourth objective of the study that has been carried out was to calculate crater-depth-versus-velocity curves using the experimentally

determined threshold velocities and eq (2.21) of Section 2. The fifth objective was to compare the slopes of the calculated curves with the slopes of the best-fit curves and in this way to test the cratering equation. The cratering equation (eq (2.21) of Section 2) is

$$\delta' = (k \bar{d}/c) [z/(z + z')] \cdot [V - V_i]$$

where δ' is crater depth, V is impact velocity, V_i is the impact velocity for which the crater depth is just zero, z is acoustic impedance, c is sound speed, \bar{d} is sphere diameter, and k is a numerical constant; primed quantities refer to the material of the target plate and unprimed quantities refer to the steel of which the steel spheres are composed.

On the basis of past experimental crater-depth-versus-velocity plots [7], the numerical constant k was found to have a value of about 17.5 for the impacts of steel spheres against target plates of metals. Unfortunately, the metals on which the constant was based were all face-centered cubics, no cratering data were collected in the low-velocity range and the value of k was not assessed from best-fit equations. To calculate crater-depth-versus-velocity curves with use of the cratering equation, it is first necessary to determine the value of the constant k more exactly.

Equation (2.21) applies to the low-velocity crater-depth-versus-velocity curves. That is, in its present state it does not take into account changes in cratering behavior that occur as a result of work-hardening or as a result of strain-rate sensitivity due to a high concentration of interstitials. The values of the constant k^* that were found for the low-velocity sections of the crater-depth-versus-velocity plots in making the statistical analysis of Section 6 are given in Table 7.8 along with the sphere diameter and the value of the constant k which was back calculated from the experimental value of the constant k^* with use of eq (2.23).

Several conclusions are immediately evident on inspecting the calculated values of the constant k in Table 7.8. On comparing the values of k obtained with 2024-0 aluminum alloy with the values of k obtained with the pure metal 1100-0 aluminum, it can be seen that there is much

Table 7.8

Values of the Constants k^* and k

Metal	Lattice Packing Type	Pure Metal or Alloy	Constant, k^* , 10^{-4} sec/cm	Constant, k	Sphere Diameter, inch
1100-O Aluminum	fcc	pure metal	0.207106	16.7559	0.5000
1100-O Aluminum	fcc	pure metal	0.199184	16.115	0.3125
1100-O Aluminum	fcc	pure metal	0.202763	16.4046	0.2188
1100-O Aluminum	fcc	pure metal	0.195204	15.793	0.175
1100-O Aluminum	fcc	pure metal	0.196604	15.9063	0.0938
Average k				16.19	
Nickel 270	fcc	pure metal	0.133543	16.4758	0.175
Nickel 270	fcc	pure metal	0.137072	16.9112	0.0938
Average k				16.694	
Copper (tough pitch)	fcc	pure metal	0.149432	16.85	0.3125
Average k				16.85	
Zinc (0.999 purity)	hex	pure metal	0.115766	11.4145	0.175
Zinc (0.999 purity)	hex	pure metal	0.116850	11.5214	0.0938
Average k				11.468	
Iron (Armco)	bcc	pure metal	0.0722171	8.53433	0.175
Iron (Armco)	bcc	pure metal	0.0681833	8.05763	0.0938
Average k				8.296	
Tantalum (arc-cast)	bcc	pure metal	0.0696130	10.142	0.175
Tantalum (arc-cast)	bcc	pure metal	0.0697379	10.1602	0.0938
Average k				10.151	
2024-O Aluminum	fcc	alloy	(0.118354)	(9.6497)	0.5000
2024-O Aluminum	fcc	alloy	0.162280	13.2311	0.3125
2024-O Aluminum	fcc	alloy	0.141801	11.5614	0.2188
Average k	(based on two sphere sizes only)			12.396	
Udimet 700 Sol'n'd.	fcc	alloy	0.0494174	5.97029	0.0938
Udimet 700 Aged	fcc	alloy	0.0636184	7.68923	0.0938

more scatter in the values of k for the alloy than for the pure metal. This suggests that inhomogeneities in the structure of an alloy may affect the value of the cratering constant k. A second observation is that there is no trend through the values of the constant k, either for the alloy or for the pure metal, which can be associated with the trend in sphere diameter. This confirms that the constant k is independent of the size of impinging spheres.

A third observation is that, by inspection, the average value of the constant k is lower for the alloy than for the pure metal. The third observation is substantiated by comparing the values of k for pure nickel with those for the nickel-based alloy Udimet 700. Carrying the third observation further, it can be seen that, although the value of k is essentially the same for the face-centered-cubic pure metals (aluminum, nickel, and copper), it has a different value for the hexagonal pure metal (zinc), and for the body-centered-cubic pure metals (iron and tantalum). Furthermore, the value of the constant k is quite different for the two body-centered-cubic pure metals (iron and tantalum) and for the two face-centered-cubic alloys (2024-0 aluminum and Udimet 700).

Agreement in the value of the constant k provides in itself a stringent test of the cratering equation. The observation that the constant k is the same for aluminum, nickel, and copper leads immediately to the conclusion that the cratering equation in its present form is correct for face-centered-cubic pure metals that are impacted by steel spheres.

The observation that the constant k is different for different lattice packing types and for alloys suggests that a dimensionless factor is missing from the cratering equation. That a dimensionless factor might be missing was pointed out in Section 2.3. The observation that the constant k is different for the two body-centered-cubic metals (iron and tantalum) indicates that the missing dimensionless factor is not limited to a difference in lattice packing type.

The metals for the study that has been carried out were chosen on the basis that, when considered two at a time, they would have similar densities and different sound speeds or similar sound speeds and different densities (see Section 1.6). The metals, along with the values of sound

speed, density, and constant k for each, are listed in groups of two or three in Table 7.9. The members of Group I are the three metals for which the values of the constant k are closely similar. On inspection of the values of sound speed and density for the members of this group, there appears to be no obvious relation between the values of these properties and the value of the constant k. A similar conclusion results from inspecting the data for the other groups. Although it appears from the data for Group II and Group III that when density is the same k varies inversely with sound speed, the data for Group IV do not support this conclusion.

The change in the value of the constant k does correlate with the difference in the gross surface contour of the craters shown in Figure 5.4. This correlation was pointed out earlier [7] when it was first observed that the slope of the crater-depth-versus-velocity curve for steel-sphere impacts against 2024-0 aluminum was lower than that of the corresponding curves for 1100-0 aluminum and for electrolytic tough pitch copper. In Figure 5.4 it can be seen that nickel, zinc, and aluminum show no buckling of the metal around the mouth of the crater; instead, the metal immediately adjacent to the crater edge is itself depressed below the original surface of the test plate. On the other hand, in the case of tantalum, iron, Udimet 700, and 2024-0 aluminum (see Reference [7]), the metal immediately adjacent to the crater edge is raised above the original surface of the test plate.

Diagnostic tests made earlier [7] in an attempt to understand this difference in crater contour showed that it is not the effect of a tension wave reflected from the opposite side of the test plate. The tentative conclusion that was drawn from these studies was that relative work-hardening capacity of the metals might be involved. It was thought that work-hardening of the metal adjacent to the sides of the crater might favor a failure in shear around the crater at 45 degrees to the direction of incidence of the sphere that impinged over a failure in shear through the thickness of the test plate [7]. However, the study of work-hardening around the craters described in Section 5.4 has produced the result that the work-hardenability of the metals due to steel-sphere impacts is in the order: nickel > iron > Udimet 700 > (zinc, tantalum, and aluminum).

Table 7.9

Comparison of the Variation in the Constant k with
Variation in the Density and Sound Speed of the Test Metal

Metal	Group	Density, g/cm ³	Sound Speed cm/sec	Constant, k
1100-O Aluminum	I	2.713	6.318×10^5	16.19
Nickel 270	I	8.902	5.652×10^5	16.694
Copper (tough pitch)	I	8.96	4.691×10^5	16.85
Iron (Armco)	II	7.874	5.874×10^5	8.296
Zinc (0.999 purity)	II	7.133	4.340×10^5	11.468
Udimet 700	II	7.92	6.100×10^5	5.97
Nickel 270	III	8.902	5.652×10^5	16.694
Copper (tough pitch)	III	8.96	4.691×10^5	16.85
1100-O Aluminum	IV	2.713	6.318×10^5	16.19
2024-O Aluminum	IV	2.768	6.370×10^5	12.396
Iron (Armco)	V	7.874	5.874×10^5	8.296
Nickel 270	V	8.902	5.652×10^5	16.694
Zinc (0.999 purity)	VI	7.133	4.340×10^5	11.468
Tantalum (arc-cast)	VI	16.6	4.081×10^5	10.151
Udimet 700	VII	7.92	6.100×10^5	5.97
1100-O Aluminum	VII	2.713	6.318×10^5	16.19

On the other hand, the ordering of the metals in terms of the value of the constant k is: (nickel, aluminum, copper) > (zinc and 2024-0 aluminum) > (tantalum and iron) > Udimet 700. This evidence does not substantiate the role of work-hardenability as an explanation of the difference in crater contour with a consequent difference in the value of the constant k .

The raised collar of metal around the crater observed for tantalum, iron, Udimet 700, and 2024-0 aluminum, which are the metals for which the value of k is reduced, resembles the cylindrical wave that is produced when a liquid drop collides with the surface of a liquid [24]. Liquids are characterized by the property of zero strength in shear. This suggests that the formation of a raised collar of metal around a crater may be associated with the yield behavior of the metal of the test plate.

An effort has been made to find a dimensionless ratio that is associated with the yield behavior of metals and that can be used as a means of approximating the value of the constant k that will be found to be characteristic of a given metal. Bennett and Sinclair [22] have reported that the ratio of flow stress to elastic modulus appears to be the same for metals of the same crystal structure. Later evidence has substantiated this report and has showed that the ratio holds not only for the pure metals but also for alloys [25].

A test was made to determine whether or not the ratio of yield stress to elastic modulus can be correlated with the change that occurs in the numerical constant k . The value of Young's modulus was determined for each of the selected metals by assessing the initial slope of the stress-strain curve. Because this method is subject to considerable error, the value of Young's modulus was also determined for each of the selected metals with use of eq (2.17) and the measured values of speed of sound in infinite medium given in Table 3.1; literature values of Poisson's ratio were used. The values of 0.2 percent offset yield strength and of Young's modulus for the selected metals are listed in Table 7.10. It can be seen from Table 7.10 that the value of Young's modulus for zinc, as determined by the two methods that were used, is quite different. From the stress-strain curve for zinc shown in Figure 5.16, it appears

Table 7.10

Yield Strength, Poisson's Ratio, and Young's Modulus from the Measured Stress-Strain Curves and Measured Sound Speeds of the Selected Metals

Metal	0.2 percent Offset Yield Strength, 10^8 dyn/cm ²	Poisson's Ratio	Young's Modulus from Stress-Strain Curve, 10^{11} dyn/cm ²	Young's Modulus from Velocity of Sound, 10^{11} dyn/cm ²
Copper (electrolytic tough pitch)	2.721 ^(a)	0.343 ^(g)	13.6 ^(a)	12.66 ^(c)
1100-0 Aluminum	1.802 ^(a)	0.345 ^(g)	6.93 ^(a)	6.89 ^(c)
0.999 Zinc	4.535 ^(b)	0.249 ^(g)	4.96 ^(b)	11.22 ^(d)
Nickel 270	6.309 ^(b)	0.312 ^(g)	19.4 ^(b)	20.39 ^(d)
2024-0 Aluminum	8.685 ^(a)	0.345 ^(g)	7.47 ^(a)	7.15 ^(c)
Armco Iron	14.76 ^(b)	0.293 ^(g)	20.8 ^(b)	20.57 ^(d)
Arc-Cast Tantalum	15.66 ^(b)	0.342 ^(g)	15.7 ^(b)	17.82 ^(d)
Udimet 700 Solutioned	85.13 ^(b)	0.320 ^(h)	23.6 ^(b)	20.59 ^(d)
Udimet 700 Aged	89.67 ^(b)	0.320 ^(h)	26.2 ^(b)	20.63 ^(d)
52100 Steel, hardened	172.4 ^(e)	0.295 ^(g)	20.68 ^(f)	20.45 ^(d)

(a) Stress-strain curve measured by Lafayette Irwin, Mechanics Section, National Bureau of Standards, Washington, D.C. See Reference [7].

(b) Stress-strain curve measured by G.R. Frey, General Electric Company, Lynn, Massachusetts. See Section 4.4 of this report.

(c) Sound speed measured by C.E. Tschiegg, Sound Section, National Bureau of Standards, Washington, D.C. See Reference [7].

(d) Sound speed measured by H.A.F. Rocha, General Electric Materials and Processes Laboratory, Schenectady, New York. See Section 4.3 of this report.

(e) Aerospace Structural Metals Handbook, Vol. 1, Ferrous Alloys, A.F. Materials Laboratory, 3rd Rev., Syracuse University Press, 1966.

(f) Crucible Steel Company, Cincinnati Office, Telephone Communication.

(g) C.J. Smithells, Metals Reference Book, 4th Ed., Plenum Press, New York, N.Y., 1967.

(h) Calculated value.

that the Hookean region is quite poorly defined; this suggests that assessment of the value of Young's modulus from the stress-strain curve does not produce very accurate results.

The values of Young's modulus found from the measured values of infinite medium sound speed were considered to be the more reliable and were used in computing the values of the ratio of 0.2 percent offset yield strength to Young's modulus that are given in Table 7.11. The values of the ratio are plotted against the values of the constant k for the selected metals in Figure 7.4. Values of yield stress are subject to considerable variation even when determined under carefully controlled conditions. It could not be hoped that the data would fall on a line even though the points are averages of two or more values. In Figure 7.4, the curved relation has been indicated roughly with a band.

It is to be expected that more is involved in the constant k than the yield behavior of the metal selected for test. It is already known that the constant k has a different value for tough pitch copper, 1100-0 aluminum, and 2024-0 aluminum when mercury drops and waterdrops are used as projectiles rather than steel spheres. It is very likely that a change in the constant k will be observed when spheres made of solids that have values of the ratio of yield stress to elastic modulus different from that of steel are used as projectiles.

It was tentatively concluded that the desired function might be the quotient of the ratio of yield stress to Young's modulus for the steel of which the steel spheres were composed divided by the ratio of yield stress to Young's modulus for the test metal. Values of this function, which is a ratio of two dimensionless ratios and is hereafter referred to as function-R, are listed in Table 7.11; they are plotted against the average values of the constant k for the selected metals in Figure 7.5. From Figure 7.5 it appeared that function-R might bear a straight-line relationship to the constant k . Curve fitting of the average values of the constant k and the values of function-R, which are given in Table 7.11, with use of the computer program ⁽²¹⁾ was carried out. Because it is not known whether or not there is a change in slope of the cratering curve for 2024-0 aluminum as a result of work-hardening, the data for

Table 7.11

Values of the Ratio of Yield Stress to Young's Modulus for the Selected Metals and the Ratio of these Ratios to the Same Ratio for Steel

Metal	Average Value of Constant k	Ratio of 0.2% Offset Tensile Yield Stress to Young's Modulus	Function R, Ratio of 84.3×10^{-4} to the Ratio (0.2% Offset Tensile Yield Stress) / (Young's Modulus)
1100-0 Aluminum	16.19	2.615×10^{-4}	32.24
Nickel 270	16.69	3.094×10^{-4}	27.25
Copper (tough pitch)	16.85	2.149×10^{-4}	39.23
Zinc (0.999 purity)	11.47	4.042×10^{-4}	20.86
Iron (Armco)	8.30	7.175×10^{-4}	11.75
Tantalum (arc-cast)	10.15	8.788×10^{-4}	9.593
2024-0 Aluminum	12.40	12.15×10^{-4}	6.938
Udimet 700 Sol'ned.	5.97	41.35×10^{-4}	2.039
Udimet 700 Aged	7.69	43.47×10^{-4}	1.939
52100 Steel, hardened	---	84.30×10^{-4}	1.0

APPENDIX A

F-Ratios for Significance of Simple Curvature of a Line With n Points
 Compiled from Standard References by Lars H. Sjordahl, Ceramic Materials
 Research, Nuclear Systems Programs, General Electric Co., Evendale, Ohio

n = v + 3	Barely Significant 90 per cent	Significant 95 per cent	Highly Significant 99 per cent
4	39.9	161	4052
5	8.53	18.5	98.5
6	5.54	10.1	34.1
7	4.54	7.71	21.2
8	4.06	6.61	16.3
9	3.78	5.99	13.7
10	3.59	5.59	12.2
11	3.46	5.32	11.3
12	3.36	5.12	10.6
13	3.28	4.96	10.0
14	3.23	4.84	9.65
15	3.18	4.75	9.33
16	--	4.67	9.07
17	--	4.60	8.86
18	3.07	4.54	8.68
19	--	4.49	8.53
20	--	4.45	8.40
--	--	--	--
∞	2.71	3.84	6.63

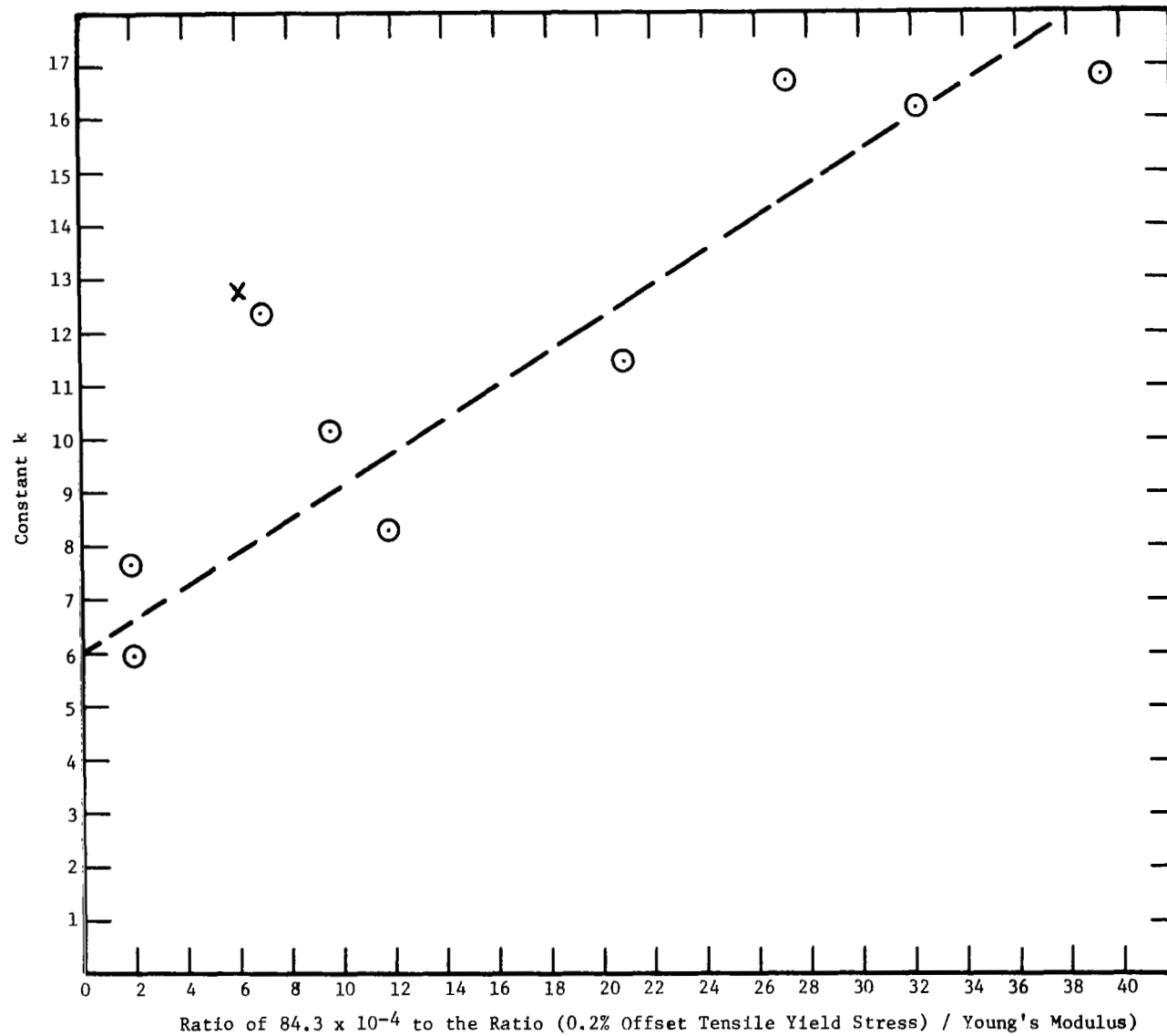


Figure 7.5. Plot of Function R (Specified Ratio for Steel to that of the Selected Metal) Against the Numerical Constant k .

2024-0 aluminum were not considered in the curve fitting. The F-ratio for the linear fit was found to be 0.176 which, for the eight data points considered, indicates that curvature is not significant. The average straight-line equation found is

$$k = 0.313744 R + 5.98103 \quad (7.6)$$

where R denotes function-R. Equation (7.6) is plotted as a dashed line in Figure 7.5. In Figure 7.5 the data point for 2024-0 aluminum, which was not used in the curve fitting, is marked with a cross.

Substituting eq (7.6) into eq (2.21) of Section 2, the revised cratering equation is found to be

$$\begin{aligned} \delta' &= (0.313744 R + 5.98103) (d/c) [z / (z + z')] \cdot [V - V_i] \quad (7.7) \\ &= K (V - V_i) \end{aligned}$$

With use of eq (7.7), values of K were calculated for each of the selected metals using the data given in Tables 7.3 and 7.11. The values of K that were found are given in Table 7.12. The theoretical loci of the crater-depth-versus-velocity plots are shown with solid lines in Figures 6.1 through 6.9. The measured values of denting velocity given in Table 7.1 were used for the quantity V_i . This was done in order to realize one of the objectives of the study in the way in which it was stated. The denting velocity should be calculated with use of eq (7.3) and the quantity E' in eq (7.3) should be calculated with use of eq (7.4).

The theoretical curves for 1100-0 aluminum, which are plotted in Figure 6.1, are in very good agreement with the experimental data and the best-fit curves. The best-fit curves shown are those found from the second statistical analysis of the data (see Table 6.3) for which scatter was reduced. The theoretical curves for nickel 270 are plotted in Figure 6.2. They are restricted to the velocity range below the threshold at which a change in slope occurs because the theoretical equation in its present form does not account for such a change in cratering characteristics. The theoretical curves for electrolytic tough pitch copper are plotted in Figure 6.3. These curves are also restricted to the velocity range below a change in slope. Comparison of these plots with those for nickel in Figure 6.2 shows that the agreement between the theoretical curves and

Table 7.12

Theoretical and Experimental Values of the
Slope of the Crater-Depth Versus Velocity Plots

Metal	Sphere Diameter, inch	Theoretical Slope, 10^{-4} sec	Experimental Slope, 10^{-4} sec	
			Value Found	95% Confidence Range
1100-0 Aluminum	0.5000	0.2527	0.2629	0.2557 to 0.2701
	0.3125	0.1579	0.1580	0.1543 to 0.1617
	0.2188	0.1106	0.1126	0.1105 to 0.1148
	0.175	0.08843	0.08670	0.08485 to 0.08856
	0.0938	0.04740	0.04677	0.04478 to 0.04876
Nickel 270	0.175	0.05235	0.05931	0.05572 to 0.06289
	0.0938	0.02806	0.03266	-- --
Copper (tough pitch)	0.5000	0.2060	0.1783	0.1569 to 0.1997
	0.3125	0.1287	0.1078	0.1043 to 0.1112
	0.2188	0.09013	0.07464	0.06526 to 0.08403
Zinc (0.999 purity)	0.175	0.05647	0.05146	-- --
	0.0938	0.03027	0.02783	0.02664 to 0.02901
Iron (Armco)	0.175	0.03636	0.03210	0.03185 to 0.03235
	0.0938	0.01949	0.01624	0.01590 to 0.01658
Tantalum (arc-cast)	0.175	0.02743	0.03093	0.03038 to 0.03148
	0.0938	0.01470	0.01660	0.01618 to 0.01703
2024-0 Aluminum	0.5000	0.1271	0.1362	0.09890 to 0.1736
	0.3125	0.07942	0.1270	0.1079 to 0.1461
	0.2188	0.05561	0.07710	0.06485 to 0.08935
Udimet 700 Sol'n'd.	0.175	0.02436	--	-- --
	0.0938	0.01306	0.01173	0.01077 to 0.01270
Udimet 700 Aged	0.175	0.02423	--	-- --
	0.0938	0.01299	0.01504	0.01122 to 0.01886

the best-fit curves is comparable in the low-velocity range.

The theoretical curves for solutioned and aged Udimet 700 are plotted in Figures 6.4 and 6.5. They are restricted to the velocity range below which dynamic behavior sets in because the theoretical equation in its present form does not account for this change in cratering behavior. The best-fit curve for the 0.175-inch-diameter spheres is missing for both of the heat-treatment states of this alloy because data were not collected at low velocities for this sphere size.

The theoretical curves for 2024-0 aluminum alloy are plotted in Figure 6.6. A second analysis of these data, with scatter reduced, was not carried out and it can be seen that the data points for the 0.5000-inch-diameter spheres are subject to wide scatter and that there is a large negative intercept velocity. No data were collected in the low velocity range and it can be seen that the best-fit curves have widely different values of intercept velocity. If the best-fit curve, E, for which the intercept velocity is negative, were translated to the right along the velocity axis until the intercept velocity had the value given in Table 7.1, it would be in good agreement with theoretical curve, E. This agreement is expected because in Table 7.12 the experimental slope for this sphere size is very close to the theoretical slope.

The theoretical curves for zinc, Armco iron, and arc-cast tantalum are shown in Figures 6.7, 6.8, and 6.9, respectively. They are restricted to the velocity ranges below the thresholds at which dynamic behavior sets in for these metals because the theoretical equation in its present form does not take this change in cratering behavior into account.

In general, from the agreement of the theoretical and experimental values of slope given in Table 7.12 and from the fit of the theoretical curves with the experimental data in Figures 6.1 through 6.9, it appears that the theoretical equation, in its revised form, gives a reasonably good representation of the experimental data. It will be of interest to collect more cratering data using rigid spheres of materials other than hardened steel to determine whether or not eq (7.7) has general validity.

In summary, on the basis of the cratering data that have been collected, it has been found that the equation for crater depth which was reported earlier is applicable only to pure face-centered-cubic metals. The restricted applicability of the equation has been traced to differences in the yield behavior of the metals which result in different crater contours. To increase the applicability of the equation, a dimensionless quotient which contains the yield stress and the elastic modulus both for the metal of the target and the metal of the sphere, has been added to the equation. The revised equation has been found to be in acceptable agreement with the available cratering data for pure metals of all three lattice packing types and for alloys. It remains to be seen whether or not it will be found to be in agreement with cratering data collected with spheres of metals other than steel.

The revised steel-sphere cratering equation is eq (7.7) where V_i is given by eq (7.3). The quantity E' in eq (7.3), which is the energy per unit volume required for flow, is given by eq (7.4) where X is the static 0.2 percent offset yield strength.

7.5 Liquid-Drop Denting Velocities from Steel-Sphere Denting Velocities

For the face-centered-cubic metals that do not exhibit an elevated dynamic strength, it should be possible to convert the denting velocity for steel-sphere impacts to the denting velocity for liquid-drop impacts. The equation for the denting velocity, V_i , for liquid-drop impacts is (see eq (1.3))

$$V_i = 19 E' (z + z') / (\rho c' z'^3)^{\frac{1}{2}}$$

where z and ρ are the acoustic impedance and the density of the liquid, respectively. The denting velocity for steel-sphere impacts, V_{iR} , is

$$V_{iR} = E' (z_R + z') / (\rho_R c' z'^3)^{\frac{1}{2}}$$

where the sub-R has been used to denote the properties of the rigid steel projectile. If the equation for V_i is divided by the equation for V_{iR} , the relation between V_i and V_{iR} is found to be

$$V_i = V_{iR} [19 \rho_R^{\frac{1}{2}} (z + z') / \rho^{\frac{1}{2}} (z_R + z')]$$

The numerical constant 19 in eq (1.3) was determined under the condition that the dynamic compressive yield strength should be used for the quantity E' . In Section 7.3 it was concluded that no dynamic elevation in yield strength occurs for the face-centered-cubic metals, and in Section 7.1.2 the value of the quantity E' , the energy per unit volume required for flow, was assessed from the static stress-strain curves. It is therefore necessary to assess the value of the numerical constant on the basis that the quantity E' will be obtained from static stress-strain curves.

The dynamic yield strength of 1100-0 aluminum is 7.239×10^8 dyn/cm² [7] and the energy per unit volume to the static 0.2 percent offset yield strength is 3.197×10^5 dyn/cm² (see Table 7.2). Using these data for 1100-0 aluminum, the numerical constant should be changed to 4.302×10^4 which is 19 multiplied by the quotient ($7.239 \times 10^8 / 3.197 \times 10^5$). The dynamic yield strength of copper is 2.394×10^9 dyn/cm² [10] and the energy per unit volume to the static 0.2 percent offset yield strength is 4.574×10^5 dyn/cm² (see Table 7.2). Using these data for copper, the numerical constant should be changed to 9.945×10^4 which is 19 multiplied by the quotient ($2.394 \times 10^9 / 4.574 \times 10^5$). The average value of the constant from the data of 1100-0 aluminum and copper is 7.124×10^4 . With this value of the constant, the relation between V_i and V_{iR} is

$$V_i = 7.124 \times 10^4 V_{iR} (\rho_R/\rho)^{\frac{1}{2}} (z + z') / (z_R + z') \quad (7.8)$$

Equation (7.8) can be tested because mercury-drop cratering data are available for 1100-0 aluminum (see Table 6.5) and both waterdrop and mercury-drop cratering data are available for copper (see Table 6.10). The density of water at 25°C is 0.99707 g/cm³ and the acoustic impedance of water at this temperature is 0.1493×10^6 g/cm² sec. The density of mercury is 13.546 g/cm³ and the acoustic impedance of mercury is 1.966×10^6 g/cm² sec. Using the values of acoustic impedance for 1100-0 aluminum and copper given in Table 7.3 and the values of steel-sphere denting velocity given in Table 7.4, it was found that the calculated value of denting velocity for single-drop impacts against 1100-0 aluminum is 12690 cm/sec when the drop liquid is mercury and that the calculated values of denting velocity for single-drop impacts against copper are 8935 cm/sec when the drop liquid is mercury and 33520 cm/sec when the drop liquid is

water. The calculated values are in good agreement with the experimental values reported in Tables 6.5 and 6.10. In only one instance (2.85-mm mercury-drop impacts against 1100-0 aluminum) is the calculated value found to be outside the 95 percent confidence range; this can be seen in Tables 6.5 A and 6.10 A.

Equation (7.8) should not be used to assess the denting velocity, V_i , of metals which exhibit a dynamic elevated yield strength or a marked change in slope.

8. SUMMARY OF PRINCIPAL CONCLUSIONS

1. The cratering process is based on conservation of momentum. This conclusion is based on the results of the initial diagnostic firings which showed (a) that movement of the target plate as a result of the impact does not affect the depth of crater produced and (b) that it makes no difference as far as crater depth is concerned whether the target plate is rigidly gripped or whether it has no support at all. The plane-wave particle velocity used in deriving the cratering equation is also based on conservation of momentum.
2. The cratering equation in its initial form applies very well to pure face-centered-cubic metals. This conclusion is based on the finding that the numerical constant k is essentially the same for pure face-centered-cubic metals (see Table 7.8). The cratering equation in its initial form is unable to give correctly the cratering curves for pure metals of other lattice types or for alloys.
3. The cratering equation in its revised form, eq. (7.7), is in acceptable agreement with the limited amount of cratering data that are available for pure metals of all three lattice packing types and for alloys. This conclusion is based on the finding that in 10 out of the 19 cases for which comparisons can be made the calculated slope of the cratering curve is either within or nearly within the 95 per cent confidence limits of the experimental slope (see Table 7.12). It remains to be seen whether or not the revised cratering equation will be in agreement with cratering data collected with spheres made of metals other than steel.
4. The cratering equation, even in its revised form, applies only to the velocity range below a change in slope of the cratering curve that may occur as a result of work-hardening or below a change in slope and/or a break in the cratering curve that may occur as a result of an increase in the yield strength of the target metal caused by the high rate of loading.
5. The additional cratering data that have been collected show that the plate thickness may be as small as one sphere diameter and as large as ten sphere diameters. It appears that plate thicknesses less than one sphere diameter will not give comparable cratering data. However, there is no evidence which indicates that ten sphere diameters is an upper limit on plate thickness; no upper limit has as yet been found.

6. Liquid-drop denting velocities can be calculated from steel-sphere denting velocities for metals which do not exhibit a dynamic elevated yield strength or a marked change in cratering behavior as a result of work-hardening.

7. The denting velocity of metals is essentially unchanged by an increase in temperature until a temperature is reached at which a marked reduction in the yield strength of the target metal occurs. This means that the denting velocity of metals, which may be found to be a good criterion of drop-impact erosion resistance, can be assessed at room temperature for high-temperature applications.

8. Evidence of an elevated dynamic yield strength was found in the cratering curves of metals of the body-centered-cubic and hexagonal close-packed lattice types. Evidence of an elevated dynamic yield strength was also found for Udimet 700 alloy; this may be due to the presence of interstitials. No evidence of an elevated dynamic yield strength was found in the cratering curves of pure face-centered-cubic metals.

9. An expression has been found by means of which the quantity E' , the energy per unit volume required for flow, can be assessed from the static 0.2 per cent offset yield stress. The quantity E' appears in the cratering equation.

10. Determination of the intercept velocity of a crater-depth-versus-velocity plot is not a good way of assessing the denting velocity of metals. The denting velocity can be calculated from the quantity, E' , the energy per unit volume required for flow.

APPENDIX A

F-Ratios for Significance of Simple Curvature of a Line With n Points
 Compiled from Standard References by Lars H. Sjodahl, Ceramic Materials
 Research, Nuclear Systems Programs, General Electric Co., Evendale, Ohio

$n = v + 3$	Barely Significant 90 per cent	Significant 95 per cent	Highly Significant 99 per cent
4	39.9	161	4052
5	8.53	18.5	98.5
6	5.54	10.1	34.1
7	4.54	7.71	21.2
8	4.06	6.61	16.3
9	3.78	5.99	13.7
10	3.59	5.59	12.2
11	3.46	5.32	11.3
12	3.36	5.12	10.6
13	3.28	4.96	10.0
14	3.23	4.84	9.65
15	3.18	4.75	9.33
16	--	4.67	9.07
17	--	4.60	8.86
18	3.07	4.54	8.68
19	--	4.49	8.53
20	--	4.45	8.40
--	--	--	--
∞	2.71	3.84	6.63

REFERENCES

1. Olive G. Engel, Waterdrop Collisions With Solid Surfaces, Nat'l. Bur. Stds. Jour. of Research 54, 281 (1955).
2. Olive G. Engel, Mechanism of High-Speed-Waterdrop Erosion of Methyl Methacrylate Plastic, Nat'l. Bur. Stds. Jour. of Research 54, 51 (1955).
3. Olive G. Engel, Erosion Damage to Solids Caused by High-Speed Collision With Rain, Nat'l. Bur. Stds. Jour. of Research 61, 47 (1958).
4. Olive G. Engel, Resistance of White Sapphire and Hot-Pressed Alumina to Collision With Liquid Drops, Nat'l. Bur. Stds. Jour. of Research 64A, 499 (1960).
5. Olive G. Engel, Model for Multiple-Drop-Impact Erosion of Brittle Solids, NASA Technical Memorandum 33-354, edited by Lance G. Hays, June 15, 1967. See also J. B. Marriott and G. Rowden, The Erosion of a Cobalt-Chromium Alloy by Liquid Impact, Phil. Trans. Roy. Soc., 260A, 144 (1966).
6. Olive G. Engel, Pits in Metals Caused by Collision With Liquid Drops and Soft Metal Spheres, Nat'l. Bur. Stds. Jour. of Research 62, 229 (1959).
7. Olive G. Engel, Pits in Metals Caused by Collision With Liquid Drops and Rigid Steel Spheres, Nat'l. Bur. Stds. Jour. of Research 64A, 61 (1960).
8. R. Garcia, F. G. Hammitt and R. E. Nystrom, Comprehensive Cavitation Damage Data for Water, Mercury, and Lead-Bismuth Alloy Including Correlations With Material and Fluid Properties, A.S.T.M. Symposium on Erosion by Cavitation or Impingement, Atlantic City, N.J., June 28, 1966. See A.S.T.M. Special Technical Publication No. 408.
9. A. H. Cottrell, Theoretical Structural Metallurgy, St. Martin's Press, New York, N.Y., 1962.
10. A. C. Whiffin, The Use of Flat-Ended Projectiles for Determining Dynamic Yield Stress, Proc. Roy. Soc. (London) A 194, 300 (1948).
11. See, for example, James F. Bell, The Dynamic Plasticity of Metals at High Strain Rates; an Experimental Generalization, published in

- Behavior of Materials Under Dynamic Loading, American Society of Mechanical Engineers, 1965. Professor Bell is the author of many other papers on this subject.
12. Professor James F. Bell, John Hopkins University, Baltimore, Md., personal communication.
 13. B. d. Saint-Venant, Journal of Mathematics Pure and Applied, 2nd Series, Vol. 12 (1867).
 14. S. Timoshenko and J. N. Goodier, Theory of Elasticity, 2nd Edition, McGraw-Hill Book Co., Inc., 1951.
 15. A. E. H. Love, Mathematical Theory of Elasticity, 4th Edition, Dover Publications, New York, N.Y., 1944.
 16. See, for example, F. W. Sears and M. W. Zemansky, University Physics, Addison-Wesley Publishing Company, Inc., Reading, Mass., 1956.
 17. See, for example, P. E. Smith, A. S. Gale, and J. H. Neelley, New Analytic Geometry, Ginn and Company, New York, N.Y., 1928.
 18. Olive G. Engel, Mechanism of Drop-Impact Erosion of Udimet 700 Alloy, to be published.
 19. R. M. Davies, The Determination of Static and Dynamic Yield Stresses Using a Steel Ball, Proc. Roy. Soc. (London) 197 A, 416 (1949).
 20. H. Raether, Zeit. Physik 124, 286 (1948).
 21. Aircraft Engine Group Material Properties Data Handbook, General Electric Company, Evendale, Ohio.
 22. P. E. Bennett and G. M. Sinclair, Parameter Representation of Low-Temperature Yield Behavior of Body-Centered Cubic Metals, Jour. Basic Engineering 88, 518 (1966).
 23. G. T. Hahn, A. Gilbert, and R. I. Jaffee, The Effect of Solutes on the Ductile-to-Brittle Transition in Refractory Metals, DMIC Memorandum 155, Defense Metals Information Center, Battelle Memorial Institute, Columbus 1, Ohio.
 24. Olive G. Engel, Crater Depth in Fluid Impacts, Jour. Appl. Physics 37, 1798 (1966).
 25. Prof. G. M. Sinclair, telephone conversation.